Tumor microenvironment models: *ex vivo*, *in vitro* and *in silico* approaches to address targeted therapies

Ana Luísa Pécurto Cartaxo

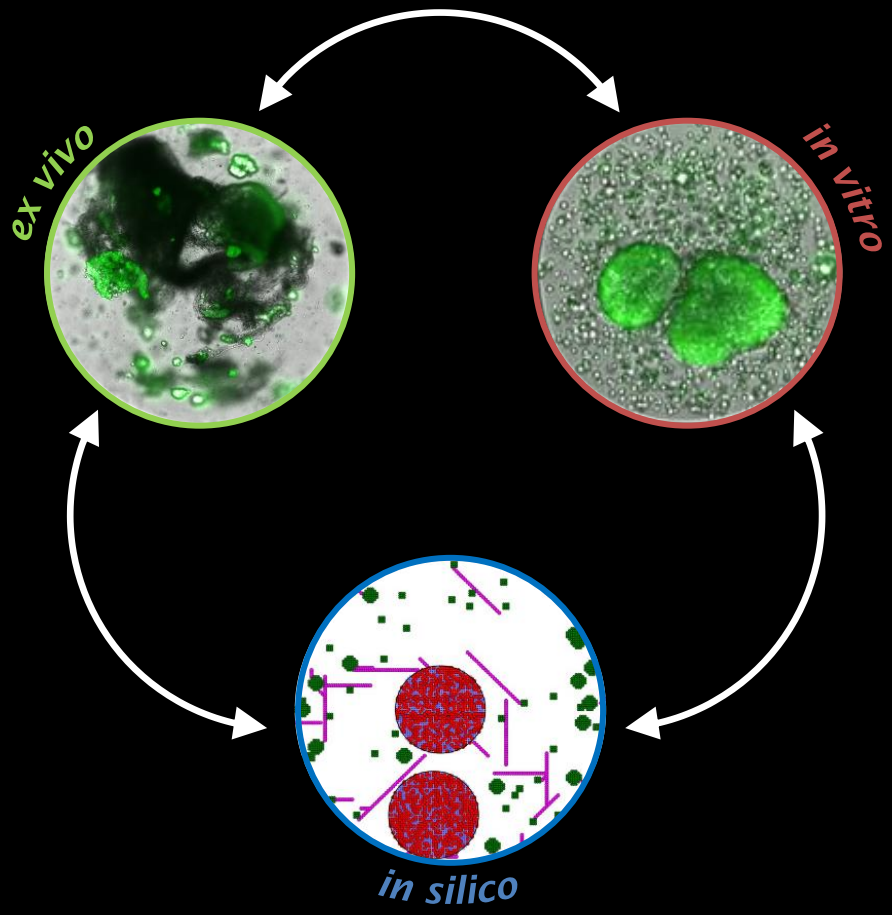

Dissertation presented to obtain the Ph.D. degree in Bioengineering

Instituto de Tecnologia Química e Biológica António Xavier | Universidade Nova de Lisboa

Oeiras,
October, 2020

UNIVERSIDADE NOVA DE LISBOA

Tumor microenvironment models: *ex vivo*, *in vitro* and *in silico* approaches to address targeted therapies

Ana Luísa Pécurto Cartaxo

Dissertation presented to obtain the Ph.D. degree in Bioengineering

Instituto de Tecnologia Química e Biológica António Xavier | Universidade Nova de Lisboa

Oeiras, October 2020

Tumor microenvironment models: *ex vivo*, *in vitro* and *in silico* approaches to address targeted therapies

Ana Luísa Pécurto Cartaxo

The work developed in this thesis was supervised by:

- **Doctor Catarina Brito**, Instituto de Biologia Experimental e Tecnológica (iBET) e Instituto de Tecnologia Química e Biológica António Xavier, Universidade Nova de Lisboa (ITQB-NOVA)

Financial support from:

Fundação para a Ciência e Tecnologia (FCT), Ph.D grant PD/BD/114047/2015

iNOVA4Health (UID/Multi/04462/2013), financially supported by FCT/MEC, through national funds and co-funded by FEDER under PT2020 Partnership Agreement

Tumor microenvironment models: *ex vivo*, *in vitro* and *in silico* approaches to address targeted therapies

Instituto de Tecnologia Química e Biológica António Xavier
Universidade Nova de Lisboa

Aos pilares da minha vida, família e amigos

Acknowledgments

I would like to express my gratitude to all the people who have contributed directly or indirectly to this thesis.

To my supervisor, Catarina Brito, for all the guidance, the scientific discussions and to always remind me to be focused on my PhD.

To the hosting institutions, iBET and ITQB, for the excellent working conditions, in particularly to Prof. Paula Alves for giving me the opportunity to work in such amazing conditions at the Animal Cell Technology Unit.

To my thesis committee members, Inês Pires da Silva, Inês Isidro and Ana Barbas, for the discussion and feedback during the several steps of my PhD work. Specially, I would like to thank Inês Isidro for her invaluable help in the *in silico* model project.

To the IPOLFG team, especially to Saudade André, for always believing in our research and for the amazing effort in providing the primary material for the *ex vivo* breast cancer model project. Also, I would like to thank Ruben Roque and Fernanda Silva for their help in the processing and analysis of samples at the hospital. More importantly, and because without them this work could not be performed, I would like to sincerely thank all patients that agreed in entering this study and give their tissues for research purposes.

To ICFO, specifically to Pablo Loza-Alvarez, for accepted receiving me in his group institution, in Barcelona. To Emilio Gualda, Maria Marsal and Monica Marro for all your "teaching lessons", support and help to make my PhD more complete and valuable.

To the “3D team”, Teresa Mendes, Rita Mendes, Francisca Arez, Nuno Lopes, Sofia Batalha, Beatriz Painho, Rodrigo Eduardo; and all ex-members, Sofia Rebelo, Marta Estrada, Ana Paula Terrasso, Daniel Simão, Lara Silva, Raquel Moita, Tatiana Martins, João Sá and Catarina Pinto, thank you for all the help, discussions and suggestions. I would like to give a very special thanks to Giacomo, who was always available to help me in all tasks of my PhD: he was crucial in the *ex vivo* breast cancer model work. Thank you for all “Molecular Biology teaching moments”, for the fruitful discussions and above all for being after all a very good friend.

To all my colleagues at the Animal Cell Technology Unit for creating such a great working environment and a special thanks to Ana Raposo for her help in managing orders and make always an effort to maintain everything on date.

To the MIT-Portugal PhD Program, for accepting me in this new step of my life. Especially to everyone involved in the Bioengineering Systems PhD, professors and colleagues for the intense learning and friendship.

Aos meus amigos, por todo o apoio emocional e por me convidarem para sair quando precisava apanhar ar e esquecer o doutoramento por breves momentos.

Ao Jaime, pela sua capacidade de me levantar sempre a moral e de me dizer incessantemente “vai correr tudo bem”. Por a tua ajuda incansável com o modelo computacional e todas as lições nocturnas de Python. Obrigado por acreditares sempre nas minhas capacidades e estares sempre ao meu lado.

À minha família pelo apoio incondicional durante estes 4 anos com fases de altos e baixos. Obrigada pelo vosso suporte e confiança; pelos momentos de motivação. Ao meu pai pelo seu forte *scientific background* que sempre "puxou" por mim e pelas discussões frutíferas a tenderem para infinito sobre o modelo computacional. À minha mãe que sempre me motivou a não desistir e ser perseverante.

Abstract

Cancer is the second leading cause of mortality worldwide, despite the extraordinary advances in the last two decades due to the development of targeted therapies. These target particular molecules required for cell growth and tumorigenesis; nonetheless, *de novo* or acquired resistance to therapy often lead to patient relapse and disease progression. There is cumulating evidence supporting the importance of tumor microenvironment (TME)-driven mechanisms in cancer progression and drug resistance. Therefore, there is a need for cancer models in which critical components of the TME, such as the non-malignant cell types and the extracellular matrix (ECM), are represented and tissue architecture is maintained.

The overarching aim of the work presented in this thesis was the development of cancer models to address targeted therapies in TME-relevant contexts.

Chapter I reviews the state-of-art, in terms of breast cancer (BC) subtypes, available therapies, relevance of the TME for therapeutic response, and available experimental and computational models.

In **Chapter II**, an *ex vivo* approach was explored to develop a BC patient-derived 3D cell model. Our strategy was based on encapsulation in alginate, an inert biomaterial, to promote the retention of the original TME, combined with dynamic culture, to promote diffusion of macromolecules and oxygen. The original tissue architecture and microenvironment components, namely epithelial, mesenchymal, endothelial, and immune cells, as well as an ECM composed of collagen fibers, were retained. Importantly, in the case of estrogen receptor α (ERα)-positive breast tumors, the

retention of the TME sustained ERα expression, at gene and protein level. Response to ERα stimulation and inhibition was observed at the level of downstream targets, demonstrating active ERα signaling. Moreover, the challenge experiments with the ERα inhibitor fulvestrant, widely used in endocrine therapy, stands as a proof-of-concept for the application of the model in the study of anti-endocrine targeted therapies.

In **Chapter III**, we focused on the biochemical and mechanical properties of the alginate capsules, since mechanical cues have been reported to influence tumor progression. For this, we employed 3D *in vitro* co-cultures of tumor cells and fibroblasts, a model previously established by our group for the reconstruction of the microenvironment of solid tumors. We showed that alginate encapsulation sustains BT474 BC spheroids phenotype and proliferation. Moreover, we observed that the mechanical properties of the capsule were affected by its content: the presence of cancer cell spheroids reduced the stiffness relatively to empty capsules; fibroblasts contributed to a stiffening of the microenvironment, when compared to the mono-culture capsules. Overall, this study contributed for the characterization of alginate capsules, employed by many research groups.

Finally, in **Chapter IV**, we addressed antibody transport within the TME. We explored the *in vitro* model system characterized in Chapter III to implement an integrated experimental and computational framework. The aim of the framework was to unravel how the several TME components influence antibody distribution. Encapsulated co-cultures were challenged with a fluorescent antibody and its location within the alginate capsules was tracked using light sheet fluorescent microscopy. The obtained

data was then used to benchmark a computational model, developed to simulate a digitized alginate capsule slice. The benchmarked model can also be used to generate other capsule configurations, according to user specifications.

In the present thesis, we created and characterized new tools to tackle the influence of TME in targeted cancer therapies. We explored experimental approaches to establish *ex vivo* and *in vitro* cancer models, in which key features of the TME could be retained or reconstructed, respectively. The *in vitro* model was complemented by *in silico* approaches to describe transport of therapeutics within the reconstructed TMEs. These distinct, yet complementary approaches, are tools that can contribute to unravel the mechanisms underlying therapeutic response of solid tumors and as drug discovery platforms to assess novel targeted therapies.

Key words: tumor microenvironment, *ex vivo* models, *in vitro* models, *in silico* models, targeted cancer therapy

Resumo

O cancro é a segunda principal causa de mortalidade a nível mundial, apesar dos avanços extraordinários nas últimas duas décadas devido ao desenvolvimento de terapias direccionadas. Estas têm como alvo moléculas específicas que são necessárias ao crescimento celular e à formação de tumores. No entanto, a resistência inata ou adquirida à terapia conduz frequentemente a reincidência e à progressão da doença. Actualmente, existem evidências que apoiam a importância dos mecanismos moleculares relacionados com o microambiente tumoral (TME) na progressão do cancro e na resistência aos fármacos. Assim, existe uma procura por modelos de cancro em que os componentes críticos do TME, tais como tipos de células não-malignas e a matriz extracelular (ECM), estejam representados e em que a arquitectura dos tecidos seja mantida.

O objectivo primário do trabalho aqui apresentado foi desenvolver modelos oncológicos para abordar terapias direccionadas no contexto do TME.

O **Capítulo I** revê o estado da arte em termos de subtipos de cancro da mama (BC), terapias existentes, a relevância do TME na resposta terapêutica, bem como modelos experimentais e computacionais já publicados.

No **Capítulo II** foi testada uma abordagem *ex vivo* de forma a desenvolver um modelo celular 3D, baseado em tecido tumoral mamário de pacientes. A nossa estratégia baseou-se no encapsulamento em alginato, um biomaterial inerte, de forma a promover a retenção do TME original. Recorreu-se a um sistema de

cultura dinâmico que facilita a difusão de macromoléculas e oxigénio. A aplicação desta estratégia resultou na retenção da arquitectura original do tecido, incluindo os componentes do microambiente tumoral (fibroblastos e células epiteliais, endoteliais e imunitárias, bem como a ECM composta por fibras de colagénio). É de salientar que, no caso de tumores mamários positivos para o receptor de estrogénio α (ERα), a manutenção do TME reteve a expressão ERα, tanto a nível transcricional e como proteico. A resposta à estimulação e inibição do ERα foi observada ao nível de genes-alvo a jusante, demonstrando assim que a sinalização ERα se encontrava activa. Além disso, as experiências com o inibidor de ERα fulvestrant (amplamente utilizado em terapia endócrina) representaram uma demonstração da aplicabilidade do modelo no estudo de terapias anti-endócrinas.

O enfoque do **Capítulo III** foi a caracterização bioquímica e mecânica das cápsulas de alginato, dado que alguns parâmetros mecânicos têm sido reportados como moduladores da progressão tumoral. Para tal, utilizámos co-culturas 3D *in vitro* de células tumorais e fibroblastos, um modelo previamente estabelecido pelo nosso grupo para reconstrução do microambiente de tumores sólidos. Com este modelo, demonstrámos que o encapsulamento com alginato sustenta o fenótipo e a proliferação de esferóides de BC, BT474. Observámos ainda que as propriedades mecânicas da cápsula foram afectadas pelo seu conteúdo: a presença de esferóides de células cancerígenas reduziu a rigidez relativamente à de cápsulas vazias; e os fibroblastos contribuíram para um endurecimento do microambiente, em relação à cápsulas de mono-cultura. Em suma, este estudo contribuiu para a caracterização de

cápsulas de alginato, amplamente utilizado por muitos grupos de investigação.

No **Capítulo IV** abordámos o transporte de anticorpos no TME. Explorámos o modelo *in vitro* caracterizado no Capítulo III, de forma a implementar um *framework* experimental e computacional integrado. O *framework* teve como objectivo a representação dos diferentes componentes do TME e da sua influência no transporte de anticorpos. As co-culturas encapsuladas foram tratadas com um anticorpo fluorescente cuja localização dentro da cápsula foi rastreada utilizando *light sheet fluorescence microscopy*. Os dados obtidos foram então utilizados para treinar um modelo computacional, desenvolvido para simular uma fatia digitalizada da cápsula de alginato. Este modelo treinado pode ser utilizado para gerar novas configurações de cápsulas, de acordo com as especificações do utilizador.

Nesta tese, criámos e caracterizámos novas ferramentas para avaliar a influência do TME na reposta a terapias de cancro dirigidas. Explorámos abordagens experimentais para estabelecer modelos de cancro *ex vivo* e *in vitro*, nos quais características importantes do TME foram respectivamente retidas e reconstruídas. O modelo *in vitro* foi complementado por abordagens *in silico*, de forma a descrever o transporte de fármacos no TME reconstruído. Estas abordagens distintas mas complementares, são ferramentas que tanto podem contribuir para descobrir os mecanismos subjacentes à resposta de tumores sólidos à terapia; bem como podem funcionar como plataformas para teste de novas terapias.

Palavras-chave: micro-ambiente tumoral, modelos *ex vivo*, modelos *in vitro*, modelos *in silico*, terapia anti-cancro dirigida

Thesis publications

Ana Luísa Cartaxo*, Marta F Estrada*, Giacomo Domenici, Ruben Roque, Fernanda Silva, Emilio J. Gualda, Pablo Loza-Alvarez, George Sflomos, Cathrin Brisken, Paula M. Alves, Saudade André, Catarina Brito; *A novel culture method that sustains ERα signaling in human breast cancer tissue microstructures*, Journal of Experimental & Clinical Cancer Research, 2020, doi: 10.21203/rs.3.rs-20405/v1, accepted for publication

Ana Luísa Cartaxo, Jaime Almeida, Emilio J. Gualda, Maria Marsal, Pablo Alvarez-Loza, Catarina Brito, Inês A. Isidro; *A computational diffusion model to study antibody transport within reconstructed tumor microenvironments*, submitted to BMC Bioinformatics

Ana Luísa Cartaxo, Henrique Almeida, Tomás Calmeiro, Daniela Gomes, Elvira Fortunato, Catarina Brito; *3D cancer cell models in alginate capsules: biochemical and mechanical characterization*, in preparation

*equally important contribution

Other publications

Nuno Lopes, **Ana Luísa Cartaxo**, Giacomo Domenici, Catarina Pinto, Sofia Rebelo, Emilio J Gualda, Pablo Loza-Alvarez, Maria José Oliveira, Catarina Brito, *Exploiting 3D cell models to recapitulate macrophage modulation in the breast cancer microenvironment*, in preparation

Table of contents

List of figures

List of tables

List of abbreviations

AB: alcian blue

ABC: ATP-binding cassette

ADC: antibody-drug-conjugate

AF: aldehyde fuschin

AFM: atomic force microscopy

APC: antigen presenting cells

AREG: amphiregulin

ATCC: American Type Culture Collection

ATP: adenosine triphosphate

BC: breast cancer

BCRP: BC resistance protein

BFGS: Broyden-Fletcher-Goldfarb-Shanno

CAA: cancer-associated adipocytes

CAF: cancer-associated fibroblast

CDK: cyclin-dependent kinase

CDX: cell line-derived xenograft

CK: cytokeratin

CSF-1: colony stimulating factor

CTRL: control

CTGF: connective tissue growth factor

CTLA4: cytotoxic T-lymphocyte-associated protein 4

CXCR: CXC-chemokine receptor

DBD: DNA binding domain

DCIS: ductal carcinoma *in situ*

DMEM: Dulbecco's Modified Eagle Medium

ECM: extracellular matrix

EDTA: ethylenediaminetetraacetic acid

EMDR: environment-mediated drug resistance

EMT: epithelial-to-mesenchymal transition

FEP: fluorinated ethylene propylene

ERBF-1: estrogen receptor promoter B associated factor 1

ERα: estrogen receptor α

ERβ: estrogen receptor β

ER+ BC: estrogen receptor α-positive breast cancer

FBS: fetal bovine serum

FDA: fluorescein diacetate

FGF: fibroblast growth factor

FSG: fish skin gelatin

GAG: glycosaminoglycan

GEMM: genetically engineered mouse model

GM-CSF: granulocyte-macrophage colony-stimulating factor

HA: hyaluronic acid

H&E: hematoxylin and eosin

HD: hanging-drop

hDF: human dermal fibroblast

HER2: human epidermal growth factor receptor 2

HGF: hepatocyte growth factor

Hsp: heat-shock protein

IFN-γ: interferon gamma

IHC: immunohistochemistry

IL: interleukin

IMDM: Iscove's Modified Dulbecco's Medium

LBD: ligand binding domain

LCIS: lobular carcinoma *in situ*

LOT: liquid overlay technique

LSFM: light sheet fluorescence microscopy

MAPK: mitogen-activated protein kinase

MDSC: myeloid-derived suppressor cell

MIDN: intraductal mouse model

MMP: matrix metalloprotease

NF-kβ: factor nuclear kappa B

nGEMM: non-germline genetically engineered mouse model

NK: natural killer

NSCLC: Non-Small Cell Lung Carcinoma

NST: no special type

PDGF: platelet-derived growth factor

PD-1: programmed cell death protein 1

PDX: patient-derived xenograft

PFA: paraformaldehyde

PI: propidium iodide

PIL: Python Imaging Library

PI3K: phosphoinositide 3-kinase

PIP3: phosphatidylinositol (3,4,5) trisphosphate

PGR: progesterone receptor gene

PR: progesterone receptor

P/S: penicillin-streptomycin

PSR: picrosirius red

PTEN: phosphatase and tensin homolog

RMSE: root mean square error

RPMI: Roswell Park Memorial Institute

RT: room temperature

SEM: scanning electron microscopy

SERD: selective ER down-regulator

SERM: selective ER modulator

SHG: second harmonic generation

SMI: small-molecule inhibitor

ST: special type

TAM: tumor-associates macrophage

TDLU: terminal duct-lobular unit

TGFβ: transforming growth factor β

TF: transcription factor

TFF1: trefoil factor-1

TME: tumor microenvironment

Timp: tissue inhibitor of metalloproteinase

TKI: tyrosine kinase inhibitor

TPEF: two-photon-excited fluorescence

VEGF: vascular endothelial growth factor

VEGFR: vascular endothelial growth factor receptor

YM: Young modulus

2D: two-dimensional

3D: three-dimensional

CHAPTER I

Introduction

Table of contents

1. Breast cancer

Breast cancer (BC) is a pathology which affects the mammary gland, characterized by an abnormal growth of cancer cells that eventually evolve and invade healthy regions [1]. The vast majority of invasive BCs, and their *in situ* precursors, originate from the terminal duct-lobular unit (TDLU) [2]. This is a structure in the breast composed of a lobule, which is a small cluster of acini, and the terminal duct [3] (Figure 1.1). BC can spread to other tissues in the body, giving origin to metastasis, mainly in lung, bone, lymph nodes and liver [4].

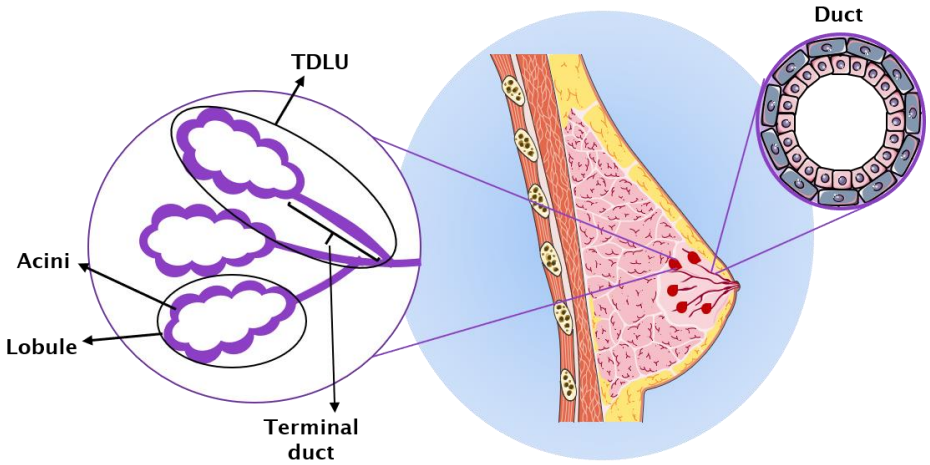

Figure 1.1: Schematic of segment of breast lobe showing the TDLU, lobules, acini and the duct system [2,3].

BC represents a major public health problem, since it is the cause of the greatest number of cancer-related deaths among women [5]. Although organ-confined disease is mainly curable, metastatic and recurrent disease has poor prognosis with a 5-year survival of only 27% [6]. In the USA, about 1 in 8 women will develop invasive BC over the course of their lifetime [7]. More than 300,000

new BC cases are predicted to be diagnosed and more than 40,000 people are predicted to die due to BC, in 2020 [7]. In 2008, the estimated total productivity loss as a result of premature mortality due to BC was $5.49 billion, for young women (aged 20–49) [8]. Metastatic BC represent a significant economic and social burden associated with high costs for healthcare systems, with direct costs alone accounting for as much as $4.2 billion per year [9]. In Europe, BC had an incidence estimated to be higher than 500,000 cases in 2018, accounting for €15 billion in 2009, which corresponded to 12% of the total cancer-related costs [10].

Fortunately, advances in the screening methods (such as digital mammography coupled with advanced computer-aid detection), early diagnosis, and breakthroughs in treatments have increased BC survival rates [11]. Since 1990, a decline in BC mortality started to be observed. This was due to the routine implementation of adjuvant therapy (that will be explained later on this chapter, section 4) and mammographic screening [12]. BC research has contributed significantly to the discovery of molecular pathways involved in tumorigenesis, that are the basis of the targeted therapies currently used in the clinics [13]. Nonetheless, BC relapse is still a relevant issue for a high number of patients: the high incidence of metastatic disease and drug resistance contribute to the high morbidity and mortality indexes [14–16]. So, it is important to uncover the molecular mechanisms which stand behind drug resistance and develop novel drugs and therapeutic regimens that overcome those mechanisms.

2. Breast cancer classification

BC is a genetically, histologically, biologically and clinically heterogeneous disease [17,18]. Given such heterogeneity, different response to therapy and outcome are reported [19,20] and various classification at histological and molecular levels have been purposed to categorize BC [2,19].

Histologically, BC can be divided according with the invasiveness status of the disease into: *in situ* or invasive. *In situ* refers to tumors confined to the ducts (ductal carcinoma *in situ*, DCIS) and lobules (lobular carcinoma *in situ*, LCIS, Figure 1.2) [2]. DCIS can be further divided in several subgroups according to the tumor architecture features [2]. Regarding the invasive BC group, which refers to tumors that are not limited to the epithelial region but that have already penetrated into the surrounding stroma [2], it includes the "no special type" (NST) and "special type" (ST). The ST represents 25% of the invasive BC cases and contains tumor with a predominant (i.e. >90% of the tumor) differentiation [2,21]. On the other hand, the NST represents the remaining 75% of the cases and contains tumor with heterogeneous features without any special differentiation patterns [20].

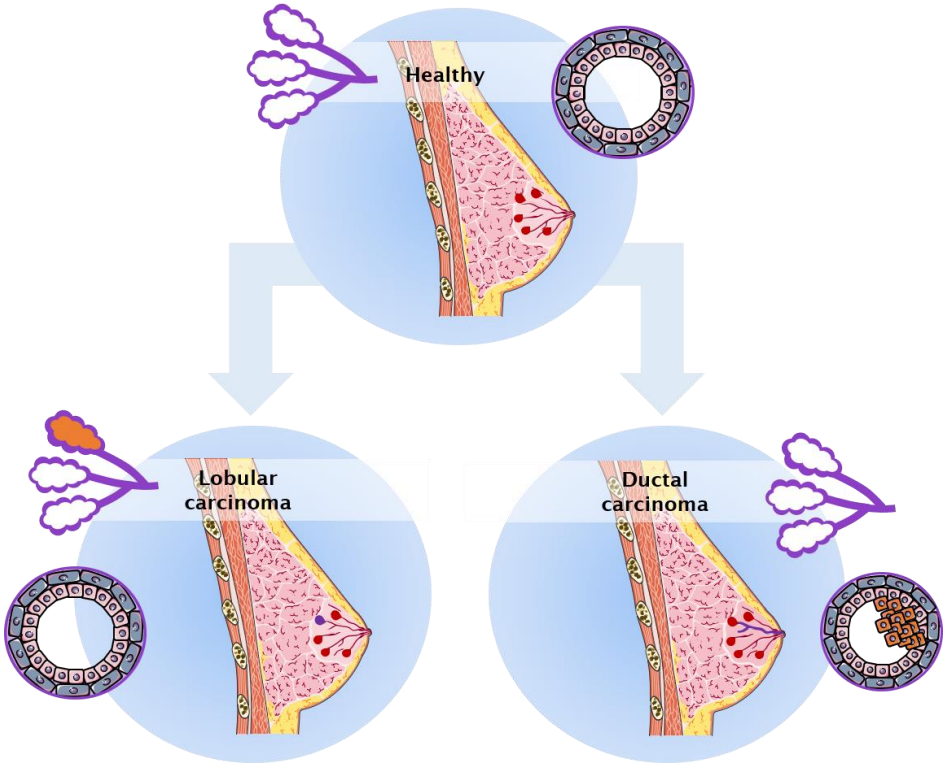

Figure 1.2: Healthy breast and two BC histological subtypes (ductal and lobular). Cancerous region is highlighted in dark purple in the mammary overall structure and the cell overgrowth highlighted in the region of the breast tissue where it occurs (orange region) [2].

It is difficult to establish a relationship between histological classification and patient outcome [22]. The significant differences, in terms of treatment and long-term survival, detected among patients having the same histological classification, support the belief that BC is an heterogeneous group of diseases [22]. This highlights the need for a BC classification based on tumor features that can be related with prognosis. In the past decade, microarray-based gene expression profiling has been extensively applied to the study of BC and led to a classification based on molecular signatures, reflecting differences on tumor cell biology rather than on morphology [20,22,23].

The molecular classification of BC was proposed for the first time in 2000 by Perou, Sorlie *et al.* [23]. It was based on the gene expression characterization patterns of a set of 65 surgical specimens of BC from 42 different individuals, using complementary DNA microarrays covering 8,102 human genes [23]. Patients were clustered into different groups according with the overall transcriptome differences. They identified four groups of samples: estrogen receptor α (ERα) positive/luminal-like, basal-like, Erb-B2+/human epidermal growth factor receptor 2 (HER2) positive and normal-like BC [23]. In a work published one year later, gene expression patterns were used as a prognostic marker with respect to overall and relapse-free survival [24]. This work suggested to further divide the "estrogen receptor positive" in two distinct groups (luminal subtype A and subtype B), with distinctive expression profile [23,24].

Currently, the standard molecular classification of BC divides tumors into five groups with unique biologic and prognostic features: luminal A, luminal B, HER2, basal-like and normal-like [20,22]. Luminal tumors display high expression levels of luminal cytokeratins (CK), such as CK8, CK18 and CK19 [25]. Luminal A includes ERα-positive and HER2-negative cells with low levels of ki67 proliferation marker [20,22]. Luminal B, with significantly worse prognosis than luminal A, includes ERα-positive and HER2-positive cells, with higher proliferation rates [20,22]. The HER2 subtype includes cells with high expression of HER2 and low expression of ERα [20,22]. This highly proliferative and aggressive BC subtype represents ~15% of all the invasive BC cases [22] and usually has an unfavorable prognosis. The basal-like BC subtype accounts for up to 15% of all BC [26]. Basal BC cells typically express basal CKs, such as CK5, CK6

and CK14, have low or undetectable ERα and HER2 levels and are highly proliferative [22]. Most basal-like BC have a triple-negative phenotype (ERα-negative, progesterone receptor (PR)-negative and HER2-negative), but up to 20% express ERα or overexpress HER2 [27]. Patients with this subtype of BC have the worst prognosis among all BC subtypes because of the intrinsic aggressiveness and high tendency to relapse rapidly. In addition, current therapeutic options for basal-like BC are limited to chemotherapy and relapse occurs frequently due to drug resistance [28].

A new molecular BC subtype, termed 'claudin-low', was proposed by Herschkowitz *et al.* [29]. Claudin-low tumors are characterized by the low expression of genes involved in tight junctions and cell-cell adhesion, including claudins 3, 4 and 7, Occludin, and E-cadherin [29]. The "claudin-low" group is characterized by inconsistent expression of basal keratins and low expression of HER2 and luminal markers, such as ERα and PR [30]. When compared with other BC subtypes, "claudin-low" highly express genes involved in immune response, cell communication, cell migration, angiogenesis, extracellular matrix and cell differentiation [30]. The majority of "claudin-low" tumors show poor prognosis [30].

Despite the high relevance of gene expression analysis, namely in grouping and stratifying BC patients, its use on clinical samples is resource and time intensive. Therefore, in the clinics, immunohistochemical detection of biomarkers of each subtype (evaluation of morphology, ERα, PR and HER2 expression status) is still the generalized methodology used in diagnosis stage and to select treatment options [31,32].

3. Estrogen receptor signaling in breast cancer

Estrogen receptor (ER) belongs to the steroid/nuclear receptor superfamily and has 2 isoforms in mammals: alpha and beta (ERα and estrogen receptor β (ERβ), respectively) [33]. The isoforms are encoded by two different genes [33], mapped on chromosome 6 and 14, respectively [34,35]. Although ERα role in BC has been extensively studied, the role of ERβ is still under investigation [36]. ERα is a ligand-modulated transcription factor, responsible for the mediation of a plethora of cellular functions from development to carcinogenesis, whose structure is schematically represented on Figure 1.3 [37,38]. The ER protein is composed of several functional domains, associated with specific roles. From the NH_2 terminal, ER structure consists on an activation function domain (AF)-1, followed by a DNA binding domain (DBD) and a hinge (H) region. Next to this region is the ligand binding domain (LBD) and the AF-2 [37].

Figure 1.3: ER structure. From the N-terminal to the C-terminal: activation function 1 region (AF-1), DNA-binding domain (DBD), hinge (H) region, ligand-binding domain (LBD), activation function 2 domain (AF-2) [37].

ERα can function both as signal transducer, activating various cell signaling pathways, and as transcription factor (TF), modulating the expression of several target genes. As signal transducer, ER is involved in non-genomic pathways, while as TF is involved in the direct and indirect genomic pathways [39] (Figure 1.4).

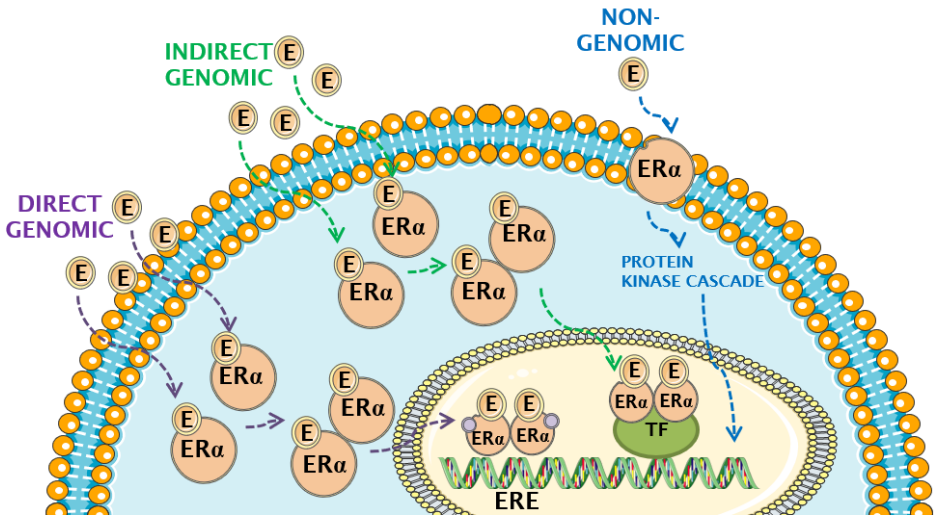

Figure 1.4: Schematic representation of the different types of estrogen receptor alpha (ERα) signaling. Upon estrogen (E) binding to ERα, one of three different pathways might be activated: direct genomic, in which the E-ER complex binds to estrogen response elements (ERE) located in the transcriptional regulatory regions of specific genes; indirect genomic, in which the E-ER complex binds to transcription factors (TF) of genes that do not have ERE; non-genomic, in which the E-ER complex activates protein kinase signaling cascades, leading to transcription of specific genes [39].

The activation/deactivation of any of the pathway types detailed on Figure 1.4 requires the presence of an ERα ligand, that interacts with the receptor by binding to the LBD region. In human, three different types of physiological estrogens are endogenously produced (endoestrogens): estrone (E1), estradiol (E2), and estriol (E3) [40]. They are produced from cholesterol in the sex glands, such as ovaries and testes, and in other organs, such as liver and brain. E2 is found both in females and males, while E3 is mainly found during pregnancy and E1 post menopause [40]. In addition to naturally produced estrogens within the body, a diverse array of small organic and inorganic molecules serve as ERα ligands [38]. In this group one can find phytoestrogens (non-steroidal polyphenolic

compounds naturally produced by plants), xenoestrogens (non-natural synthetic chemical compounds with estrogenic effects), metalloestrogens (small inorganic compounds in the form of heavy metal ions) and several molecules used in therapy, as described later in section 4 [38]. ERα ligands can have both stimulatory and inhibitory effects [38]. ERα inhibitors, such as tamoxifen and fulvestrant, compete with the estrogen for the binding to ERα and block the downstream signaling. This way, they hamper cell growth and proliferation and reduce tumor progression [41,42]. These inhibitors will be further explained in the section 4 of this chapter.

The inactive ERα exists in a molecular complex with: 1) chaperones – heat-shock proteins (hsp), namely hsp70 and hsp90, which bind to the ERα's LBD region; 2) co-chaperons, such as immunophilin and p23, which bind to hsp [37,43,44]. This complex inactivates the transcriptional regulatory capabilities of ER but maintains its ability to bind to ligands [43]. Upon estrogen binding, receptor dimerization, dissociation of hsp and association of co-regulatory proteins occurs [33]. In these conditions, ERα is able to bind to estrogen responsive elements (EREs; which are 13 bp palindromic consensus sequence separated by a 3-base spacer [45]) present in the transcriptional regulatory regions of ERα-target genes. Here, ERα interacts directly with coactivator proteins and components of the RNA polymerase II transcription initiation complex, leading to enhanced transcription [33] (direct genomic pathway, Figure 1.4). Around one third of all estrogen responsive genes do not bear an ERE region [46]. In these cases, the regulation of gene expression by ERα occurs by indirect genomic pathways

(Figure 1.4). ERα interacts with other DNA-bound transcription factors and stabilizes their binding to the DNA and/or recruits coactivators [33,39].

Several genes have been identified as estrogen-responsive genes, due to the presence of functional ERE in their promoter [46]. Among them, one can find the trefoil factor-1 *TFF1*, also known as *pS2* [47], and others reported by Lone *et al.* [46]. *pS2* is an estrogen-specific response gene, since only estrogen but not progestins, glucocorticoids, and androgens, can induce it [48]. pS2 role is controversial, as it has been reported by different groups to have either the capacity to induce or inhibit tumorigenicity [49,50]. Buache *et al.* performed pS2 gain- and loss-of-function experiments in four human mammary epithelial cell lines [49]. They concluded that constitutive expression of *pS2* led to an increase in cell migration and invasion. Moreover, they observed that tumorigenicity capacity of MCF7-pS2 (MCF7 with pS2 overexpression) was the same as the parental MCF7. Additionally, they showed that cells with pS2 knock-down had similar proliferation but higher colony-forming ability. In an *in vivo* mice model, they showed that in *pS2* knock-down, tumors appeared earlier and had higher incidence than in their control counterpart [49], suggesting that pS2 inhibits tumorigenesis. In a different study, overexpression of pS2 in BC cell lines resulted in increased cell proliferation and survival [50]. Additionally, it also increased cell migration and invasion and led to an increase in tumor size, in xenograft models. Ablation of pS2 led to a reduction in cell viability *in vitro* and tumor regression *in vivo*. Then, they concluded that pS2 clearly possess oncogenic functions in mammary carcinoma cells [50].

Another relevant gene controlled by ER is the progesterone receptor gene (*PGR*). Progesterone receptor (PR) works closely and in a reciprocal manner with ERα. In fact, it is not only an ERα-induced gene target but also an ERα-associated protein that modulates its behavior [31]. In one hand, *PGR* only has half ERE region in its promoter. The binding of ER to that region revealed to work more as an inhibitor than a stimulator, as it is expected when full ERE is present [51]. On the other hand, as described by Mohammed *et al.,* progesterone inhibited estrogen-mediated growth, both in an *in vivo* mouse model and in primary ERα-positive BC explants. Moreover, they showed that PR boosts the anti-proliferative effect of tamoxifen, in a MCF7 BC cell line xenograft model [31]. They concluded that PR controls the chromatin binding and transcriptional activity of ERα [31], revealing the combined action between ERα and PR.

In the group of genes regulated through indirect genomic pathways [46], one can find amphiregulin (*AREG*). Peterson *et al.* showed that AREG is required for estrogen-dependent growth of xenografts generated from the ER-positive cell line, MCF7 [52]. AREG, which is a ligand for the epidermal growth factor receptor (EGFR), is a critical mediator of the estrogen response in ER-positive BC [52].

ER is also involved in non-genomic signaling (Figure 1.4), in which estrogen binds to ER located in the cell membrane, leading to activation of several protein kinase cascade (e.g. ERK/MAPK, p38/MAPK, PI3K/AKT) [53–57]. This eventually leads to indirect changes in gene expression through phosphorylation of transcription factors and activation of several pathways [57]. Mitogen-activated protein kinase (MAPK) pathways constitute a highly conserved

family of kinase modules that work by transferring extracellular signals to the effectors that control diverse cellular processes, such as proliferation, differentiation, migration and apoptosis [56]. MAPK are involved in initiation of cancer and are activated by phosphorylation [56]. p38/MAPK activity can suppress tumor development and its signaling is important in cellular responses to conventional cancer therapies, including chemotherapy[56]. ERK/MAPK has been associated with the ability of cancer cells to grow independently of normal proliferation signals and is deregulated in approximately 30% of human tumors [56]. PI3K/AKT is an important pathway regulating the signaling of multiple biological processes such as apoptosis, metabolism, cell proliferation and cell growth [53]. The AKT signaling cascade, upon activation, induce production of phosphatidylinositol (3,4,5) trisphosphates (PIP3) by phosphoinositide 3-kinase (PI3K). These lipids work as plasma membrane docking sites for proteins such as AKT. In turn, AKT, that needs then to be phosphorylated to become active, can be inhibited by tumor suppressor phosphatase and tensin homolog (PTEN) through dephosphorylation [53].

In addition to the above-mentioned pathways, ERα can be activated in the absence of ligand. This activation requires phosphorylation, in specific residues, that may be induced by growth factors, such as epidermal growth factor (EGF) and insulin-like growth factor. This involves MAPK phosphorylation cascades, mentioned above, and guanine nucleotide-binding protein p21ras [57,58].

ER expression itself is regulated by: TFs, DNA methylation, histone modification, RNA-binding proteins and microRNAs [59]. Several promoters have been discovered upstream of the

translation start site of human ER: estrogen receptor promoter B associated factor 1 (ERBF-1), AP2, forkhead box protein (FOXO3a), forkhead transcription factor (FOXM1), nuclear proteins recognize G-A-T-A nucleotide sequences (GATA-3), zinc finger repressor B-lymphocyte-induced maturation protein (BLIMP1) and factor nuclear kappa B (NF-kβ), which are reviewed in [59].

ERα is involved in the BC carcinogenesis by controlling cell proliferation and metastasis. Among the genes regulated by ERα are *cyclin D1* and *c-myc* [59], which are proto-oncogenes involved in cell proliferation and survival [60,61]. Estrogen and ERα are also involved in the BC metastization process by controlling the expression of *Snail* and *e-cadherin* [62,63]. Loss of e-cadherin and increased expression of snail is correlated with the epithelial-to-mesenchymal transition and consequently to BC metastasis [64].

4. Targeted breast cancer therapies

BC therapy is typically based on the combination of several types of treatments which include non-targeted therapies, such as chemotherapy, radiotherapy, surgery and immunotherapy, and targeted therapies, which include hormonal therapy, antibodies and small-molecule inhibitors [65,66].

4.1 Hormonal therapy

Hormonal therapy, also known as endocrine therapy, is included in the group of targeted therapy, since it acts only in cells carrying a specific cellular target. In the context of BC, hormone therapy targets the hormonal receptor ERα and is part of the recommended therapy for ER-positive BC patient, being applied

usually during 5-10 years or more [67,68]. These therapies halt tumor progression by blocking either estrogen synthesis or ER signaling pathways [67]. This type of therapy has been shown to be advantageous by reducing recurrence rates for almost 50%, when comparing with untreated patients [69]. Hormone therapies are divided according to their mechanism of action: aromatase inhibitors, selective ER modulators (SERMs) and ER down-regulators (Figure 1.5) [70].

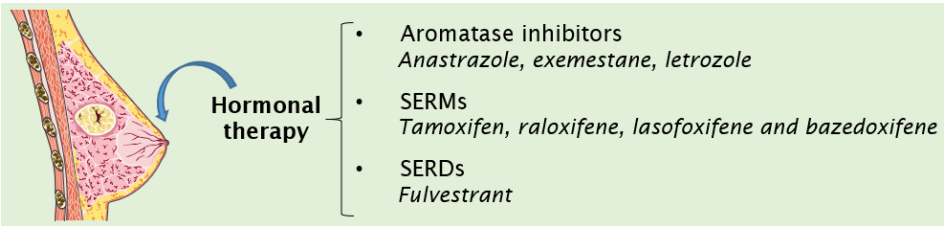

Figure 1.5: Types of breast cancer hormonal therapy. BC endocrine therapies include 3 different categories of molecules: aromatase inhibitors, which inhibit the production of estrogen from androgens; the selective ER modulators (SERMs) that agonizes/antagonize ER; selective ER down-regulators (SERDs), that fully antagonize ERα [70].

Aromatase inhibitors, such as the anastrozole, letrozole and exemestane, are chemical compounds that hamper aromatase activity. These enzymes are involved in the conversion of androgens, such as testosterone, into estrogen. By blocking this enzyme, it is possible to reduce the amount of endogenous ligand (estrogen) available to bind to the receptor (ERα) [70]. This type of hormonal therapy is only used in post-menopausal women, alone as adjuvant therapy or sequentially with SERM therapy, such as tamoxifen [68].

Another anti-endocrine therapy approach is based on the use of molecules that block specifically ERα signaling named SERMs. These are competitive inhibitors of estrogen binding to ERα,

such as tamoxifen and raloxifene [71]. Tamoxifen, also known as ICI 46 474, is a non-steroidal anti-ER compound, belonging to the triphenylethylene chemical group of SERMs, that was developed to treat post-menopausal women carrying advanced disease [72]. Nowadays it is used in both pre- and post-menopausal women [68,70,72]. SERMs have mixed agonist and antagonist activity, depending on the target tissue [70]. In the case of the BC tissue, tamoxifen works as an antagonist, blocking transcription of estrogen-regulated genes, reducing tumor proliferation [70].

The third type of BC hormonal therapy is based on selective ER down-regulators (SERDs), that act similarly to ER modulators but have exclusively antagonist effect on the receptor [73]. Fulvestrant, also known as ICI 182 780, is a SERD. It binds to ER, inducing a structural change in the receptor that inactivates the AF-1 and AF-2 domains and inhibits the receptor dimerization. These changes lead to an increase in receptor surface hydrophobicity, reducing its translocation to the nucleus and promoting consequent faster proteasomal degradation [42,74–76]. So, fulvestrant is both an ER competitor and selective estrogen receptor degrader [77]. Upon fulvestrant binding, *ER* mRNA level is maintained and ER protein level is reduced [78]. ICI 182 780 is currently indicated for the treatment of postmenopausal women with metastatic ERα-positive BC, after non-steroidal aromatase inhibitor treatment failure [70].

Resistance to endocrine therapy might be intrinsic to the patient or acquired during treatment. In this last case are included: (1) mutations in amino acids in ERα, resulting in the constitutive transactivation of ERα in the absence of the ligand; (2) altered expression of ERα co-activators and co-repressors; (3) enhanced expression of transcription factors to which ERα binds in the

indirect genomic pathways; (4) microRNA action, for example, miRNA 221 and 222, that down-regulate the cell cycle inhibitor p27, which leads to continued cell division independent of ER blockers [79].

4.2 Antibody therapy

With the advances in cancer research, several cellular biomarkers have been proposed and their relationship with cancer development and progression has been reported. These discoveries boosted the development of more specific therapies, the so-called targeted anti-cancer agents, such as monoclonal antibodies and small-molecule inhibitors [80].

Antibodies have the capacity to selectively target cells expressing a specific antigen [80–82]. Since they are designed to act on a specific cellular target, they virtually present higher efficiency and less side-effects on non-targeted tissues, when comparing with non-targeted therapies [83]. In the case of BC, examples are the anti-HER2 antibodies. In the clinical setting, trastuzumab and pertuzumab antibodies have been used to target the HER2 receptor [84]. Trastuzumab was, in fact, the first monoclonal antibody approved for the treatment of a solid tumor by the Food and Drugs Administration, in 1998 [81]. It is used in both metastatic and adjuvant settings [81]. In clinical studies, combination of trastuzumab with chemotherapy and hormonal therapy showed a benefit in terms of increased disease-free survival and overall survival [85,86]. Food and Drugs Administration also approved the use of an antibody-drug-conjugate (ADC) called trastuzumab-emtansine (Kadcyla®), which consists on Trastuzumab conjugated with the anti-proliferative molecule emtansine. This is derived from the

chemotherapy agent maytansine [87,88], which blocks microtubule polymerization, thus inducing apoptosis in target cells. This ADC was approved to be used as an adjuvant treatment of patients with HER2-positive early BC who have residual invasive disease after neoadjuvant taxane and trastuzumab-based treatment [87].

The major drawback related with anti-cancer antibodies is the development of resistance. In fact, the majority of patients who achieve an initial response to trastuzumab-based regimens develop resistance within one year [89]. Another drawback is related with the fact that several molecules and related pathways that are targeted by anti-cancer antibodies are also present in healthy cells, where they contribute to cell normal growth and homeostasis [90]. One example is the HER2 which is also present on healthy tissues, although at a much lower extent (to 100 vs 2 copies of the gene per cell, in cancer and healthy tissue, respectively) [91].

4.3 Small-molecule inhibitors

Small-molecule inhibitors (SMIs) are usually ≤500 Da in size, which allows them to translocate through the plasma membrane. Once inside the cell, they interact either with the cytoplasmic domain of cell-surface receptors, such as HER2 or EGFR, or intracellular signaling molecules, such as apoptotic proteins [80]. SMIs present several advantages over antibodies such as: (1) oral bioavailability, (2) generally good tolerance and (3) due to their small size, they can penetrate" sanctuary sites" in the human body [92].

Examples of SMIs approved for the treatment of BC include: lapatinib, palbociclib and ribociclib [93]. Lapatinib is a tyrosine kinase inhibitor (TKI) that targets HER2 and is approved for the treatment

of HER2-positive BC [93,94]. TKI are homologous of the adenosine triphosphate (ATP), which allow them to compete for the ATP-binding domain of protein kinases (present on HER2, for example), preventing its phosphorylation and subsequent activation of the signal transduction pathways. This results in apoptosis and reduction of cellular proliferation [94]. Lapatinib was approved by Food and Drugs Administration as a combination treatment with the aromatase inhibitor letrozole in HER2-positive, advanced BC patients that have failed standard chemotherapeutic treatment [80]. Palbociclib and ribociclib are cyclin-dependent kinase (CDK) inhibitors that have been approved by Food and Drugs Administration for the treatment of advanced-stage hormone receptor-positive and HER2-negative BC, in combination with letrozole [93,95,96]. Palbociclib inhibits specifically CDK4 and CDK6 [96], that play important role in tumorigenesis since they control the G1-S phase transition during cell cycle progression [95]. So, inhibition of CDK leads to reduced cell cycle progression and cell proliferation [95].

5. The role of tumor microenvironment in the response to anti-cancer therapy

The tumor mass is not only composed by cancer cells; actually, other non-cancerous cells, can be found in the tumor environment (TME), such as fibroblasts, adipocytes, endothelial, immune cells, pericytes, myoepithelial cells and various progenitor cells [97]. Besides them, several non-cellular components, such as extracellular matrix (ECM) and secreted signaling molecules (e.g., cytokines and growth factors) are also a part of the TME (Figure 1.6). This intricate network of cellular and non-cellular components

has been reported to be a critical mediator of anti-cancer drug treatment outcome by playing important roles in tumor progression [97,98]. While the TME of early-stage tumors confers anti-malignancy functions, some cancer cells can tolerate the immune suppression and, in turn, reprogram the TME into one exerting pro-malignancy functions [99]. So, the understanding of the TME changes during this cancer progression is of high relevance when developing therapeutic strategies to tackle the tumor at a specific stage.

Some tumors present natural resistance to therapy, not responding to the drugs from the beginning (innate resistance)[100]. In other cases, an initial response to the treatment is observed through cancer progression impairment, but cancer relapses due to acquired drug resistance [101]. Tumor cell-driven mechanisms behind this resistance include the activation of DNA-repair mechanisms, alterations in drug metabolism and drug transporters [101]. The latter can be responsible for an increasing drug elimination through the ejection of cytostatic therapeutic compounds to the extracellular space [100] and has a major influence in the failure of chemotherapy strategies [100]. Among those drug transporters are ATP-binding cassette (ABC) efflux transporters, such as P-glycoprotein, which are ubiquitously expressed and normally involved in transport of solutes [100].

In this thesis section, the TME components, highlighted in Figure 1.6, are presented in the perspective of therapy-related effects.

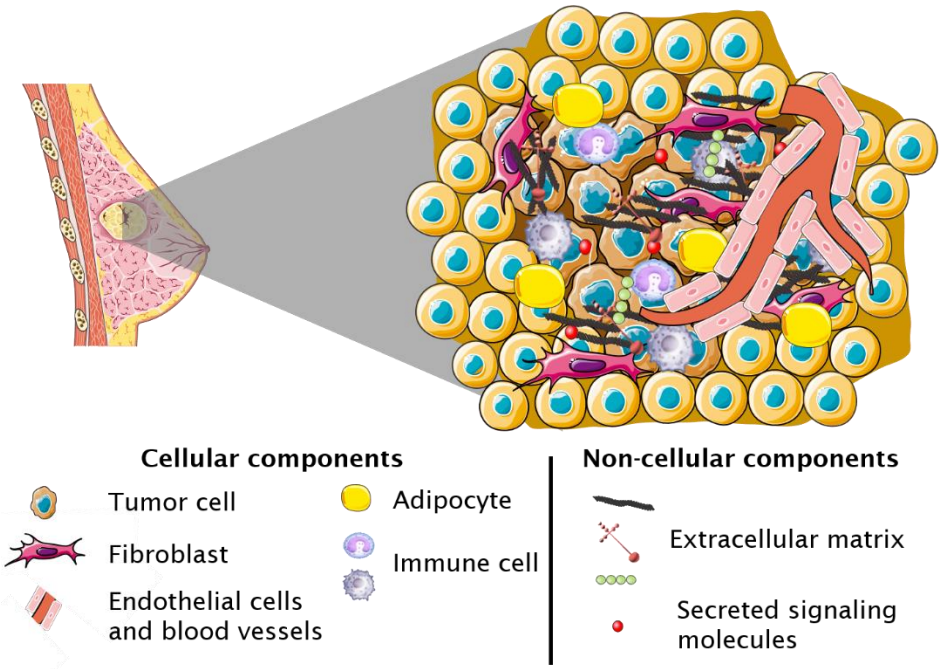

Figure 1.6: Breast cancer tumor microenvironment contains tumor cells and other cellular and non-cellular components. Non-tumor TME cellular components include fibroblasts, endothelial cells, immune cells, adipocytes and pericytes. Non-cellular TME components include extracellular matrix, (such as collagen fibers and glycosaminoglycans) and signaling molecules (such as cytokines and growth factors) [97,98].

5.1. Cellular components

5.1.1. Tumor cells

Tumor cells arise from healthy cells by a progressive series of transformations that lead to malignancy [102]. Together with uncontrolled growth, tumor cells are further characterized by genomic alteration, increased cell mobility, changes at the cellular surface, among others [103]. However, tumor cells are a heterogeneous population with variations at the morphological, genetic, epigenetic and phenotypic levels [104].

Tumor cells are the principal component of the TME and the *primum movens* of tumorigenesis and metastasis so, for that reason, they are the main target of anti-cancer therapies [80,105]. A multidrug resistance transporter of the ATP-binding cassette superfamily of transporters, termed BC resistance protein (BCRP), was proposed to be involved in drug resistance [106]. Overexpression of the full-length BCRP cDNA in MCF7 cells conferred resistance to mitoxantrone, doxorubicin, and daunorubicin and reduced daunorubicin accumulation and retention [106]. Alternatively, continuous exposure of tumor cells to anti-cancer drugs can lead to the development of acquired resistance, due to genetic and/or epigenetic changes leading to a proapoptotic pathway blockade, and/or constitutive expression of anti-apoptotic proteins, as well as increased efficiencies in cellular DNA damage repair mechanisms [107].

5.1.2. Fibroblasts

Fibroblasts are mesenchymal cells derived from the embryonic mesoderm. They are the pillar of the connective tissue that holds the human body together. Fibroblasts produce ECM structural proteins (e.g., fibrous collagen and elastin), adhesive proteins (e.g., laminin and fibronectin), and ground substance (e.g., glycosaminoglycans (GAGs)) [108]. In healthy tissue, in a wound healing scenario, fibroblasts sense and respond to mechanical changes and damage signals in the tissue and differentiate into activated fibroblasts (myofibroblasts) [109]. These cells are responsible for tissue repair and wound healing through ECM production and remodeling and cross-talk with immune cells.

There are increasing evidence for the relevance of fibroblasts in the TME. In the "tumor is a wound that do not heal" theory it is hypothesized that the fibroblasts present on the tumor initially act in an anti-tumorigenic manner (by restraining growth and eliciting an anti-tumor immune response) [109]. However, fibroblasts are activated by cancer cells to become pro-tumorigenic cells, cancer-associated fibroblasts (CAFs) [110]. CAFs secrete survival cues that enhance cancer cell survival, remodel ECM to tumor invasion and reshape tumor immunity to generate an immunosuppressive environment, promoting tumor development [109,110]. CAFs are a vastly heterogeneous stromal cell population, representing one of the major components of TME. In BC setting, CAFs are the most prominent stromal cell type [109].

CAFs origin is controversial; in fact, not all CAFs derive from tumor-resident fibroblasts. CAFs have been shown to have diverse origins [110], including bone marrow-derived mesenchymal cells [111], adipocytes [112] and endothelial cells [113]. CAFs are multiple subpopulations that have been divided in several CAFs subtypes: F1 tumor-restraining, F2 tumor-promoting, F3 secretory and F4 ECM-remodeling [114]. CAFs secretome include, transforming growth factor β (TGFβ), EGF, interleukins, fibroblast growth factors (FGFs), platelet-derived growth factors (PDGFs), protein ligands in the WNT signaling pathways, connective tissue growth factor (CTGF), prostaglandin E2 (PGE2), vascular endothelial growth factor (VEGF) and metabolites, such as lactate [110]. Several reports have shown that CAFs involvement in pro-tumorigenic functions occurs generally via modifications in their secretome [110].

CAFs are key players in therapy resistance and disease relapse [114,115]. The mechanisms behind these include induction of

epithelial-to-mesenchymal transition (EMT), activation of survival pathways, immune reprogramming or stemness-related programs and metabolic reprogramming in tumor cells [114,115].

CAF-mediated drug resistance can be explained by environment-mediated drug resistance (EMDR): (1) based on soluble factors which include cytokines, chemokines and growth factors secreted by fibroblasts; (2) mediated by cell-adhesion between tumor cells and either fibroblasts or ECM components [116,117]. Within group (1), a study by Straussman *et al.* used 23 stromal cell types to study their ability to influence the innate resistance of 45 cancer cell lines to 35 anti-cancer drugs [118]. They suggested that anti-cancer drugs capable of killing tumor cells when cultured alone, frequently rendered ineffective when tumor cells were cultured in the presence of stroma. This effect was particularly pronounced with targeted agents compared with chemotherapy. They studied in detail the mechanism of stroma-mediated innate resistance to the RAF inhibitor PLX4720, in melanoma cells. The authors showed that hepatocyte growth factor (HGF) secreted by stromal cells induced the activation of the MET receptor tyrosine kinase. This lead to reactivation of the MAPK and PI3K/AKT pathways, and consequently resistance to RAF inhibition [118]. Within the group (2), it has was reported that adhesion of tumor cells to CAFs works as a drug-resistance mechanism, possibly via *N*-cadherin homotypic binding, which activates anti-apoptotic protein AKT/PKB, increasing pro-survival AKT signaling in melanoma cells [119,120].

5.1.3. Endothelial cells

Endothelial cells are the cells lining the blood vessels. In pre-malignant stages of epithelial tumors, cancer cells are surrounded by a basal lamina that separates them from the connective tissue [121]. In a more advanced stage of the disease, due to the big size of the cancer cell clusters and long distance to blood vessel, a hypoxia environment is created. This induces cancer cells to release pro-angiogenic factors, such as VEGFA. Upon binding of this factor to specific receptors in neighboring endothelial cells, such as vascular endothelial growth factor receptor (VEGFR), angiogenesis is triggered [122]. This process involves an intricate communication between endothelial cells and the surrounding matrix, involving maturation of primary blood vessels by pericytes and recruitment of vascular muscle cells. This results in the formation of immature and heterogeneous vasculature characterized by irregular and leaky blood vessels [121,122]. These blood vessels with anomalous morphology and excessive branching lead to an increase of interstitial fluid pressure (IFP) and irregular blood flow throughout the TME, promoting further hypoxia [121]. This high IFP makes difficult the delivery of anti-cancer drugs to target sites within the TME and has been correlated with poor prognosis [105].

Anti-angiogenic therapy, which consists on angiogenic inhibitors, targets endothelial cells, since: (1) the survival of tumor cells is highly dependent on endothelial cells and these cells are in much less number so, it is easier to target them than the cancer cells; (2) since endothelial cells from different tissues are very similar, a unique effective anti-angiogenic drug might be sufficient to target those cells in different tumor types; (3) endothelial cells are genetically more stable than cancer cells, so they are less prone

to mutation and as a consequence develop therapy resistance [123]. Although in the beginning anti-angiogenic drugs were considered to be less toxic than other cytotoxic drugs, it has been shown that they may induce severe side effects including lethal hemoptysis and intestinal perforation [123].

Since the approval of the first anti-angiogenic therapy (bevacizumab to treat advanced colorectal cancer) in 2004, several other anti-angiogenic therapies have been approved to be used alone or in combination with chemotherapy [124]. Currently, in the BC context, bevacizumab is the anti-VEGF monoclonal antibody most extensively evaluated [125]. It was approved in 2008 by Food and Drugs Administration to treat metastatic HER2-negative BC. However, in 2011, Food and Drugs Administration withdrew this approval due to contradicting lack of overall-survival [125].

Similarly, to cancer cells and fibroblasts, endothelial cells have also revealed acquired drug resistance. Gilbert *et al.* reported, using a lymphoma mouse model, that endothelial cells release interleukin-6 (IL-6) and tissue inhibitor of metalloproteinase (Timp-1) in the thymus, upon chemotherapy. This creates a "chemo-resistant niche", located in the thymus, that promotes the survival of lymphoma cells that can serve as a reservoir for eventual future tumor relapse [126]. Additionally, it has been reported that endothelial cells overexpress p-glycoprotein transporter, when compared with normal endothelial cells, which confers them resistance to doxorubicin and paclitaxel [127]. Bani *et al.* showed that TKI and anti-angiogenic compounds can reverse this resistance *in vitro*, leading to an increase of intracellular drug accumulation [127]. They concluded that TKI interfere with ATPase activity of p-glycoprotein,

impairing its functionality, namely in excreting drug from endothelial cells [127].

5.1.4. Immune cells

The immune system is as intricate and complex system that aims to defend the organism from non-self-entities, such as bacteria, virus or even cancer [128]. It involves several types of immune cells and their secreted signaling molecules. Altogether, the final role is to that neutralize, degrade or induce apoptosis of pathogens, infected cells or cells that are not recognized as "self" [128]. Through a range of mechanisms, the cancer cells tend to escape immune surveillance and destruction, leading to tumor progression [129]. In fact, within the TME, not only anti-tumor immune cells but also pro-tumorigenic immune cells can be found, playing distinct roles in the different stages of tumor progression [130]. In the group of tumor-antagonizing immune cells one can name: effector T cells (including CD8+ cytotoxic T cells and effector CD4+ T cells), natural killer (NK) cells, dendritic cells (DCs), M1-polarized macrophages and N1-polarized neutrophils [130]. The group of tumor-promoting immune cells consists mainly in M2-polarized macrophages, N2-polarized neutrophils, regulatory T-cells (T-regs) and myeloid-derived suppressor cells (MDSCs) [130]. B-cells have a controversial role and so, are not included in neither of those groups [130].

In the tumor setting, DCs are thought to endocytose dead neoplastic cells or cellular debris and their main function is to work as antigen presenting cells (APC) [130,131]. They are also involved in sensing antigens released by cancer cells. Upon this stimulus, DCs become APC, and are transported to the lymph node. There, DCs prime resident T-cells, by exposing to them the cancer antigens. T

cells become activated effector T-cells (differentiation of antigen-specific T cells) which have cytotoxic capacity [131,132]. This process involves the MHC, present on the surface of DCs, and the T-cell receptor, localized on the surface of effector T-cells surface. This interaction triggers a series of proliferative events that lead to the expansion of the differentiated effector T cells populations [132,133]. These are trafficked to the tumors mediated by interactions between CXC-chemokine receptor 3 (CXCR3) expressed by T-cells with chemokines (such as CXCL9 and CXCL10) secreted by dendritic cells [130,132]. In the tumor site, effector T-cells recognize cancer cells through interaction between its T cell receptor and the cancer antigen bound to MHC [134]. After binding to its target, they secrete killing molecules, such as death ligands like FasL and TNF-related apoptosis inducing ligand [135]. This leads to the release of additional tumor-associated antigens that are sensed by DCs, initiating the cycle once again [134]. Each of these steps are the result of coordination of stimulatory and inhibitory effects [134]. This multi-step process was proposed by Chen and Mellman as the “cancer-immunity cycle” [134] (Figure 1.7).

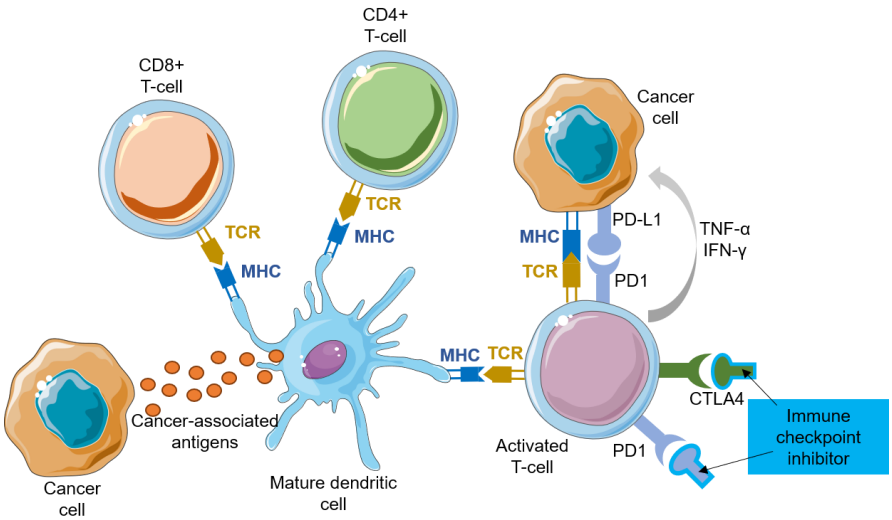

Figure 1.7: Schematic representation of the immune-tumor network in the "cancer-immunity cycle". Cancer cells release antigens which are sensed by dendritic cells (DCs)/antigen-presenting cells (APCs). These cells start presenting cancer antigens on their surface, which are recognized by several T-cell types, such as CD8+, CD4+ and activated T-cells. Upon this contact, they become activated T-cells and are recruited from the lymph node to the tumor site. There, they recognize cancer cells and release molecules to kill cancer cells [134]. Immune checkpoint inhibitor acts by binding to either programmed cell death protein 1 (PD1) or cytotoxic T-lymphocyte-associated protein 4 (CTLA4) present of the surface of T-cells, stimulating the release of anti-cancer molecules [136].

The step of activation and regulation of CD8+ T-cells, upon presentation of cancer cell antigens by DCs, requires two signals: the first one came from the T-cell receptor (TCR), and the second one, co-stimulatory signal from immune checkpoints [130]. These immune checkpoints can have either inhibitory or stimulatory effects. Within the inhibitory immune checkpoints, cytotoxic T-lymphocyte-associated protein 4 (CTLA-4) and programmed cell death protein 1 (PD-1) are some examples [130]. Within the stimulatory immune checkpoints, ICOS, OX-40 and GITR are some examples [130].

Another relevant immune cell type present in the TME is the macrophage that represents the main immune cell population of the TME in most cancers [137]. Its major functions include maintenance of tissue homeostasis, engulfment and digestion of foreign substances and clearance of cellular debris and cancer cells [138]. Macrophages play roles both in innate and adaptative immunity. In the cancer context, tumor-associates macrophages (TAMs) are obtained by differentiation of monocytes that are recruited to the tumor site [138] or from embryonic-derived macrophages already present in the tumor site [137]. Upon monocyte recruitment and differentiation process, macrophages polarize into: classically activated macrophages (M1 macrophages) or alternatively activated macrophages (M2 macrophages) [138]. The phenotype of TAMs is plastic and M1 and M2 are only the two extreme phenotypes of the several intermediate polarization states in which macrophages can be [138]. M1 macrophages, whose activation can be induced with interferon gamma (IFN-γ) and granulocyte-macrophage colony-stimulating factor (GM-CSF), produce pro-inflammatory cytokines with the role to kill non-self-entities [138]. On the other hand, M2 macrophage polarization can be obtained by stimulation with colony stimulating factor 1 (CSF-1), interleukin (IL)-4, IL-13, IL-10. These macrophages are involved in tissue remodeling and angiogenesis [138]. So, TAMs have a dual role in tumorigenesis: they can promote tumor progression (by the secretion of IL-6, IL-8, and IL-10) or have anti-tumorigenic activity [138].

Macrophages have been reported to be involved in resistance against several types of chemotherapy in different types of cancer [139]. In BC, one example of TAM-mediated chemoresistance was described by Hughes *et al.* [140]. They used a mouse model to

show the existence of a subpopulation of M2 TAMs that promotes tumor relapse, by accelerating tumor regrowth. These cells, that express VEGFA, accumulate near vascularized areas of the tumor upon chemotherapy [140]. Another study by Shree *et al.* showed an increased macrophage infiltration and cathepsin protease levels in mammary tumors, *in vivo*, upon chemotherapy [141]. Then, using a co-culture *in vitro* assay with BC cell lines with primary bone marrow-derived macrophages, they concluded that macrophage-derived cathepsins prevent tumor cell death upon chemotherapy [141].

Anti-cancer treatment targeting macrophages have been proposed by several strategies, such as by PD-1/PD-L1 blockade therapy or by using inhibitors of CSF-1R [138].

5.1.5. Other cell types

Other cell types found in the TME includes adipocytes. Analogously as it occurs for fibroblasts, normal adipocytes in the tumor environment are converted to cancer-associated adipocytes (CAAs) [142]. There, they become storage of ketone bodies, fatty acids, pyruvate, and lactate that are seized by tumor cells. Additionally, they play roles in inflammation, metabolism and exosomes of cancer cells [142]. In fact, CAAs release several factors, such as chemokine (C-C motif) ligand (CCL)2, CCL5, IL-6 and VEGF that alter BC cells in terms of p38/MAPK, ERK/MAPK and ER cancer cell pathways [142]. In a study developed by Lehuédé *et al.*, adipocytes were shown to promote doxorubicin resistance in both human and murine BC cell lines. Adipocytes increase the nuclear efflux of doxorubicin and its expulsion from tumor cells, in a process

mediated by major vault protein (MVP). In fact, co-culture of BC cells with adipocytes increased the MVP levels in cancer cells, when comparing with cancer cells cultured alone [143]. Other studies also suggest that adipocytes and lipids metabolism can be responsible for drug-resistance in tumor cells [144].

5.2. Non-cellular components

5.2.1. Extracellular Matrix

ECM is an interlocking mesh of water, minerals, proteoglycans, and fibrous proteins actively interacting between them and with the cellular compartment [145,146]. Based on biochemical and structural characteristics, ECM can be classified as basement membrane or interstitial ECM [145].

In normal tissues, the basement membrane is a barrier, located at the basal side of epithelial or endothelial cells, that allows the diffusion of gases and transport of signaling molecules [145]. This membrane is composed mainly of collagen IV, laminin, fibronectin, and several types of proteoglycans [145]. On the other hand, the interstitial ECM, mostly produced by mesenchymal cells such as fibroblasts, consists mainly of collagens I and III, fibronectin, GAGs and proteoglycans [145]. In general, healthy tissue ECM differs from tumor ECM: this last one usually contains a more densely packed network of highly aligned collagen fibers [147].

In the BC setting, ECM components include collagens, fibronectin, laminins, GAGs and proteoglycans and non-structural proteins, reviewed in [148]. The predominant component of the ECM is fibrillar collagen, whose structure and mechanical properties strongly influence tumor cellular phenotype [145]. During tumor

development both the basement membrane and the interstitial ECM suffer modifications. Cancer progression and development of metastasis is characterized by the epithelial-to-mesenchymal transition (EMT). In this process, epithelial cells acquire a mesenchymal phenotype associated with increased motility, expression of ECM remodeling enzymes, such as matrix metalloproteases (MMPs), and enhanced survival. These MMPs are crucial for cancer evasion, since they are enzymes that degrade molecules present in both the basement membrane and the interstitial ECM [145], allowing cell to migrate through the tumor interstitium. When cancer cells reach the basement membrane, MMP 2 and 9 degrade collagen IV and allow cancer cells to evade the tumor site and enter the blood stream [149].

The ECM is responsible for hampering intra-tumoral diffusion of therapeutic antibodies and physical masking of target receptors on tumor cells [150].

Collagen has been reported to highly influence antibody diffusion [151–153]. Kihara *et al.* determined the diffusion coefficients of biomolecules of various radius (1-10 nm) in a collagen gel cultured with fibroblasts. They analyzed the diffusion of those biomolecules in collagen gels and they concluded that it is smaller near the cell vicinity, when comparing with collagen solution alone. Diffusion revealed to be restricted in the proximity of the cells, where collagen fibers are highly condensed [151]. Netti *et al.*, using 4 different tumor cell lines (colon adenocarcinoma, glioblastoma, sarcoma and mammary carcinoma) grown in mice, found a correlation between IgG tumor penetration and the extension of the collagen network. They concluded that less penetrable tissues had an extended collagen network, which could be reversed by

collagenase treatment. Additionally, they suggested that, possibly by binding and stabilizing GAGs, collagen influences the tissue resistance to macromolecule transport [152]. Davies *et al.* measured the diffusion coefficient of nonspecific IgG in three rhabdomyosarcoma subclones growing as *in vitro* multicellular spheroids or *in vivo*. They reported that, the higher the amount of collagen and sulphated GAGs, the lower was the antibody diffusion coefficient, for spheroids grown *in vivo* [153]. On the other hand, Beyer *et al.* performed immunohistochemical studies of tumor sections from BC patients and xenografts. They observed co-localization of HER2 protein and laminin in HER2-positive BC and ovarian cancer biopsies. This suggest that laminin can mask HER2 on the tumor cell surface and, as a result, reduce therapeutic antibody access to its target site [150].

Hyaluronic acid (HA) is accumulated in most human tumors, especially in various adenocarcinomas, such as BC [154], and has been reported also to play important roles in drug resistance. Ricciardelli *et al.* showed that carboplatin treatment increased the expression of production of HA. Also, they proved that HA can regulate the expression of ABC drug transporters, in ovarian cancer cells, contributing then to chemoresistance [155]. In another work, Chen and Bourguignon showed that HA-CD44 binding is behind a chemoresistance mechanism in MDA-MB-468 BC cells [156]. The authors showed that HA binding to CD44 promoted c-Jun nuclear translocation and consequent transcription of miR-21 gene (which is involved in BC progression). This led to enhanced expression of Bcl2 and inhibitors of the apoptosis family of proteins, which were already correlated to chemoresistance by suppressing apoptosis [156].

5.2.2. Cytokines

Cytokine is a general term which include a large variety of chemokines, growth factors, pro- and anti-angiogenic factors, adipokines, soluble receptors and extra-cellular proteases [107]. They are involved in several tumorigenic processes related with tumor development and metastasis, such as inflammation, angiogenesis, cell migration and apoptosis [107].

Cytokines have been reported to play relevant roles in drug resistance [107]. Conze *et al.* showed that expression of *IL-6* increased drug resistance by activation of C/EBP transcription factors and consequent induction of expression of *mdr1* gene (which encodes the p-glycoprotein transporter). This lead to a reduction of intracellular concentration of anti-cancer drugs [157]. Another study found that, in a multidrug-resistant human BC cell line (MCF7/R), both IL-6 and IL-8 proteins levels were increased when in comparison with the parental sensitive cell line (MCF7). Drug resistance against paclitaxel and doxorubicin was partially neutralized upon anti-IL-6 and anti-IL-8 antibody treatment or inhibition of endogenous IL-6 and IL-8 with small interference RNA, showing the relevance of these two secreted molecules on cancer chemoresistance [158].

Cytokines have been also reported to induce resistance to antibody anti-cancer therapy. Kim *et al.* reported that AREG, a ligand of EGFR, confers trastuzumab resistance to HER2 positive BC. They showed that addition of AREG, in a colony-forming assay, increased cell proliferation and reduced the anti-proliferative effect of the anti-HER2 antibody trastuzumab. Additionally, they state that: (1) the mechanism behind this observation involves the AKT and ERK pathways, which were activated by AREG and (2) AKT and

ERK were phosphorylated upon trastuzumab treatment in the presence of AREG [159].

6. Breast cancer models

The study of BC development and testing of new promising anti-cancer compounds are conducted in BC models. Broadly, these models can be divided into 2 main groups: experimental and computational (*in silico*) models. Within the first group, 3 types can be defined according with the biological sources and cell culture technique used: *in vitro* (cell-based approaches), *in vivo* (animal models) and *ex vivo* (tumor tissue cultured outside the body) [160] (Figure 1.8).

6.1. In vitro models

In vitro cancer models, based on cell culture of cancer-derived cell lines, have leveraged the study of tumor-associated phenomena, such as tumor cell growth, migration and invasion and drug delivery [161]. Currently, *in vitro* models range in complexity and can be classified into 2-dimensional (2D) or 3-dimensional (3D) cell models [161]. The vast majority of these models are based on cancer cell lines commercially available. In the specific context of BC, more than 90 cell lines exist [162] and several *in vitro* models have been reported along the years and reviewed by many [163–165].

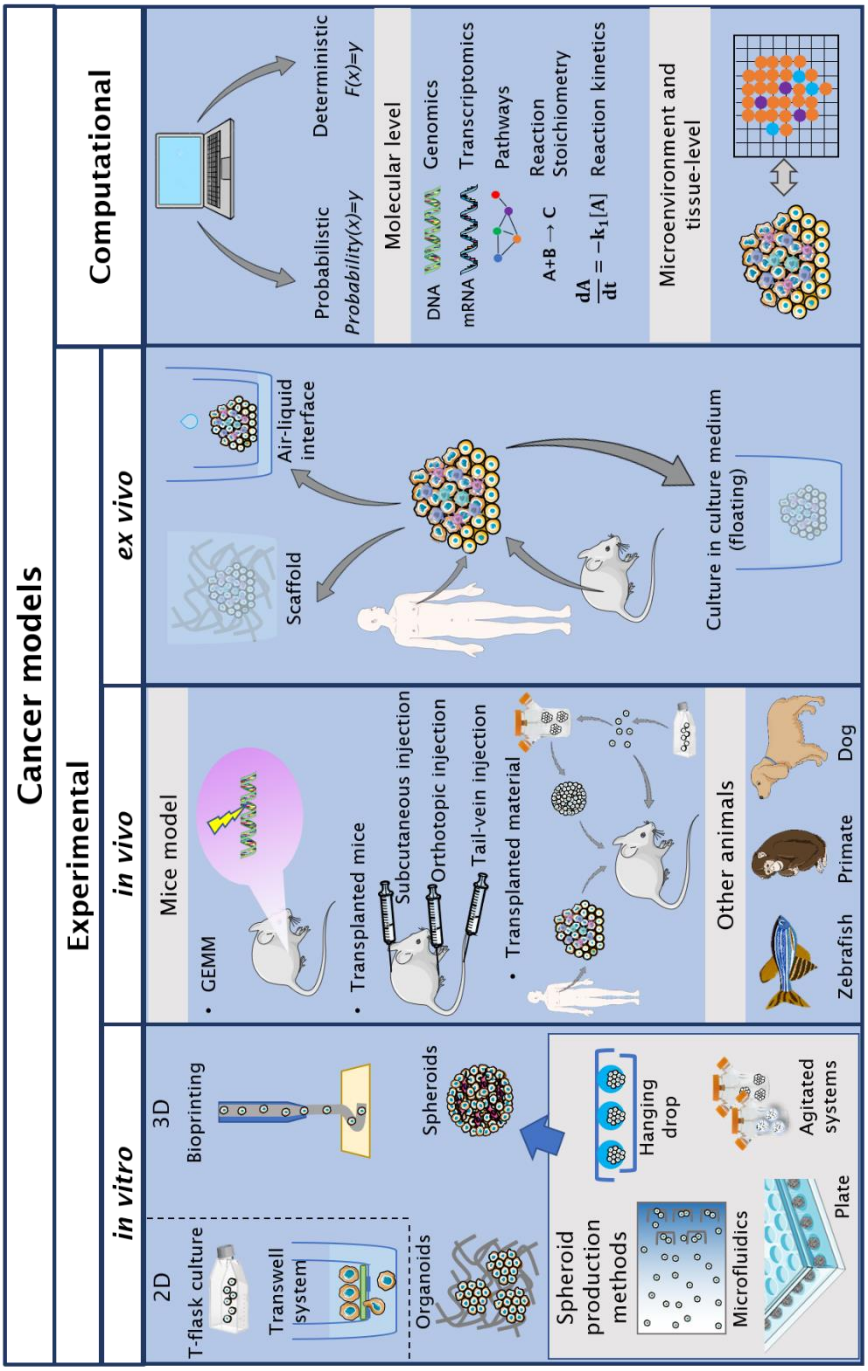

See caption in the next page.

Figure 1.8: Tumor models used in cancer research can be divided in 2 main groups: experimental (in vitro, in vivo or ex vivo) and computational, or in silico [163,164,166–173].

6.1.1 2D cell culture

In vitro 2D cell cultures are the standard models used for screening candidate anti-cancer therapeutics [174]. These models include culture of cells directly on flat substrates as monolayers [175] (Figure 1.8). In the 2D cell culture methods, cells are grown in unrealistic conditions that do not recreate the physiological and pathophysiological situations [161,175]. Mechanical and biochemical signals and cell-to-cell communication sensed by the cells in 2D conformations are clearly different from the *in vivo* situation [175]. Therefore, cells cannot retain their tissue-specific architecture since they are forced to be in a flattened and stretched shape, with forced polarity [175]. Despite its simplicity, most cancer biology research was based on those models [175]. The 2D cultures have several advantages such as: can be easily implemented, are low cost and easily adapted to high-throughput systems [161,175]. Additionally, several cell types, ECM components and soluble factors can be also included to increase the complexity of 2D models [176,177].

The transwell systems, considered by many as a 2.5 D system, is employed in the assessment of the migration and invasion potential of cancer cells, that can be induced by several cues, such as chemical attractants[161]. The transwell platform comprises two chambers: in the most common setting of migration assays, cells are seeded on the top chamber (insert) onto a porous membrane, while in the bottom chamber, a chemoattractant is

added. Cell migration is assessed by evaluation of cell movement towards the bottom chamber [161]. In the case of invasion assays, a component mimicking basement membrane is added on top of the porous membrane of the insert prior to cell seeding. This allows to assess the potential of cancer cells to invade through that membrane, as it occurs in the first stages of cancer evasion [161]. Several variations of the transwell system exist and were reviewed by Katt *et al.* [161]. The transwell system also allows co-culture and 3D cell culture. It has been employed by several authors to mimic cellular barriers, such as the blood brain barrier [178]. Endothelial and epithelial layers can be cultured in the upper and lower side of the upper chamber, respectively, while the tumor cells are cultured in the lower chamber [179]. In other configurations tumor or stromal spheroids can be included in those chambers [180,181]. The major advantage of the transwell system is that the cellular compartments are physically separated, facilitating endpoint analysis in the distinct cell compartments. On the other hand, this can also be seen as a disadvantage as most of the times these configurations have low physiological relevance [161].

6.1.2 3D cell culture

The growing recognition of the importance of the TME in cancer progression and therapy resistance (as referred in section 5), together with technological and methodological advances, contributed to the recent shift from simple 2D flat cell culture to complex cell models that include several cell types, ECM components and soluble factors [161], in conditions physiologically and pathophysiologically more relevant. In these models, several

variables present on the TME can be included and studied, such as different cell types, ECM and biochemical cues [161].

Amongst the 3D cell models available, the spheroids, the organoids and the systems based on bioprinting will be discussed in further detail.

Spheroids

Spheroids are the simplest 3D cell culture system. Their preparation can be achieved by: (1) stimulating single cells to generate spherical colonies by proliferation or (2) inducing single cells to aggregate into clusters that later grow in size due to cell proliferation [182]. Techniques to prepare spheroids can be divided into dynamic or static methodologies. Agitation-based culture systems and microfluidic systems [183] (in the dynamic group) [184] and liquid overlay technique [185,186], hanging-drop [187–189], microwell arrays [187] and embedding in matrices [190] (in the static group) have been used to prepare spheroids (Figure 1.8, reviewed in [161,187,191]).

Agitation-based culture systems include gyratory rotation techniques, rotary culture systems and stirred suspension culture systems [184]. In these systems, hydrodynamic forces generated by the agitation promote cell collisions, increasing adhesion binding kinetics at the cellular and molecular level, leading to spheroid formation [184]. During the aggregation process, stirring rates must be controlled to promote cell aggregation while avoiding cell and spheroid damage by the shear stress [184]. These systems allow spheroid mass production and long-term culture. However, control of size and composition, when preparing spheroids containing several cell types, is cell-type dependent and has to be adjusted [184]. Moreover, high shear stress is sometimes imposed to control

spheroid size, hampering the use of these system with shear stress-sensible cells [161].

Several groups have proposed the use of microfluidics technique to prepare spheroids [192]. One case includes the microfluidic-based methodology that uses patterned polymers together with PDMS to create molds, or PDMS molds with v-bottom microwells, where cells are seeded [193,194]. Microfluidics methods allow to control spheroid size and growth parameters. Moreover, they allow performing the aggregation under perfusion condition [161], reducing nutrient and oxygen deprivation and waste products accumulation. The major drawback of these systems is related with the difficulty in collecting the spheroids and the preparation of the device itself [161,195]. The most used type of microfluidic based-methodology is named microwell-based microfluidic spheroid formation chip (μSFC) [192]. It consists on a chip containing microwells connected by microchannels to the inlet. A cell suspension is introduced in the inlet, fills the microchannels and then deposit on the bottom of the microwells. In each of those microwells, a spheroid is formed [192]. One example of this methodology applied in the BC context, was proposed by Wu *et al.*, who established a proof-of-concept of the utilization of the platform for MCF-7 spheroid self-assembly [196]. The authors claim that this platform allows the formation of large amount of uniform spheroids (with narrow size distribution) and also the characterization of spheroids dynamics. They are formed due to trapping of cancer cells in U-shape traps and their compactness is assured by a continuous perfusion system [196]. However, validation of the platform with additional cell lines is still required considering that aggregation capacity may vary between cell lines and cell types [184,197].

Regarding the static culture methods, the liquid overlay technique (LOT) is based on a non-adhesive surface and gravity. As cells cannot adhere to the substrate, cell-cell interactions are promoted by proximity, leading to the formation of spheroids [185]. It is a cost-effective technique that allows easy monitoring of spheroid formation. However, spheroid size and cell number cannot be controlled [195]. In the hanging-drop (HD) technique, a droplet of single cell suspension is formed and left static, leading to cell sedimentation in the bottom of the droplet by gravity. Like in the LOT technique, gravity promotes cell-cell contact and spheroid formation [185]. Although HD is cost-effective, it is also time-consuming and does not allow for long-term cultures [195]. Microwell arrays, which are round-bottom nonadherent 96-well plates where cells are seeded, can also be used to prepare spheroids [187]. Commercially available multiwell plates, including round bottom nonadherent wells or wells at the micro scale, like the AggreWell™ system, can be also used to prepare spheroids. These are simple methods that allow easy monitoring of the aggregation process, in which co-cultures can be easily implemented [195]. Due to their inherent static nature, these methods can promote nutrient and oxygen deprivation and waste accumulation, reducing its potential to be used when long-term aggregation periods are needed [161].

Alternative methods include the embedding of single cells in scaffolds and hydrogels to give origin to spheroids. Examples include AlgiMatrix [190] and carboxymethyl cellulose. The later compound, when added to culture medium, increases its viscosity, preventing the cells from sediment or adhere to the culture device, leading to spheroid formation [185]. Combinations of the methods above described were already reported. An example is the work

proposed by Frei *et al.* that presented a platform joining hanging-drop and microfluidics to prepare spheroids [198].

The abovementioned methods can be applied to a single cell type, originating mono-cultures, or to a combination of multiple cell types, originating co-cultures [176,177]. After spheroid preparation, they can be cultured *per se* on the same platform they were prepared (e.g. microfluid device, spinner vessel [175]) or can be combined with scaffolds for long-term maintenance (e.g. encapsulation in a hydrogel [199,200]).

Organoids

Another type of 3D model widely used is the organoid. The term mammary organoid has been used since the 1980s, when Mina Bissel seminal work established that functional differentiation of mammary epithelial tissue was dependent on 3D architecture and interaction with basement membrane [201]. Recently, organoids have been defined as 3D multicellular structures in which cells self-organize to recapitulate some of the organ functions [166,202]. Within the scope of this current definition, organoids can be established from embryonic stem cells, induced pluripotent stem cells, somatic stem cells, and cancer cells (in this case are also called tumoroids). The establishment of tumoroids starts with cancer cells isolated from cancer tissue. Those cells are cultured in basement membrane mimetics, in the presence of specific growth factors and small molecule inhibitors which expand and differentiate the epithelial cell population [203]. Sachs *et al.* reported the derivation of more than one hundred breast cancer organoids, which recapitulated the diversity of the disease [204]. These organoids were obtained by isolating BC cells from surgical BC tissue. After mincing and

enzymatic digestion cells are placed in basement membrane mimetics (e.g., Matrigel) and cultured in the presence of niche factors, which *in vivo* are secreted by the stroma, and have been previously reported to be required for the formation of organoids [205].

Organoids have been used to study genetic mutations leading to tumor initiation and progression [206]. Additionally, organoids have been applied in drug development [203], in particular in precision medicine approaches, aiming to determine individual patient drug sensitivity or identify predictive biomarkers [203].

Bioprinting

Bioprinting is a recently proposed technology with great potential to generate not only spheroids but also more complex 3D cancer cell models. It consists on printing to a substrate or liquid reservoir, in a layer by layer fashion, several components (that can include cells, ECM and biomaterials) with a tailored pattern, in order to mimic native tissue architecture [167]. Then, this technology allows to reproduce both the structural heterogeneity and biomolecule gradients that play important roles in cancer [167,207]. Bioprinting can be achieved using one of three techniques: microextrusion bioprinting, laser-assisted bioprinting or inkjet bioprinting, which have different spatial resolution, allow different cell densities to be printed and different gelation methods [167]. In the case of the microextrusion bioprinting, a continuous flow of bioink is generated through pneumatic or mechanical forces. In the case of the laser-assisted, a laser is used to guide or induce cell deposition. In the case of the inkjet bioprinting, bioink droplets are created by a heater or a piezoelectric actuator [167]. To prepare 3D

cell models using bioprinting, two possible strategies exist: first to print the scaffold and then to seed the cells (two-step fabrication) or, alternatively, print both at the same time (one-step fabrication). An alternative is based on scaffold-free printing, in which only the several cell types, capable of producing their own matrix, are printed [167]. One example of the use of 3D bioprinting for generation of BC models is the work by Wang *et al.*. The authors bioprinted primary BC cells surrounded by different thicknesses of adipose derived mesenchymal stem/stromal cells (ADMSCs), to mimic different obesity status and challenged the model with chemotherapy to address resistance [208]. Another example that highlights the potential of bioprinting to recapitulate cellular organization of the tumor tissue is the work by Langer *et al.*. The authors prepared scaffold-free co-cultures of tumor cells (several BC subtypes) surrounded by stromal cells (different cell types) [209]. They demonstrated that the several cell types could be successfully co-cultured and that chemotherapy and targeted therapies sensitivity could be assessed in the system [209].

Organ-on-a-chip

Numerous technologies have been proposed in recent years for the generation of advanced *in vitro* tumor models. One of the most relevant examples is the organ-on-chip and human-on-a-chip concept [168]. These consist on the 3D combination and deposition, on a microfluidic device, of cells and ECM, which are perfused through hollow microchannels with culture medium in order to maintain cell viability for long periods of time [168], simulating the connections between organs by the circulatory system. One example of BC tumor-on-chip was presented by Choi *et al.* [210]. They

created a chip containing a layer of epithelial cells on top of a layer of fibroblasts, separated by an ECM-derived membrane. On top of epithelial cell layer, BC spheroids were deposited to mimic the initial phases of BC development (ductal carcinoma *in situ*). This tumor-on-chip model was used as a proof-of-concept to test a chemotherapy drug which was perfused in the lower channel to simulate intravenous administration [210].

6.2. In vivo models

Animal models are a gold standard in cancer research. Mouse is the most used animal, since is easy to maintain and handle, has a short reproductive cycle and share genomic and physiological properties with humans [211]. Mouse model can be created by genetically engineering strategies, human/mouse cell/tissue transplantation or viral/physical/chemical insults [169].

Genetically engineered mouse model (GEMM) are genetically modified mice containing in its genome cloned human cancer genes (such as the *HRas* oncogene). This model however fails to recapitulate sporadic cancer appearance due to accumulation of genetic events in a single cell, as it occurs in human cancers [212]. So, other mouse models have been developed and currently several types of GEMM models are available, such as the conditional GEMM. In this model, a given allele is phenotypically wild type until stimulation, with exogenous chemicals or viruses, is performed in a tissue- and time-specific manner. These allow somatic inactivation of tumor suppressors or activation of oncogenes, by recurring for example to the Cre-lox system [213,214]. These models are germline GEMMs since mice carry genetically engineered alleles in all cells, including the germline. Their preparation requires several

steps, such as targeting embryonic stem cells, generation of chimeras, germline transmission and complex mice intercrosses. Therefore, their development and validation are time-consuming, laborious, and expensive [212] and so, they are not easily adapted to high-throughput translational research and drug testing [215]. This led to the development of non-germline GEMMs (nGEMMs; mouse models carrying genetically engineered alleles in somatic cells, but not in germline cells) [212,215]. One example is the clusters of regularly interspaced short palindromic repeats (CRISPR)/Cas9-based mouse model [216].

Other mouse model is the transplantation mouse or xenograft, which it is based on immunocompromised mice lacking an effective immune system in order to avoid transplant rejection [217]. According with the origin of the tissue/cells to be transplanted, they can be categorized into: cell line-derived xenografts (CDXs), if human established cell lines are implanted; patient-derived xenografts (PDX), if human tumor tissue is grafted [217]. Alternatively, syngeneic mouse models (graft using cancer cells from mice) can also be prepared [212]. Transplantation models can also be categorized according with the place within the mouse body where cells/tissue are/is transplanted: orthotopic (transplanted to the same body site from which the tumor was originated), ectopic (when transplanted to a different site from the site of origin) and intravenous, usually injected in mouse tail-vein, for metastasis study *in vivo* [218]. The subcutaneously-injected mice model is the standard model used in the development and evaluation of new drugs in the pharma industry [219].

The representative potential of CDX is low since, contrarily to the heterogeneous tumors observed in humans with several cell

populations, an homogenous mass of tumor is injected in mice [220]. To surpass this problem, tumor tissue-transplanted mouse models (PDXs) were developed, in order to obtain the different cell populations of the original tumor. PDX models allow preservation of many relevant features of the primary human tumor, including histological features, behavioral characteristics (such as invasiveness and metastatic capacity) and most importantly, response to therapy [217]. However, in PDX, human tumor tissue availability is as issue. Another important aspect is that PDXs are generated in immunocompromised mice, therefore the influence of the immune system cannot be addressed. Moreover, the initially transplanted human stroma and immune infiltrate tend to be replaced by mice stroma over passage [217]. In order to circumvent the drawbacks related to the absence of the immune system, the latest developments in mice models have been focused on humanized mice, which consists in immunodeficient mice engrafted with human cells or tissues, in order to overcome the differences between mice and human physiology [221]. Syngeneic mouse models circumvent the need for an immune-compromised animal, allowing to evaluate the role of the immune response in cancer progression [218]. These enabled the investigation and development of various immune therapies [222] nonetheless, they may not represent human specific signaling.

In BC, ER represents a very important receptor, as described previously. So, having an ER-positive BC animal model is of high relevance. As observed in 2D culture, upon xenotransplantation *in vivo*, the most aggressive cell subtypes tend to overpopulate the transplant, biasing these models towards the triple-negative BC subtype [217]. Additionally, only a few ER-positive cell lines can

generate xenografts in mice and they require estrogen supplementation [223]. The challenges of modelling ER-positive BC in mice has been recently reported [224]. A comparison study of all BC GEMM showed that only the Stat1$^{-/-}$ and the Pik3ca-H1047R models develop ER-positive tumors [225]. CDX mouse models of ER-positive BC cell lines are based on: (1) BT474 cell line (subcutaneous) [226], MCF7 cell line (orthotopic transplantation into mammary fat pad) [227] and T47D cell line (subcutaneous) [228]. Xenografts of ER-positive BC are typically injected in the mammary fat pad, which leads to changes in tumor cell phenotype. In fact, it was demonstrated that when luminal tumor cells were injected in the mammary fat pad, their characteristics were lost and cells acquired a basal-like phenotype [223]. Moreover, the engraftment rate is very low (2.5%) and ER+ tumor cells need exogenous estrogen to grow. Due to all of these drawbacks, injection in the milk ducts was proposed by Behbod *et al.* as a more relevant site of injection: intraductal mouse models (MIND) [229]. This system was latter better characterized by Sflomos *et al.* [223]. The authors observed that tumor cells were able to recreate advanced BC stages, such as the breakdown the basement membrane and invasion of the stromal space into the fat pat. In this case, engraftment rates increases to 30-100% and there was no need for estrogen supplementation [223]. This strategy is a great improvement over the models described previously, since it allows the engrafted cells to be maintained in a luminal-epithelial like phenotype, typical of the ER-positive tumors. However, this strategy still has drawbacks, such as the technical difficulties in performing the implantation, the long time needed for engraftment and expansion of tumor cells in mice (at least one month), the lack

of immune system, and the exclusive presence of murine cells in the stromal compartment [223].

In addition to mice, other animal models that have proposed for cancer research, such as zebrafish [230]. These small fishes have high genetic homology to humans, and their embryos are transparent, which facilitates analysis of engrafted cancer cell growth and metastasis. Zebrafish is easy to maintain and has reasonable cost [230]. Moreover, it allows genetic manipulation at low cost and within short time [230]. Within the BC field, Drabsch *et al.* demonstrate that the zebrafish sustains invasion and metastasis upon transplantation of human BC cell lines with different metastatic potentials into the blood. Moreover, they showed that that animal model can be used to study the role TGF-β signaling in BC invasion and metastasis [231]. Additionally, dogs and primates have also been used as spontaneous BC models [170,171].

Even though animal models have assisted the discovery of cellular and molecular mechanisms associated to cancer tumorigenesis and the drug development process, they are still far from being able to recapitulate fully human cancer etiology, development and metastization, which reduces their predictive value [217,232–235].

6.3. Ex vivo models

Ex vivo models consist on the culture of freshly isolated tumor samples with the aim to preserve the original tissue architecture and heterogeneity, and the surrounding microenvironment [172]. The most described *ex vivo* models are based on tissue slice and explant culture. In these models, the tumor samples can be from

human or animal origin [236] and can be cultured: (1) in suspension in culture media [172], (2) in an air-liquid interface [237], (3) in a scaffold that mimics the ECM [238].

In the 60s Matoska and Stricker, suggested the culture of cubes of tumor tissue combined with a collagen gel support. However, problems related with oxygen and nutrient diffusion were reported due to the size of the microtissues [172]. To overcome oxygen and nutrient diffusion problems associated with that technique, Nissen *et al.* later adapted the methodology to obtain uniform, microscopically controlled tissue slices [239]. In fact, since then several other models were proposed based on these tissue slices. An example is the model proposed by van der Kuip *et al.* that used a tissue punch to generate 0.2 mm thick BC tissue slices that were cultured for 3 days in suspension. This method was used as a drug testing platform to address taxol sensitivity [172].

Several *ex vivo* BC models were developed which aimed at retaining ERα, given its role in BC carcinogenesis and as it is a target of endocrine therapy (as described above). Milani *et al.* [240] reported the maintenance of epithelial–mesenchymal interactions and viability of BC tissue slices for 24h, which were employed to evaluate the vitamin D pathway [240]. To overcome possible oxygen and nutrient diffusion problems, due to the size of the tissue slices, Parajuli and Doppler proposed the use of precision cut slices, which allow to control the slice thickness. They applied this strategy to mammary tumor collected from mice and studied the action of cytokines and cytotoxic drugs for up to 48 h: apoptotic scores and gene expression were assessed in tissue slices treated with IFN-γ and cell death was induced by doxorubicin [241]. Additionally, Pennington *et al.* showed that breast tumor tissue slices could be

infected by an oncolytic adenovirus and that the virus was able to replicate in the slices [242]. Davies *et al.* performed a comparison study between different strategies to culture of breast tumor tissue, among others[237]. They compared tissue slices floating in culture medium or placed on a filter support, in direct contact with air. Tissue morphology and integrity was better for tissue slices cultured on the filters and in the presence of atmospheric oxygen. However, the authors observed necrosis and stress biomarkers in the area of the tissue in contact with the filter, whereas the area in contact with the air was enriched in mitotic cells [237]. Additionally, ERα-positive cells were not efficiently retained in filter supports [237]. Naipal *et al.* reported an optimization that combines manual or automated tissue slicing (to obtain an optimized tumor slice thickness), specific growth medium and shake-based dynamic culture [243]. Results revealed that cell proliferation was preserved for 7 days of dynamic culture, without significant morphological differences from the original tissue. The authors also showed that those tissue slices could be used to study chemotherapy [243]. Muraro *et al*. reported the use of a perfusion-based bioreactor combined with a collagen scaffold to culture BC tissue [238]. They showed that cell viability was higher in perfused tissue when compared with the one cultured in static conditions. Even though, in the perfused system, after 14 days, viable cells represented only 20-25% of the total cells in the tumor fragments. Tissue slices cultured in the perfusion system sustained the patterns of cancer driving genes of the original tissue [238]. To show that the system could be used to test BC therapies, perfused tissue slices were incubated with standard-of-care compounds. When incubated with an ERα targeted therapy, fulvestrant, for 21 days, a reduction in ERα-positive

epithelial cells was observed [238]. When treated with an antibody against HER2, pertuzumab, a reduction of viable HER2-positive tumor cells was reported [238]. However, no ERα or HER2 signaling pathways were assessed to verify the functionality of those cellular receptors: only cell viability was evaluated.

The *ex vivo* ERα-positive BC models described were able to maintain cell viability, architecture and hormonal receptor expression typically for a week. This brings difficulties when trying to use those models for long-term monitoring of disease progression and for interrogation of the long-term effects of drug treatments. Furthermore, reaching robust conclusions is more difficult than when using cell lines due to the inherent heterogeneity between patients and material limitation [244]. In regard to analysis endpoints, several techniques routinely applied to *in vitro* models might be difficult to apply on *ex vivo* tissues, due to the limited amount of material [244,245]. Additionally, some of the methodology used to supports BC tissue take advantage of collagen scaffolds that are biologically active animal-derived biomaterials which bring variability and ethical concerns [246].

Overall, tissue slices and explants seem a promising and powerful way to create valuable cancer models, retaining the original tumor tissue architecture including the cellular and non-cellular components of the TME [244]. This represents an invaluable tool to study the role of 3D architecture and stromal interactions with the tumor cells [245]. Since the original features of the tumor tissue are maintained, treatment responses are potentially closer to ones observed in patients than in *in vitro* models where tissue cell populations and architecture is hardly recapitulated.

6.4. In silico models

In silico refers to analyses "performed in a computer" or "via computer simulation" [160]. It includes both the processing of large-scale data and the use of computational models that represent key features of a physical system, as mathematical equations [160,247], in order to describe its behavior.

Computational models used in cancer research can be divided in two main groups: probabilistic and deterministic models [248]. In the former, the events have a certain probability to occur, so they are associated with a degree of randomness [248]. In the latter, the events are described by mathematical equations that always produce the same output for a given input [248].

A cancer model can represent different biological levels, based on the scale of the phenomena to be modeled: (1) molecular level, which considers genomic, transcriptomic and signaling pathways, together with biochemical reactions; or (2) microenvironment and tissue level, in which events are considered at the scale larger than the nano-scale [249,250]. In this last case, the representation of the tumor and its components can be achieved following several different strategies (Figure 1.9), which differ on how cells are represented: continuum masses or as sets of discrete elements [173,251]. Discrete cells can be distributed homogeneously in a grid-like pattern, where all cells have a specific number of neighboring cells, or heterogeneously, leading to a variable number of neighboring cells [173,251].

A

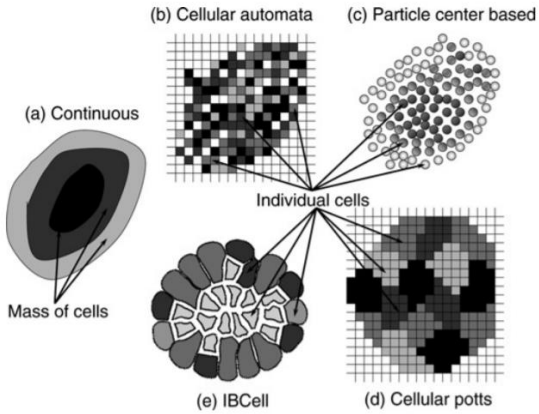

B

	Continuous	Cellular automata	Particle-based	Cellular Potts	IBCell
Number of cells represented	Density - concentrations of cells	Large numbers	Large numbers	Moderate to large numbers	Moderate numbers
Cellular details included	Cell densities	Cells modeled as points	Cells modeled as points	Cells modeled as deformable bodies	Cells modeled as deformable bodies
Cell-cell interactions	Averaged over the populations of cells	Fixed number of neighbors	Variable numbers of neighbors	Variable numbers of neighbors	Variable numbers of neighbors
Extracellular extensions	Direction fields for ECM fibers orientation *~*~* BM modeled as a region of different density *~*~* Chemical fields – cont. model	Concentrations of chemical fields (nutrients, waste products, enzymes) modeled as continuous fields – hybrid models *~*~* Density of the ECM modeled as continuous or discrete fields – hybrid models			Concentrations of chemical fields – cont. *~*~* Density of ECM – fluid parameter *~*~* ECM fibers modeled as bundles of springs
Intracellular extensions	Signaling pathways – cont. models	Signaling pathways modeled as continuous equations on the cell scale - hybrid models		Signaling pathways modeled as continuous equations on receptors scale	
Experimental parameterization	Average measurements	Whole cell measurements	Whole cell measurements	Cell membrane based	Cell membrane receptor based
Underlying lattice	Off-lattice	On-lattice	Off-lattice	On-lattice	Off-lattice
Underlying mathematics	Partial differential equations (PDE)	Monte-Carlo simulations	Potential energy	Energy minimization	Fluid dynamics

See caption in the next page.

Figure 1.9: Different types of computational models exist to model tumors. **A)** Schematic representation of different mathematical models of multicellular systems. (a) in a continuous model, the properties of the cells are considered as an average of all the cells of a specific type; (b) in a cellular automata model each cell is allocated to a lattice and has independent features; (c) in a particle center-based cells are allocated off-lattice with variable number of neighbors; (d) in cellular Potts each cell is allocated to several lattices; (e) in IBCell cells have variable shape with different dimensions; **B)** table summing up the features of each model type; adapted from Rejniak and McCawley [173].

Among the several tumor-related phenomena that have been modelled *in silico,* great relevance can be attributed to models that tackle anti-cancer drug delivery and distribution within the TME (several TME elements can influence therapy resistance, as previously explained in section 5). During tumor drug delivery, several steps can be considered from the moment of drug administration until this reaches its target cells in the TME [252]. Here we focus entirely on the drug transport phase between leaving the vasculature and reaching the target cancer cells (Figure 1.10).

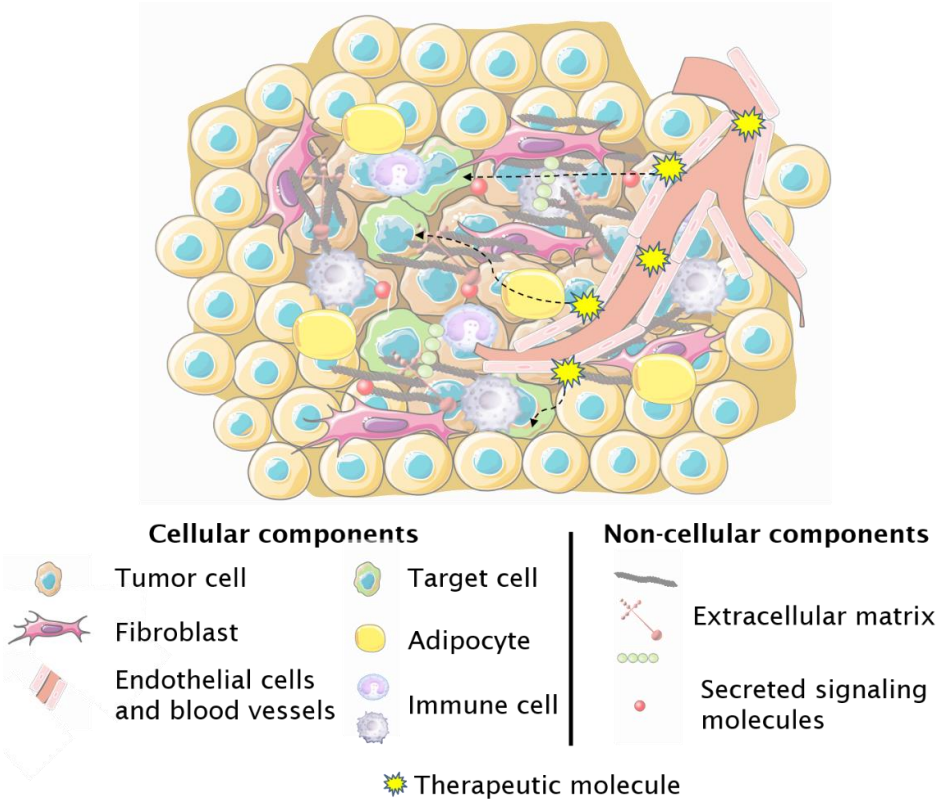

Figure 1.10: Schematic representation of drug transport barriers, within the tumor interstitium, that hinder drug delivery between the vasculature and the target cell. Therapeutic molecules (identified by the blue and yellow stars) enter the blood stream after systemic injection. Near the tumor site, these molecules cross over the vascular wall and reach the tumor interstitium. There they face several barriers, such as different cell types (immune cells in purple and fibroblasts in pink) and ECM components, e.g. collagen fibers (purple lines), GAGs (red spheres) and laminin (light red crosses), until they reach the target cancer cell (green cell) [252]. This transport phase is represented by the dashed black arrows.

Within the TME, the preferential drug transport mechanism is highly variable, ranging from pure diffusion to a combined convection diffusion mechanism. The following contributions use diffusion as their core transport mechanism within the TME. Groh *et al.* assessed the spatio-temporal evolution of drug concentration

within the tumor using diffusion-based models [253]. The tumor was modelled by three different approaches: (1) cell-centre model, in which the computational nodes surround the central vessel; (2) radially symmetric models with circular-compartment regions and (3) continuum homogeneous model. In any of the cases, drug delivery is performed by a vessel located in the center of the tumor. Three-compartments are considered: (1) the extracellular space; the intracellular space, which include (2) free and (3) bound intracellular drug compartments. In each of those compartments, drug balance equations (including diffusion in the continuum model) are applied [253]. Xie *et al.* developed a hybrid three-dimensional computational model to study how the environment influences drug diffusion and drug-tumor interactions, among other features [254]. Drug concentration over time is calculated by a continuum diffusion-reaction model. This is combined with a discrete cell automaton model (accounting for the evolution of the invasive solid tumor), creating then the hybrid model. The tumor is defined by an avascular or vascular circular shape structure that include proliferative, necrotic, invasive and quiescent cells and deposited and degraded ECM [254]. Another example is the work developed by Hamis *et al.* who also developed a hybrid model by the combination of a cell automaton model with continuum model defined by differential equations [101]. This on-lattice model considers intra-, inter- and extra-cellular dynamics to study chemotherapy drug by a reaction-diffusion model that includes also includes drug diffusion, production, consumption and decay rates. The model was defined with cellular resolution and in each lattice point a blood vessel, ECM and either sensitive or resistance cells might be allocated [101].

Other contributions on the topic consider instead the combined convective-diffusive transport. Venkatasubramanian *et al.* assessed the effect of an heterogeneous environment on drug efficacy, using a model based on mass balance equations [255]. For the drug balance equation, diffusive and convective (due to cell movement) transport were considered. In this case, the drug diffusivity coefficient accounts for combined effects of both extracellular diffusion and transmembrane transport (drug binding and uptake). Additionally, to account not only for the transport but also for the effect of the drug, a pharmacokinetic model was applied [255]. Rejniak *et al.* studied the role of tumor architecture on the interstitial molecule transport by diffusion and advection [256]. For that, they simulated the transport of a drug from a capillary, located on one side of the computational domain, with several types of tumor architectures (cells with different radius and in different amounts) [256]. Later Karolak and Rejniak improved this model by applying a modular approach in which drug concentration can be set as continuum or discrete, drug transport can be set either as diffusion, advection or combination of both and the cellular uptake can occur by membrane diffusion or receptor binding [257]. Mascheroni and Penta investigated the impact of the geometry of the tumor vasculature on drug transport [258]. The model they developed considers two different scales: micro- and macro-scale. While in the macro-scale the domain is homogeneous, in the micro-scale the differences in the vasculature are considered. The computational solution solves the macroscopic problem of the homogeneous domain, assuming the drug is transported by both advection and diffusion, in both the capillaries and the tumor interstitium [258].

Collagen fibers are one of the most relevant components in hindering drug transport within the TME, as explained in Section 5. Therefore, the ability to model this ECM element can be crucial in understanding its influence in drug distribution. This study is not restricted to models tailored specifically towards this problem. In fact, some models that were not designed for the study of collagen fibers or the transport of drugs can be considered. One example is the work developed by Ogston, that studied the transport of compact particles through solutions of chain-polymers [259]. Clague and Phillips studied the effect of solute-fiber interaction (hydrodynamic interactions) on the hindered diffusion of a spherical macromolecule in random media comprised of cylindrical fibers [260]. Stylianopoulos *et al.* developed a model considering steric, hydrodynamic and electrostatic interactions [261] between fibers and molecules to diffuse. In these models the fibers can be seen as the collagen fibers, while the particles are the drug molecules.

To assess if computational models can recapitulate specific phenomena, they need to be both calibrated and validated with data. These data can be either direct measurements of variables of interest in the developed model (obtained experimentally [262] or from clinical data [263]) or more complex data, that require additional processing to be used, such as images. For instance, the concept of using image digitization in order to create inputs for a computational model was used by Rejniak and co-workers. They apply it to *in vivo* data, in order to benchmark a pharmacokinetics/ pharmacodynamics tumor model [262,264] and also to organoid cultures to study differences between healthy and malignant cells [262]. *In vivo* data was also used by Boujelben *et al.* and Caraguel *et*

al. [265,266]. The first group used that data to recreate an accurate tumor vasculature where the simulation was applied [265] and the second group used fluorescence *in vivo* imaging as reconstructed input to the computational framework [266]. Computational models can also be benchmarked by experimental data in the sense that any discrepancies between the results of the two models can point out important components of the systems that were overlooked in the computational model, or even suggest additional experimental models and settings to clarify that difference [247,267].

Computational models can run numerous independent experiments in a relatively fast and efficient fashion. Data can be extracted without interfering with the system evolution and all the variables of the system can be controlled or modified [268]. While computational models cannot replace experimental models, they can be used as a complementary tool [160] to support the reducing, refining and replacing (3Rs) animal experiments [253]. Computational models can be used to investigate mechanisms behind experimental observations and to simulate many scenarios as a basis to select the most relevant experiments and thus reduce experimental burden and costs.

7. Aims and scope of this thesis

The tumor microenvironment is currently acknowledged as a potential source of targets for cancer therapy and a driving force of clinical drug resistance to targeted therapies. The aim of this thesis was to develop and characterize cancer models that recapitulate key aspects of the tumor microenvironment, suitable to address efficacy and resistance mechanisms of targeted

therapies. To achieve this goal, we employed *in vitro*, *ex vivo* and *in silico* approaches for modeling BC (Figure 1.11).

In **Chapter II**, the main objective was to develop a strategy for preservation of BC tissue *ex vivo*, retaining the TME components for culture periods long enough to address targeted therapies and resistance mechanisms. We developed a strategy based on entrapment of BC tissue into alginate and culture under dynamic conditions. We reasoned that by using alginate encapsulation to promote the original TME retention, while resourcing to dynamic culture to guarantee efficient diffusion of nutrients and oxygen, tissue microstructures would retain architectural integrity. Moreover, we hypothesized that retention of the original microenvironment would favor the maintenance of ERα-positive BC phenotype and ERα signaling, a driving force of this type of tumor and the target of endocrine therapy. Therefore, the second objective of Chapter II was to evaluate the presence of ER transcript and protein in *ex vivo* cultures of ER-positive BC and interrogate ER signaling.

In **Chapter III**, we explored TME *in vitro* cell models, based on alginate encapsulation of cancer cell lines and fibroblasts. The objective was to characterize biological, biochemical and mechanically those models. We employed an array of methodologies, namely atomic force microscopy, scanning electron microscopy, immunofluorescence and histochemistry to characterize the biomaterial and cellular components of the cell models.

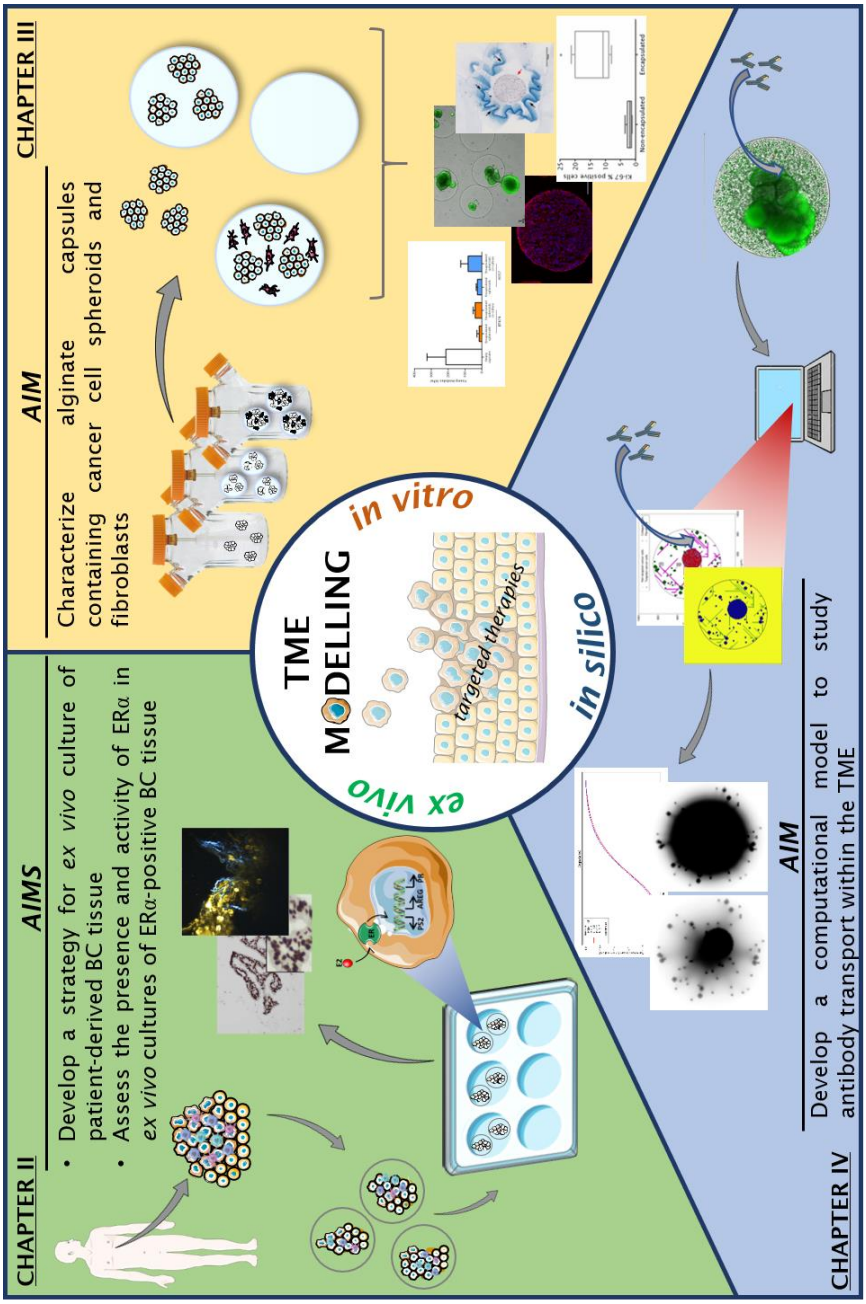

See caption in the next page.

Figure 1.11: Schematic representation of the research objectives pursued in this thesis and the experimental approaches followed to attain them. BC: breast cancer; ERα: estrogen receptor α; TME: tumor microenvironment.

In **Chapter IV**, the objective was to implement a computational framework to study antibody transport within the TME. The *in vitro* model characterized in Chapter III was challenged with fluorescent antibodies, whose distribution was live-tracked using light sheet microscopy. An *in silico* model comprising diffusive transport and saturation mechanisms was calibrated with the *in vitro* experimental data to recapitulate antibody transport.

8. Author contribution and acknowledgements

ALC wrote this chapter based on the referred bibliography.

The author would like to acknowledge Giacomo Domenici for discussion on several topics of this chapter.

9. References

1. National Breast Cancer Foundation, I. What is cancer? (2019).
2. Makki, J. Diversity of breast carcinoma: Histological subtypes and clinical relevance. Clin. Med. Insights Pathol. 8, 23–31 (2015).
3. Banik, U., Parasuraman, S., Adhikary, A. K. & Othman, N. H. Curcumin: The spicy modulator of breast carcinogenesis. J. Exp. Clin. Cancer Res. 36, 1–16 (2017).
4. Lee, Y. N. (Margaret. Breast carcinoma: Pattern of metastasis at autopsy. J. Surg. Oncol. 23, 175–180 (1983).
5. WHO. Breast cancer. WHO (2015). Available at: https://www.who.int/cancer/prevention/diagnosis-screening/breast-cancer/en/.
6. Cancer.net. Breast Cancer: Statistics. (2020). Available at: https://www.cancer.net/cancer-types/breast-cancer/statistics.
7. Society, A. C. How Common Is Breast Cancer? Current year estimates for breast cancer (2020). Available at: https://www.cancer.org/cancer/breast-cancer/about/how-common-is-breast-cancer.html.
8. Ekwueme, D. U. et al. Health and Economic Impact of Breast Cancer Mortality in Young Women, 1970–2008. Am J Prev Med 46, 71–79 (2014).
9. Allen, J. M. Economic/Societal Burden of Metastatic Breast Cancer: A US Perspective. Am. J. Manag. Care 16, 697–704 (2010).
10. Luengo-Fernandez, R., Leal, J., Gray, A. & Sullivan, R. Economic burden of cancer across the European Union: a population-based cost analysis. Lancet Oncol. 14, 1165–1174 (2008).
11. Nounou, M. I. et al. Breast cancer: Conventional diagnosis and treatment modalities and recent patents and technologies. Breast Cancer Basic Clin. Res. 9, 17–34 (2015).
12. Burton, R. & Bell, R. The Global Challenge of Reducing Breast Cancer Mortality. Oncologist 18, 1200–1202 (2013).
13. Lord, C. J. & Ashworth, A. Biology-driven cancer drug development: Back to the future. BMC Biol. 8, (2010).
14. Moiseenko, F., Volkov, N., Bogdanov, A., Dubina, M. & Moiseyenko, V. Resistance mechanisms to drug therapy in breast cancer and other solid tumors: An opinion. F1000Research 6, 1–8 (2017).
15. Breastcancer.org. Metastatic Breast Cancer. (2020). doi:https://www.breastcancer.org/symptoms/types/recur_metast
16. Hess, K. R., Pusztai, L., Buzdar, A. U. & Hortobagyi, G. N. Estrogen receptors and distinct patterns of breast cancer relapse. Breast Cancer Res. Treat. 78, 105–118 (2003).
17. Stingl, J. & Caldas, C. Molecular heterogeneity of breast carcinomas and the cancer stem cell hypothesis. Nat. Rev. 7, 791–799 (2007).
18. Turashvili, G. & Brogi, E. Tumor heterogeneity in breast cancer. Front. Med. 4, (2017).
19. Russnes, H. G., Lingjærde, O. C., Børresen-Dale, A. L. & Caldas, C. Breast Cancer Molecular Stratification: From Intrinsic Subtypes to Integrative Clusters. Am. J. Pathol. 187, 2152–2162 (2017).
20. Weigelt, B., Geyer, F. C. & Reis-Filho, J. S. Histological types of breast cancer: How special are they? Mol. Oncol. 4, 192–208 (2010).
21. Page, D. L. Special types of invasive breast cancer, with clinical implications. Am. J. Surg. Pathol. 27, 832–835 (2003).

22. Eliyatkin, N., Yalcin, E., Zengel, B., Aktaş, S. & Vardar, E. Molecular Classification of Breast Carcinoma: From Traditional, Old-Fashioned Way to A New Age, and A New Way. J. Breast Heal. 11, 59–66 (2015).
23. Perou, C. M. et al. Molecular portraits of human breast tumours. Nature 406, 747–752 (2000).
24. Sorlie, T. et al. Gene expression patterns of breast carcinomas distinguish tumor subclasses with clinical implications. Proc. Natl. Acad. Sci. 98, 10869–10874 (2001).
25. Vilardell, F. et al. Importance of assessing CK19 immunostaining in core biopsies in patients subjected to sentinel node study by OSNA. Virchows Arch. 460, 569–575 (2012).
26. Badve, S. et al. Basal-like and triple-negative breast cancers: A critical review with an emphasis on the implications for pathologists and oncologists. Mod. Pathol. 24, 157–167 (2011).
27. Lachapelle, J. & Foulkes, W. D. Triple-negative and basal-like breast cancer:Implications for oncologists. Curr. Oncol. 18, 161–164 (2011).
28. Toft, D. J. & Cryns, V. L. Minireview: Basal-like breast cancer: From molecular profiles to targeted therapies. Mol. Endocrinol. 25, 199–211 (2011).
29. Herschkowitz, J. I. et al. Identification of conserved gene expression features between murine mammary carcinoma models and human breast tumors. Genome Biol. 8, 1–17 (2007).
30. Prat, A. et al. Phenotypic and molecular characterization of the claudin-low intrinsic subtype of breast cancer. Breast Cancer Res. 12, (2010).
31. Mohammed, H. et al. Progesterone receptor modulates estrogen receptor-α action in breast cancer. Nature 523, 313–317 (2015).
32. Alluri, P. & Newman, L. A. Basal-like and triple-negative breast cancers. Searching for positives among many negatives. Surg. Oncol. Clin. N. Am. 23, 567–577 (2014).
33. Klinge, C. M. Estrogen receptor interaction with estrogen response elements. Nucleic Acids Res. 29, 2905–2919 (2001).
34. NCBI. ESR1 estrogen receptor 1 [Homo sapiens (human)]. (2019).
35. NCBI. ESR2 estrogen receptor 2 [Homo sapiens (human)]. (2019).
36. Song, P. et al. Estrogen receptor β inhibits breast cancer cells migration and invasion through CLDN6-mediated autophagy. J. Exp. Clin. Cancer Res. 38, 1–18 (2019).
37. Sommer, S. & Fuqua, S. A. W. Estrogen receptor and breast cancer. Semin. Cancer Biol. 11, 339–352 (2001).
38. Farooq, A. Structural and Functional Diversity of Estrogen Receptor Ligands. Curr Top Med Chem 15, 1372–1384 (2015).
39. Björnström, L. & Sjöberg, M. Mechanisms of estrogen receptor signaling: Convergence of genomic and nongenomic actions on target genes. Mol. Endocrinol. 19, 833–842 (2005).
40. Samavat, H. & Kurzer, M. S. Estrogen Metabolism and Breast Cancer. Cancer Lett. 356, 231–243 (2016).
41. Goodsell, D. S. The Molecular Perspective: Tamoxifen and the Estrogen Receptor. Oncologist 7, 163–164 (2002).
42. Osborne, C. K., Wakeling, A. & Nicholson, R. I. Fulvestrant: an oestrogen receptor antagonist with a novel mechanism of action. Br. J. Cancer 90, 2–6 (2004).
43. Knoblauch, R. & Garabedian, M. J. Role for Hsp90-Associated Cochaperone p23 in Estrogen Receptor Signal Transduction. Mol. Cell. Biol. 19, 3748–3759 (1999).

44. Smith, D. F. & Toft, D. O. The intersection of steroid receptors with molecular chaperones: Observations and questions. Mol. Endocrinol. 22, 2229–2240 (2008).
45. Gruber, C. J., Gruber, D. M., Gruber, I. M. L., Wieser, F. & Huber, J. C. Anatomy of the estrogen response element. TRENDS Endocrinol. Metab. 15, (2004).
46. Lone, R. O., Frith, M. C., Karlsson, E. K. & Hansen, U. Genomic Targets of Nuclear Estrogen Receptors. Mol. Endocrinol. 18, 1859–1875 (2004).
47. Berry, M., Nunez, A. & Chambon, P. Estrogen-responsive element of the human pS2 gene is an imperfectly palindromic sequence. Proc Natl Acad Sci U S A. 86, 1218–1222 (1989).
48. Stack, G. et al. Structure and function of the pS2 gene and estrogen receptor in human breast cancer cells. in Breast Cancer: Cellular and Molecular Biology 40, 185–206 (1988).
49. Buache, E. et al. Deficiency in trefoil factor 1 (TFF1) increases tumorigenicity of human breast cancer cells and mammary tumor development in TFF1-knockout mice. Oncogene 30, 3261–3273 (2011).
50. Amiry, N. et al. Trefoil factor-1 (TFF1) enhances oncogenicity of mammary carcinoma cells. Endocrinology 150, 4473–4483 (2009).
51. Petz, L. N. et al. Differential regulation of the human progesterone receptor gene through an estrogen response element half site and Sp1 sites. J. Steroid Biochem. Mol. Biol. 88, 113–122 (2004).
52. Peterson, E. A. et al. Amphiregulin is a critical downstream effector of estrogen signaling in ERα-positive breast cancer. Cancer Res. 75, 4830–4838 (2015).
53. Carnero, A., Blanco-Aparicio, C., Renner, O., Link, W. & Leal, J. The PTEN/PI3K/AKT Signalling Pathway in Cancer, Therapeutic Implications. Curr. Cancer Drug Targets 8, 187–198 (2008).
54. Barrantes, I. D. B. & Nebreda, A. R. Roles of p38 MAPKs in invasion and metastasis. Biochem. Soc. Trans. 40, 79–84 (2012).
55. De Luca, A., Maiello, M. R., D'Alessio, A., Pergameno, M. & Normanno, N. The RAS/RAF/MEK/ERK and the PI3K/AKT signalling pathways: Role in cancer pathogenesis and implications for therapeutic approaches. Expert Opin. Ther. Targets 16, 17–27 (2012).
56. Keyse, S. M. Dual-specificity MAP kinase phosphatases (MKPs) and cancer. Cancer Metastasis Rev. 27, 253–261 (2008).
57. Vrtačnik, P., Ostanek, B., Mencej-bedrač, S. & Marc, J. The many faces of estrogen signaling. Biochem. Medica 24, 329–342 (2014).
58. Kato, S. et al. Activation of the Estrogen Receptor Through Phosphorylation by Mitogen-Activated Protein Kinase. Science (80-.). 270, 102–106 (1999).
59. Hua, H., Zhang, H., Kong, Q. & Jiang, Y. Mechanisms for estrogen receptor expression in human cancer. Exp. Hematol. Oncol. 7, 1–11 (2018).
60. Gabay, M., Li, Y. & Felsher, D. W. MYC Activation Is a Hallmark of Cancer Initiation and Maintenance. Cold Spring Harb Perspect Med 36, 186–194 (2009).
61. Ewen, M. E. & Lamb, J. The activities of cyclin D1 that drive tumorigenesis. Trends Mol. Med. 10, 158–162 (2004).
62. Fujita, N. et al. MTA3, a Mi-2/NuRD complex subunit, regulates an invasive growth pathway in breast cancer. Cell 113, 207–219 (2003).
63. Oesterreich, S. et al. Estrogen-mediated Down-Regulation of E-cadherin in Breast Cancer Cells. Mol. Cell. Biol. 0133, 5203–5208 (2003).
64. Wang, Y., Shi, J., Chai, K., Ying, X. & Zhou, B. The Role of Snail in EMT and Tumorigenesis. Curr. Cancer Drug Targets 13, 963–972 (2014).

65. Oncology, A. S. of C. of. Breast Cancer: Types of Treatment. (2019). Available at: https://www.cancer.net/cancer-types/breast-cancer/types-treatment.
66. Cardoso, F. et al. Early breast cancer: ESMO Clinical Practice Guidelines for diagnosis, treatment and follow-up. Ann. Oncol. 30, 1194–1220 (2019).
67. National Cancer Institute. Hormone Therapy to Treat Cancer. (2015).
68. Moo, T. et al. Overview of Breast Cancer Therapy. PET Clin. 13, 339–354 (2018).
69. Abe, O. et al. Relevance of breast cancer hormone receptors and other factors to the efficacy of adjuvant tamoxifen: Patient-level meta-analysis of randomised trials. Lancet 378, 771–784 (2011).
70. Puhalla, S., Bhattacharya, S. & Davidson, N. E. Hormonal therapy in breast cancer: A model disease for the personalization of cancer care. Mol. Oncol. 6, 222–236 (2012).
71. Fabian, C. J. & Kimler, B. F. Chemoprevention for High-Risk Women: Tamoxifen and Beyond. Breast J. 7, 311–320 (2001).
72. Jordan, V. C. The role of tamoxifen in the treatment and prevention of breast cancer. Curr. Probl. Cancer 16, 134–176 (1992).
73. Robertson, J. F. Estrogen receptor downregulators: New antihormonal therapy for advanced breast cancer. Clin. Ther. 24, (2002).
74. Carlson, R. W. The History and Mechanism of Action of Fulvestrant. Clin. Breast Cancer 6, S5–S8 (2005).
75. Lai, A. C. & Crews, C. M. Induced protein degradation: an emerging drug discovery paradigm. Nat. Rev. Drug Discov. 16, 101–114 (2017).
76. Yeh, W. L. et al. Fulvestrant-Induced Cell Death and Proteasomal Degradation of Estrogen Receptor α Protein in MCF-7 Cells Require the CSK c-Src Tyrosine Kinase. PLoS One 8, (2013).
77. Nathan, M. R. & Schmid, P. A Review of Fulvestrant in Breast Cancer. Oncol. Ther. 5, 17–29 (2017).
78. Mcclelland, R. A., Manning, L., Gee, M. W., Anderson, E. & Clarke, R. Effects of short-term antiestrogen treatment of primary breast cancer on estrogen receptor mRNA and protein expression and on estrogen-regulated genes. Breast Cancer Res. Treat. 41, 31–41 (1996).
79. Haque, M. M. & Desai, K. V. Pathways to Endocrine Therapy Resistance in Breast Cancer. Front. Endocrinol. (Lausanne). 10, 1–7 (2019).
80. Seebacher, N. A., Stacy, A. E., Porter, G. M. & Merlot, A. M. Clinical development of targeted and immune based anti-cancer therapies. J. Exp. Clin. Cancer Res. 38, 1–39 (2019).
81. Adler, M. J. & Dimitrov, D. S. Therapeutic Antibodies Against Cancer. Hematol. Oncol. Clin. North Am. 26, 447–481 (2012).
82. Grimsley, A., Shah, K. S. & McKibbin, T. Monoclonal antibodies in cancer. Cancer Immun. 12, 337–359 (2012).
83. Lu, R. M. et al. Development of therapeutic antibodies for the treatment of diseases. J. Biomed. Sci. 27, 1–30 (2020).
84. Mcmaster, M. L., Kristinsson, S. Y., Turesson, I., Bjorkholm, M. & Landgren, O. Adaptative Immune Responses and HER2/neu Positive Breast Cancer. Clin. Lymphoma 9, 19–22 (2010).
85. Suman, V. J. et al. Trastuzumab plus Adjuvant Chemotherapy for Operable HER2-Positive Breast Cancer. new Engl. J. Med. Orig. 353, 1673–1684 (2005).
86. Slamon, Ld. et al. Adjuvant Trastuzumab in HER2-Positive Breast Cancer. N. Engl. J. Med. 365, 1273–1283 (2011).

87. FDA. FDA approves ado-trastuzumab emtansine for early breast cancer. (2019). Available at: https://www.fda.gov/drugs/resources-information-approved-drugs/fda-approves-ado-trastuzumab-emtansine-early-breast-cancer.
88. Peddi, P. F. & Hurvitz, S. A. Trastuzumab emtansine: the first targeted chemotherapy for treatment of breast cancer. Futur. Oncol. 9, 319–326 (2013).
89. Nahta, R. & Esteva, F. J. HER2 therapy: Molecular mechanisms of trastuzumab resistance. Breast Cancer Res. 8, 1–8 (2006).
90. Palumbo, M. O. et al. Systemic cancer therapy: Achievements and challenges that lie ahead. Front. Pharmacol. 4, 1–9 (2013).
91. English, D. P., Roque, D. M. & Santin, A. D. HER2 expression beyond breast cancer: Therapeutic implications for gynecologic malignancies. Mol. Diagnosis Ther. 17, 85–99 (2013).
92. Lin, N. U. & Winer, E. P. New targets for therapy in breast cancer: Small molecule tyrosine kinase inhibitors. Breast Cancer Res. 6, 204–210 (2004).
93. Roskoski, R. Small molecule inhibitors targeting the EGFR/ErbB family of protein-tyrosine kinases in human cancers. Pharmacol. Res. 139, 395–411 (2019).
94. Segovia-Mendoza, M., González-González, M. E., Barrera, D., Díaz, L. & García-Becerra, R. Efficacy and mechanism of action of the tyrosine kinase inhibitors gefitinib, lapatinib and neratinib in the treatment of her2-positive breast cancer: Preclinical and clinical evidence. Am. J. Cancer Res. 5, 2531–2561 (2015).
95. Liu, M., Liu, H. & Chen, J. Mechanisms of the CDK4/6 inhibitor palbociclib (PD 0332991) and its future application in cancer treatment (Review). Oncol. Rep. 39, 901–911 (2018).
96. Wu, P., Nielsen, T. E. & Clausen, M. H. FDA-approved small-molecule kinase inhibitors. Trends Pharmacol. Sci. 36, 422–439 (2015).
97. Mittal, S., Brown, N. J. & Holen, I. The breast tumor microenvironment: role in cancer development, progression and response to therapy. Expert Rev. Mol. Diagn. 18, 227–243 (2018).
98. Frankel, T., Lanfranca, M. P. & Zou, W. The role of tumor microenvironment in cancer immunotherapy. Adv. Exp. Med. Biol. 1036, 51–64 (2017).
99. Liu, T. et al. Cancer-associated fibroblasts: An emerging target of anti-cancer immunotherapy. J. Hematol. Oncol. 12, 1–15 (2019).
100. Choi, C. H. ABC transporters as multidrug resistance mechanisms and the development of chemosensitizers for their reversal. Cancer Cell Int. 5, 1–13 (2005).
101. Hamis, S., Nithiarasu, P. & Powathil, G. G. What does not kill a tumour may make it stronger: In silico insights into chemotherapeutic drug resistance. J. Theor. Biol. 454, 253–267 (2018).
102. Dobrzyński, L., Fornalski, K. W., Reszczyńska, J. & Janiak, M. K. Modeling Cell Reactions to Ionizing Radiation: From a Lesion to a Cancer. Dose-Response 17, 1–19 (2019).
103. Baba, A. & Câtoi, C. Tumor cell morphology. in Comparative Oncology (2007).
104. Gay, L., Baker, A. M. & Graham, T. A. Tumour Cell Heterogeneity. F1000Research 5, 1–14 (2016).
105. Heldin, C. H., Rubin, K., Pietras, K. & Östman, A. High interstitial fluid pressure - An obstacle in cancer therapy. Nat. Rev. Cancer 4, 806–813 (2004).
106. Doyle, L. A. et al. A multidrug resistance transporter from human MCF-7 breast cancer cells. Med. Sci. 95, 15665–15670 (1998).
107. Jones, V. S. et al. Cytokines in cancer drug resistance: Cues to new therapeutic strategies. Biochim. Biophys. Acta - Rev. Cancer 1865, 255–265 (2016).

108. Kendall, R. T. & Feghali-Bostwick, C. A. Fibroblasts in fibrosis: Novel roles and mediators. Front. Pharmacol. 5, 1–13 (2014).
109. Monteran, L. & Erez, N. The dark side of fibroblasts: Cancer-associated fibroblasts as mediators of immunosuppression in the tumor microenvironment. Front. Immunol. 10, 1–15 (2019).
110. LeBleu, V. S. & Kalluri, R. A peek into cancer-associated fibroblasts: Origins, functions and translational impact. DMM Dis. Model. Mech. 11, 1–9 (2018).
111. Raz, Y. et al. Bone marrow-derived fibroblasts are a functionally distinct stromal cell population in breast cancer. J. Exp. Med. 215, 3075–3093 (2018).
112. Alt, E. et al. Adipose tissue-derived stem cells differentiate into carcinoma-associated fibroblast-like cells under the influence of tumor-derived factors. Anal. Cell. Pathol. 33, 61–79 (2010).
113. Zeisberg, E. M., Potenta, S., Xie, L., Zeisberg, M. & Kalluri, R. Discovery of endothelial to mesenchymal transition as a source for carcinoma-associated fibroblasts. Cancer Res. 67, 10123–10128 (2007).
114. Kalluri, R. The biology and function of fibroblasts in cancer. Nat. Rev. Cancer 16, 582–598 (2016).
115. Fiori, M. E. et al. Cancer-associated fibroblasts as abettors of tumor progression at the crossroads of EMT and therapy resistance. Mol. Cancer 18, 1–16 (2019).
116. Dittmer, J. & Leyh, B. The impact of tumor stroma on drug response in breast cancer. Semin. Cancer Biol. 31, 3–15 (2015).
117. Meads, M. B., Gatenby, R. A. & Dalton, W. S. Environment-mediated drug resistance: A major contributor to minimal residual disease. Nat. Rev. Cancer 9, 665–674 (2009).
118. Straussman, R., Morikawa, T. & Shee, K. Tumor microenvironment induces innate RAF-inhibitor resistance through HGF secretion. Nature 487, 500–504 (2012).
119. Li, G., Satyamoorthy, K. & Herlyn, M. N-cadherin-mediated intercellular interactions promote survival and migration of melanoma cells. Cancer Res. 61, 3819–3825 (2001).
120. Flach, E. H., Rebecca, V. W., Herlyn, M., Smalley, K. S. M. & Anderson, A. R. A. Fibroblasts contribute to melanoma tumor growth and drug resistance. Mol. Pharm. 8, 2039–2049 (2011).
121. Roma-Rodrigues, C., Mendes, R., Baptista, P. V & Fernandes, A. R. Targeting Tumor Microenvironment for Cancer Therapy. Int. J. Mol. Sci. 20, E840 (2019).
122. De Palma, M., Biziato, D. & Petrova, T. V. Microenvironmental regulation of tumour angiogenesis. Nat. Rev. Cancer 17, 457–474 (2017).
123. Hida, K. & Maishi, N. Abnormalities of tumor endothelial cells and cancer progression. Oral Sci. Int. 15, 1–6 (2018).
124. Al-Husein, B., Abdalla, M., Trepte, M., DeRemer, D. L. & Somanath, P. R. Antiangiogenic therapy for cancer: An update. Pharmacotherapy 32, 1095–1111 (2012).
125. Aalders, K. C., Tryfonidis, K., Senkus, E. & Cardoso, F. Anti-angiogenic treatment in breast cancer: Facts, successes, failures and future perspectives. Cancer Treat. Rev. 53, 98–110 (2017).
126. Gilbert, L. A. & Hemann, M. T. DNA damage-mediated induction of a chemoresistant niche. Cell 143, 355–366 (2010).
127. Bani, M. R., Decio, A., Giavazzi, R. & Ghilardi, C. Contribution of tumor endothelial cells to drug resistance: anti-angiogenic tyrosine kinase inhibitors act as p-glycoprotein antagonists. Angiogenesis 20, 233–241 (2017).

128. Lewis, J. S., Roy, K. & Keselowsky, B. G. Materials that harness and modulate the immune system. MRS Bull. 39, 25–34 (2014).
129. Messerschmidt, J. L., Prendergast, G. C. & Messerschmidt, G. L. How Cancers Escape Immune Destruction and Mechanisms of Action for the New Significantly Active Immune Therapies: Helping Nonimmunologists Decipher Recent Advances. Oncologist 21, 233–243 (2016).
130. Lei, X. et al. Immune cells within the tumor microenvironment: Biological functions and roles in cancer immunotherapy. Cancer Lett. 470, 126–133 (2020).
131. Gardner, A. & Ruffell, B. Dendritic Cells and Cancer Immunity. Trends Immunol. 37, 855–865 (2016).
132. Farhood, B., Najafi, M. & Mortezaee, K. CD8+ cytotoxic T lymphocytes in cancer immunotherapy: A review. J. Cell. Physiol. 234, 8509–8521 (2019).
133. Obst, R. The timing of T cell priming and cycling. Front. Immunol. 6, 1–10 (2015).
134. Chen, D. S. & Mellman, I. Oncology meets immunology: The cancer-immunity cycle. Immunity 39, 1–10 (2013).
135. Martínez-Lostao, L., Anel, A. & Pardo, J. How Do Cytotoxic Lymphocytes Kill Cancer Cells? Clin. Cancer Res. 21, 5047–5056 (2015).
136. Shimodaira, S. et al. An update on Dendritic Cell-Based Cancer Immunotherapy. Immunome Res. 12, (2016).
137. Laviron, M. & Boissonnas, A. Ontogeny of Tumor-Associated Macrophages. Front. Immunol. 10, 1799 (2019).
138. Zhou, J. et al. Tumor-Associated Macrophages: Recent Insights and Therapies. Front. Oncol. 10, 1–13 (2020).
139. Larionova, I. et al. Interaction of tumor-associated macrophages and cancer chemotherapy. Oncoimmunology 8, 1–15 (2019).
140. Hughes, R. et al. Perivascular M2 macrophages stimulate tumor relapse after chemotherapy. Cancer Res. 75, 3479–3491 (2015).
141. Shree, T. et al. Macrophages and cathepsin proteases blunt chemotherapeutic response in breast cancer. Genes Dev. 25, 2465–2479 (2011).
142. Wu, Q. et al. Cancer-associated adipocytes: Key players in breast cancer progression. J. Hematol. Oncol. 12, 1–15 (2019).
143. Lehuédé, C. et al. Adipocytes promote breast cancer resistance to chemotherapy, a process amplified by obesity: Role of the major vault protein (MVP). Breast Cancer Res. 21, 1–17 (2019).
144. Cao, Y. Adipocyte and lipid metabolism in cancer drug resistance. J. Clin. Invest. 129, 3006–3017 (2019).
145. Poltavets, V., Kochetkova, M., Pitson, S. M., Samuel, M. S. & Samuel, M. S. The Role of the Extracellular Matrix and Its Molecular and Cellular Regulators in Cancer Cell Plasticity. Front. Oncol. 8, 1–19 (2018).
146. Walker, C. & Mojares, E. Role of Extracellular Matrix in Development and Cancer Progression. Int. J. Mol. Sci. 19, 1–31 (2018).
147. Xenaki, K. T., Oliveira, S., Bergen, P. M. P. Van & Henry, K. A. Antibody or Antibody Fragments: Implications for Molecular Imaging and Targeted Therapy of Solid Tumors. Front. Immunol. 8, (2017).
148. Insua-Rodríguez, J. & Oskarsson, T. The extracellular matrix in breast cancer. Adv. Drug Deliv. Rev. 97, 41–55 (2016).
149. Peter Chen & Parks, W. C. Role of Matrix Metalloproteinases in Epithelial Migration. J Cell Biochem 108, 1233–1243 (2009).
150. Beyer, I. et al. Controlled extracellular matrix degradation in breast cancer tumors improves therapy by trastuzumab. Mol. Ther. 19, 479–489 (2011).

151. Kihara, T., Ito, J. & Miyake, J. Measurement of biomolecular diffusion in extracellular matrix condensed by fibroblasts using fluorescence correlation spectroscopy. PLoS One 8, e82382 (2013).
152. Netti, P. A., Berk, D. A., Swartz, M. A., Grodzinsky, A. J. & Jain, R. K. Role of extracellular matrix assembly in interstitial transport in solid tumors. Cancer Res. 60, 2497–2503 (2000).
153. Davies, C. de L., Berk, D., Pluen, A. & Jain, R. Comparison of IgG diffusion and extracellular matrix composition in rhabdomyosarcomas grown in mice versus in vitro as spheroids reveals the role of host stromal cells. Br. J. Cancer 86, 1639–1644 (2002).
154. Sironen, R. K. et al. Hyaluronan in human malignancies. Exp. Cell Res. 317, 383–391 (2011).
155. Ricciardelli, C. et al. Chemotherapy-induced hyaluronan production: A novel chemoresistance mechanism in ovarian cancer. BMC Cancer 13, (2013).
156. Chen, L. & Bourguignon, L. Y. W. Hyaluronan-CD44 interaction promotes c-Jun signaling and miRNA21 expression leading to Bcl-2 expression and chemoresistance in breast cancer cells. Mol. Cancer 13, 1–13 (2014).
157. Conze, D. et al. Autocrine production of interleukin 6 causes multidrug resistance in breast cancer cells. Cancer Res. 61, 8851–8858 (2001).
158. Shi, Z. et al. Enhanced chemosensitization in multidrug-resistant human breast cancer cells by inhibition of IL-6 and IL-8 production. Breast Cancer Res. Treat. 135, 737–747 (2012).
159. Kim, J. W. et al. Amphiregulin confers trastuzumab resistance via AKT and ERK activation in HER2-positive breast cancer. J. Cancer Res. Clin. Oncol. 142, 157–165 (2016).
160. Jean-Quartier, C., Jeanquartier, F., Jurisica, I. & Holzinger, A. In silico cancer research towards 3R. BMC Cancer 18, 1–12 (2018).
161. Katt, M. E., Placone, A. L., Wong, A. D., Xu, Z. S. & Searson, P. C. In Vitro Tumor Models: Advantages, Disadvantages, Variables, and Selecting the Right Platform. Front. Bioeng. Biotechnol. 4, 1–14 (2016).
162. Dai, X., Cheng, H., Bai, Z. & Li, J. Breast Cancer Cell Line Classification and Its Relevance with Breast Tumor Subtyping. J. Cancer 8, 3131–3141 (2017).
163. Guiro, K. & Arinzeh, T. L. Bioengineering Models for Breast Cancer Research. Breast Cancer Basic Clin. Res. 9s2, 57–70 (2016).
164. Arrigoni, C., Bersini, S., Gilardi, M. & Moretti, M. In vitro co-culture models of breast cancer metastatic progression towards bone. Int. J. Mol. Sci. 17, (2016).
165. Montagner, M. & Sahai, E. In vitro Models of Breast Cancer Metastatic Dormancy. Front. cell Dev. Biol. 8, 37 (2020).
166. Little, M. H. Organoids: A special issue. Dev. 144, 935–937 (2017).
167. Knowlton, S., Onal, S., Yu, C. H., Zhao, J. J. & Tasoglu, S. Bioprinting for cancer research. Trends Biotechnol. 33, 504–513 (2015).
168. Sontheimer-Phelps, A., Hassell, B. A. & Ingber, D. E. Modelling cancer in microfluidic human organs-on-chips. Nat. Rev. Cancer 19, 65–81 (2019).
169. Yee, N. S., Igntenko, N., Finnberg, N., Lee, N. & Stairs, D. Animal models in cancer biology. Cancer Growth Metastasis 8, 115–118 (2015).
170. Nguyen, F. et al. Canine invasive mammary carcinomas as models of human breast cancer. Part 1: Natural history and prognostic factors. Breast Cancer Res. Treat. 167, 635–648 (2018).
171. Xia, H.-J. & Chen, C.-S. Progress of non-human primate animal models of cancers. Zool. Res. 32, 70–80 (2011).
172. van der Kuip, H. et al. Short term culture of breast cancer tissues to study the activity of the anticancer drug taxol in an intact tumor environment. BMC Cancer 6, 1–11 (2006).

173. Rejniak, K. A. & McCawley, L. J. Current trends in mathematical modeling of tumor-microenvironment interactions: A survey of tools and applications. Exp. Biol. Med. 235, 411–423 (2010).
174. Monteiro, M. V, Gaspar, V. M., Ferreira, L. P. & Mano, J. F. Hydrogel 3D in vitro tumor models for screening cell aggregation mediated drug response. Biomater. Sci. 8, 1855–1864 (2020).
175. Hoarau-Véchot, J., Rafii, A., Touboul, C. & Pasquier, J. Halfway between 2D and Animal Models: Are 3D Cultures the Ideal Tool to Study Cancer-Microenvironment Interactions? Int J Mol Sci 19, (2018).
176. Sundarakrishnan, A., Chen, Y., Black, L. D., Aldridge, B. B. & Kaplan, D. L. Engineered cell and tissue models of pulmonary fibrosis. Adv. Drug Deliv. Rev. 129, 78–94 (2018).
177. Gambar, G., Gaeble, M., Keilhol, U., Regenbrecht, C. R. A. & Silvestri, A. From chemotherapy to combined targeted therapeutics: In vitro and in vivo models to decipher intra-tumor heterogeneity. Front. Pharmacol. 9, 1–18 (2018).
178. Stone, N. L., England, T. J. & O'Sullivan, S. E. A novel transwell blood brain barrier model using primary human cells. Front. Cell. Neurosci. 13, 1–11 (2019).
179. Yeste, J., Illa, X., Alvarez, M. & Villa, R. Engineering and monitoring cellular barrier models. J. Biol. Eng. 12, 1–19 (2018).
180. Sherman, H. & Rossi, A. E. A novel three-dimensional glioma blood-brain barrier model for high-throughput testing of tumoricidal capability. Front. Oncol. 9, 1–7 (2019).
181. Mosaad, E., Chambers, K., Futrega, K., Clements, J. & Doran, M. R. Using high throughput microtissue culture to study the difference in prostate cancer cell behavior and drug response in 2D and 3D co-cultures. BMC Cancer 18, 1–11 (2018).
182. Mueller-Klieser, W. J. A review on cellular aggregates in cancer research. Cancer Res. Clin. Oncol. 113, 101–122 (1987).
183. Lim, W. & Park, S. A microfluidic spheroid culture device with a concentration gradient generator for high-throughput screening of drug efficacy. Molecules 23, (2018).
184. Santo, V. E. et al. Adaptable stirred-tank culture strategies for large scale production of multicellular spheroid-based tumor cell models. J. Biotechnol. 221, 118–129 (2016).
185. Metzger, W. et al. The liquid overlay technique is the key to formation of co-culture spheroids consisting of primary osteoblasts, fibroblasts and endothelial cells. Cytotherapy 13, 1000–1012 (2011).
186. Costa, E. C., Melo-Diogo, D. de, Moreira, A. F., Carvalho, M. P. & Correia, I. J. Spheroids formation on non-adhesive surfaces by Liquid Overlay Technique: considerations and practical approaches. Biotechnol J. 13, (2018).
187. Fennema, E., Rivron, N., Rouwkema, J., Blitterswijk, C. Van & Boer, J. De. Spheroid culture as a tool for creating 3D complex tissues. Trends Biotechnol. 31, 108–115 (2013).
188. Kelm, J. M., Timmins, N. E., Brown, C. J., Fussenegger, M. & Nielsen, L. K. Method for generation of homogeneous multicellular tumor spheroids applicable to a wide variety of cell types. Biotechnol. Bioeng. 83, 173–180 (2003).
189. Amann, A. et al. Development of an innovative 3D cell culture system to study tumour - Stroma interactions in non-small cell lung cancer cells. PLoS One 9, (2014).
190. Godugu, C. et al. AlgiMatrixTM Based 3D Cell Culture System as an In-Vitro Tumor Model for Anticancer Studies. PLoS One 8, (2013).
191. Hirschhaeuser, F. et al. Multicellular tumor spheroids: An underestimated tool is catching up again. J. Biotechnol. 148, 3–15 (2010).

192. Moshksayan, K. et al. Spheroids-on-a-chip: Recent advances and design considerations in microfluidic platforms for spheroid formation and culture. Sensors Actuators, B Chem. 263, 151–176 (2018).
193. Fukuda, J. et al. Micromolding of photocrosslinkable chitosan hydrogel for spheroid microarray and co-cultures. Biomaterials 27, 5259–5267 (2006).
194. Ungrin, M. D., Joshi, C., Nica, A., Bauwens, C. & Zandstra, P. W. Reproducible, ultra high-throughput formation of multicellular organization from single cell suspension-derived human embryonic stem cell aggregates. PLoS One 3, (2008).
195. Benien, P. & Swami, A. 3D tumor models: History, advances and future perspectives. Futur. Oncol. 10, 1311–1327 (2014).
196. Wu, L. Y., Di Carlo, D. & Lee, L. P. Microfluidic self-assembly of tumor spheroids for anticancer drug discovery. Biomed. Microdevices 10, 197–202 (2007).
197. Heredia-Soto, V. et al. High-throughput 3-dimensional culture of epithelial ovarian cancer cells as preclinical model of disease. Oncotarget 9, 21893–21903 (2018).
198. Frey, O., Misun, P. M., Fluri, D. A., Hengstler, J. G. & Hierlemann, A. Reconfigurable microfluidic hanging drop network for multi-tissue interaction and analysis. Nat. Commun. 5, (2014).
199. Estrada, M. F. et al. Modelling the tumour microenvironment in long-term microencapsulated 3D co-cultures recapitulates phenotypic features of disease progression. Biomaterials 78, 50–61 (2016).
200. Rebelo, S. P. et al. 3D-3-culture: A tool to unveil macrophage plasticity in the tumour microenvironment. Biomaterials 163, 185–197 (2018).
201. Howlett, A. R. & Bissell, M. J. Regulation of mammary epithelial cell function: a role for stromal and basement membrane matrices. Protoplasma 159, 85–95 (1990).
202. Huch, M., Knoblich, J. A., Lutolf, M. P. & Martinez-Arias, A. The hope and the hype of organoid research. Dev. 144, 938–941 (2017).
203. Xu, H. et al. Organoid technology and applications in cancer research. J. Hematol. Oncol. 11, 1–15 (2018).
204. Sachs, N. et al. A Living Biobank of Breast Cancer Organoids Captures Disease Heterogeneity. Cell 172, 373-386.e10 (2018).
205. Sato, T. & Clevers, H. SnapShot: Growing Organoids from Stem Cells. Cell 161, 1700-1700.e1 (2015).
206. Matano, M. et al. Modeling colorectal cancer using CRISPR-Cas9-mediated engineering of human intestinal organoids. Nat. Med. 21, 256–262 (2015).
207. Denisona, T. A. & Bae, Y. H. Tumor heterogeneity and its implication to drug delivery. J Control Release 164, 187–191 (2012).
208. Wang, Y. et al. 3D Bioprinting of Breast Cancer Models for Drug Resistance Study. ACS Biomater. Sci. Eng. 4, 4401–4411 (2018).
209. Langer, E. M. et al. Modeling Tumor Phenotypes In Vitro with Three-Dimensional Bioprinting. Cell Rep. 26, 608–623 (2019).
210. Choi, Y. et al. A microengineered pathophysiological model of early-stage breast cancer. Lab Chip 15, 3350–3357 (2015).
211. Walsh, N. et al. Humanized mouse models of clinical disease. Physiol. Behav. 176, 139–148 (2017).
212. Kersten, K., Visser, K. E., Miltenburg, M. H. & Jonkers, J. Genetically engineered mouse models in oncology research and cancer medicine. EMBO Mol. Med. 9, 137–153 (2017).
213. Jonkers, J. & Berns, A. Conditional mouse models of sporadic cancer. Nat. Rev. Cancer 2, 251–265 (2002).

214. Cheon, D.-J. & Orsulic, S. Mouse Models of Cancer. Annu. Rev. Pathol. Mech. Dis. 6, 95–119 (2011).
215. Heyer, J., Kwong, L. N., Lowe, S. W. & Chin, L. Non-germline genetically engineered mouse models for translational cancer research. Nat. Rev. Cancer 10, 470–480 (2010).
216. Cong, L. et al. Multiplex Genome Engineering Using CRISPR/Cas Systems. Science 339, 819–823 (2013).
217. Holen, I., Speirs, V., Morrissey, B. & Blyth, K. In vivo models in breast cancer research: progress, challenges and future directions. Dis. Model. Mech. 10, 359–371 (2017).
218. Rashid, O. M. & Takabe, K. Animal models for exploring the pharmacokinetics of breast cancer therapies. Expert Opin Drug Metab Toxicol. 11, 221–230 (2015).
219. Everitt, J. I. The Future of Preclinical Animal Models in Pharmaceutical Discovery and Development:A Need to Bring In Cerebro to the In Vivo Discussions. Toxicol. Pathol. 43, 70–77 (2015).
220. Vargo-gogola, T. & Rosen, J. M. Modelling breast cancer: one size does not fit all. Nat. Rev. Cancer 7, (2014).
221. Allen, T. M. et al. Humanized immune system mouse models: progress, challenges and opportunities. Nat. Immunol. 20, 770–774 (2019).
222. Park, M. K., Lee, C. H. & Lee, H. Mouse models of breast cancer in preclinical research. Lab. Anim. Res. 6055, 160–165 (2018).
223. Sflomos, G. et al. A Preclinical Model for ERa-Positive Breast Cancer Points to the Epithelial Microenvironment as Determinant of Luminal Phenotype and Hormone Response. Cancer Cell 29, 407–422 (2016).
224. Özdemir, B. C., Sflomos, G. & Brisken, C. The challenges of modeling hormone receptor-positive breast cancer in mice. Endocr. Relat. Cancer 25, R319–R330 (2018).
225. Pfefferle, A. D. et al. Transcriptomic classification of genetically engineered mouse models of breast cancer identifies human subtype counterparts. Genome Biol. 14, (2013).
226. Jensen, M. R. et al. NVP-AUY922: A small molecule HSP90 inhibitor with potent antitumor activity in preclinical breast cancer models. Breast Cancer Res. 10, 1–12 (2008).
227. Cochrane, D. R. et al. Role of the androgen receptor in breast cancer and preclinical analysis of enzalutamide. Breast Cancer Res. 16, 1–19 (2014).
228. Cerliani, J. P. et al. Interaction between FGFR-2, STAT5, and progesterone receptors in breast cancer. Cancer Res. 71, 3720–3731 (2011).
229. Behbod, F. et al. An intraductal human-in-mouse transplantation model mimics the subtypes of ductal carcinoma in situ. Breast Cancer Res. 11, 1–11 (2009).
230. Zhao, S., Huang, J. & Ye, J. A fresh look at zebrafish from the perspective of cancer research. J. Exp. Clin. Cancer Res. 34, 1–9 (2015).
231. Drabsch, Y., He, S., Zhang, L., Snaar-Jagalska, B. E. & ten Dijke, P. Transforming growth factor-β signalling controls human breast cancer metastasis in a zebrafish xenograft model. Breast Cancer Res. 15, (2013).
232. Shanks, N., Greek, R. & Greek, J. Are animal models predictive for humans? Philos. Ethics, Humanit. Med. 4, 1–20 (2009).
233. Whittle, J. R., Lewis, M. T., Lindeman, G. J. & Visvader, J. E. Patient-derived xenograft models of breast cancer and their predictive power. Breast Cancer Res. 17, (2015).
234. Schuh, J. C. L. Trials, Tribulations, and Trends in Tumor Modeling in Mice. Toxicol. Pathol. 32, 53–66 (2004).

235. Mak, I. W. Y., Evaniew, N. & Ghert, M. Lost in translation: animal models and clinical trials in cancer treatment. Am. J. Transl. Res. 6, 114–118 (2014).
236. Hickman, J. A. et al. Three-dimensional models of cancer for pharmacology and cancer cell biology: Capturing tumor complexity in vitro/ex vivo. Biotechnol. J. 9, 1115–1128 (2014).
237. Davies, E. J. et al. Capturing complex tumour biology in vitro: Histological and molecular characterisation of precision cut slices. Sci. Rep. 5, 1–17 (2015).
238. Muraro, M. G. et al. Ex-vivo assessment of drug response on breast cancer primary tissue with preserved microenvironments. Oncoimmunology 6, 1–12 (2017).
239. Nissen E, Tanneberger S, Weiss H, B. E. In vitro cultivation of vital tissue slices: a new variation of organ culture technics. Biomed Biochim Acta 42, 907–916 (1983).
240. Milani, C. et al. Human breast tumor slices: A model for identification of vitamin D regulated genes in the tumor microenvironment. J. Steroid Biochem. Mol. Biol. 121, 151–155 (2010).
241. Parajuli, N. & Doppler, W. Precision-cut slice cultures of tumors from MMTV-neu mice for the study of the ex vivo response to cytokines and cytotoxic drugs. Vitr. Cell. Dev. Biol. - Anim. 45, 442–450 (2009).
242. Pennington, K., Chu, Q. D., Curiel, D. T., Li, B. D. L. & Mathis, J. M. The Utility of a Tissue Slice Model System to Determine Breast Cancer Infectivity by Oncolytic Adenoviruses. J Surg Res 163, 270–275 (2010).
243. Naipal, K. A. T. et al. Tumor slice culture system to assess drug response of primary breast cancer. BMC Cancer 16, 1–13 (2016).
244. Nath, S. & Devi, G. R. Three-dimensional culture systems in cancer research : Focus on tumor spheroid model. Pharmacol. Ther. 163, 94–108 (2016).
245. Bana, E. & Bagrel, D. In Vitro Breast Cancer Models as Useful Tools in Therapeutics? Intechopen (2011).
246. Campuzano, S. & Pelling, A. E. Scaffolds for 3D Cell Culture and Cellular Agriculture Applications Derived From Non-animal Sources. Front. Sustain. Food Syst. 3, 1–9 (2019).
247. Mckenna, M. T., Weis, J. A., Brock, A., Quaranta, V. & Yankeelov, T. E. Precision Medicine with Imprecise Therapy: Computational Modeling for Chemotherapy in Breast Cancer. Transl. Oncol. 11, 732–742 (2018).
248. Crespo, I., Coukos, G., Doucey, M.-A. & Xenarios, I. Modelling approaches in tumor microenvironment. J. Cancer Immunol. Ther. 01, (2018).
249. Munshi, A. & Sharma, V. In silico disease models of breast cancer. in Omics Approaches in Breast Cancer: Towards Next-Generation Diagnosis, Prognosis and Therapy 1–545 (2014).
250. Edelman, L. B., Eddy, J. A. & Price, N. D. In silico models of cancer. Wiley Interdiscip. Rev. Syst. Biol. Med. 2, 438–459 (2010).
251. Metzcar, J., Wang, Y., Heiland, R. & Macklin, P. A Review of Cell-Based Computational Modeling in Cancer Biology. Clin. Cancer Informatics 3, 1–13 (2019).
252. Zhao, Z., Ukidve, A., Kim, J. & Mitragotri, S. Targeting Strategies for Tissue-Specific Drug Delivery. Cell 181, 151–167 (2020).
253. Groh, C. M. et al. Mathematical and computational models of drug transport in tumours. J. R. Soc. Interface 11, (2014).
254. Xie, H. et al. Modeling three-dimensional invasive solid tumor growth in heterogeneous microenvironment under chemotherapy. PLoS One 13, 1–26 (2018).

255. Venkatasubramanian, R., Henson, M. A. & Forbes, N. S. Integrating Cell Cycle Progression, Drug Penetration and Energy Metabolism to Identify Improved Cancer Therapeutic Strategies. J Theor Biol. 23, 1–7 (2008).
256. Rejniak, K. A. et al. The role of tumor tissue architecture in treatment penetration and efficacy: an integrative study. Front. Oncol. 3, 1–13 (2013).
257. Karolak, A. & Rejniak, K. A. Micropharmacology: An In silico approach for assessing drug efficacy within a tumor tissue. Bull. Math. Biol. 81, 3623–3641 (2018).
258. Mascheroni, P. & Penta, R. The role of the microvascular network structure on diffusion and consumption of anticancer drugs. Int. j. numer. method. biomed. eng. 33, 1–24 (2017).
259. Ogston, A. G., Preston, B. N. & Wells, J. D. On the Transport of Compact Particles Through Solutions of Chain-Polymers. Proc. R. Soc. A Math. Phys. Eng. Sci. 333, 297–316 (1973).
260. Clague, D. S. & Phillips, R. J. Hindered diffusion of spherical macromolecules through dilute fibrous media. Phys. Fluids 8, 1720–1731 (1996).
261. Stylianopoulos, T. et al. Diffusion of Particles in the Extracellular Matrix: The Effect of Repulsive Electrostatic Interactions. Biophys. J. 99, 1342–1349 (2010).
262. Karolak, A. & Rejniak, K. A. Mathematical Modeling of Tumor Organoids: Toward Personalized Medicine. in Tumor Organoids 35–49 (2018).
263. Green, A. J., Johnson, C. J., Adamson, K. L. & Begent, R. H. J. Mathematical model of antibody targeting: important parameters defined using clinical data. Phys. Med. Biol. 46, 1679–1693 (2001).
264. Karolak, A. et al. Targeting ligand specificity linked to tumor tissue topological heterogeneity via single-cell micro-pharmacological modeling. Sci. Rep. 8, 1–14 (2018).
265. Boujelben, A. et al. Multimodality imaging and mathematical modelling of drug delivery to glioblastomas. Interface Focus 6, (2016).
266. Caraguel, F., Lesart, A. C., Estève, F., Van Der Sanden, B. & Stéphanou, A. Towards the design of a patient-specific virtual tumour. Comput. Math. Methods Med. 2016, (2016).
267. Fischer, H. P. Mathematical modeling of complex biological systems: From parts lists to understanding systems behavior. Alcohol Res. Heal. 31, 49–59 (2008).
268. Brodland, G. W. How computational models can help unlock biological systems. Semin. Cell Dev. Biol. 48, 62–73 (2015).

CHAPTER II

A novel culture method that sustains ERα signaling in human breast cancer tissue microstructures

This chapter was adapted from:

Ana Luísa Cartaxo*, Marta F Estrada*, Giacomo Domenici, Ruben Roque, Fernanda Silva, Emilio J. Gualda, Pablo Loza-Alvarez, George Sflomos, Cathrin Brisken, Paula M. Alves, Saudade André, Catarina Brito; *A novel culture method that sustains ERα signaling in human breast cancer tissue microstructures*, Journal of Experimental & Clinical Cancer Research, 2020, doi: 10.21203/rs.3.rs-20405/v1

* These authors equally contributed to this work

Table of contents

Abstract

Estrogen receptor α (ERα) signaling is a defining and driving event in most breast cancers; ERα is detected in malignant epithelial cells of 75% of all breast cancers (classified as ER-positive breast cancer) and, in these cases, ERα targeting is the main therapeutic strategy. However, the biological determinants of ERα heterogeneity and the mechanisms underlying therapeutic resistance are still elusive, hampered by the challenges in developing experimental models recapitulative of intra-tumoral heterogeneity and in which ERα signaling is sustained. *Ex vivo* cultures of human breast cancer tissue have been proposed to retain the original tissue architecture, epithelial and stromal cell components and ERα. However, loss of cellularity, viability and ERα expression are well-known culture-related phenomena.

Breast cancer samples were collected and brought to the laboratory. Then they were minced, enzymatically digested, entrapped in alginate and cultured for one month. The histological architecture, cellular composition and cell proliferation of tissue microstructures were assessed by immunohistochemistry. Cell viability was assessed by measurement of cell metabolic activity and histological evaluation. The presence of ERα was accessed by immunohistochemistry and RT-qPCR and its functionality evaluated by challenge with 17β-estradiol and fulvestrant.

We describe a strategy based on entrapment of breast cancer tissue microstructures in alginate capsules and their long-term culture under agitation, successfully applied to tissue obtained from 63 breast cancer patients. After one month in culture, the architectural features of the encapsulated tissue microstructures

were similar to the original patient tumors: epithelial, stromal and endothelial compartments were maintained, with an average of 97% of cell viability compared to day 0. In ERα-positive cases, fibers of collagen, the main extracellular matrix component *in vivo*, were preserved. ERα expression was at least partially retained at gene and protein levels and response to ERα stimulation and inhibition was observed at the level of downstream targets, demonstrating active ER signaling.

The proposed model system is a new methodology to study *ex vivo* breast cancer biology, in particular ERα signaling. It is suitable for interrogating the long-term effects of anti-endocrine drugs in a set-up that closely resembles the original tumor microenvironment, with potential application in pre- and co-clinical assays of ERα-positive breast cancer.

Key words: cancer, patient-derived tissue microstructures, 17β-estradiol, estrogen receptor alpha, fulvestrant, encapsulation, alginate

1. Background

Breast cancer (BC) is the most commonly diagnosed cancer among women worldwide [1]. It is a heterogeneous disease with distinct biological features and clinical outcomes. Almost 75% of diagnosed BC express estrogen receptor-alpha (ERα), being classified as ERα-positive (ER+) BC [2]. ERα acts as a ligand-dependent transcription factor for genes associated with cell survival, proliferation, and tumor growth [3]. Therefore, targeting the ERα-signaling pathway is the main therapeutic strategy for the treatment of ER+ BCs. Nonetheless, the disease often progresses in 30% of the patients undergoing hormonal therapy due to resistance [2]. Thus, there is a need to select patients that would respond to endocrine therapy and to elucidate the molecular mechanisms behind endocrine resistance, as well as to identify biomarkers that predict drug response and resistance and novel therapeutic targets in resistant tumors.

When cultured in classical 2D monolayers, ER+ BC cell lines fail in recapitulating the typical intratumoral ERα heterogeneity [4] and, due to cell confluency, cannot be kept continuously for more than one week [5], hampering the possibility to perform cycles of drug treatment for more than one week. Only a few ER+ cell lines can generate xenografts in mice, requiring supplementation with estrogen [6]. Recently, an estrogen supplementation-independent *in vivo* model was reported, based on intraductal implantation of ER+ tumor cells. The demonstration that the intraductal but not the mammary fat pad microenvironment favors epithelial malignant cells of the luminal subtype, consolidated the role of the tumor microenvironment (TME) in sustaining ER+ tumor cells [6]. Although

there is a report showing that it is possible to propagate normal primary breast ER+ cells in 2D [7], there are no reports for propagation of primary ER+ BC cells using this culture system. In fact, ER+ BC primary cells cultured in 2D loose cellularity and ERα expression after a short culture period.

Ex vivo cultures have been explored to sustain ER+ malignant epithelial cells within the original BC microenvironment [8]. Typically, these models retain tissue architecture and heterogeneity for short periods of time, around 3 to 4 days of culture [9,10]. Naipal *et al.* reported extension of culture time up to 7 days by exploring dynamic culture conditions [11]. Recently, Muraro *et al*. reported high cell viability and maintenance of ER expression up to 14 days in culture, when combining a collagen scaffold and a medium perfusion system [8]. Nonetheless, this methodology supports BC tissue maintenance by taking advantage of collagen scaffolds, biologically active animal-derived biomaterials which bring variability, as well as environmental and ethical concerns [12].

Here, we hypothesized that retention of the original microenvironment would favor the maintenance of ER+ BC phenotype and ERα signaling. We implemented an *ex vivo* strategy based on the encapsulation of tissue microstructures in alginate, an inert biomaterial, combined with dynamic culture, aiming to maintain the original tissue structure, cell populations and extracellular matrix (ECM). We have recently shown that alginate microencapsulation of cancer cell spheroids and TME cellular components promotes tumor-stromal crosstalk and retention of secreted ECM components towards reconstruction of TME features [13,14]. Therefore, we reasoned that by using alginate encapsulation to promote the original TME retention, while resourcing to dynamic

culture to guarantee efficient diffusion of nutrients and oxygen, tissue microstructures would retain architectural integrity and potentially ER signaling.

2. Methods

2.1. Ethics statement

BC samples were collected at the Lisbon Oncology Hospital (Instituto Português de Oncologia de Lisboa Francisco Gentil – IPOLFG). The use of patient material was approved by the IPOFLG ethics committee and all patients have signed an informed consent form to agree to donate the material for research purposes. All tissues were anonymized before transfer to the laboratory for further processing.

2.2. Cell culture

MDA-MB-231 cell line was obtained from the American Type Culture Collection (ATCC). MDA-MB-231 cells were cultured in Dulbecco's Modified Eagle Medium (DMEM) high glucose and pyruvate medium (Gibco), supplemented with 10% (v/v) fetal bovine serum (FBS, Gibco) and 1% (v/v) Penicillin/Streptomycin (P/S, Gibco) at 37˚C in 5% CO2. Mycoplasma contamination was routinely checked.

2.3. Collection and processing of patient material

This study was elaborated on treatment-naïve patient-derived BC tissue. The method for processing and culture was successfully applied to 63 female breast tumors (Table 1). Tumor samples were collected during surgery and immediately submerged in phenol red-free DMEM/F-12 (Gibco), supplemented

with 1% (v/v) P/S (Gibco) and 10% (v/v) FBS (Gibco). Samples were kept at 4 ˚C and transported to the laboratory within 1 to 3 hours after surgery (Figure 2.1A). Sixty-three BC samples were collected, with an average weight of 315±225 mg (Figure S2.1).

Tissue samples were mechanically dissociated with two surgical scalpels to obtain pieces of 1 to 2 mm of diameter. Subsequently, the minced tissue was resuspended in phenol red-free DMEM/F-12, HEPES medium (Gibco) containing 0.09 U/mL of Collagenase A (Roche), 30 U/mL of Benzonase (Merck Millipore), 10% (v/v) FBS (Gibco) and 1% (v/v) P/S (Gibco). Digestion was performed in an incubator at 37 ˚C, in a humidified atmosphere containing 5% CO_2. After 12-15 hours of enzymatic digestion, tumor fragments (tissue microstructures, average of 1 mm^3) were sedimented by centrifugation at 100x g for 5 min at 4 ˚C and washed with Phosphate-Buffered Saline (PBS; Life Technologies) (Figure 2.1A).

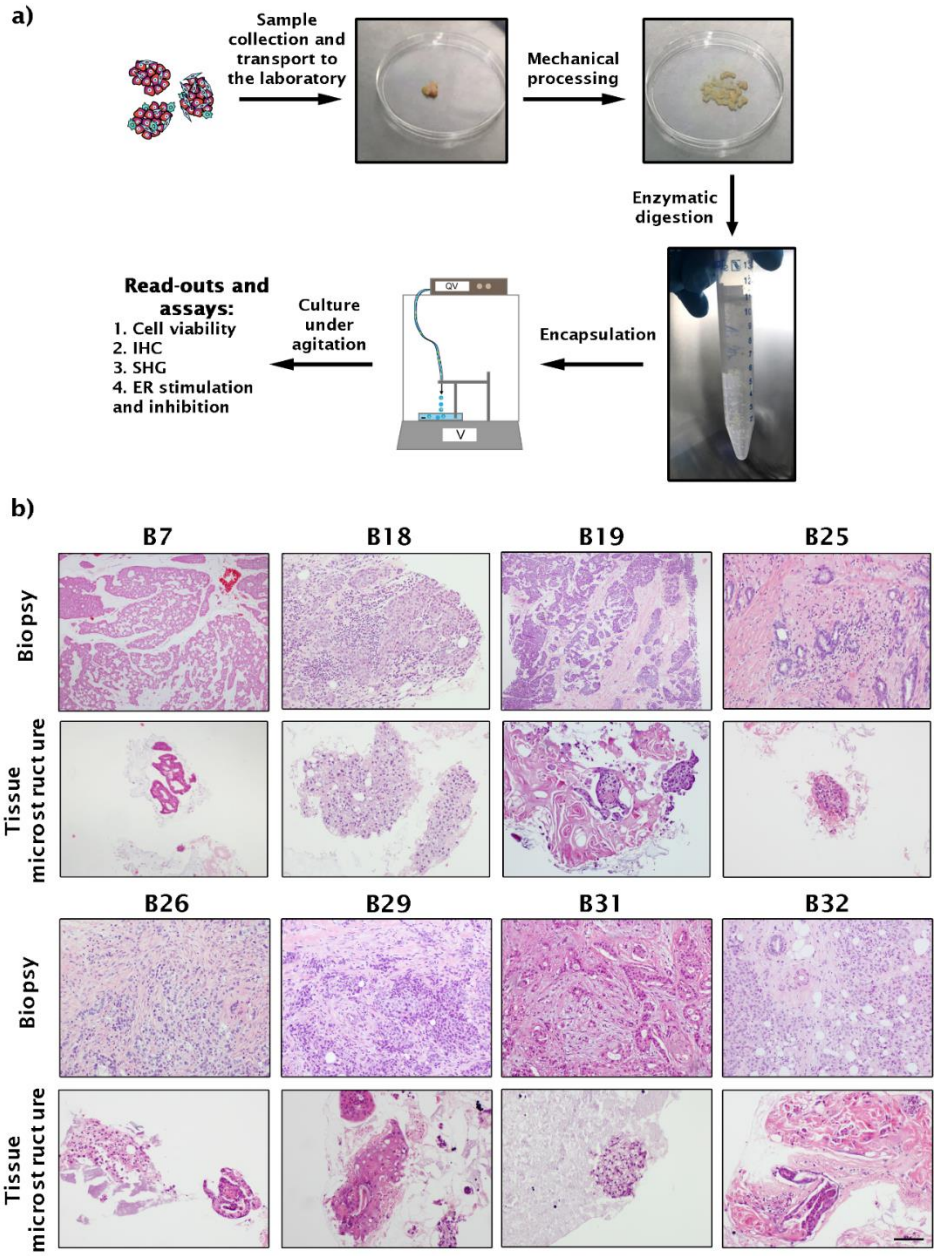

See caption in the next page.

Figure 2.1: Alginate encapsulated tissue microstructures maintained parental tumor architecture. **a** Experimental workflow for the establishment of long-term cultures of BC patient-derived tissue microstructures: samples were collected at the hospital and brought to the laboratory within 1-3 hours of surgery. Tissue samples were mechanical processed and subjected to mild enzymatic digestion. The obtained BC tissue microstructures were encapsulated in alginate and cultured for up to one month. Along culture, tissue microstructures were interrogated: cell viability assessment, immunohistochemistry analysis (IHC), Second Harmonic Generation (SHG) microscopy and estrogen receptor α (ER) stimulation and inhibition were performed. **b** Hematoxylin and eosin of biopsy (top row) and corresponding encapsulated microstructures at one month of culture (bottom row) (scale: 200 μm).

Table 2.1: Clinico-pathological parameters of the breast cancer patients. pT: primary tumor; pN: primary node.

Clinico-pathological parameters	**(n)**	
Female tumor samples	63	
Mean age at diagnosis	62 (42-89)	
Hormone receptors	**(n)**	**Percentage of tumors**
ERα status	59	94
PR status	51	81
HER2 status	11	17
Triple negative status	1	2
Histological subtype	**(n)**	**Percentage of tumors**
Invasive breast carcinoma of no-special type (NST)	51	81
Lobular carcinoma	10	16
Mucinous carcinoma	2	3
Tumor grade*	**(n)**	**Percentage of tumors**
1	2	3
2	50	79
3	9	14
Not defined	2	3
Tumor size**	**(n)**	**Percentage of tumors**
pT1	38	60
pT2	22	35
pT3	3	5
Lymph node involvement status**	**(n)**	**Percentage of tumors**
pN0	41	65
pN1	21	33
pN2	1	2

** Tumor grade was classified according with WHO Classification of Tumors (5th edition, volume 2).*

*** Tumor staging (pT and pN) was classified according with the American Joint Committee on Cancer TNM system (8th revision).*

2.4. Tissue microstructure encapsulation and culture

Tissue microstructures were entrapped in alginate, employing protocols previously developed by our team [14]. Briefly, tissue microstructures were dispersed in 1 mL of 2% (w/v) of Ultrapure Ca^{2+} MVG alginate (UP MVG NovaMatrix, Pronova Biomedical, Oslo, Norway) dissolved in NaCl 0.9% (w/v). Encapsulation was performed using an electrostatic bead generator (Nisco VarV1, Zurich, Switzerland), with an air flow rate of 10 mL/h, at 5.3 V under air pressure of 1 bar, using a 1.1 mm nozzle. The resulting alginate droplets containing tissue micro fragments (1-2 fragments/droplet) were cross-linked in a 100 mM $CaCl_2$/10 mM HEPES (pH 7.4) solution for 10 min, washed three times in a 0.9% (w/v) NaCl solution and finally equilibrated in culture medium. Encapsulated tissue microstructures were then transferred into 6-well plates and placed under orbital shaking (100 rpm), in a humidified incubator, with 5% CO_2. Encapsulated tissue microstructures cultures were maintained up to 30 days, with 50% medium exchange every 3-4 days (Figure 2.1A). Cultures were maintained in human mammary epithelial cell (HMEC) culture medium: DMEM/F12 phenol red free with 1% P/S (v/v) solution (both from Life Technologies), 5 ng/mL Epidermal Growth Factor (EGF), 10 μg/mL Insulin, 0.5 μg/mL Hydrocortisone, 0.5 μg/mL Transferrin, 0.1 mM Isoprotenol, 0.1 mM Ethanolamine, 0.1 mM O-Phosphoethanolamine, 70 μg/mL Bovine Pituitary Extract (all reagents are from Sigma-Aldrich) and 100 μg/mL Primocin (InvivoGen Europe). Non-encapsulated tissue microstructures were maintained under the same culture conditions. Encapsulated tissue microstructures were assessed for cell viability, architecture, cell populations, ECM deposition, ERα presence and signaling, as

described below; the extent of assessment performed for each sample was determined by the initial sample size.

2.5. Cell viability assessment

Cell viability was correlated with resazurin reduction capacity (PrestoBlue™ Cell Viability Reagent, ThermoFischer Scientific), according to manufacturer's instructions. Encapsulated and non-encapsulated samples were incubated for 1 hour with PrestoBlue reagent in culture medium, at 37˚C, in a humidified atmosphere incubator, containing 5% CO_2. Medium was sampled in quadruplicate and resazurin reduction evaluated by fluorescence detection (ext/em 560/590 nm) in a fluorimeter (Infinite®200 PRO NanoQuant, Tecan Trading AG). Resazurin reduction was evaluated for 1 month, once a week. Data is represented as fold-change in resazurin reduction relative to the first week of the assay.

2.6. Histological and immunohistochemistry analysis

Samples were collected after 1 month of culture and alginate capsules were de-polymerized with 50 mM ethylenediaminetetraacetic acid (EDTA) for 5 min at RT. De-encapsulated tissue microstructures were centrifuged at 300x g, 5 min at 4 ˚C, washed with PBS, fixed with formol overnight at RT. For paraffin cell-block preparation, the cellular suspension was centrifuged for 5 min, at 1270x g, resuspended in 10% (v/v) buffered formalin (VWR BDH Chemicals, ref. 9713.9010) to which a drop of haematoxylin was added for specimen counterstain, and stored in a 1.5 mL microtube. The remaining supernatants were subjected to a second centrifugation, for 5 min, at 1990x g. The supernatant was discarded and four drops of liquefied HistoGel

(Thermo Scientific, ref. HG-4000-012) were added to the pellet. After gentle homogenization with a Pasteur pipette and centrifugation for 2 min, at 1990x g, the sample was placed at -20˚C for 5 min to solidify. The cone shape solidified sample was removed from the microtube, cut along the meridional section and placed in a biopsy cassette, which was then immerged in a container with buffered formalin to be included in paraffin. After processing, the samples were sectioned and stained with hematoxylin and eosin (H&E) (Dako CoverStainer for H&E equipment, Agilent, Santa Clara, CA, USA). Paraffin blocks were sectioned (3 μm) for H&E and immunohistochemical staining. Immunohistochemistry (IHC) was carried out using standard procedures implemented at IPOLFG; antigen retrieval was done using Cell Conditioning 1 (CC1, Ventana) and tissue staining was performed using an automated IHC/ISH slide staining Ventana BenchMark Ultra (all from Ventana Medical Systems, Inc). Antibodies and details on the protocol used are indicated in Table S1. Histologic analysis was performed by an expert breast pathologist. IHC analysis was performed for cultures derived from BC samples of 18 patients. Due to primary material limitations, E-cadherin, CD45, ki-67, ER and p63 levels were assessed in 8 different samples; vimentin was assessed in 9 and CD31 in 2.

2.7. Multi-photon microscopy

Fibrillar Collagen was assessed by multi-photon microscopy. After 1 month in culture, encapsulated tissue microstructures were collected, fixed in PFA 4% (w/v) in PBS for 30 min, washed thrice with PBS and kept at 4˚C until further analysis. Samples were imaged with two-photon-excited fluorescence (TPEF), second

harmonic generation (SHG) and infrared (IR) absorption in a home-made multiphoton microscope [15]. The excitation laser was a Ti:Sapphire at 810 nm and the laser power, at entrance of the microscope, was of 40 mW. Initial tests performed with 100 mW resulted in no observable sample damage. The Illumination objective was an Olympus 25x 1.05 W. The TPEF signal was collected through a photomultiplier tube (PMT) in backward direction (using a LP410 filter) while IR absorption and SHG (405/25 filter) were collected in forward direction through a Nikon 25x 1.10 W objective, using a photodetector and a PMT respectively. During acquisition, 3-4 images were averaged to reduce noise.

2.8. Challenge with ERα agonist and antagonist

At day 28-30 of culture, encapsulated BC tissue microstructures were stimulated with 10 nM 17β-estradiol (Sigma-Aldrich). Three days before 17β-estradiol challenge, encapsulated tissue microstructures were washed thrice with PBS and were then kept in phenol red-free HMEC medium without insulin, hydrocortisone and EGF, which may trigger activation or phosphorylation of ER [16–21]. Alternatively, a 50% culture medium exchange was performed by the time of 17β-estradiol challenge. Control wells were also included, in which only ethanol (17β-estradiol vehicle) was added to a final concentration of 0.001% (v/v). After 24h of exposure, encapsulated tissue microstructures were collected and alginate dissolved (as described in section 6 of Materials and Methods). Challenge with 17β-estradiol was performed in encapsulated microstructures derived from 16

different patients, of which 9 in depleted medium and 7 in complete medium.

Encapsulated tissue microstructures were also challenged with fulvestrant (ICI182,780), an ER antagonist and degrader. For these experiments, 3-5 days after encapsulation HMEC medium was supplemented with 1 μM fulvestrant [22,23] (Tocris Bioscience). Twice a week, half volume of culture medium was changed and fulvestrant was replenished to keep a constant concentration. After 2 weeks, samples were centrifuged at 300x g, 5 min at 4 ˚C, washed with PBS and processed for IHC (as detailed above) or RT-qPCR analysis. Samples for RT-qPCR were stored in RNAlater Stabilization Solution (Roche), according with the manufacturer's instructions, until further analysis; samples for western blot were snap frozen at -80 ˚C. Challenge with fulvestrant was performed in encapsulated microstructures derived from 8 different patients, of which 7 were evaluated by RT-qPCR and 3 by Western Blot.

2.9. Gene expression analysis

Tissue microstructures were thawed, total RNA was extracted in a tissue lyser (Precellys Evolution Homogenizer, Bertin Instruments) and purified using the RNAeasy Kit (Qiagen), according to the manufacturer's instructions. Reverse transcription was performed using Sensiscript RT kit (Qiagen), also according with the manufacturer's instructions. qPCR was performed in triplicates, using the SYBR green I Master kit (Roche), in a LightCycler 480 II (Roche). We evaluated expression of ERα (*ESR1)* and its downstream target genes, *pS2*, *AREG* and *PGR* [24], and of two housekeeping genes, *RPL22* [13] and *36B4* [24]. Primer sequences are provided in Table S2. Due to the scarcity of ERα negative BC

samples, a ERα and PR negative BC cell line, MDA-MB-231, was employed as basal expressing control [25]. Results are shown as fold change in mRNA amount compared to the vehicle control (CTRL), calculated according to the $2^{-\Delta\Delta Ct}$ method [26], considering a geometric mean of the 2 housekeeping genes used.

2.10. Western Blot analysis

Samples were thawed, resuspended in Laemmly Buffer (20% Glycerol, 4% SDS in 100 mM Tris Buffer, pH 6.8) and lysed in a Tissue homogenizer (Precellys Evolution, Bertin Instruments). BC Microstructure lysates were recovered, sedimented to remove cell debris, sonicated and stored at -80 ˚C until use.

Protein quantification was performed in a Nanodrop ND-2000C (Thermo Scientific). Proteins were denatured and loaded in an electrophoresis gel (NuPAGE 4-12% Bis-Tris Gel) under reducing conditions for 50 min (200 V) and then electrophoretically transferred using a Bio-Rad wet system (30 V, 18 hours, 4˚C) into Nitrocellulose membranes. Membranes were blocked for 1 h in TBS with 0.1% (w/v) Tween 20, 5% (w/v) non-fat dried milk and further incubated with the primary antibodies (Mouse anti-Human ERα, 1D5 Clone, Dako, final dilution 1:500; Rabbit anti-β tubulin, H-235, SC-9104, SantaCruz, final dilution 1:1000, used as loading control) and respective secondary HRP-conjugated secondary antibodies (Sheep anti Mouse IgG NA931; Donkey anti Rabbit IgG NA934; GE Healthcare, final dilution 1:20000). Membranes were developed using Amersham ECL Select Western Blot Detection Reagent (GE Healthcare) and visualized using a ChemiDoc System (BioRad).

2.11. Statistical analysis

Statistical analysis was performed using GraphPad Prism version 6.0 (GraphPad Software). Data were analyzed as indicated in the figure legends. The Mann-Whitney test was performed to evaluate statistical difference between conditions. Data are presented as mean ± SD, unless otherwise specified.

3. Results

3.1. Alginate encapsulated tissue microstructures maintain parental tumor tissue characteristics for at least one month of culture

To establish an ER+ BC *ex vivo* model, we investigated the possibility of retaining the TME and consequently ERα signaling of patient-derived tissue microstructures immobilized within alginate capsules and cultured under agitation (Figure 2.1A). Encapsulated tissue microstructures were cultured for up to 30 days, showing high cell viability, as indicated by maintenance of resazurin reduction capacity along culture time (97±28% by the end of week 4, relatively to the beginning of the culture, Figure S2.2A). Moreover, detection of extracellular lactate in culture medium (data not shown), as an indicator of high metabolic activity [27] corroborated the high cell viability within the encapsulated tissue microstructures.

The original tumors were very heterogeneous, not only between but also within patients (Figure 2.1B): tissue architecture varied in epithelial versus stromal content, cell organization and on the presence/absence of immune cells (CD45+ cells). A complete mixture of malignant epithelial cells and stromal cells was rarely observed. Instead, there were islets of tumor cells surrounded by

multiple stromal cells (Figure 2.1B, upper panels). These histopathological characteristics were maintained in encapsulated tissue microstructures cultured for a month (Figure 2.1B, lower panels). By day 30 of culture, E-cadherin, vimentin, CD31 and CD45 were immunohistochemically-detected (Figure 2.2A). The detection of membranous E-cadherin indicated that carcinoma cells maintained the typical cell-cell adhesions and differentiated phenotype [28]. On the other hand, vimentin detection confirmed the presence of stromal cells. CD45, also known as leucocyte common antigen, is a transmembrane glycoprotein present in all nucleated cells of the hematopoietic lineage [29] and has been broadly used to assess immune cell population presence in breast tissue, such as tumor-infiltrating lymphocytes [30–32]. $CD45^+$ cells were detected in 5 out of the 8 cases which presented immune cells in the original tissue (Figure 2.2A). In two analyzed tissue microstructures, CD31 positivity confirmed the presence of endothelial cells (Figure 2.2A). Absence of cells positive for the basal/myoepithelial marker p63 was observed similarly to the original tumors (Figure S2.2B). Ki67-positive cells were also detected at different levels, indicating the presence of proliferating cells even after one month of culture (Figure 2.2B). Although at low levels, this is consistent with the parental tissues, where the median of proliferating cells was 20% (Q1=15; Q3=30). Second harmonic generation analysis (SHG) of encapsulated BC tissue microstructures revealed dense and organized/fibrillar collagen fibers in peripheral regions of the samples analyzed, surrounding areas of cellularity (Figure 2.3). As a culture control, non-encapsulated tissue microstructures were cultured in parallel. A significant decrease in resazurin reduction ability after 3-4 weeks of culture was observed, suggesting a

reduced cell viability of these cultures. Remarkably, cell viability was increased in encapsulated versus non-encapsulated tissue microstructures (Figure S2.2C).

Altogether, we were able to extend the lifespan of BC explant cultures for up to one month whilst maintaining tissue architecture, the different cell types of the BC microenvironment, and cell viability.

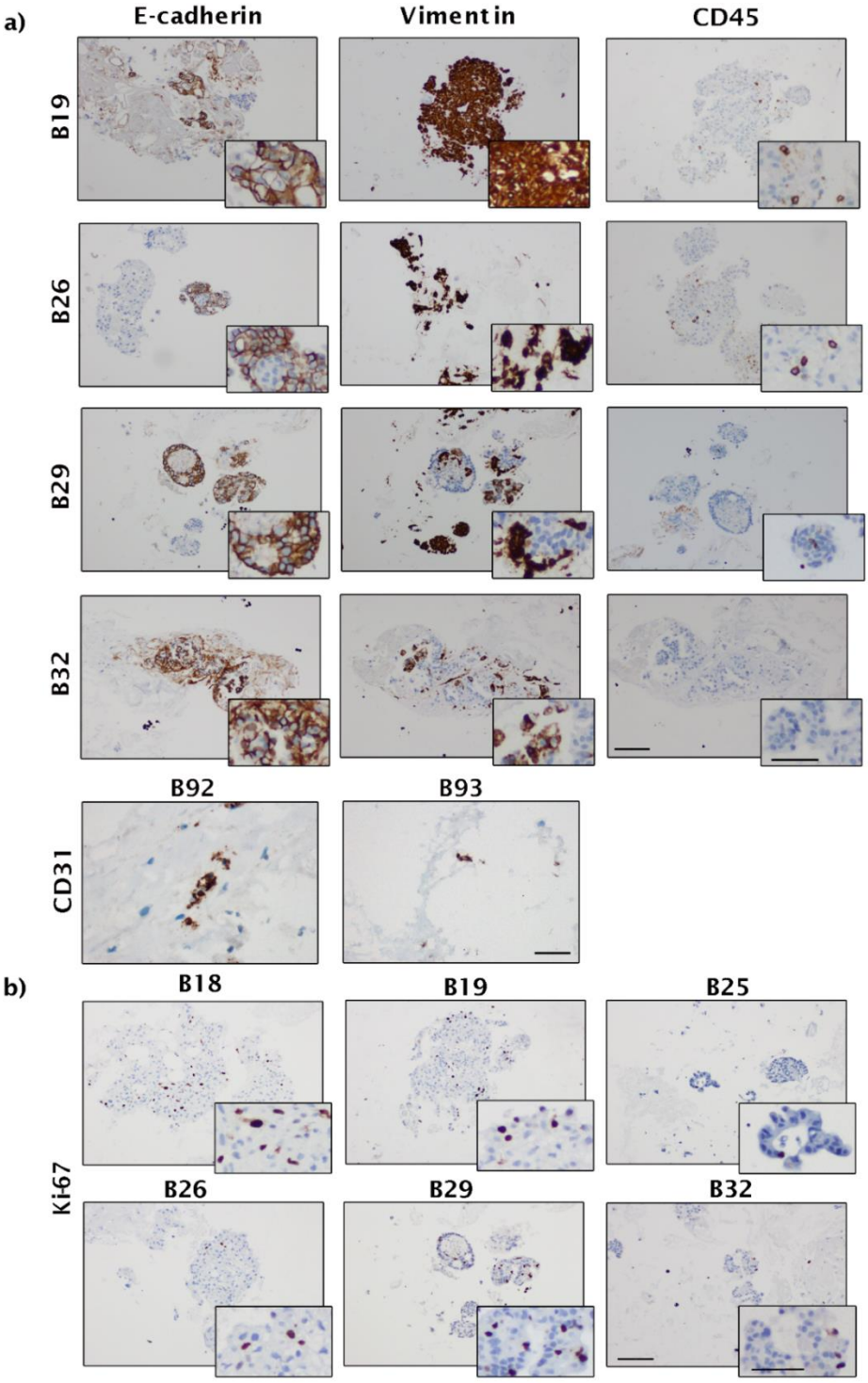

See caption in the next page.

Figure 2.2: Alginate encapsulated tissue microstructures maintained cell populations and contain proliferating cells. **a** Immunohistochemistry analysis of: E-cadherin (epithelial cells); vimentin (stromal cells); CD45 (immune cells); CD31 (endothelial cells) at one month of culture **b** Immunohistochemistry analysis of Ki-67 (cell proliferation) of encapsulated microstructures at one month of culture (scale bars: 200 µm for low magnification and 100 µm for high magnification).

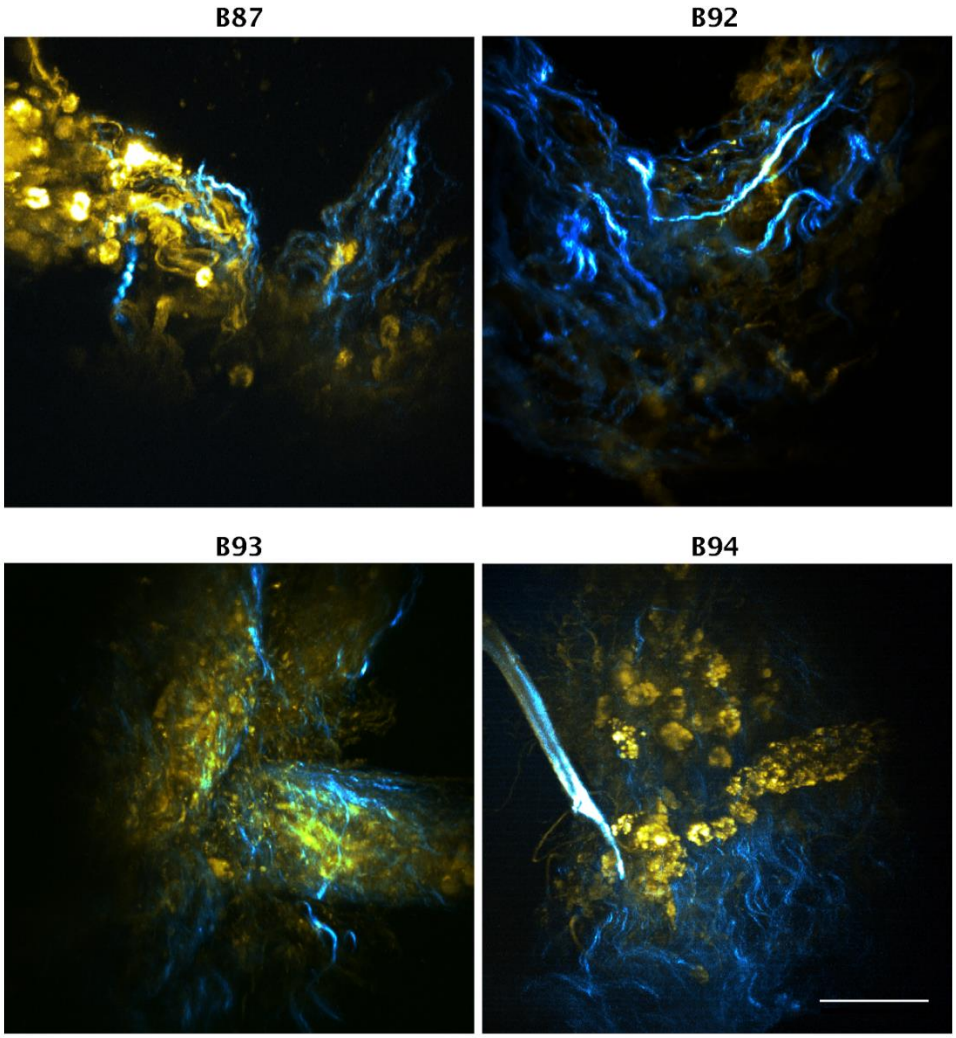

Figure 2.3: Encapsulated tissue microstructures maintained collagen fibrillar structures. Second Harmonic Generation (SHG) microscopy at one month of culture: yellow – Two-Photon Excitation Microscopy (TPEF); blue - collagen fibers (scale bar: 50 µm).

3.2. ERα expression and functionality are sustained over 1 month of culture

After one month in culture, ER+ carcinoma cells were still detected in the encapsulated tissue microstructures by IHC analysis (Figure 2.4A), typically in lesser extent that in the original sample. When sample material was not sufficient for IHC evaluation, mRNA was quantified, relatively to MDA-MB-231, a human cancer cell line which does not express ERα nor PR [25] (Figure S2.3A). All samples presented higher expression of the ERα gene (*ESR1)* than MDA-MB-231 cells, indicating ERα gene expression after one month of culture (Figure S2.3B and Figure S2.5).

To assess ERα function, encapsulated tissue microstructures derived from ER+ BC from 9 distinct patients were stimulated with 10 nM 17β-estradiol for 24 hours and the mRNA levels of the ER target genes evaluated: protein PS2 (also known as Trefoil Factor 1 -TFF1-, *pS2)*, progesterone receptor (*PGR*) and amphiregulin (*AREG*) [24]. *AREG* and *PGR* were upregulated upon challenging with 17β-estradiol compared to vehicle-controls (mean fold increase in *AREG* and *PGR* expression of 3.4±5.6 and 6.3±11 respectively, Figure 2.4B, Figure S2.4A). Strikingly, we detected a generalized upregulation of *pS2* (in 7 out of 9 tissue microstructures), with a mean fold increase in gene expression of 45±45, compared to the vehicle-treated control (Figure 2.4B, Figure S2.4A and Figure S2.5). In general, there was a trend for a positive correlation between *ESR1* basal expression and the expression of the three ER target genes upon estrogen challenge (Figure S2.4B, R>0 by Pearson Correlation), even though not significant, probably due to the intrinsic variability of primary tumors and the sample size. Tissue microstructure cultures derived from ER-negative BC tumors were

also treated with 17β-estradiol and no upregulation of ER downstream genes was observed (Figure S2.4C). This data further corroborates that the original phenotype is maintained in culture. A different set of encapsulated tissue microstructures derived from ER+ BC samples of 7 tumors, were maintained in HMEC medium until 17β-estradiol challenge. These showed a mild stimulation of ERα target genes (on average, 2.3-, 1.8- and 1.2-fold increase relatively to vehicle control for *pS2*, *PGR* and *AREG*, respectively, Figure S2.4D).

To further confirm intact ERα signaling in encapsulated tissue microstructures, cultures derived additional ER+ BC samples were exposed to fulvestrant (or ICI182,720), a ERα full antagonist [33] widely used in endocrine therapy [34]. After 2 weeks of exposure, a generalized down regulation of *AREG* compared to vehicle controls was observed (Figure 2.4C). For two of the tumors, we also evaluated *PGR* and *pS2* response and observed a strong reduction of mRNA levels compared to vehicle controls (Figure 2.4D). Additionally, we assessed ERα protein levels in three of the tumors and observed a tendency for reduction compared to vehicle control conditions (Figure S2.6). Collectively, these results indicate that *ERα* is expressed in encapsulated tissue microstructures derived from ER+ BC samples and can respond to stimulation and inhibition.

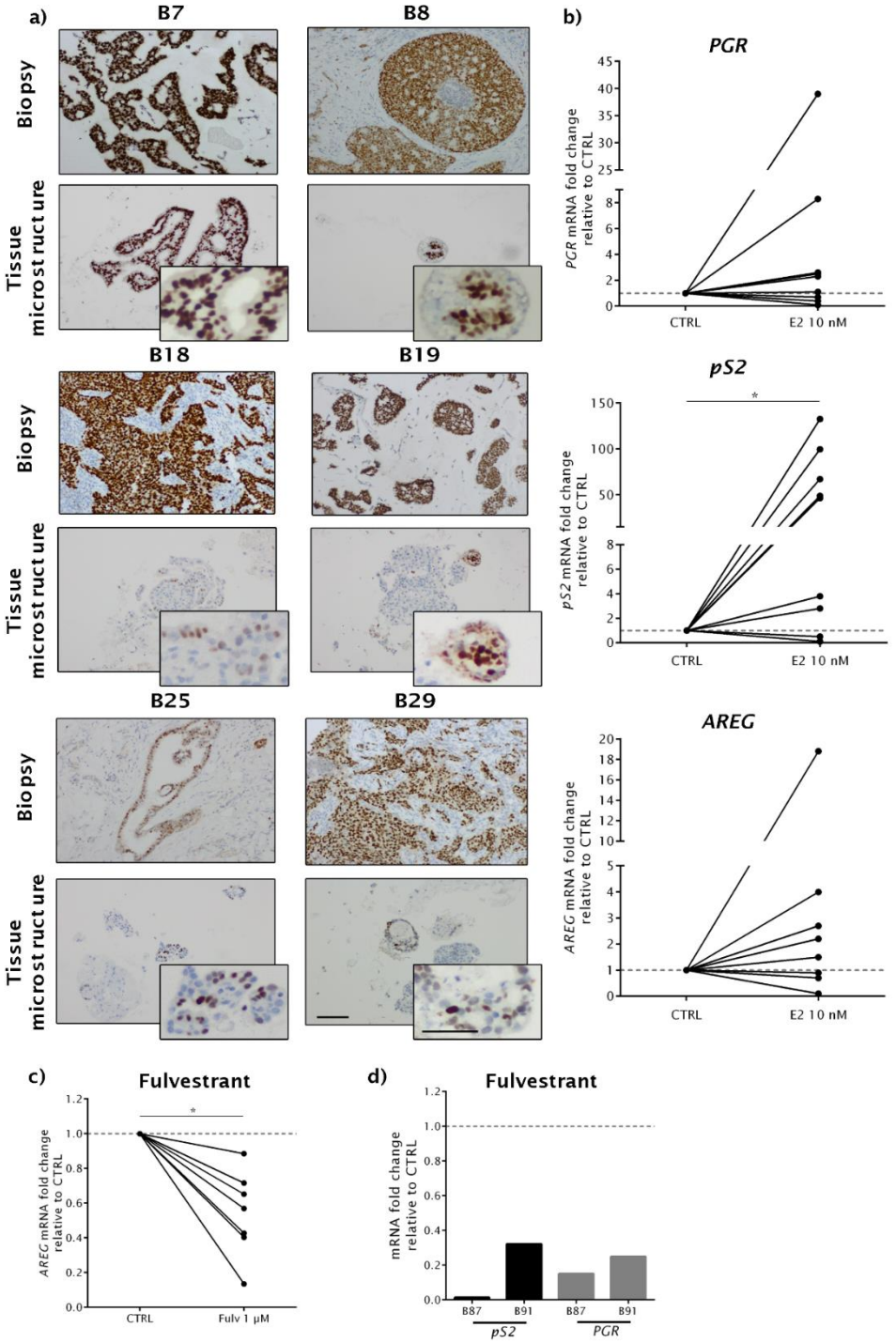

See caption in the next page.

Figure 2.4: Estrogen receptor α (ER) expression and functionality are maintained in alginate encapsulated tissue microstructures up to 1 month of culture. **a** Immunohistochemistry detection of ER in biopsy (top row) and encapsulated tissue microstructures culture for a month (bottom row) (scale bars: 200 μm for low magnification and 100 μm for high magnification). **b** Encapsulated tissue microstructures were cultured for 3 days in depleted medium and stimulated with 17β-estradiol; expression of ER downstream target genes was assessed by RT-qPCR (amphiregulin - *AREG*, progesterone receptor - *PGR* and protein PS2 - *pS2*, N=9). Data are shown as fold change in gene expression upon 17β-estradiol challenge relatively to vehicle-exposed control (CTRL). **c**,**d** Encapsulated tissue microstructures were cultured for 3-5 days in complete medium, before challenge with fulvestrant for two weeks; ER downstream targets were assessed by RT-qPCR (*AREG*, *PGR* and *pS2*, N=7). Data are shown as fold change in gene expression upon fulvestrant challenge relatively to vehicle-exposed control. Statistical analysis was performed by the Mann-Whitney test (**p-value*<0.001).

4. Discussion

ERα signaling is considered a defining and driving event contributing to ER+ BC carcinogenesis; ERα overexpression in primary tumors has been linked to disease progression, influencing patient survival [35–37]. Nonetheless, approximately 30% of patients with ER+ BC fail to respond to endocrine therapy [2]. Several reports have shown the intricate relation between response to therapy and TME components, such as fibroblasts [38–40] and ECM components [41,42]. Therefore, it is paramount to define the biological determinants of ERα intra-tumoral heterogeneity and the mechanisms underlying therapeutic resistance. However, this knowledge has been hampered by the challenges in developing experimental models recapitulative of intra-tumoral ERα heterogeneity and in which ERα signaling is sustained, essential to address long-term effects of tumor-stromal interactions in ERα signaling and drug response mechanisms against ER.

Here, we propose a culture strategy in which patient-derived tissue microstructures retain ER+ carcinoma cells for at least one month of culture; of note, these cells still respond to ER stimulation and inhibition, therefore constituting a functional *ex vivo* model of ER-positive BC. Tissue microstructures that were entrapped in alginate capsules and cultured under dynamic conditions maintained high cellularity, low levels of tumor cell proliferation, as reported for human ER+ BC [43] and parental tissue architecture (including epithelial, stromal and endothelial cell compartments and deposited fibrillar collagen). Although all interrogation was limited to one month of culture, as we have not detected signs of tissue microstructure decline in cell viability up to that timepoint, we conjecture that the lifespan of encapsulated tissue microstructures could be extended for even longer periods.

We hypothesized that using tissue microstructures within the millimeter size range would be more favorable to attain an accurate representation of intra-tumoral heterogeneity and TME, than more miniaturized *ex vivo* models. To overcome the major limitations of *ex vivo* cultures – the reduced lifespan and zonation due to diffusional gradients [44], we resourced to dynamic culture conditions. Agitation improves mass transfer, promoting nutrient and oxygen diffusion, reducing the formation of gradients typically observed for tissue microstructures within the above mentioned size range [45,46]. Moreover, we encapsulated in alginate, a biocompatible, inert hydrogel [47] since it has defined composition and confers support and protection from agitation-induced shear stress [14,48,49]. This contributes to the preservation of tissue architecture and cell viability, but also promotes the built-up of relevant cell microenvironment factors. In fact, we have previously

shown that cells entrapped in alginate capsules, and cultured under agitation, accumulate secreted soluble factors (e.g., cytokines) and ECM components, promoting homotypic and heterotypic cellular crosstalk, cell migration and reconstruction of cancer-related microenvironments [13,14], such as an immunosuppressive microenvironment in a non-small cell lung cancer model [13]. In terms of ECM components, we not only observed the maintenance of TME cellular components in the encapsulated tissue microstructures, such as the stromal cells, which are involved in the secretion of collagen [50], but also ECM components as collagen fibers. These were detected by SHG microscopy, a technique broadly applied to BC tissue [51]. In all the encapsulated tissue microstructures analyzed fibrillar collagen presence was observed. Increased collagen density has been shown to directly promote BC tumorigenesis [52]. Moreover, collagen is strongly associated with mammographic density used as a measurement of risk of BC [53] and is responsible for drug resistance since it prevents the penetration of therapeutic agents, such as antibodies [54].

The preservation of tumor heterogeneity and TME are critical to closely mimic the *in vivo* situation [4,55]. We observed a high degree of heterogeneity between distinct parental tissues - not only the levels of ER-positivity were different, but also the percentages and physical distribution of carcinoma and stromal cells - that were recapitulated in the derived tissue microstructures. In 5 out of 8 tissue microstructure cultures derived from tumors with immune cell infiltrate, CD45-positive cells were retained even after one month of culture, although in low amounts. This is in accordance with the typically low frequency of immune cell infiltrates in ER+ tumors [56].

After 1 month in culture, p63 was not detected in tissue microstructures, in accordance with what is reported for luminal BC. In fact, the myoepithelial marker p63 is present in basal cells of a variety of healthy epithelial tissues [57], such as in normal breast tissue. However, its expression in BC is rare [58,59]. On the other hand, tissue microstructures presented low levels of Ki-67; in fact, ERα-positive subtypes have lower proliferative indexes than other BC subtypes [60]. The intrinsic low levels of cell proliferation and the reduced amount of patient tissue available to set-up tumor microstructure cultures, limit their application in high throughput assays.

The maintenance of ER+ cells in culture is a major accomplishment, as ERα ablation *ex vivo* has been a major issue in ER+ BC research [61]. The sustained expression of ERα is pivotal for the study of the luminal A BC subtype, as cell proliferation is ER-dependent and targeted therapies typically rely on prolonged treatment with ERα antagonists [62]. After one month in culture, we detected ER+ cells in the encapsulated tissue microstructures, typically in a less extent than in the original tumor. ERα functionality was evaluated by challenging encapsulated tissue microstructures, with either activator (17β-estradiol) or inhibitor (fulvestrant) molecules. Our results show differential expression of *PGR*, *AREG* and *pS2* in tissue microstructures originated from different ER+ BC patients, suggesting that the model reflects inter-patient heterogeneity. This may be in terms of basal expression levels of the target genes analyzed, ER transcriptional response and potential presence of ER-independent regulatory pathways [4,63]. *pS2* is a well-known direct downstream ERα target, which is under the positive control of an ERE consensus sequence located 400 bp

before transcription starting site [64]. Our results show a higher upregulation of *pS2* when comparing with *AREG* and *PGR*. In fact, it has been reported for the ER+ MCF-7 BC cell line that, upon estrogen exposure, *pS2* expression strongly increases compared to *PGR*, at mRNA and also at protein levels [65,66]. We have also observed the effects of fulvestrant at the level of ERα protein, as the drug is described to accelerate ERα degradation [33].

Aiming to retain ER+ cells, we employed a culture medium enriched in molecules with reported ER stimulatory effects, such as insulin, hydrocortisone and EGF [16–21]. 17β-estradiol and EGF may also be produced by the breast fibroblasts present in culture [67–69]. Our observation of reduced effects upon 17β-estradiol stimulation in tissue microstructures cultured in complete medium compared with tissue microstructures cultured in depleted medium in the 3 days preceding stimulation, corroborates the presence of soluble ER activators in culture. Further studies are required to understand the signaling events that contribute to the maintenance of ERα signaling under the culture conditions here presented, which will potentially also contribute to further disclose its role in ER+ BC.

5. Conclusions

Overall, we advocate a new methodology for ER+ BC TME modelling, in which the original cell populations, the native ECM and tissue architecture are represented, and ER function sustained. This *ex vivo* culture system can contribute to the study of breast cancer biology, in particular ERα signaling and microenvironmental-driven molecular mechanisms. Moreover, due to the extended culture time, the system can be a useful tool to

study novel anti-endocrine therapies and other therapeutic modalities.

List of abbreviations

AREG: amphiregulin; BC: breast cancer; CTRL: control; ERα: estrogen receptor α; ER+ BC: estrogen receptor α-positive breast cancer; H&E: hematoxylin and eosin; IHC: immunohistochemistry; PGR: progesterone; SHG: second harmonic generation; TME: tumor microenvironment; TPEF: two-photon-excited fluorescence

Ethics approval and consent to participate

All procedures performed in studies involving human participants were in accordance with the ethical standards of the institutional and/or national research committee. Informed consent was obtained from all individual participants included in the study. Anonymized patient tumor samples were obtained from the IPOLFG after institutional review board approval (UIC/1088).

Consent for publication

All authors have given consent for publication.

Availability of data and materials

All data generated or analyzed during this study are included in this published article (and its supplementary information files).

Competing interests

The authors declare that they have no competing interests.

Funding

We acknowledge funding sources: Fundação para a Ciência e Tecnologia (FC) for the PhD fellowships SFRH/BD/52208/2013 and PD/BD/114047/2015; iNOVA4Health (UIDB/04462/2020), a program financially supported by FCT/Ministry of Education and Science, Portugal, through national funds and co-funded by FEDER under the PT2020 Partnership Agreement; "The Discoveries Centre for Regenerative and Precision Medicine" (European Commission Horizon 2020 Research and Innovation programme, under the Grant Agreement number 739572); iBETXplore starting grant (3D-ABC-PI-717); the Spanish Ministry of Economy and Competitiveness through the "Severo Ochoa" program for Centres of Excellence in R&D (SEV-2015-0522); Fundació Privada Cellex; Fundació Mir-Puig; Generalitat de Catalunya through the CERCA program"; European Commission Horizon 2020 LASERE LAB Europe (grant agreement 654148); the Biltema and ISREC Foundation; CANCERA-Paulssons.

6. Authors' contributions

MFE, CBrisken, PMA, CBrito: study conceptualization. ALC, MFE, GD, GS, CBrito: experimental design. ALC, MFE, GD, RR, FS, EG: data acquisition. ALC, MFE, GD, EG, SA and CBrito: Data analysis. ALC, MFE, GD, SA and CBrito: data interpretation. PLA, SA, PMA, CBrito: resources. ALC, MFE and CBrito: Manuscript preparation. ALC, MFE, GD, RR, FS, EG, PLA, GS, CBrisken, PMA, SA and CBrito: manuscript revision and editing. All authors read and approved the final manuscript.

7. Acknowledgments

We grateful acknowledge Dr Elizabeth Anderson for scientific advice and fruitful discussion. The Histopathology Unit at Instituto Gulbenkian Ciência, Oeiras, Portugal, is acknowledged for technical support.

8. References

1. Noone, A. *et al.* Cancer incidence and survival trends by subtype using data from the Surveillance Epidemiology and End Results Program, 1992–2013. *Cancer Epidemiol Biomarkers Prev.* **26**, 1–19 (2017).
2. Diaz Bessone, M. I., Gattas, M. J., Laporte, T., Tanaka, M. & Simian, M. The Tumor Microenvironment as a Regulator of Endocrine Resistance in Breast Cancer. *Front. Endocrinol. (Lausanne).* **10**, 1–10 (2019).
3. Rothenberger, N. J., Somasundaram, A. & Stabile, L. P. The role of the estrogen pathway in the tumor microenvironment. *Int. J. Mol. Sci.* **19**, (2018).
4. Martelotto, L. G., Ng, C. K. Y., Piscuoglio, S., Weigelt, B. & Reis-filho, J. S. Breast cancer intra-tumor heterogeneity. *Breast Cancer Res.* **16**, 1–11 (2014).
5. Antoni, D., Burckel, H., Josset, E. & Noel, G. Three-Dimensional Cell Culture: A Breakthrough in Vivo. *Int. J. Mol. Sci.* **16**, 5517–5527 (2015).
6. Sflomos, G. *et al.* A Preclinical Model for ERa-Positive Breast Cancer Points to the Epithelial Microenvironment as Determinant of Luminal Phenotype and Hormone Response. *Cancer Cell* **29**, 407–422 (2016).
7. Fridriksdottir, A. J. *et al.* Propagation of oestrogen receptor-positive and oestrogen-responsive normal human breast cells in culture. *Nat. Commun.* **6**, (2015).
8. Muraro, M. G. *et al.* Ex-vivo assessment of drug response on breast cancer primary tissue with preserved microenvironments. *Oncoimmunology* **6**, 1–12 (2017).
9. Tanos, T. *et al.* Progesterone / RANKL Is a Major Regulatory Axis in the Human Breast. *Sci. Transl. Med.* **5**, 1–10 (2013).
10. van der Kuip, H. *et al.* Short term culture of breast cancer tissues to study the activity of the anticancer drug taxol in an intact tumor environment. *BMC Cancer* **6**, 1–11 (2006).
11. Naipal, K. A. T. *et al.* Tumor slice culture system to assess drug response of primary breast cancer. *BMC Cancer* **16**, 1–13 (2016).
12. Campuzano, S. & Pelling, A. E. Scaffolds for 3D Cell Culture and Cellular Agriculture Applications Derived From Non-animal Sources. *Front. Sustain. Food Syst.* **3**, 1–9 (2019).
13. Rebelo, S. P. *et al.* 3D-3-culture: A tool to unveil macrophage plasticity in the tumour microenvironment. *Biomaterials* **163**, 185–197 (2018).
14. Estrada, M. F. *et al.* Modelling the tumour microenvironment in long-term microencapsulated 3D co-cultures recapitulates phenotypic features of disease progression. *Biomaterials* **78**, 50–61 (2016).
15. Mathew, M., Santos, S. I. C. O., Zalvidea, D. & Loza-Alvarez, P. Multimodal

optical workstation for simultaneous linear, nonlinear microscopy and nanomanipulation: Upgrading a commercial confocal inverted microscope. *Rev. Sci. Instrum.* **80**, 1–11 (2009).
16. Kato, S. *et al.* Activation of the Estrogen Receptor Through Phosphorylation by Mitogen-Activated Protein Kinase. *Science (80-.).* **270**, 102–106 (1999).
17. Moerkens, M., Zhang, Y., Wester, L., van de Water, B. & Meerman, J. H. N. Epidermal growth factor receptor signalling in human breast cancer cells operates parallel to estrogen receptor α signalling and results in tamoxifen insensitive proliferation. *BMC Cancer* **14**, 1–16 (2014).
18. Karmakar, S., Jin, Y. & Nagaich, A. K. Interaction of glucocorticoid receptor (GR) with estrogen receptor (ER) α and activator protein 1 (AP1) in dexamethasone-mediated interference of ERα activity. *J. Biol. Chem.* **288**, 24020–24034 (2013).
19. Lanzino, M. *et al.* Interaction between estrogen receptor alpha and insulin/IGF signaling in breast cancer. *Curr Cancer Drug Targets* **8**, 597–610 (2008).
20. Weigel, N. L. & Zhang, Y. Ligand-independent activation of steroid hormone receptors. *J. Mol. Med.* **76**, 469–479 (1998).
21. Chen, D. *et al.* Phosphorylation of human estrogen receptor α at serine 118 by two distinct signal transduction pathways revealed by phosphorylation-specific antisera. *Oncogene* **21**, 4921–4931 (2002).
22. Dolfi, S. C. *et al.* Fulvestrant treatment alters MDM2 protein turnover and sensitivity of human breast carcinoma cells to chemotherapeutic drugs. *Cancer Lett.* **350**, 52–60 (2014).
23. Regan, R. M. O. *et al.* Development and Therapeutic Options for the T reatment of Raloxifene-Stimulated Breast Cancer in Athymic Mice. *Cancer Ther. Preclin.* **12**, 2255–2264 (2006).
24. Domenici, G. *et al.* A Sox2–Sox9 signalling axis maintains human breast luminal progenitor and breast cancer stem cells. *Oncogene* **38**, 3151–3169 (2019).
25. Dai, X., Cheng, H., Bai, Z. & Li, J. Breast Cancer Cell Line Classification and Its Relevance with Breast Tumor Subtyping. *J. Cancer* **8**, 3131–3141 (2017).
26. Livak, K. J. & Schmittgen, T. D. Analysis of Relative Gene Expression Data Using Real- Time Quantitative PCR and the 2/deltadeltaCt Method. *Methods* **25**, 402–408 (2001).
27. Matthew G. Vander Heiden, Cantley, L. C. & Thompson, C. B. Understanding the Warburg Effect: The Metabolic Requirements of Cell Proliferation. *Science (80-.).* **324**, 1029–1033 (2010).
28. Gloushankova, N. A., Rubtsova, S. N. & Zhitnyak, I. Y. Cadherin-mediated cell-cell interactions in normal and cancer cells. *Tissue Barriers* **5**, 1–15 (2017).
29. Altin, J. G. & Sloan, E. K. The role of CD45 and CD45-associated molecules in T cell activation. *Immunol. Cell Biol.* **75**, 430–445 (1997).
30. Buisseret, L. *et al.* Tumor-infiltrating lymphocyte composition , organization and PD-1 / PD-L1 expression are linked in breast cancer. **6**, (2017).
31. Holl, E. K. *et al.* Examining Peripheral and Tumor Cellular Immunome in Patients With Cancer. *Front. Immunol.* **10**, 1767 (2019).
32. Garaud, S. *et al.* Tumor-infiltrating B cells signal functional humoral immune responses in breast cancer. *JCI Insight* **4**, (2019).
33. Osborne, C. K., Wakeling, A. & Nicholson, R. I. Fulvestrant: an oestrogen

receptor antagonist with a novel mechanism of action. *Br. J. Cancer* **90**, 2–6 (2004).
34. Vergote, I. & Robertson, J. F. R. Fulvestrant is an effective and well-tolerated endocrine therapy for postmenopausal women with advanced breast cancer: Results from clinical trials. *Br. J. Cancer* **90**, S11–S14 (2004).
35. Amir, E. *et al.* Prospective Study Evaluating the Impact of Tissue Confirmation of Metastatic Disease in Patients With Breast Cancer. *J. Clin. Oncol.* **30**, 587–592 (2020).
36. Burns, K. A. & Korach, K. S. Estrogen receptors and human disease: an update. *Arch Toxicol* **86**, 1491–1504 (2016).
37. Lindstro, L. S. *et al.* Clinically Used Breast Cancer Markers Such As Estrogen Receptor , Progesterone Receptor , and Human Epidermal Growth Factor Receptor 2 Are Unstable Throughout Tumor Progression. *J. Clin. Oncol.* **30**, (2020).
38. Pontiggia, O. *et al.* The tumor microenvironment modulates tamoxifen resistance in breast cancer: A role for soluble stromal factors and fibronectin through β1 integrin. *Breast Cancer Res. Treat.* **133**, 459–471 (2012).
39. Brechbuhl, H. M. *et al.* Fibroblast subtypes regulate responsiveness of luminal breast cancer to estrogen. *Clin Cancer Res.* **23**, 1710–1721 (2018).
40. Morgan, M. M. *et al.* Mammary fibroblasts reduce apoptosis and speed estrogen-induced hyperplasia in an organotypic MCF7-derived duct model. *Sci. Rep.* **8**, 1–13 (2018).
41. Jansen, M. P. H. M. *et al.* Molecular classification of tamoxifen-resistant breast carcinomas by gene expression profiling. *J. Clin. Oncol.* **23**, 732–740 (2005).
42. Sampayo, R. G. *et al.* Fibronectin rescues estrogen receptor α from lysosomal degradation in breast cancer cells. *J. Cell Biol.* **217**, 2777–2798 (2018).
43. Alco, G. U. L. *et al.* Clinical and histopathological factors associated with Ki-67 expression in breast cancer patients. *Oncol. Lett.* **9**, 1046–1054 (2015).
44. Davies, E. J. *et al.* Capturing complex tumour biology in vitro: Histological and molecular characterisation of precision cut slices. *Sci. Rep.* **5**, 1–17 (2015).
45. Mekala, N. K., Baadhe, R. R. & Potumarthi, R. Mass transfer aspects of 3D cell cultures in tissue engineering. *Asia-Pacific J. Chem. Eng.* **9**, 318–329 (2014).
46. Rouwkema, J., Koopman, B. F. J. M., Blitterswijk, C. A. V., Dhert, W. J. A. & Malda, J. Supply of nutrients to cells in engineered tissues. *Biotechnol. Genet. Eng. Rev.* **26**, 163–178 (2009).
47. Sun, J. & Tan, H. Alginate-Based Biomaterials for Regenerative Medicine Applications. *Materials (Basel).* **6**, 1285–1309 (2013).
48. Wilson, J. L., Najia, M. A., Saeed, R. & McDevitt, T. C. Alginate Encapsulation Parameters Influence the Differentiation of Microencapsulated Embryonic Stem Cell Aggregates. *Biotechnol Bioeng.* **111**, 618–631 (2014).
49. Miranda, J. P. *et al.* Extending Hepatocyte Functionality for Drug-Testing Applications Using High-Viscosity Alginate–Encapsulated Three-Dimensional Cultures in Bioreactors. *Tissue Eng. Part C Methods* **16**, (2010).
50. Kanta, J. Collagen matrix as a tool in studying fibroblastic cell behavior. *Cell Adhes. Migr.* **9**, 308–316 (2015).
51. Tilbury, K. & Campagnola, P. J. Applications of second-harmonic

generation imaging microscopy in ovarian and breast cancer. *Perspect. Medicin. Chem.* **7**, 21–32 (2015).
52. Provenzano, P. P. *et al.* Collagen density promotes mammary tumor initiation and progression. *BMC Med.* **6**, 1–15 (2008).
53. Li, T. *et al.* The association of measured breast tissue characteristics with mammographic density and other risk factors for breast cancer. *Cancer Epidemiol. Biomarkers Prev.* **14**, 343–349 (2005).
54. Netti, P. A., Berk, D. A., Swartz, M. A., Grodzinsky, A. J. & Jain, R. K. Role of extracellular matrix assembly in interstitial transport in solid tumors. *Cancer Res.* **60**, 2497–2503 (2000).
55. Rijal, G. Native-mimicking in vitro microenvironment: an elusive and seductive future for tumor modeling and tissue engineering. *J. Biol. Eng.* 1–22 (2018).
56. Stanton, S. E. & Disis, M. L. Clinical significance of tumor-infiltrating lymphocytes in breast cancer. *J. Immunother. cancer* **4**, 59 (2016).
57. Wang, X. *et al.* p63 Expression in Normal , Hyperplastic and Malignant Breast Tissues. *Breast cancer* **9**, 0–3 (2002).
58. Ribeiro-silva, A. & Ramalho, L. N. Z. The Relationship Between p63 and p53 Expression in Normal and Neoplastic Breast Tissue. *Arch Pathol Lab Med* **127**, 336–340 (2003).
59. Wang, X. *et al.* p63 Expression in Normal, Hyperplastic and Malignant Breast Tissues. *Breast cancer* **9**, 0–3 (2002).
60. Makki, J. Diversity of breast carcinoma: Histological subtypes and clinical relevance. *Clin. Med. Insights Pathol.* **8**, 23–31 (2015).
61. Kang, K. S. *et al.* Expression of estrogen receptors in a normal human breast epithelial cell type with luminal and stem cell characteristics and its neoplastically transformed cell lines. *Carcinogenesis* **18**, 251–257 (1997).
62. Jia, M., Dahlman-Wright, K. & Gustafsson, J. Å. Estrogen receptor alpha and beta in health and disease. *Best Pract. Res. Clin. Endocrinol. Metab.* **29**, 557–568 (2015).
63. Lindstro, L. S. *et al.* Intratumor Heterogeneity of the Estrogen Receptor and the Long-term Risk of Fatal Breast Cancer. *JNCI J Natl Cancer Inst* **110**, 726–733 (2018).
64. Lin, C.-Y. *et al.* Discovery of estrogen receptor alpha target genes and response elements in breast tumor cells. *Genome Biol.* **5**, R66 (2004).
65. Kim, J. *et al.* Anticancer effect of metformin on estrogen receptor-positive and tamoxifen-resistant breast cancer cell lines. *Oncol. Rep.* **35**, 2553–2560 (2016).
66. Fleury, L., Gerus, M., Lavigne, A. C., Richard-Foy, H. & Bystricky, K. Eliminating epigenetic barriers induces transient hormone-regulated gene expression in estrogen receptor negative breast cancer cells. *Oncogene* **27**, 4075–4085 (2008).
67. Buchsbaum, R. J. & Oh, S. Y. Breast cancer-associated fibroblasts: Where we are and where we need to go. *Cancers (Basel).* **8**, 1–19 (2016).
68. Kurobe, M., Furukawa, S. & Hayashi, K. Synthesis and secretion of an epidermal growth factor (EGF) by human fibroblast cells in culture. *Biochem Biophys Res Commun.* **131**, 1080–1085 (1985).
69. Majety, M., Pradel, L. P., Gies, M. & Ries, C. H. Fibroblasts influence survival and therapeutic response in a 3D co-culture model. *PLoS One* **10**, 1–18 (2015).

9. Supplementary information

Table S2.1: Immunohistochemistry analysis: reagents and conditions used for.

Primary antibody clone	Supplier	Dilution	Antigen retrieval	Detection system
E-cadherin (NCH 38)	Dako (M3612)	1:80 (28 minutes)	40 min with CC1*	Optiview#
Oestrogen receptor (SP1)	Ventana (28 minutes)	Pre-diluted (28 minutes)	64 min with CC1*	Ultraview#
KI67 (30-9)	Ventana (790-4286)	Pre-diluted (16 minutes)	32 min with CC1*	Optiview#
CD45 (2B11-PD7/26)	Dako (M0701)	1:1000 (32 minutes)	56 min with CC1*	Optiview#
Vimentin (clone V9)	Dako (M0725)	1:150 (12 minutes)	24 min with CC1*	Optiview#
P63 (clone 4A4)	Biocare Medical (CM163C)	1:200 (24 minutes)	48 min with CC1*	Optiview#
CD31 (clone 1A10)	Novocastra (NCL-CD31-1A10)	1:80 (16 minutes)	32 min with CC1*	Optiview#

Table S2.2: RT-qPCR analysis: primer sequences.

Symbol	Gene name	Forward Primer (5'-3')	Reverse primer (3'-5')
ERα	Estrogen receptor α	CCACCAACCAGTGC ACCATT	GGTCTTTTCGTA TCCCACCTTTC
PGR	Progesterone receptor	CGCGCTCTACCCTG CACTC	TGAATCCGGCCT CAGGTAGTT
pS2	Protein PS2/ Trefoil factor 1	TCGGGGGTCGCCTT TGGAGCAG	GAGGGCGTGAC ACCAGGAAAAC CA
AREG	Amphiregulin	TGGAAGCAGTAACA TGCAAATGTC	GGCTGCTAATGC AATTTTTGATAA
RPL22	Ribosomal protein L22	CACGAAGGAGGAGT GACTGG	TGTGGCACACC ACTGACATT
36B4	Acidic ribosomal phosphoprotein P0	GTGTTCGACAATGG CAGCAT	GACACCCTCCA GGAAGCGA

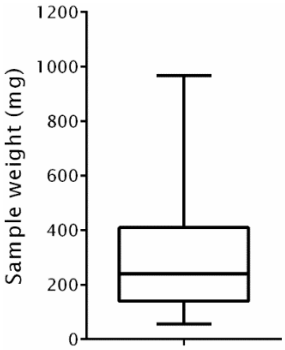

Figure S2.1: Sample weight.

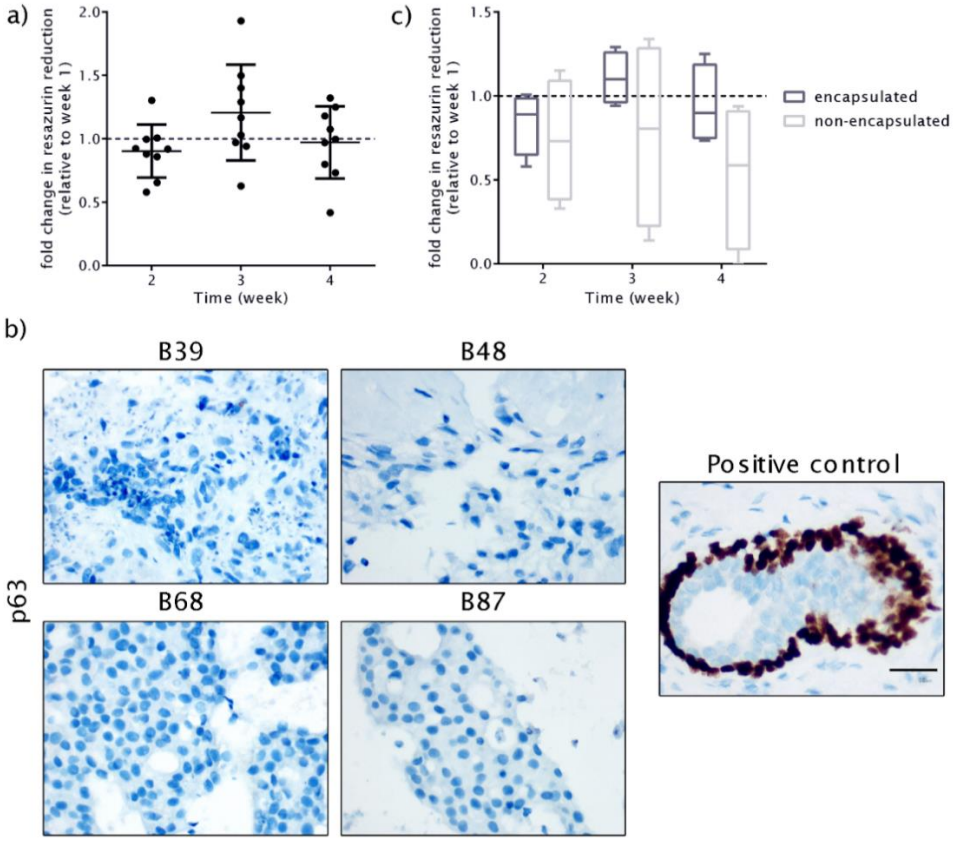

Figure S2.2: Encapsulated BC tissue microstructures do not present myoepithelial markers and maintain high metabolic viability. **a** Metabolic activity was assessed along culture. **b** Immunohistochemistry analysis of p63 (myoepithelial cells) at one month of culture; (scale bar: 60 μm). **c** Metabolic activity was assessed in encapsulated and non-encapsulated tissue microstructures derived from the same patients.

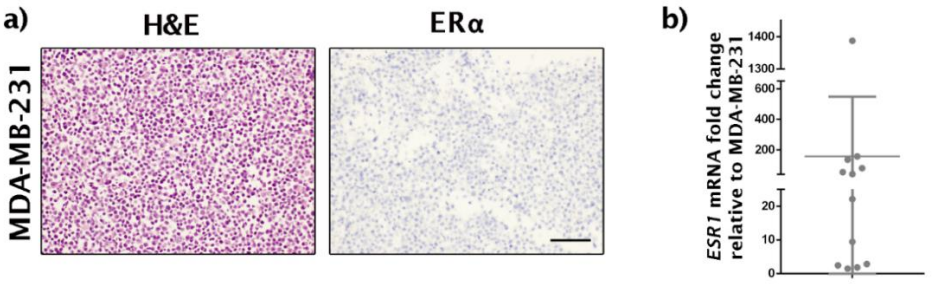

Figure S2.3: **a** Hematoxylin and eosin staining and immunohistochemistry for ERα of MDA-MB-231 (ER-negative cell line) cells cultured in 2D (scale: 200 µm). **b** ERα gene (*ESR1)* expression in encapsulated microstructures cultured for one month relatively to MDA-MB-231 cells.

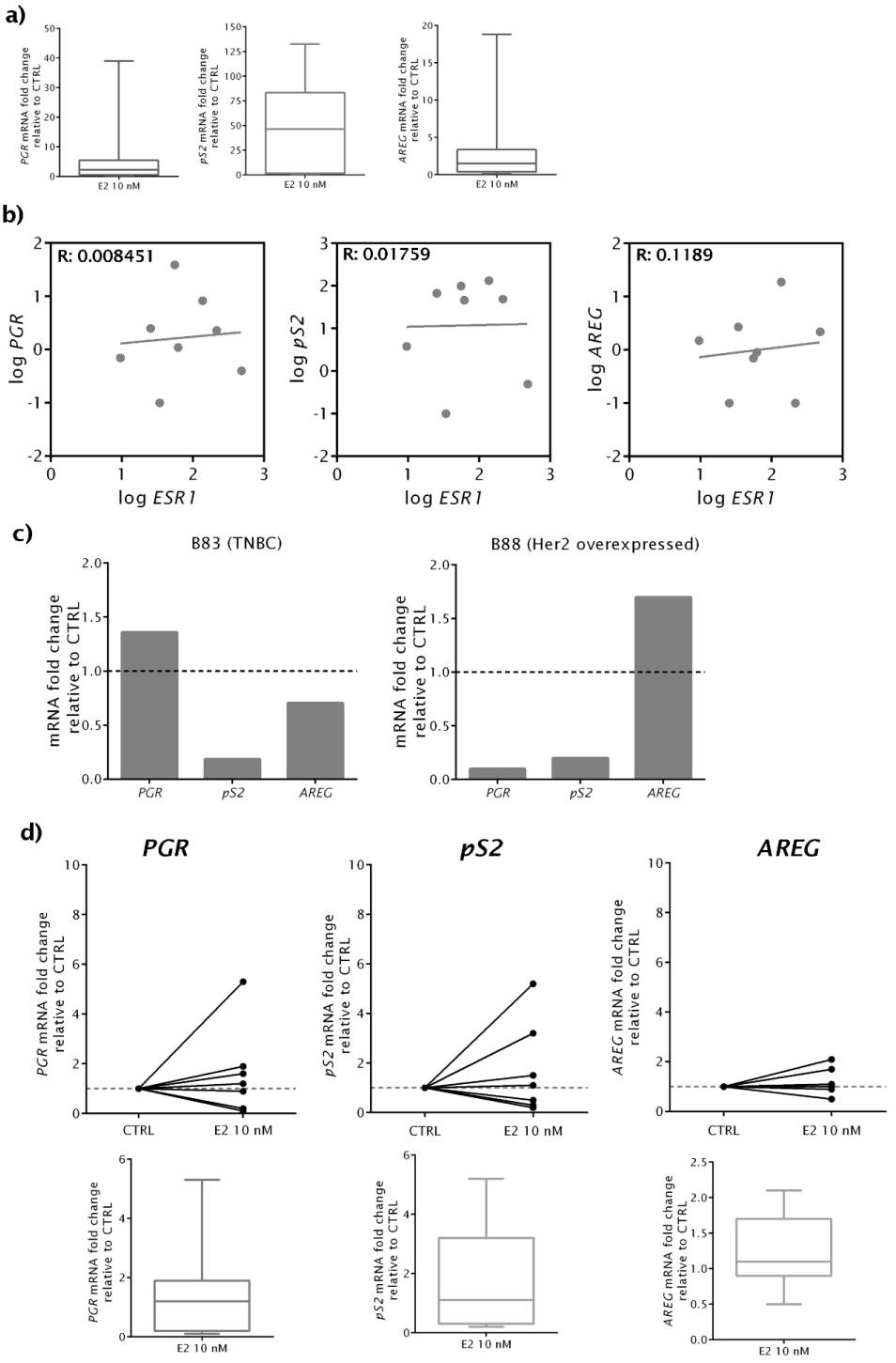

See caption in the next page.

Figure S2.4: **a** Encapsulated tissue microstructures were cultured for three days in depleted medium before stimulation with 17β-estradiol; expression of ER downstream target genes was assessed by RT-qPCR (amphiregulin - *AREG*, progesterone receptor - *PGR* and protein PS2 - *pS2*, N=9); quantitative evaluation of data shown in Figure 2.3b). **b** Correlation diagrams of expression of ERα gene (*AREG*) and ER target genes (*PGR, pS2* and *AREG*). The dots represent the log (mRNA fold change relative to control) of each gene for a given BC patient microtissue and the lines represent the linear regression (Pearson correlation with R indicated on each graph). For all cases, no significant correlation was found (*p-value*>0.7). **c** ER-negative BC encapsulated tissue microstructures cultured in complete medium were challenged with 17β-estradiol and expression of ER downstream target genes was assessed by RT-qPCR (*AREG*, *PGR pS2*, N=2). **d** Encapsulated tissue microstructures cultured in complete medium were challenged with 17β-estradiol and ER downstream target genes were assessed by RT-qPCR (*AREG*, *PGR* and *pS2,* N=7). Data are shown as fold-change in gene expression upon 17β-estradiol challenge relatively to vehicle-exposed control (CTRL).

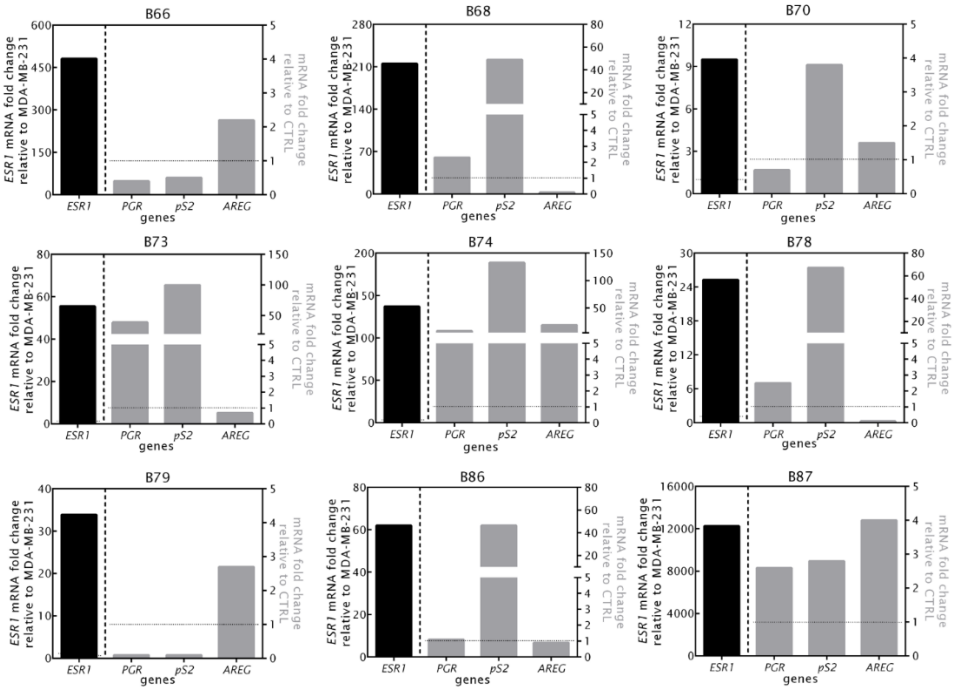

Figure S2.5: Encapsulated tissue microstructures were cultured for three days in depleted medium before stimulation with 17β-estradiol; expression of ER downstream target genes was assessed by RT-qPCR (amphiregulin - *AREG*, progesterone receptor - *PGR* and protein PS2 - *pS2*). Data is presented individually for each tumor.

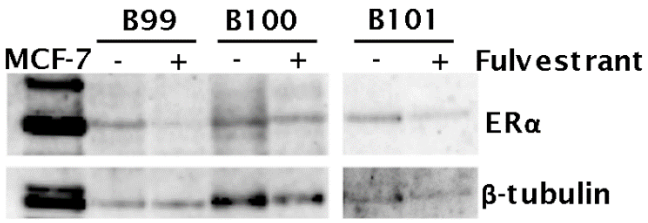

Figure S2.6: Encapsulated tissue microstructures were cultured for 3-5 days in complete medium, before challenge with fulvestrant for two weeks; ERα protein was detected by western blot; β-tubulin was used as loading control (N=3, representative blot out of 2 technical replicates).

CHAPTER III

3D cancer cell models in alginate capsules: biochemical and mechanical characterization

This chapter was adapted from:

Ana Luísa Cartaxo, Henrique Almeida, Tomás Calmeiro, Daniela Gomes, Elvira Fortunato, Catarina Brito; *3D cancer cell models in alginate capsules: biochemical and mechanical characterization*, in preparation

Table of contents

Abstract

Cancer is the second leading cause of mortality worldwide. Currently there is an effort towards the development of *in vitro* cancer models more predictive of clinical efficacy, such as three-dimensional (3D) cell models. Biomaterials have been broadly used as scaffolds and supports for cells in 3D configurations. Alginate, a natural polysaccharide with high biocompatibility and bio-inert has been explored by several authors for generation of 3D cell models. Alginate encapsulation combined with agitation-based culture systems has been proposed by our group as a system able to recreate tumor microenvironment features. In this study, alginate capsules containing cancer cell spheroids, alone (mono-cultures) or together with fibroblasts (co-cultures), were produced using an electrostatic bead generator. Encapsulated mono- and co-cultures were maintained in spinner vessels; non-encapsulated cell spheroids were also cultured, as control. Analysis by scanning electron microscopy revealed the surface porosity of the capsules. These retained their sphericity and size during the two weeks of culture. Encapsulation sustained the phenotype and proliferation of the tumor cells, avoiding the fusion of spheroids observed in non-encapsulated cultures. After two weeks of culture, capsule stiffness was evaluated by atomic force microscopy. The presence of cells decreased the Young modulus of alginate capsules. Moreover, capsules containing co-cultures of tumor cells and fibroblasts presented higher Young modulus than capsules containing tumor cell mono-cultures, in accordance with the increased stiffness reported for advanced breast cancer.

Collectively, the results presented contribute to the characterization of alginate encapsulated cancer cell models.

Key words: 3D cell models, alginate, cancer, cell encapsulation, co-culture, Young modulus

1. Background

Cancer cell models based on three-dimensional (3D) culture and co-culture of different cell types have been proposed over the last years to better represent features of cancer than 2D cell models [1]. Biomaterial-based 3D cell models have been proposed by numerous authors, from naturally-derived (e.g. Matrigel, collagen, silk, alginate) to synthetic (e.g. poly-lactic acid, poly-glycolic acid), or hybrid and semi-synthetic (e.g. modified hyaluronic acid, chitosan-poly-caprolactone) materials[2]. Due to its interesting properties, alginate has been widely used, either alone or in combination with other biomaterials to create scaffolds for seeding or embedding of cells [3–6]. Alginate is biocompatible and bio-inert [7]. Also, it is a transparent biomaterial which makes it compatible with light microscopy techniques [8], highly employed in cell biology studies. Mechanical properties of alginate hydrogels, such as the Young modulus (YM), can be controlled by the cell density [9], ion cross-linking concentration [10] and alginate composition [11] and concentration [12–14]. Cells and their surrounding microenvironment can regulate cell features in a reciprocal manner [9,15]. On one hand, the use of high density of cells can physically interfere with the cross-linking reaction, inducing the formation of softer alginate hydrogels [9]. On the other hand, in 3D hydrogels, material stiffness, plays a key role by influencing cell phenotype and behavior [16]. In fact, durotaxis, i.e. migration in response to a stiffness gradient, generally causes cells to migrate toward stiffer regions [17].

Our group developed an *in vitro* 3D cell co-culture system based on cell immobilization in alginate capsules and dynamic culture to recapitulate features of the tumor microenvironment (TME) [6]. Capsules containing cancer cell spheroids, co-cultured with

other cell types found in the TME, such as fibroblasts and immune cells, recapitulate specific features, such as the presence of the epithelial and stromal compartments, tumor-fibroblast cross-talk, e.g. mediated by secretion of pro-inflammatory cytokines and extracellular matrix components, such as collagen I [6].

Herein, we focused on the characterization of the biomaterial compartment of these models. Alginate capsules (1.1% w/v; crosslinked with barium), containing tumor cell spheroids in mono-culture or in co-culture with fibroblasts, were generated and characterized biologically, biochemically and mechanically.

2. Materials and methods

2.1. Cell lines and 2D cell culture

BT474 breast cancer (BC) cell line derived from a human ductal carcinoma was selected in this study since it is among the most frequently used luminal-like BC cell lines. A lung cancer cell line, NCI-H157 (#CRL-5802; from now on referred as H157), previously characterized by our team as encapsulated cancer cell model [18], was also employed. Both cells were obtained from American Type Culture Collection (ATCC). Human dermal fibroblasts (hDFs) isolated from human skin were obtained from Innoprot. For the three different cell types, 2D static cultures (in T-flasks) were maintained at 37 ºC in an incubator with humidified atmosphere containing 5% CO_2 and 21% of O_2. Tumor cells were sub-cultured twice a week at $1x10^4$ and $2.5x10^4$ cell/cm^2 seeding cell densities, for H157 and BT474, respectively; hDFs were split once a week at a seeding density of $0.5x10^4$ cell/cm^2. For each sub-culture, cells were trypsinized by exposing the cell monolayer to 0.05% trypsin-ethylenediaminetetraacetic acid (trypsin-EDTA; Invitrogen) for 3-5 min, until total cell dislodging from the plasticware surface. Cell were resuspended in complete medium to inactivate trypsin and viable cells were counted using trypan blue exclusion method [19]. All cell lines were routinely checked for the absence of mycoplasma contamination. They were cultured in adherent and static conditions until establishment of the 3D cultures (Figure 3.1), using as culture media Dulbecco's Modified Eagle Medium (DMEM) low glucose supplemented with 10% fetal bovine serum (FBS, Life Technologies) and 100 U/mL penicillin-streptomycin (P/S, Life Technologies), 2% GlutaMAX (Life Technologies) and glucose (Sigma Aldrich) to a final concentration

of 2 g/L or Roswell Park Memorial Institute (RPMI) 1640 with 10% FBS and 100 U/mL P/S for BT474, DMEM supplemented with 10% FBS, 100 U/mL P/S, 1 mM sodium pyruvate (Life Technologies), 12 mM HEPES (Life Technologies) and 0.1mM non-essential amino acids (Life Technologies) for H157 and Iscove's Modified Dulbecco's Medium (IMDM, Life Technologies) supplemented with 10% FBS and 100 U/mL P/S for hDFs.

2.2. Generation of alginate capsules

A solution of 1.1% (w/v) of Ultrapure Ca^{2+} MVG alginate (UP MVG NovaMatrix, Pronova Biomedical, Oslo, Norway), dissolved in NaCl 0.9% (w/v), was prepared in sterile conditions. Microencapsulation was performed using an electrostatic bead generator (Nisco Encapsulator) with an air flow rate of 10 mL/h, at 5.3 volts, with air pressure of 1 bar. Alginate droplets were cross-linked in a 20 mM $BaCl_2$ bath, adjusted to 290-300 mOsm using NaCl, buffered at pH 7.4. The resulting microcapsules were washed three times in a 0.9% (w/v) NaCl solution. A nozzle with 0.7 mm diameter was employed to generate alginate microcapsules with a diameter of approximately 700 μm.

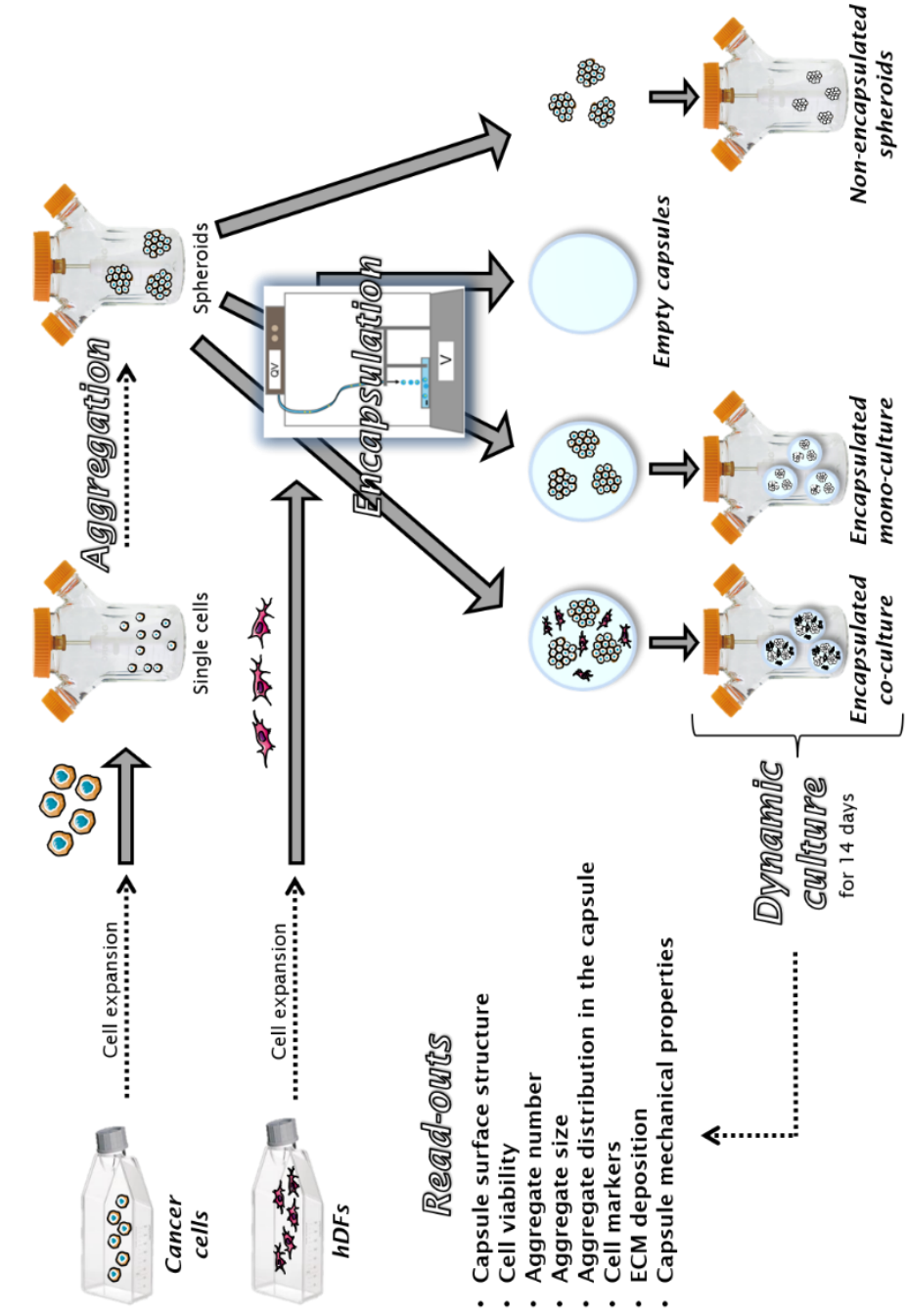

See caption in the next page.

Figure 3.1: Schematic representation of the experimental layout. Cancer cell lines were expanded, collected and inoculated as single cell suspensions in a spinner vessel, for aggregation. The cancer cell spheroids formed were encapsulated, either alone (leading to the formation of encapsulated mono-cultures), or together with human fibroblasts (leading to the formation of encapsulated co-cultures). As a control, non-encapsulated spheroids are also maintained in culture. Empty alginate capsules were also prepared. Encapsulated and non-encapsulated cultures were maintained for 14 days under dynamic conditions. Biochemically and mechanically characterization of the system was performed by scanning electron microscopy, atomic force microscopy, immunofluorescence and immunohistochemistry.

2.3. Generation of tumor cell spheroids in stirred-tank culture systems

Twenty-five million tumor cells were inoculated as single cell suspension into wall-baffled spinner-flasks with straight blade paddle impeller (Corning® Life Sciences), placed on a magnetic stirrer in an incubator at 37 ºC, with humidified atmosphere containing 5% CO_2 and 21% of O_2 (Figure 3.1), as described before [20]. To prevent cell attachment to the spinner vessel walls, these have been previously coated with 2-3 mL of dimethyldichlorosilane (Merck 8.03452, Germany), as described previously [21]. Stirring rates were set as described in our previous report [20], according to the cell line characteristics, in order to promote initial spheroid formation and limiting spheroid fusion.

2.4. Cell microencapsulation and culture in stirred-tank culture systems

Tumor cell spheroids were collected for encapsulation once compact and spherical spheroids formed (at day 1 and 3 of culture, for BT474 and H157 cells, respectively). For mono-cultures, $2x10^4$ spheroids were collected from spinner vessel culture, washed with

Phosphate-Buffered Saline (PBS; Thermo Fisher Scientific) and dispersed in 1 mL of 1.1% (w/v) of Ultrapure Ca^{2+} MVG alginate (UP MVG NovaMatrix, Pronova Biomedical, Oslo, Norway), dissolved in NaCl 0.9% (w/v) solution, as previously described [6,18,20]. Alternatively, for the establishment of co-cultures of tumor cells with fibroblasts, a single cell suspension of $4x10^6$ hDFs was mixed with a suspension of $2x10^4$ tumor cell spheroids and dispersed in 1 mL of the alginate solution. Encapsulation was performed as detailed in section 2.2. The resulting cell-loaded microcapsules (diameter of approximately 700 μm) were washed three times in a 0.9% (w/v) NaCl solution and once in culture medium before being transferred to new spinner vessel. At the same time, spheroids were also collected from the spinner vessel and directly transferred to a different spinner vessel, as non-encapsulated condition. Non-encapsulated and encapsulated mono- and co-cultures were kept in the culture medium of each cell line (section 2.1). Cultures were maintained at 80 rpm, up to 14 days. Each 3-4 days, 50% of the culture medium was replaced with fresh culture medium. Samples were collected throughout the culture period for further characterization, at specific time points (See section 2.5).

2.5. Spheroid and capsule characterization

During BT474 aggregation period, several samples were collected (0, 22, 24, 27, 30 and 49 h after spinner inoculation). Non-encapsulated and encapsulated mono- and co-cultures were also sampled at various time-points: 0, 2, 5, 7, 9, 12 and 14 days after encapsulation. The characterization methods are detailed in subsequent subsections.

2.5.1. Cell viability

Cell viability was assessed by a cell membrane integrity assay which uses: the cell permeant dye fluorescein diacetate (FDA; Sigma-Aldrich, Steinheim, Germany), which is metabolized into fluorescein by cytoplasmic esterases [22]; the cell impermeant dye, propidium iodide (PI; Invitrogen), which binds DNA [21]. FDA was used at 10 μg/mL, to label live cells, and PI at 1 μM to identify dead cells. Spheroids or capsules were incubated for 5 min at room temperature (RT) with the fluorescent labels and then analyzed using a fluorescence microscope (DMI6000 Leica Microsystems GmBH, Wetzlar, Germany).

2.5.2. Spheroid distribution within capsules

Encapsulated spheroid distribution was evaluated for mono-culture capsules at days 0, 2, 5, 7, 9, 12 and 14 of culture. At each time point, mono-capsules were imaged in a fluorescence microscope (DMI6000, Leica Microsystems GmbH, Wetzlar, Germany). For the analysis, a group of cells was considered a spheroid when individual cells could not be counted. Spheroid distribution per microcapsule was analyzed by manually counting the number of capsules and the number of spheroids in each capsule, present in 1 mL of culture.

2.5.3. Spheroid size

Spheroid size was evaluated during aggregation and in mono- and co-culture capsules at days 0, 2, 5, 7, 9, 12 and 14 of culture. Non-encapsulated spheroids were analyzed directly. Alginate microcapsules were dissolved in a chelating solution (100 mM EDTA, 10 mM HEPES, pH 7.4, for 5 min at RT, and washed twice

with PBS, to harvest the cancer spheroids. Spheroids were imaged in a fluorescence microscope (DMI6000, Leica Microsystems GmbH, Wetzlar, Germany). Spheroid area and Feret's diameter were measured by adjusting the threshold until the border of each spheroid and quantification was performed using ImageJ open source software (Rasband, W.S., ImageJ, U. S. National Institutes of Health, Bethesda, Maryland, USA, https://imagej.nih.gov/ij/, 1997-2018).

2.5.4. Cell phenotype and proliferation

Samples were collected at day 14 of culture and fixed in 4% (w/v) paraformaldehyde (PFA, ≥95%, Fluka) with 4% (w/v) sucrose (≥99.5%, Sigma-Aldrich), in PBS, for 30 min at RT. Then, they were washed 3 times with PBS and kept at 4 ºC until further analysis. For cryo-sectioning, samples were dehydrated with 30% (w/v) sucrose overnight. Then they were embedded in Tissue-Tek O.C.T. (Sakura, Alphen aan den Rijn, Netherlands) and frozen at −80 ºC. Samples were sectioned at a thickness of 10 μm using a cryo-microtome (Cryostat I, Leica, Wetslar, Germany).

Immunofluorescence (IF) was performed according to previously published methods [23]. In brief, cells were permeabilized for 10 min with 0.1% Triton X-100 (w/v) and blocked for 30 min with 0.2% (w/v) Fish Skin Gelatin (FSG; Sigma–Aldrich). Primary antibodies (Table S1) were diluted in 0.2% (w/v) FSG and incubated for 2 h, at RT and secondary antibodies (Table S1) diluted in 0.125% (w/v) FSG and incubated for 1 h, at RT. Samples were mounted in ProLong Gold Antifade Mountant containing DAPI (Life Technologies) and visualized using a fluorescence microscope (DMI6000, Leica Microsystems GmbH, Wetzlar, Germany).

For Ki-67 quantification, ImageJ open source software (Rasband, W.S., ImageJ, U. S. National Institutes of Health, Bethesda, Maryland, USA, https://imagej.nih.gov/ij/, 1997-2018) was used. The percentage of Ki-67 positive cells was obtained by diving the number of cells expressing Ki-67 by the total number of cells present in the spheroid. This analysis was performed for a minimum of three spheroids per experiment, from two independent experiments.

2.5.5. Extracellular matrix deposition

At day 14, encapsulated mono- and co-cultures were collected and fixed as described above (Section 2.5.4). Then, capsules were embedded in 2% (w/v) high melting temperature agarose (Lonza), dehydrated in a graded series of ethanol and embedded in paraffin wax (Merck Millipore). Paraffin blocks were then sectioned (3 μm thickness) on a rotary microtome (RM 2135, Leica).

Spheroid's structure and compactness and cell distribution were assessed by visual inspection of Hematoxylin and Eosin (H&E; Sigma-Aldrich) staining. The presence of collagen fibers was assessed by Picrosirius Red (PSR; Polysciences Europe GmbH, Eppelheim, Germany) staining. Glycosaminoglycans (GAGs) and alginate were stained with Alcian Blue (AB; Polysciences Europe) and Aldehyde Fuschin (American MasterTech). Both these stainings were performed in accordance with supplier instructions. Histological slides were digitalized in a NanoZoomer SQ whole slide scanner (Hamamatsu Photonics) and viewed and processed in QuPath software.

2.5.6. Capsule morphology

The surface of empty capsules was assessed by scanning electron microscopy (SEM). Capsules were dried on adhesive carbon tabs (12 mm, Agar Scientific) or on silicon wafers and coated with iridium in order to avoid charging effects during image acquisition. SEM was carried out in a Zeiss AURIGA CrossBeam microscope. Surface analysis was done on secondary electron imaging mode using acceleration voltages of 2 and 5 keV. Pore size was measured for 77 different pores. Capsule size was measured in two different capsules. Membrane thickness was measured in one capsule.

2.5.7. Capsule's mechanical properties assessment

In the last culture day (14 days after microencapsulation), capsules from mono- and co-cultures were collected and fixed as previously detailed. Atomic force microscopy (AFM)-based mechanical dynamic characterization was performed to compare the nanoscale elastic properties and behavior of empty, mono- or co-culture capsules. Alginate microcapsules were embedded in 1% (w/v) high melting temperature agarose (Lonza), forming a thin film, which maintained the capsules in a fixed position during AFM acquisitions. These capsules were covered with PBS to maintain hydration before and during AFM measurements in a MFP-3D Stand Alone (Asylum Research) AFM system operated in alternate contact mode (AC mode). Elastic behavior was studied through load-unload force curves (force spectroscopy) in liquid environment (PBS) using commercially available silicon nitride probes (Long cantilever of Olympus TR-800PB; f_0 = 13 kHz, 0.16 N/m; Olympus Corporation). The probes were left to stabilize at least 3 hours prior to calibration through Sader's method [24]. The Youngs modulus of the samples

was approximated by fitting Sneddon's model [25] to the force curves on augmented reality built-in software packages in IgorPro (Wavemetrics). A minimum of 28 force curves were obtained for a minimum of three capsules of each condition. For the analysis of empty capsules, 3 independent capsules batches were used. For the cell-containing capsules, 1 batch of capsules was used for each condition.

2.6. Statistical analysis

Statistical analysis was carried out using GraphPad Prism 5 software. All experiments and analysis were performed at least in triplicate. The statistical test applied and the considered corresponding *p-value* are referred on the legend of each corresponding graph.

3. Results

Empty hydrogel alginate capsules were prepared by crosslinking of alginate with barium chloride using an electrostatic bead generator. Capsule morphology and membrane thickness were assessed by SEM. Empty alginate capsules were left to dry on carbon tape/silicon wafer, covered with a thin film of iridium and then imaged (Figure 3.2A-E). We observed a capsule diameter of 204±1 μm (Figure 3.2A), which differed from the average diameter observed for hydrated capsules (around 700 μm, Figure 3.4). Alginate capsules are hydrogels, cross-linked polymeric networks which retain a significant fraction of water within their structure [26]; during drying for SEM preparation, capsules loose water by evaporation, which probably justifies the observed capsule shrinkage. We observed that capsules were composed by surface thick membrane (approximately 10 μm, Figure 3.2B). At the capsule

surface, we could identify pores (Figure 3.2C, D and E), with an average size of around 113 nm (Figure 3.2F).

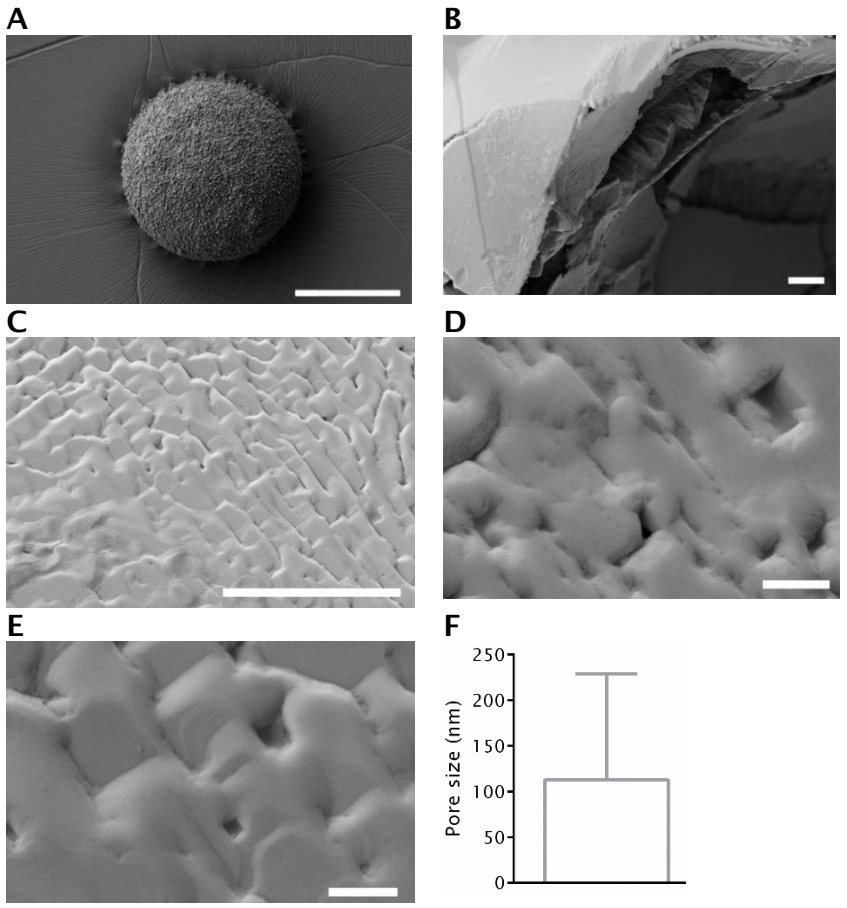

Figure 3.2: Scanning electron microscopy of alginate microcapsules. Alginate capsules were dried on carbon tape, coated with iridium and imaged: **A)** individual capsule, scale bar: 100 µm; **B)** membrane region of a capsule; scale bar: 10 µm; **C), D) and E)** pore region of the membrane of several capsules; (C) scale bar: 10 µm; (D) and (E) scale bar: 1 µm; **F)** pore size distribution. Data is represented as mean ± SD (N=2). In A), B), and C), representative micrographs are presented.

BT474 spheroids were prepared from single cells, as previously described by our group [20]. Spheroids were harvested from culture when they reached an average diameter of 120 µm, which corresponded to 22 h post inoculation (Figure S3.1). Spheroids were encapsulated either alone or with fibroblasts, to generate mono- and co-cultures, respectively. In parallel, non-encapsulated spheroids were also maintained in culture.

Alginate capsules containing both mono- and co-cultures were measured at 2 hours of culture, to allow for equilibration in culture medium. The diameter observed for mono- and co-cultures was of 755 ± 20 and 780 ± 20, respectively (Figure 3.3). By day 14 of culture, no major differences were observed, in the average diameter of capsules from mono- and co-cultures (672 ± 42 and 713 ± 26, respectively Figure 3.3). Moreover, capsules retained their spherical shape along culture time, with no detectable deformed or broken capsules by day 14 of culture (Figure 3.4A).

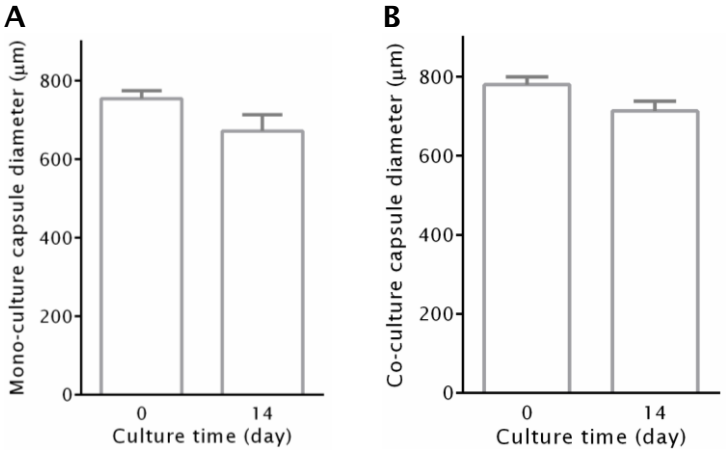

Figure 3.3: Alginate capsule diameter along culture time, in mono- and co-cultures. At 2 hours (Day 0) and day 14 of culture, 1 mL of capsule suspension was collected and the size of alginate capsules was evaluated. Data is represented as mean ± SD (N=2).

Concerning the cellular compartment, typically, 1 to 3 tumor cell spheroids were distributed per capsule, with fibroblasts organized around them, as previously described by our group for another BC cell line [6]. Both cell types maintained high cell viability over the 14 days of culture (Figure 3.4A), without significant changes in the number of spheroids per capsule (Figure S3.1A). On the other hand, BT474 non-encapsulated spheroids reached a diameter of 580 ± 71 μm by day 14, higher that their encapsulated counterparts (Figure 3.4B and Figure S3.2B). In both the mono- and co-culture encapsulated conditions, spheroid protrusion from the alginate capsules was observed during culture, without compromising capsule structure (Figure 4A). Compactness and roundness of the BT474 encapsulated spheroids were maintained through culture in both mono- and co-cultures (Figure 3.4A and Figure 3.7A).

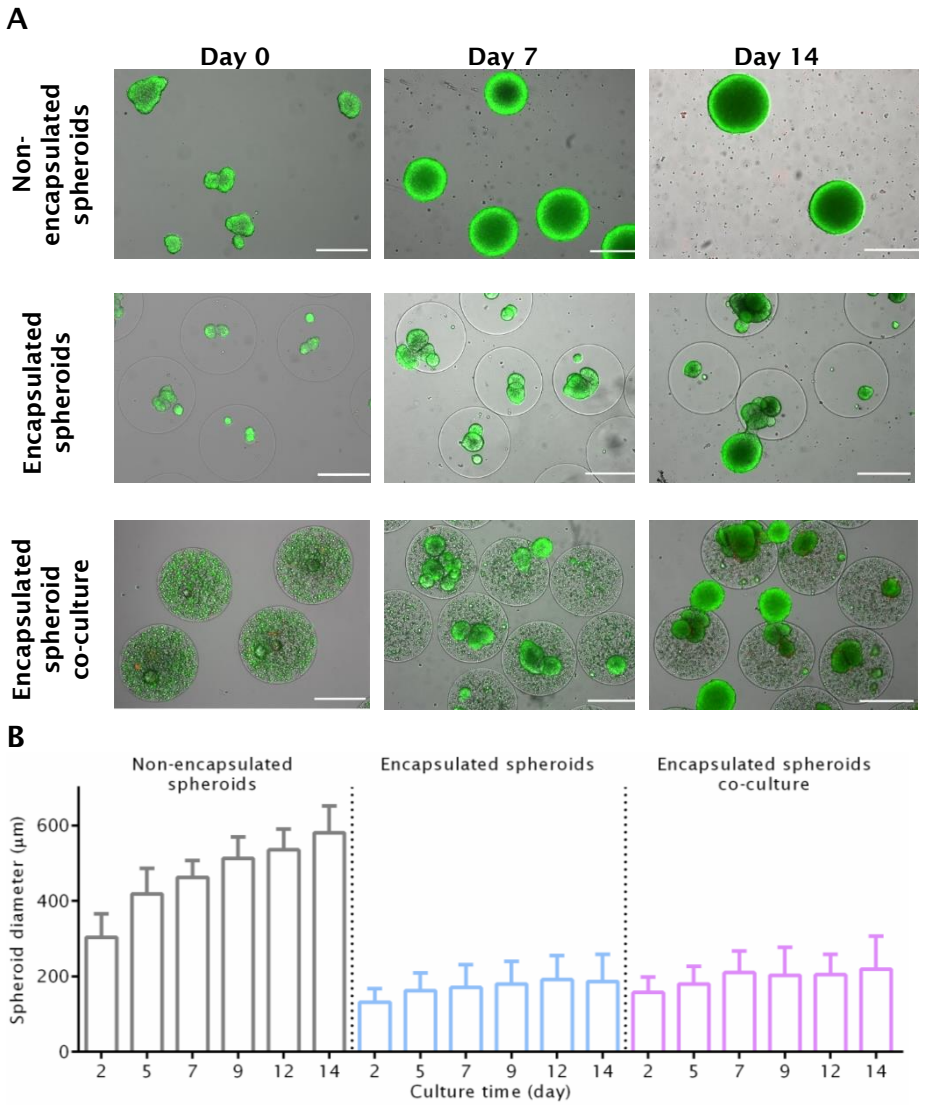

Figure 3.4: Non-encapsulated and encapsulated BT474 cell spheroids, in mono-culture or in co-culture with fibroblasts. **A)** At day 0, 7 and 14 of culture, cell viability was assessed by live/dead assay (FDA-green, live cells; PI-red, dead cells) for non-encapsulated spheroids, encapsulated spheroids in mono-culture and in co-culture with fibroblasts; scale bar: 500 µm. Representative pictures of 3 independent experiments. **B)** At day 2, 5, 7, 9, 12 and 14, spheroid diameter of non-encapsulated (grey), encapsulated mono- (blue) and co-cultures (purple) was evaluated. Data is represented as mean ± SD (N≥2).

In terms of tumor cell phenotype, encapsulation did not affect BT474 cells, which formed compact spheroids, with BT474 cells presenting cortical F-actin (Figure 3.5A and B) in the cell-cell interaction regions, as previously described for carcinoma cell lines [27]. Moreover, BT474 cells continued to express the luminal cell marker CK-18 [28], associated with their epithelial nature (Figure S3.3). The BT474 cell line is a luminal B BC cell line, which overexpresses Human Epidermal Growth Factor Receptor 2 (HER2) (Figure S3.3), an important breast carcinogenesis driver, used in the discrimination of BC subtypes and as therapeutic target [29,30]. By day 14 of culture, encapsulated spheroids and their non-encapsulated counterparts presented similar detection of CK-18 (Figure 3.5C and D) and HER2 (Figure 3.5E and F). Immunodetection of the proliferation marker Ki-67, at day 14 of culture, showed a low number of positive cells dispersed throughout the spheroids, both in non-encapsulated and encapsulated spheroids (Figure 3.5G and H). Quantification of Ki67-positive cells indicated that encapsulated mono-cultures featured higher levels of proliferation that the non-encapsulated counterparts (Figure 3.5I).

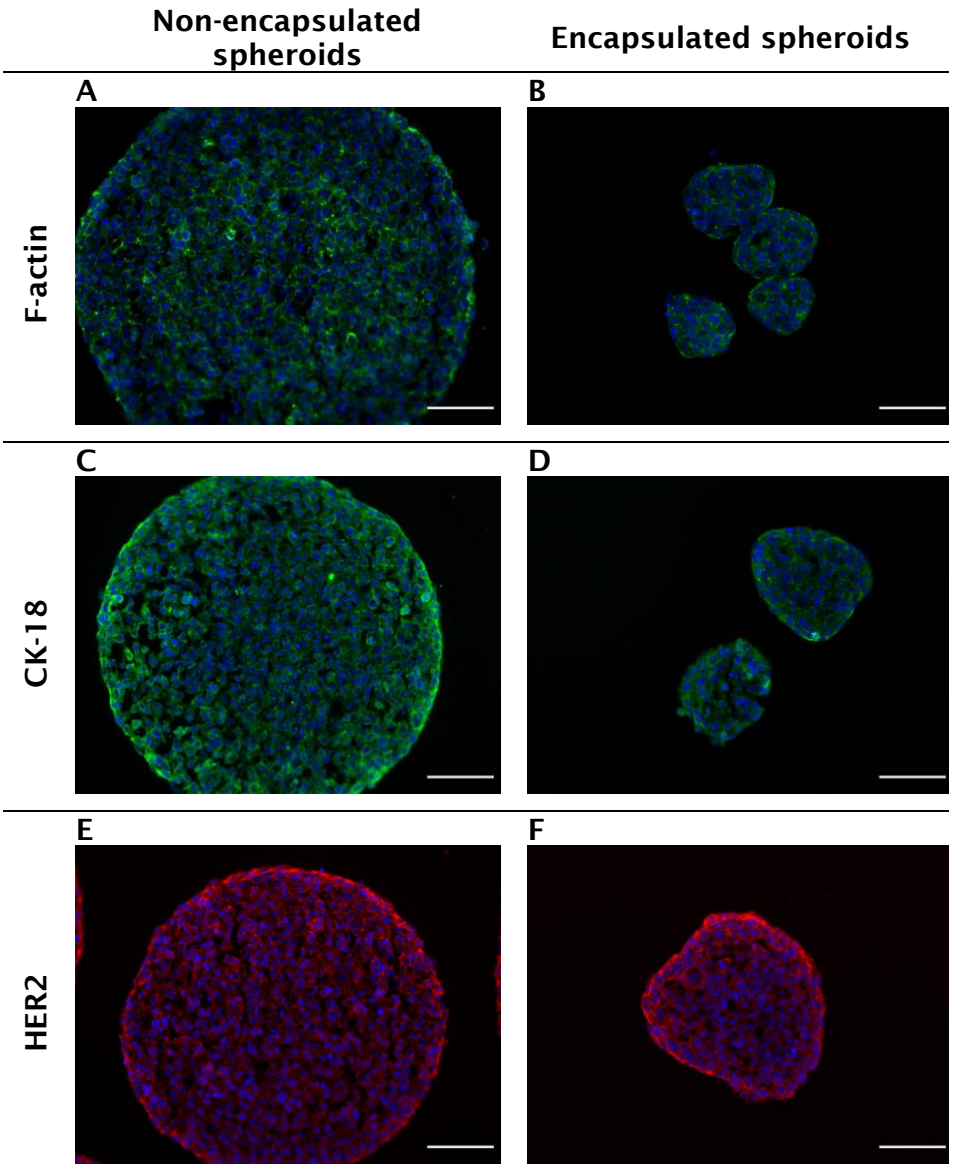

Figure continues on the next page.

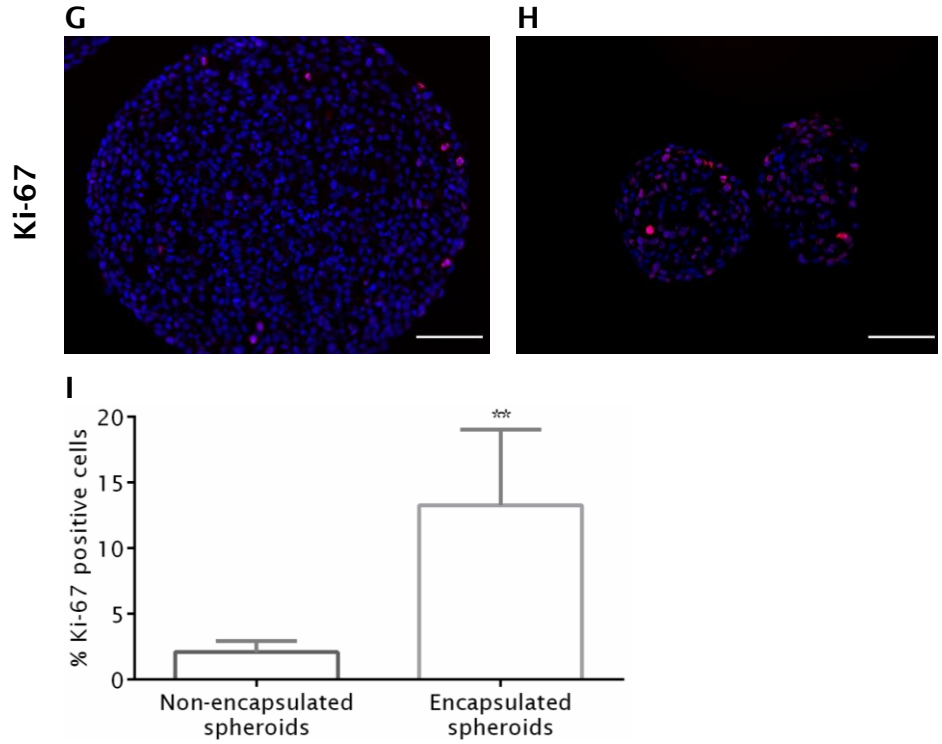

Figure 3.5: Phenotypic characterization of encapsulated and non-encapsulated BT474 spheroids. After 14 days of culture, non-encapsulated and encapsulated BT474 spheroids were immunolabelled for f-actin (**A** and **B**), CK-18 (**C** and **D**), HER2 (**E** and **F**) and Ki-67 (**G** and **H**), scale bar: 100 µm; **I)** Quantification of Ki-67 levels, data is presented as mean ± SD (N=6). Statistical analysis was performed using the non-parametric Mann-Whitney with ** *p-value*<0.01.

After two weeks of culture, the stiffness of the alginate capsules containing mono- and co-cultures were assessed by AFM. This scanning probe microscopy has nanometric resolution and the YM can be obtained from the data [31].

The YM determined for empty capsules was of 214±112 kPa. Capsules from mono- and co-cultures with 14 days presented lower YM (Figure 3.6): 16±13 and 40±12 kPa, for BT474 encapsulated mono- and co-cultures, respectively. In fact, encapsulated co-cultures were stiffer than the mono-cultures. To assess if the

presence of fibroblasts induced generalized higher stiffness of the capsules, we have analyzed encapsulated cultures from another tumor cell line (H157). Once again, the YM of encapsulated co-cultures was higher than for mono-cultures (81±44 and 26±8 kPa, respectively).

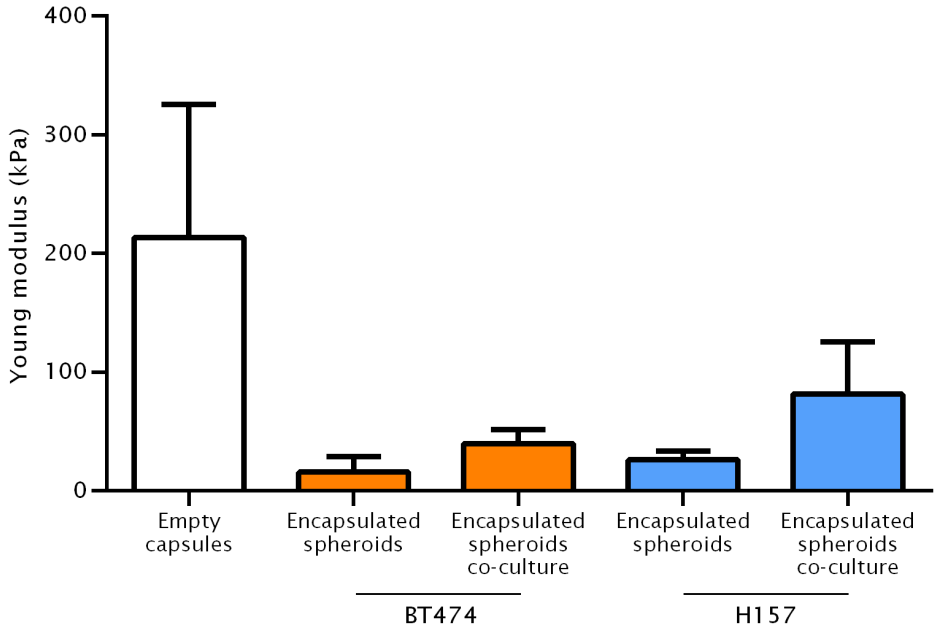

Figure 3.6: Young modulus of alginate capsules: empty, from mono- and co-cultures Young modulus of empty and 14-days cultured capsules was analyzed through AFM. BT474 mono and co-cultures represented in orange; H157 mono and co-cultures represented in blue). Data represented as mean ± SD (N=3).

In a previous study of the lab, we have observed that encapsulated co-cultures of H157 cells, fibroblasts and macrophages presented increased deposition of extracellular matrix (ECM) components in the capsules, namely collagen I and IV and fibronectin [18]. As collagen is described as mainly produced by fibroblasts [32] and deposition of collagen has been associated with stiffening of tumor tissue [33], we reasoned that ECM deposition in

encapsulated co-cultures might be responsible for the stiffening detected by AFM. To assess ECM matrix deposition, encapsulated cultures were stained for two of the most described components of the ECM, collagens and GAGs.

In encapsulated BT474 mono-cultures, picrosirius red staining of collagen was detected within spheroids (pink staining, Figure 3.7); there was no detectable collagen deposition within the capsules. Under polarized light, collagen fibrillar form was detected in very limited regions, in between tumor cells (white yellowish staining, Figure 3.7E and F); in accordance, we could not detect collagen fibers by second-harmonic generation microscopy (data not shown). No differences were observed when comparing encapsulated mono- and co-cultures (Figure 3.7).

GAGs were detected with alcian blue (that stains acidic polysaccharides and negatively charged mucins in blue) and aldehyde fucshin (that stains sulfated GAGs in purple). A light purple staining was observed in BT474 spheroids (Figure 3.7G and H), indicating low GAG accumulation relative to H157 spheroids, which were strongly stained (Figure S3.4). In all tested conditions, no accumulation of GAGs was detected outside of the spheroids, except the blue concentric ring surrounding the cells, probably indicative of the alginate capsule's membrane (Figure 3.7G and H).

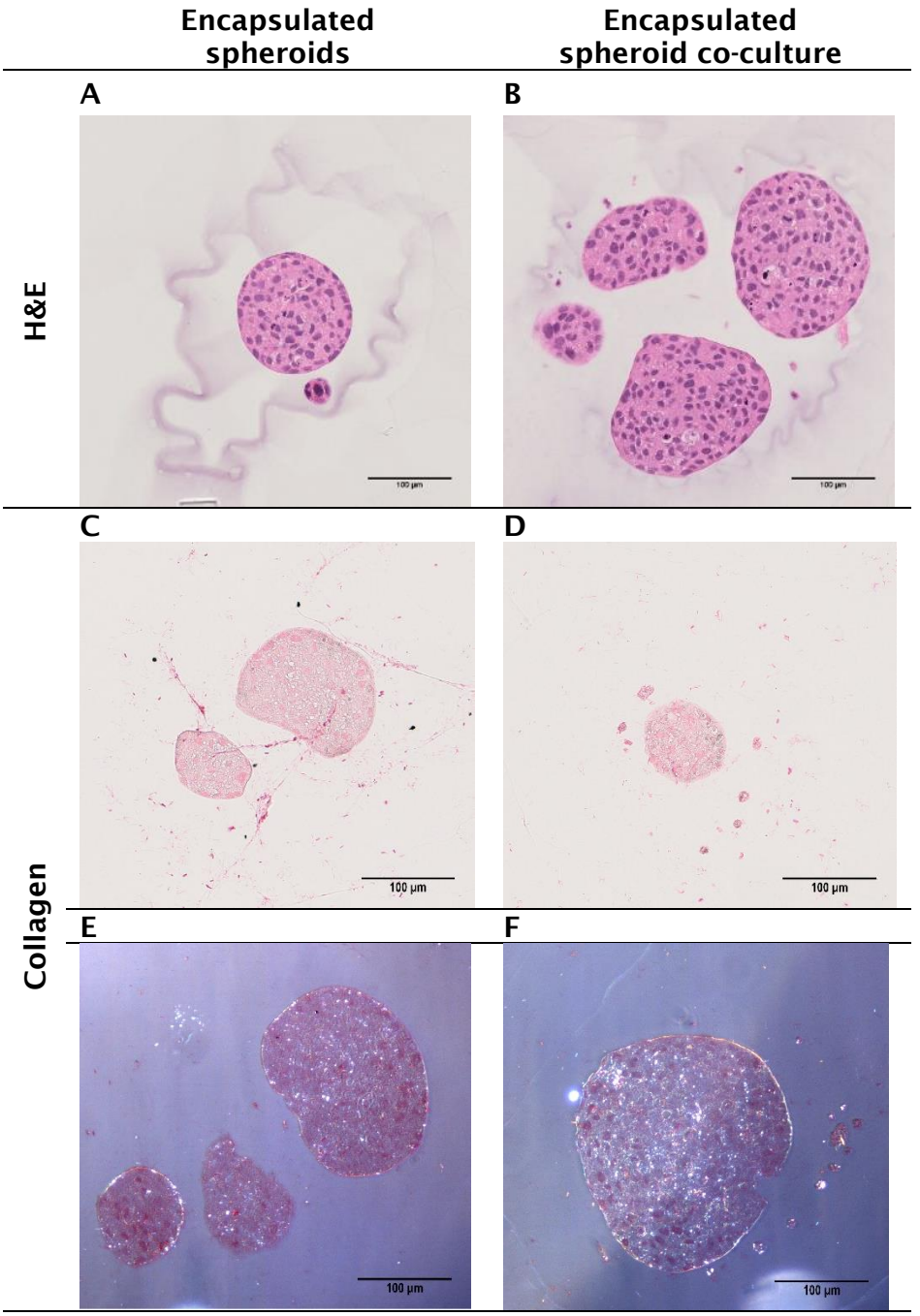

Figure continues on the next page.

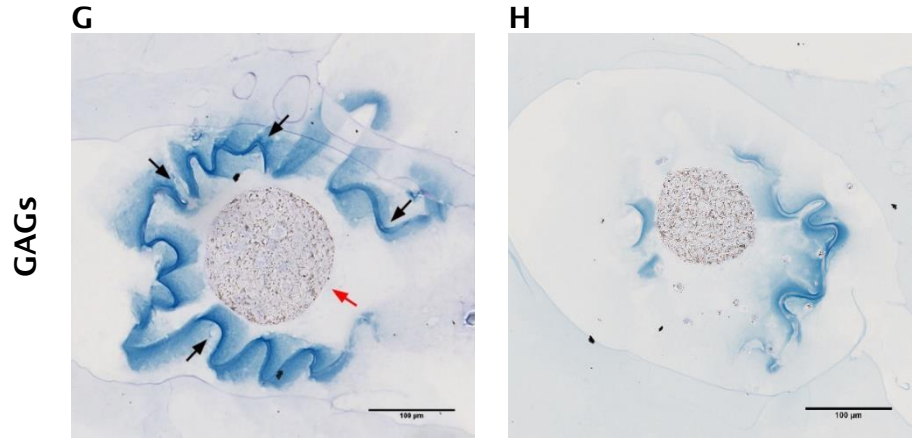

Figure 3.7: BT474 mono- or co-culture capsules show low accumulation of collagen and GAGs after 2 weeks of culture. After 14 days of culture, alginate capsules were fixed with PFA and **A)**, **B)** H&E; **C)**, **D)** Alcian blue/aldehyde fuschin under light microscopy **E)**, **F)** Alcian blue/aldehyde fuschin under polarized light; **G)**, **H)** Picrosirius red histochemical evaluations were performed; black arrows point at the capsule while the red arrows point at the spheroid, scale bar: 100 µm (N=1).

4. Discussion

Several 3D models of the TME have been developed based on the combination of cells and biomaterials. Specifically, alginate has been applied by several authors to create models of breast [6], lung [18] and liver cancer [34]. In this work, we have characterized 3D cancer cell models composed of alginate microencapsulated tumor cell spheroids together with human fibroblasts. By structural analysis, we show that empty alginate capsules have surface porosity. By comparison of non-encapsulated and encapsulated spheroids, we concluded that encapsulation avoided spheroid fusion and sustained cancer cell phenotype, as shown by typical epithelial cell markers, and proliferation. Mechanical evaluation of both empty and cell-containing alginate capsules revealed that the

presence of cells made alginate capsules smoother and the addition of fibroblasts increased capsule stiffness.

Capsules were cultured in a dynamic system that allow culture sampling in a non-destructive manner [35]. Also, agitation contributes to the maintenance of high cell viability by promoting a homogeneous distribution of oxygen and nutrients and a reduced formation of chemical and thermal gradients[35]. Characterization of empty alginate capsules revealed a hydrogel with a non-smooth porous surface. This may suggest that the capsule does not hamper the diffusion of macromolecules [6], including cytokines, released by the several cell types, as observed previously by our group using alginate co-culture capsules containing MCF-7 cells and fibroblasts [6]. Additionally, the size of capsule' pores is higher than antibodies. This suggests that these capsules can also be challenged with antibodies, which are currently used in clinics as cancer therapeutics. The average pore size we measured in the alginate capsules, within the nanometer range, is in agreement with the reported values on the literature for alginate hydrogels, reviewed by Simpliciano *et al.* [36]. The surface morphology we observed in the empty alginate capsules is in agreement with the observations reported by Arica *et al.* [37]. The authors prepared empty and ibuprofen-loaded calcium alginate beads and analyzed their surface morphology by SEM. Results revealed beads with rough surface morphology and visible large wrinkles, for both blank and drug-loaded particles [37].

During two weeks of culture, capsules maintained their sphericity and size, without visible damage. In co-cultures, fibroblasts arranged themselves around the tumor spheroids creating distinct epithelial and stromal compartments, as

previously observed for co-cultures of MCF7 cells and fibroblasts [6]. Encapsulation sustained the phenotype of the cancer cells, as suggested by the sustained detection of CK-18 and HER2. Encapsulated spheroids maintained their size over the two weeks of culture, compared to non-encapsulated spheroids, for which significant higher diameters were observed, concomitant with a significant decrease in spheroid concentration. This is probably due to spheroid fusion, induced by the agitation in the non-encapsulated spheroids, and avoided by the space limitation imposed by the capsule in encapsulated spheroids. Moreover, we observed lower detection levels of Ki-67 in non-encapsulated than encapsulated spheroids, suggesting that spheroid fusion, rather than cell proliferation explains the increased diameter of non-encapsulated spheroids over encapsulated ones, for the same culture time. Encapsulated spheroids from co-cultures showed higher diameter than those from mono-cultures. This is in agreement with what has been reported by Jeong *et al.* when culturing HT-29 cells as tumor spheroids in a collagen-matrix inside a microfluidic chip [38]. They compared spheroid diameter after 3 and 5 days of culture under mono- or co-culture with fibroblasts. In both time points, they observed larger spheroids in co-culture compared to mono-culture [38].

To mechanically characterize the alginate encapsulated model, stiffness was evaluated through analysis of YM, inferred by AFM. The YM depends solely on the intrinsic mechanical properties of the materials, being independent of the device geometry [11]. Cell-containing capsules were softer that empty capsules, with YM obtained for mono- and co-culture BT474 capsules falling within the range of BC tissue YM (10-43 kPa) [39]. The lower stiffness of

capsules containing cells could be explained by the time in culture medium itself, which can be enough to soften the capsules with cells, by influence of culture medium compounds on the alginate capsules network. Additionally, the difference of stiffness between empty and cell-containing capsules is in agreement with was observed by Tian and Chen [9]. Using alginate hydrogels with varying quantity of cells, they concluded that an increase in cell density leads to a decrease in scaffold strength. Nonetheless, when comparing mono- and co-culture capsules, we observed that the latter were stiffer, for both cell lines analyzed, despite the higher number of cells encapsulated. This may be explained by the secretion of molecules by fibroblasts and tumor cells under the influence of the fibroblasts. Secreted molecules, such as collagen, can interfere with the overall mechanical properties of the hydrogels. In fact, deposition of collagen has been associated with stiffening of tumor tissue [33]. Aiming to elucidate if increased ECM deposition in co-cultures could explain the differences in YM observed, we employed histochemical methods to detect collagens and GAGs. We could not see differences between mono- and co-culture conditions, as there was no detectable ECM outside the cellular compartment of the capsules. Nonetheless, in previous works by our group we have detected collagens within capsules of co-cultures of several tumor cell lines and fibroblasts, employing immunofluorescence and colorimetric methods [6,18]. A possibility is that the processing of the paraffin embedded samples was too harsh, as in fact, also fibroblasts were almost not detected. Further studies are required to elucidate the presence of ECM components within the capsules and their influence on the mechanical properties of the system.

Collectively, the results presented contribute to the characterization of alginate encapsulated cancer cell models. These models can be a useful tool to study for example anti-cancer therapy distribution within the TME. In fact, not only chemotherapeutic drugs but also antibodies can be tested since alginate capsule' pore size is bigger than the antibody size [40]. This potential application is studied in more detailed in the Chapter IV of this thesis.

5. Author Contribution

ALC, HA and CB conceptualized the study. ALC, HA and CB designed the experiments. ALC performed the cell culture procedures. ALC performed the culture characterization. ALC and HA performed the ECM characterization. TC conducted the AFM experiments. DG and TC conducted the SEM imaging. ALC wrote the chapter. CB corrected the chapter.

6. Acknowledgements

The author acknowledges IGC Histopathology unit, for the preparation of paraffin embedding lamina, stainings and scanning; Pedro Payno from Trinity College Dublin for the polarized light microscopy analysis; Emilio Gualda from The Institute of Photonic Sciences - ICFO, Barcelona Spain for the second-harmonic generation microscopy analysis. The work was supported by FCT PhD fellowship PD/BD/114047/2015 to L. Cartaxo and iNOVA4Health unit "iNOVA4Health Research Unit (LISBOA-01-0145-FEDER-007344), which is co-funded by Fundação para a Ciência e

Tecnologia/Ministério da Ciência e do Ensino Superior, through national funds, and by FEDER under the PT2020 Partnership Agreement.

7. References

1. Jensen, C. & Teng, Y. Is It Time to Start Transitioning From 2D to 3D Cell Culture? *Front. Mol. Biosci.* **7**, 1–15 (2020).
2. Liu, Z. & Vunjak-Novakovic, G. Modeling tumor microenvironments using custom-designed biomaterial scaffolds. *Physiol. Behav.* **176**, 139–148 (2011).
3. Florczyk, S. J. *et al.* 3D porous chitosan-alginate scaffolds: A new matrix for studying prostate cancer cell-lymphocyte interactions in vitro. *Adv. Healthc. Mater.* **1**, 590–599 (2012).
4. Cavo, M. *et al.* A new cell-laden 3D Alginate-Matrigel hydrogel resembles human breast cancer cell malignant morphology, spread and invasion capability observed 'in vivo'. *Sci. Rep.* **8**, 1–12 (2018).
5. Chaicharoenaudomrung, N. *et al.* Fabrication of 3D calcium-alginate scaffolds for human glioblastoma modeling and anticancer drug response evaluation. *J. Cell. Physiol.* **234**, 20085–20097 (2019).
6. Estrada, M. F. *et al.* Modelling the tumour microenvironment in long-term microencapsulated 3D co-cultures recapitulates phenotypic features of disease progression. *Biomaterials* **78**, 50–61 (2016).
7. Sun, J. & Tan, H. Alginate-Based Biomaterials for Regenerative Medicine Applications. *Materials (Basel).* **6**, 1285–1309 (2013).
8. Andersen, T., Auk-Emblem, P. & Dornish, M. 3D Cell Culture in Alginate Hydrogels. *Microarrays* **4**, 133–161 (2015).
9. Tian, X. & Chen, X. Effects of cell density on mechanical properties of alginate hydrogel tissue scaffolds. *J. Biomimetics, Biomater. Tissue Eng.* **19**, 77–85 (2014).
10. Cavo, M. *et al.* Microenvironment complexity and matrix stiffness regulate breast cancer cell activity in a 3D in vitro model. *Sci. Rep.* **6**, 1–13 (2016).
11. Ceccaldi, C. *et al.* Alginate scaffolds for mesenchymal stem cell cardiac therapy: Influence of alginate composition. *Cell Transplant.* **21**, 1969–1984 (2012).
12. Pebworth, M., Cismas, S. A. & Asuri, P. A Novel 2.5D Culture Platform to Investigate the Role of Stiffness Gradients on Adhesion-Independent Cell Migration. *PLoS One* **9**, e110453 (2014).
13. Khavari, A., Nydén, M., Weitz, D. A. & Ehrlicher, A. J. Composite alginate gels for tunable cellular microenvironment mechanics. *Sci. Rep.* **6**, 1–10 (2016).
14. Kaklamani, G., Cheneler, D., Grover, L. M., Adams, M. J. & Bowen, J. Mechanical properties of alginate hydrogels manufactured using external gelation. *J. Mech. Behav. Biomed. Mater.* **36**, 135–142 (2014).
15. Dolan, E. B. *et al.* Advanced Material Catheter (AMCath), a minimally invasive endocardial catheter for the delivery of fast-gelling covalently cross-linked hyaluronic acid hydrogels. *J. Biomater. Appl.* **33**, 681–692 (2018).
16. Ahearne, M. Introduction to cell – hydrogel mechanosensing. *Interface*

Focus **4**, (2014).
17. Hadden, W. J., Young, J. L., Holle, A. W., Mcfetridge, M. L. & Yong, D. Stem cell migration and mechanotransduction on linear stiffness gradient hydrogels. *PNAS* **114**, 5647–5652 (2017).
18. Rebelo, S. P. *et al.* 3D-3-culture: A tool to unveil macrophage plasticity in the tumour microenvironment. *Biomaterials* **163**, 185–197 (2018).
19. Protocol, B. Trypan Blue Exclusion Test of Cell Viability. 2–3 (1997).
20. Santo, V. E. *et al.* Adaptable stirred-tank culture strategies for large scale production of multicellular spheroid-based tumor cell models. *J. Biotechnol.* **221**, 118–129 (2016).
21. Rebelo, S. P., Costa, R., Sousa, M. F. Q., Brito, C. & Alves, P. M. Establishing liver bioreactors for in vitro research. in *Protocols in In Vitro Hepatocyte Research* vol. 1250 1–390 (2015).
22. Clarke, J. M., Gillings, M. R., Altavilla, N. & Beattie, A. J. Potential problems with fluorescein diacetate assays of cell viability when testing natural products for antimicrobial activity. *J. Microbiol. Methods* **46**, 261–267 (2001).
23. Rebelo, S. P. *et al.* HepaRG microencapsulated spheroids in DMSO-free culture: novel culturing approaches for enhanced xenobiotic and biosynthetic metabolism. *Arch. Toxicol.* **89**, 1347–1358 (2015).
24. Sader, J. E., Larson, I., Mulvaney, P. & White, L. R. Method for the calibration of atomic force microscope cantilevers. *Rev. Sci. Instrum.* **66**, 3789–3798 (1995).
25. Sneddon, I. N. The relation between load and penetration in the axisymmetric boussinesq problem for a punch of arbitrary profile. *Int. J. Eng. Sci.* **3**, 47–57 (1965).
26. Ahmed, E. M. Hydrogel: Preparation, characterization, and applications: A review. *J. Adv. Res.* **6**, 105–121 (2015).
27. Cui, X., Hartanto, Y. & Zhang, H. Advances in multicellular spheroids formation. *J. R. Soc. Interface* **14**, (2017).
28. Abd El-Rehim, D. M. *et al.* Expression of luminal and basal cytokeratins in human breast carcinoma. *J. Pathol.* **203**, 661–671 (2004).
29. Gusterson, B. A., Ross, D. T., Heath, V. J. & Stein, T. Basal cytokeratins and their relationship to the cellular origin and functional classification of breast cancer. *Breast Cancer Res.* **7**, 143–148 (2005).
30. Holliday, D. L. & Speirs, V. Choosing the right cell line for breast cancer research. *Breast Cancer Res.* **13**, (2011).
31. Roa, J. J., Oncins, G., Díaz, J., Sanz, F. & Segarra, M. Calculation of Young's Modulus Value by Means of AFM. *Recent Pat. Nanotechnol.* **5**, 27–36 (2011).
32. Alkasalias, T., Moyano-Galceran, L., Arsenian-Henriksson, M. & Lehti, K. Fibroblasts in the tumor microenvironment: Shield or spear? *Int. J. Mol. Sci.* **19**, 1–21 (2018).
33. Cox, T. R. & Erler, J. T. Molecular pathways: Connecting fibrosis and solid tumor metastasis. *Clin. Cancer Res.* **20**, 3637–3643 (2014).
34. Wang, Q. *et al.* Cytoskeletal reorganization and repolarization of hepatocarcinoma cells in APA microcapsule to mimic native tumor characteristics. *Hepatol. Res.* **35**, 96–103 (2006).
35. Serra, M., Brito, C., Correia, C. & Alves, P. M. Process engineering of human pluripotent stem cells for clinical application. *Trends Biotechnol.* **30**, 350–359 (2012).
36. Simpliciano, C. *et al.* Cross-Linked Alginate Film Pore Size Determination Using Atomic Force Microscopy and Validation Using Diffusivity

Determinations. *J. Surf. Eng. Mater. Adv. Technol.* **03**, 1–12 (2013).
37. Arica, B. *et al.* In vitro and in vivo studies of ibuprofen-loaded biodegradable alginate beads. *J. Microencapsul.* **22**, 153–165 (2005).
38. Jeong, S. Y., Lee, J. H., Shin, Y., Chung, S. & Kuh, H. J. Co-culture of tumor spheroids and fibroblasts in a collagen matrix-incorporated microfluidic chip mimics reciprocal activation in solid tumor microenvironment. *PLoS One* **11**, 1–17 (2016).
39. Samani, A., Zubovits, J. & Plewes, D. Elastic moduli of normal and pathological human breast tissues: An inversion-technique-based investigation of 169 samples. *Phys. Med. Biol.* **52**, 1565–1576 (2007).
40. Tan, Y. H. *et al.* A Nanoengineering Approach for Investigation and Regulation of Protein Immobilization. *ACS Nano* **2**, 2374–2384 (2008).

8. Supplementary material

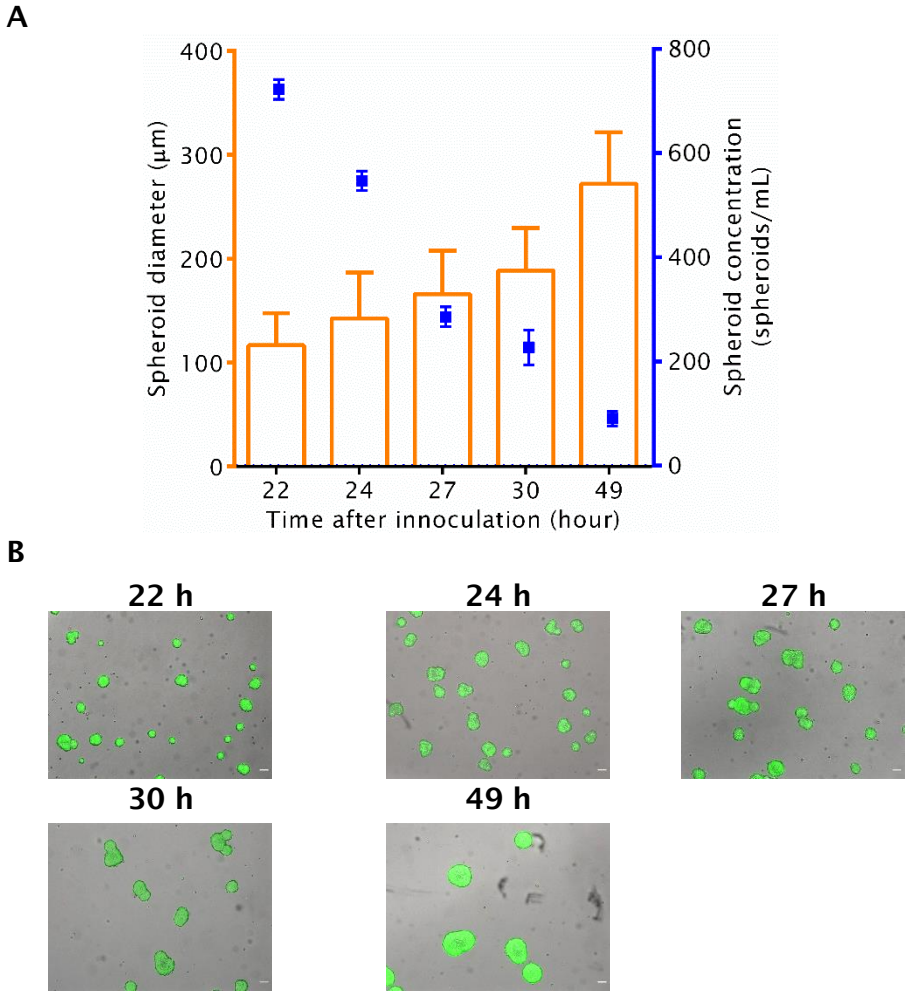

Figure S3.1: BT474 cell line forms spherical and compact spheroids after one day of culture in spinner vessel. **A)** Spheroid diameter and spheroid concentration throughout culture time was measured (N=1); data is represented as mean ± SD; **B)** Live/dead assay (FDA-green; PI-red) (scale bar 100 µm).

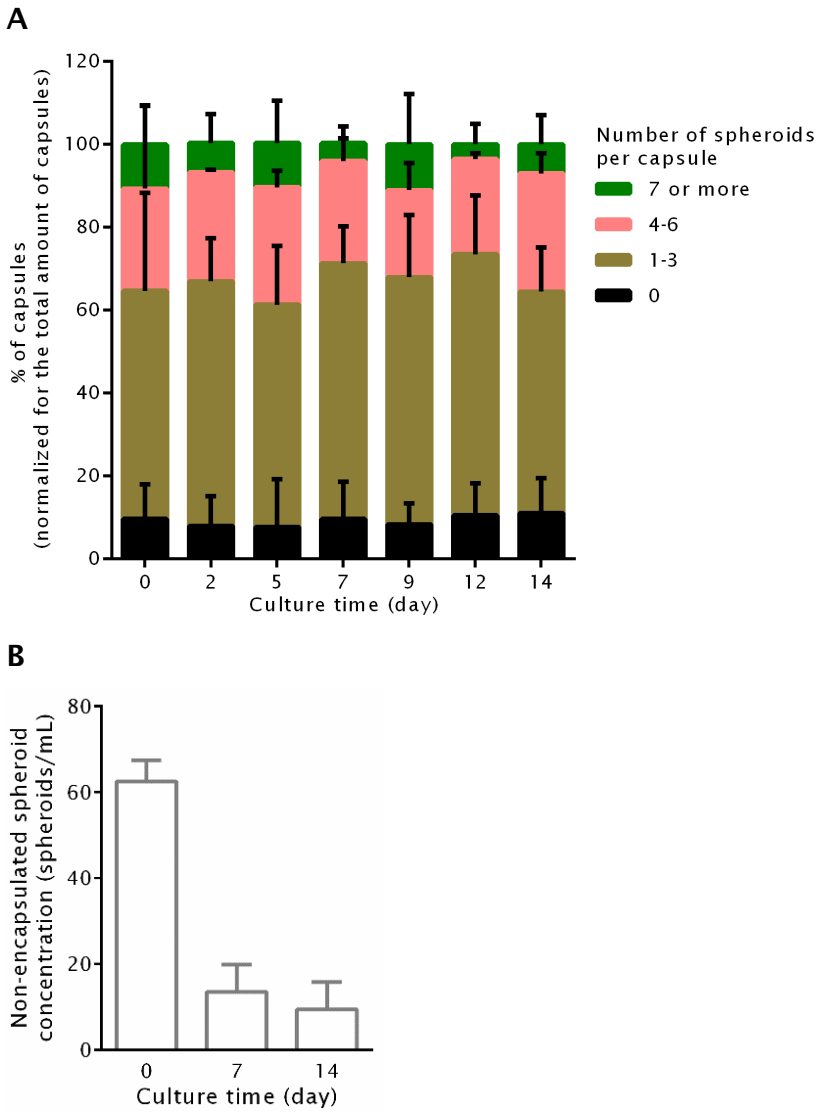

Figure S3.2: Spheroid distribution per capsule and spheroid concentration in non-encapsulated cultures. **A)** At day 0, 7 and 14 days of culture of encapsulated mono-culture, 1 mL of culture was collected and the quantity of spheroids inside each alginate capsule was counted (N≥2). **B)** At day 0, 7 and 14, of non-encapsulated culture, 1 mL culture was collected and the number of spheroids was counted (N=2).

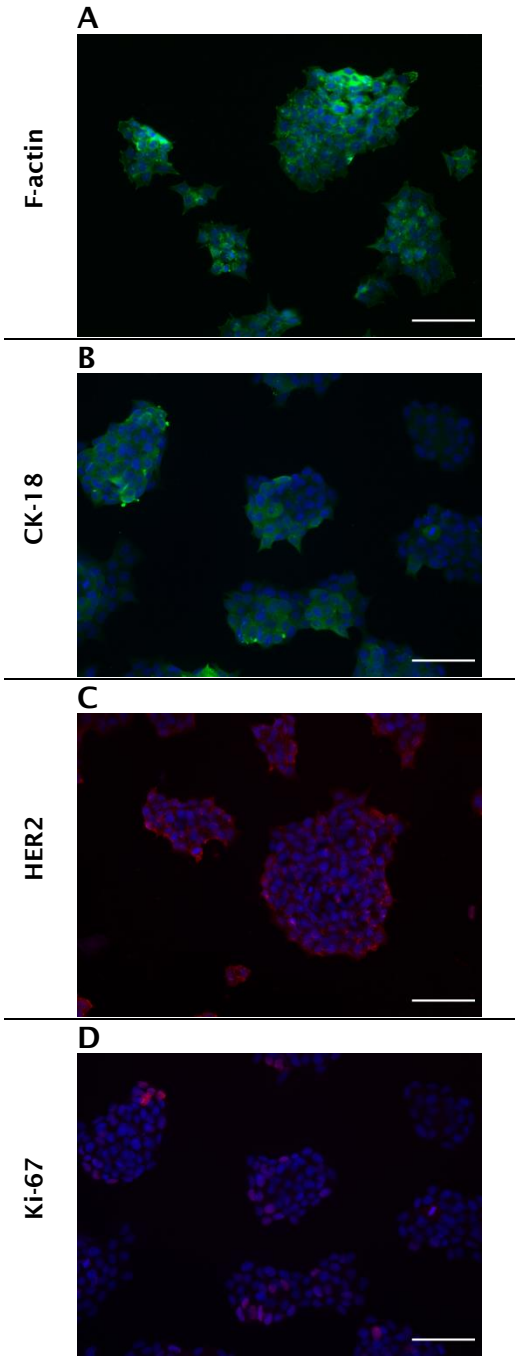

Figure S3.3: Immunofluorescence microscopy of BT474 cells cultured in 2D. BT474 cells cultured in 2D were immunolabelled for f-actin (**A**), CK-18 (**B**), HER2 (**C**) and Ki-67 (**D**).

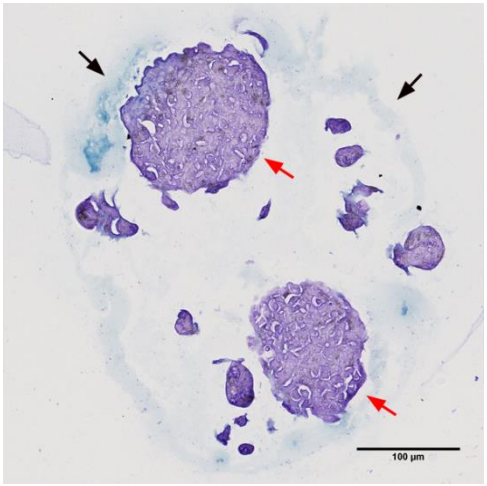

Figure S3.4: GAG detection in encapsulated cultures of H157 tumor cells. After 14 days of culture, alginate capsules were fixed with PFA and aldehyde fuschin and alcian blue staining were performed to detect glycosaminoglycans in general and alginate, respectively (N=1); scale 100 µm.

Table S3.1: Antibodies used for immunodetection.

Antibody description	Clone	Origin	Reference	Supplier
Anti-Ki67	SP6	rabbit	ab27619	Abcam
Anti-CK-18 – FITC conjugate	CY-90	mouse	F 4772	Sigma
Anti-HER2	-	rabbit	A0485	DAKO
Anti-phalloidin – 488 conjugate	-	-	A12379	Life Technologies
Anti-rabbit Alexa 594	-	goat	A-11037	Life Technologies
Anti-mouse Alexa 488	-	goat	A11001	Life Technologies

CHAPTER IV

A computational diffusion model to study antibody transport within reconstructed tumor microenvironments

This chapter was adapted from:

Ana Luísa Cartaxo, Jaime Almeida, Emilio J. Gualda, Maria Marsal, Pablo Alvarez-Loza, Catarina Brito, Inês A. Isidro; *A computational diffusion model to study antibody transport within reconstructed tumor microenvironments*, submitted to BMC Bioinformatics

Table of contents

Abstract

Antibodies revolutionized cancer treatment over the past decades. Despite their successfully application, there are still challenges to overcome to improve efficacy, such as the heterogeneous distribution of antibodies within tumors. Tumor microenvironment features, such as the distribution of tumor and other cell types and the composition of the extracellular matrix may work together to hinder antibodies from reaching the target tumor cells. To understand these interactions, we propose a framework combining *in vitro* and *in silico* models. We took advantage of *in vitro* cancer models previously developed by our group, consisting of tumor cells and fibroblasts co-cultured in 3D within alginate capsules, for reconstruction of tumor microenvironment features.

In this work, a computational model of antibody transport within alginate capsules was established, assuming a purely diffusive transport, combined with an exponential saturation effect that mimics the saturation of binding sites on the cell surface. Our tumor microenvironment *in vitro* models were challenged with a fluorescent antibody and its transport recorded using light sheet fluorescence microscopy. Diffusion and saturation parameters of the computational model were adjusted to reproduce the experimental antibody distribution, with root mean square error under 5%. This computational framework is flexible and can simulate different random distributions of tumor microenvironment elements (fibroblasts, cancer cells and collagen fibers) within the capsule. The random distribution algorithm can be tuned to follow the general patterns observed in the experimental models.

We present a computational and microscopy framework to track and simulate antibody transport within the tumor microenvironment that complements the previously established *in vitro* models platform. This framework paves the way to the development of a valuable tool to study the influence of different components of the tumor microenvironment on antibody transport.

Key words: antibody diffusion, tumor microenvironment, 3D *in vitro* cancer models, computational modelling, light sheet fluorescence microscopy

1. Background

The value of antibodies as antitumor therapies has been largely demonstrated over the last two decades [1]. Despite the generalized success, there are still challenges to overcome, such as the largely reported poor tissue penetration and heterogeneous distribution of antibodies within solid tumors [2]. Efficacy of therapeutic antibodies is conditioned by several transport barriers, from systemic administration until reaching the target cells [3]. These barriers ultimately cause a reduction of the therapeutic molecule concentration that reaches the target tumor cells, decreasing its therapeutic effect [3–5]. Specifically within the tumor microenvironment (TME), higher heterogeneity is found when comparing with healthy tissue: tumors present altered vasculature, desmoplastic and inflammatory microenvironment and extracellular matrix (ECM) alterations [6]. Within the ECM, collagen fibers and glycosaminoglycans (GAGs) have been previously described as influencing the transport of therapeutic molecules [7–9]. So, it is crucial to assess antibody transport within this intricate network with high impact on therapy efficiency.

Experimental (i.e. *in vitro*, *in vivo* and *ex vivo*) and computational (*in silico*) models have been developed to help understand how tumor heterogeneity influences drug distribution within the TME [6,10,11]. Those two types of models can and should be combined to develop a comprehensive framework to study and try to answer that question.

Several computational models have been developed over the years to describe and simulate the transport and interactions of drugs within the tumor by considering the main transport mechanisms, such as diffusion and convection, degradation and

internalization [10,12–16]. These models can be used to study the complex interaction between several tumor components and drug pharmacokinetics and distribution. They can represent the tumor with different levels of detail, from a simplistic homogeneous tumor mass to complex heterogeneous non-equally distant cancer cells. However, they do not consider the impact on antibody distribution of specific elements of the TME, such as collagen fibers, that have been reported to have a severe influence in this distribution [7–9].

The assessment and tracking of distribution of drugs *in vivo*, in tumor tissue or in tumor-like structures or complex cell cultures/tissue mimetics is also technically challenging [13,17] and typically relies on methods that do not allow real-time tracing of antibody distribution [17–20] due to limitations of microscopy techniques and of the biological sample [17,21].

Our group has been developing modular 3D cell models of the tumor microenvironment. These *in vitro* cancer models, comprise cancer cells, and fibroblasts and other cellular components, that can be conjugated in different amounts and proportions, to mimic features observed in patient tumors [22,23].

In this work, 3D *in vitro* cancer models were used as an experimental platform to assess antibody distribution within the TME. Light sheet fluorescence microscopy (LSFM) was implemented to perform real-time antibody tracking with high resolution 3D imaging over time, together with low photobleaching of the sample fluorescence [24]. An *in silico* model of antibody diffusion within the TME, developed specifically as a complement to the 3D *in vitro* models, was calibrated based on these data. Assuming a purely diffusive antibody transport and considering that binding sites on

cell surface become saturated over time, Fick's law was combined with an exponential saturation equation. The computational model was able to describe the antibody concentration profile observed experimentally with very good agreement. Additionally, we show this platform can be used to generate random spatial distributions of the TME elements (tumor cell spheroids, fibroblasts and ECM fibers) inside the capsule, following a tunable stochastic approach.

2. Results

2.1. Experimental observation of antibody diffusion through 3D capsule

Antibody transport within the alginate capsule was tracked using a custom-made LSFM setup. A fluorescent anti-CD44 antibody was used to challenge the encapsulated co-culture of tumor cells and fibroblasts. Over time, fluorescent signal was increasingly detected in cells within the capsules, following a radial trend from the periphery to the inside of the capsule (Additional file 1). The central plane of the 3D capsule acquisition was selected to allow visualization and model calibration (Figure 4.1, Additional file 2).

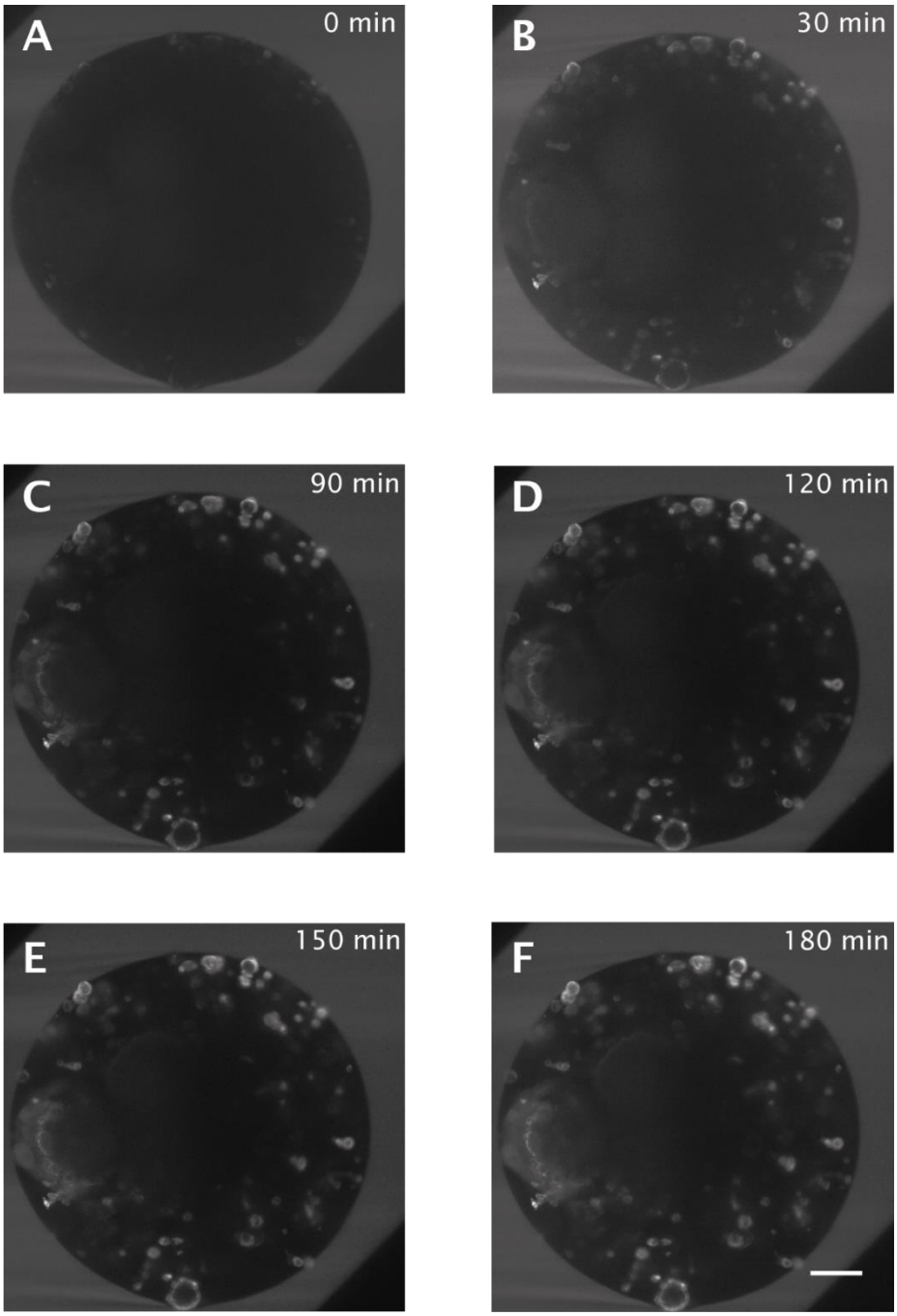

Figure 4.1: Fluorescence after antibody challenge for a representative capsule section. A) *0 min;* ***B)*** *30 min;* ***C)*** *90 min;* ***D)*** *120 min;* ***E)*** *150 min;* ***F)*** *180 min after the antibody challenge; scale bar: 100 µm.*

Image processing was used to trace antibody fluorescent signal profiles in defined regions of interest (ROIs), corresponding to cell spheroids or clusters of few cells (Figure 4.2A). For cell cluster II, close to the capsule periphery, we observed a fast increase in fluorescence intensity, which stabilized early into a plateau (Figure 4.2C). For cell cluster V, further away from the periphery, we observed a delay in the increase in fluorescence intensity and the plateau was reached at least 30 min later (Figure 4.2F).

The delay time had a positive correlation with the cell cluster distance to the capsule periphery, although with a high variability (Figure 4.2B-F, Figure S4.A). It is reasonable to expect the presence of heterogeneous physical and biological barriers in the antibody diffusion path which can influence the delay time. For example, cluster III was farther away from the periphery than cluster I, but both show a similar delay (Figure S4.A).

The experimental fluorescence profiles were fitted with mathematical models for S-shaped curves, often used to describe population growth [25]. All selected clusters had the best fit, with $R^2>0.98$, with the Richards model, given by

$$P(t)=\frac{M}{[1+\alpha\ \exp(-M\,\beta\ t)]^{\gamma}} \quad (1)$$

$$\alpha=\left[\left(\frac{M}{P_0}\right)^{\frac{1}{\gamma}}-1\right]\exp(M\,\beta\ t_0) \quad (2)$$

in which P is the mean fluorescence and α, β, γ and M are constants [25].

The fitted smoothed curves describe well the overall fluorescence intensity profiles (Figure 4.2, Table 4.1). Nonetheless, for some of the cell clusters, when the fluorescence intensity

becomes detectable, the adjusted curve showed a slight bias towards a shorter delay than was seen in the experimental data (Figure 4.2C, E). Consistently with the previous observations, the curve parameters do not follow a clear trend depending on the cluster distance to the capsule periphery or the cluster size.

Table 4.1: Properties for selected cell clusters and parameters for the adjusted fluorescence profiles.

Cell cluster	Distance to capsule periphery (μm)	Area (μm^2)	Fitted parameters			
			M	β	γ	R^2
I	83.0	232	54.1	6.42×10^{-4}	4.40	0.9868
II	88.1	270	80.2	4.88×10^{-4}	15.1	0.9884
III	115.0	211	55.2	10.1×10^{-4}	2.44	0.9980
IV	124.7	265	109	4.40×10^{-4}	1.87	0.9978
V	127.3	439	75.0	7.09×10^{-4}	1.78	0.9925

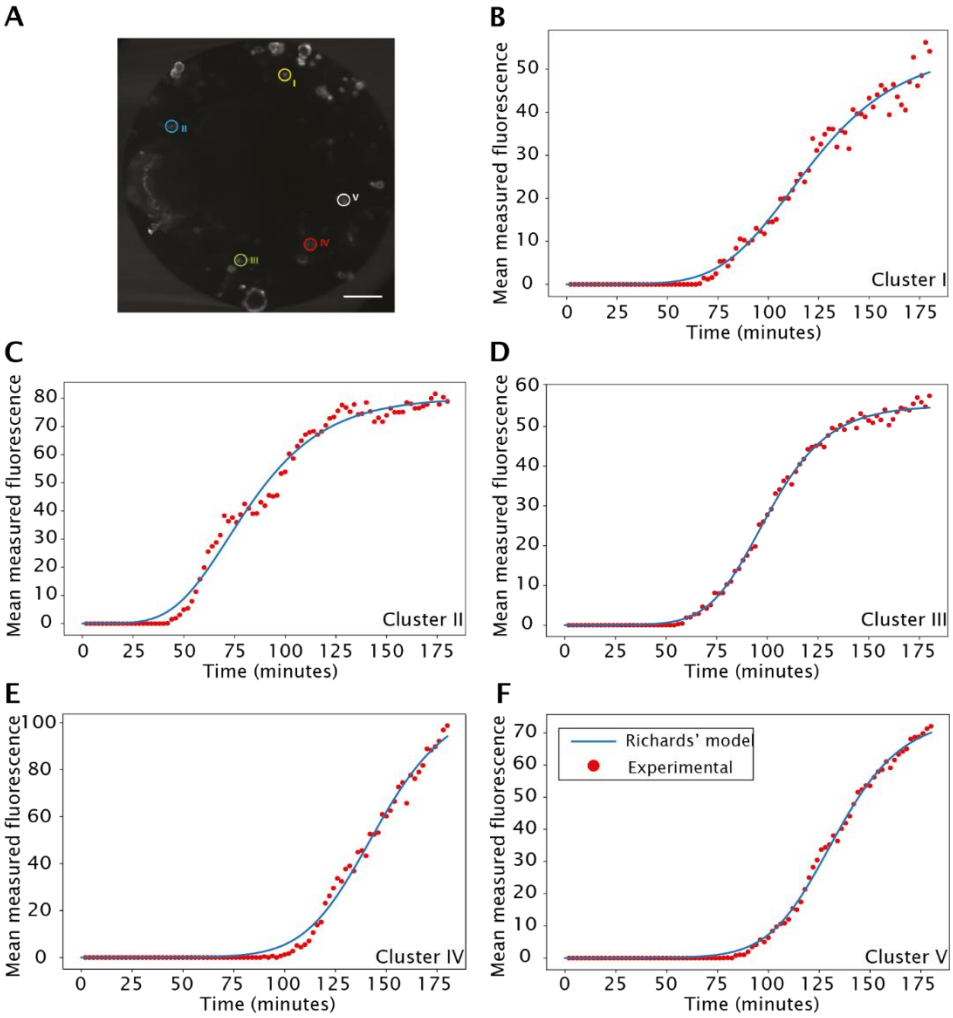

Figure 4.2: Fluorescence profiles for selected cell clusters and fitted curves. **A)** Definition of selected cell clusters (scale bar: 100 μm); **B-F)** Experimental mean fluorescence profiles from LSFM data (red dots) and fitted curves (blue lines) for the selected cell clusters I through V, respectively. Curve parameters for Eq. (1-2) are shown in the Table 1.

2.2. Computational model emulates antibody transport within the capsule

A digitization approach was used to obtain a capsule section equivalent to the one used in the experimental study (Figure S4.2A-C). The initial diffusivities (Figure S4.2D) were set taking into

account the range of values for this parameter reported on the literature [26–28] and the experimental results over time (Figure 4.1). By changing D_{medium} the "radially moving front" of the antibody distribution can be controlled. Based on experimental observations, D_{medium} was fixed at 0.15 $\mu m^2/s$ and D_{cell} was subsequently fixed at 0.0015 $\mu m^2/s$.

The computational model has antibody distribution profiles over time which are very similar to the ones obtained experimentally, when looking to diffusion through the extracellular intra-capsule space (Figure 4.3, Additional file 3). The model diffusivity coefficients decrease over time on the exposed surface of the cell spheroids, as imposed by the saturation equation (Figure S4.3, Additional file 4).

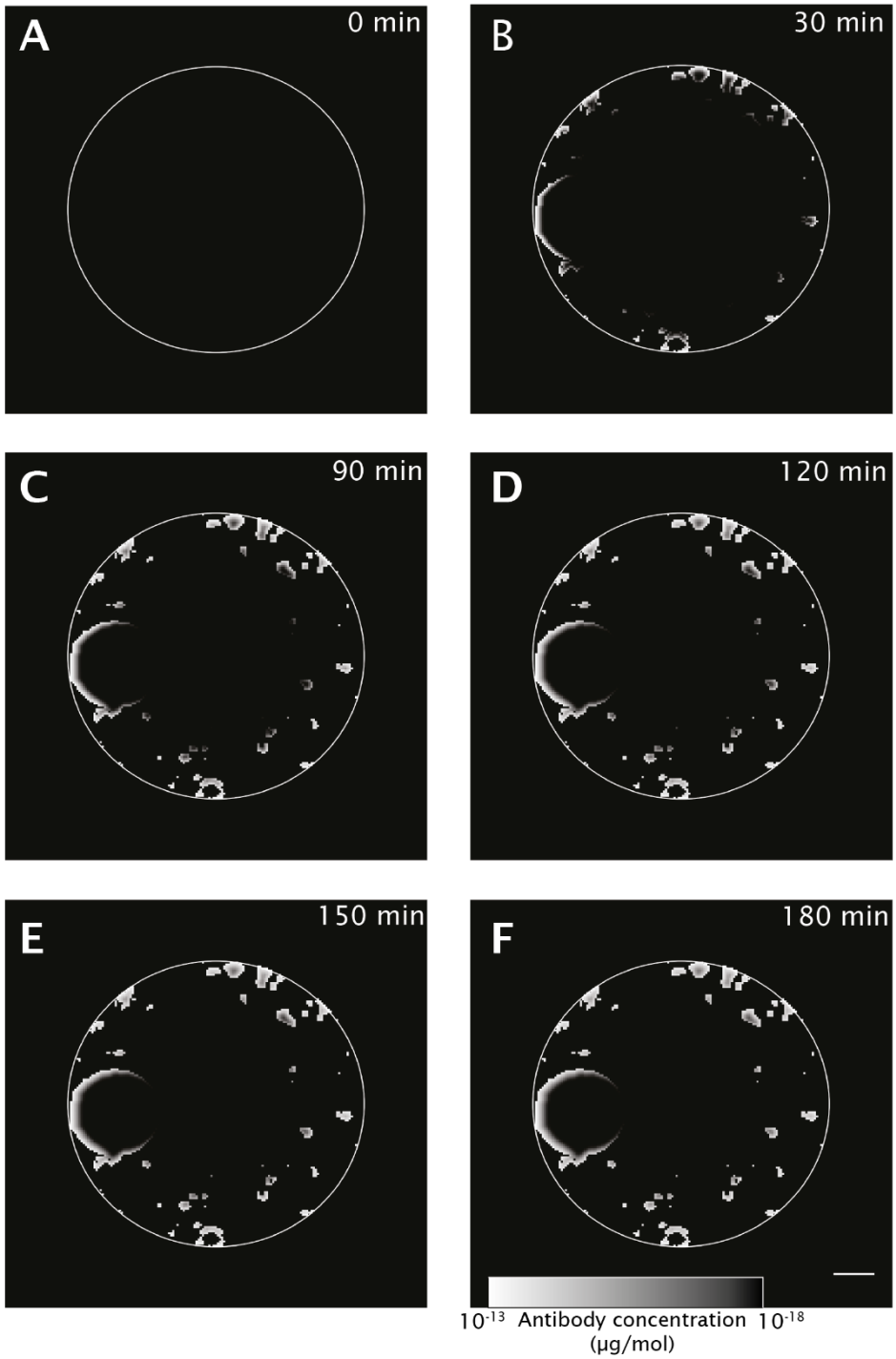

See caption in the next page.

Figure 4.3: Simulated antibody concentration profile throughout the digitized capsule, over time. Computational images for selected timepoints using saturation parameters $a = 1$, $n = 1$ and $p = 1$: **A)** 0 min; **B)** 30 min; **C)** 90 min; **D)** 120 min; **E)** 150 min; **F)** 180 min; white circumference represents the capsule periphery; scale bar: 100 μm.

Antibody concentration profiles in the cell clusters were adjusted to account for binding and saturation of the antigens. To fit the computational model, the parameters of the saturation equation, Eq. (4), were adjusted by minimizing the root mean square error (RMSE) between the normalized experimental and computational profiles, for the 5 selected cell clusters (Figure 4.4A). The proposed model, using Fick's law combined with exponential saturation, was able to represent the experimental profiles with an RMSE up to 5% (Figure 4.4B-F and Table 2). The best parameters varied between cell clusters, even for clusters with similar distance to the capsule periphery such as clusters I and II and clusters IV and V.

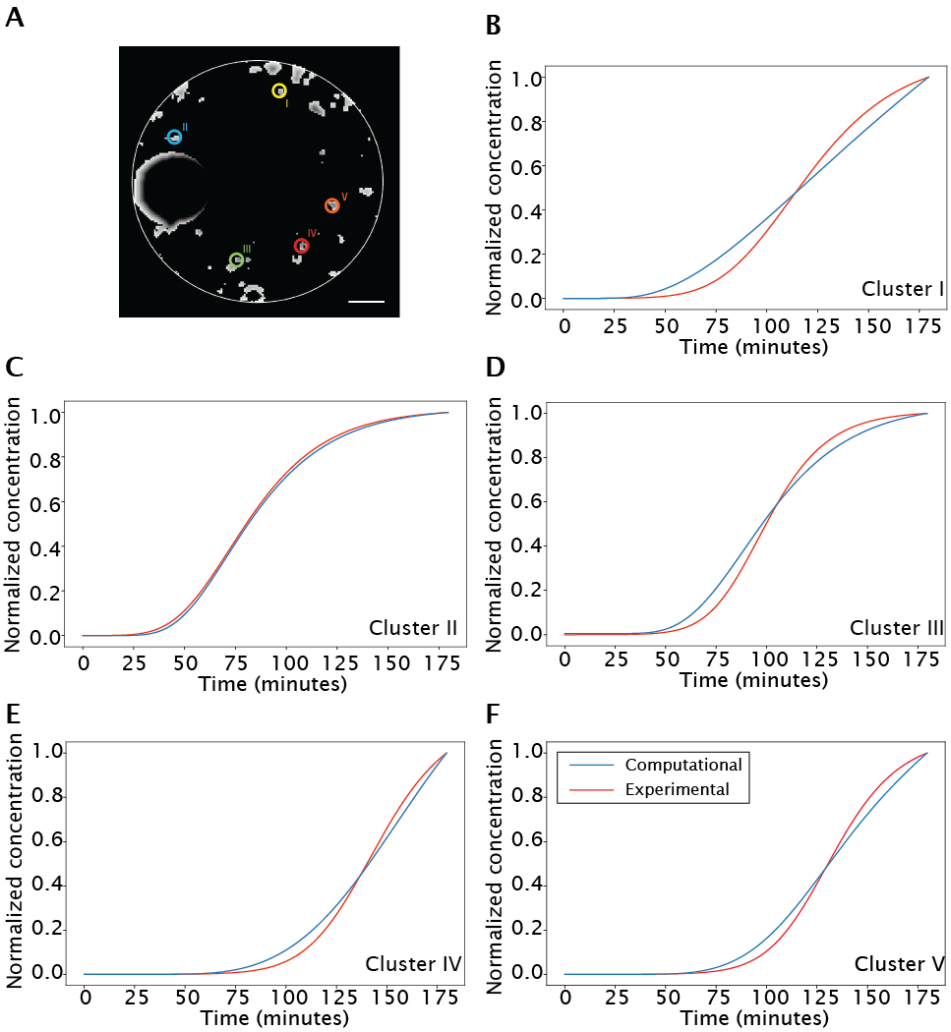

Figure 4.4: Computational antibody concentration profiles after fitting of the saturation parameters a, n and p to selected cell clusters. Adjusted computational curve: blue line; smoothed experimental data: red line; scale bar: 100 µm.

Table 4.2: Fitted saturation parameters for the computational model and RMSE.

Cell cluster	a	n	p	RMSE
I	1.01	1.73	1.33	0.05
II	1.00	1.00	1.00	0.01
III	1.13	0.53	1.34	0.04
IV	0.43	1.91	1.40	0.03
V	0.79	1.57	1.42	0.03

Even though a 5% RMSE was considered low, the systematic deviation observed consistently in the same direction across cell clusters (lower log phase slope for the computational model) suggests the influence of biological or biophysical mechanisms not considered in the model. Consistently, representing signal delay as function of cluster distance to capsule periphery showed that the computational delay is smaller than the experimental by approximately 10 min (Figure S4.A). Comparing the slope against cluster area showed that, with the exception of cluster II, there is an approximately constant deviation between the computational and experimental models (Figure S4.B).

The computational model was also tested without the saturation equation, Eq. (4). The sigmoidal profile observed experimentally cannot be replicated with any combination of the adjusted parameters, in this case D_{cell} and D_{medium} (Figure S4.4 and Table S4.1), meaning that a purely diffusive model is unable to explain the behavior observed in the experimental runs.

2.3. Implementation of a modular framework: tuned random distribution of TME elements inside the capsule

The framework used to create the capsules allows us to simulate several distinct but equivalent capsules, i.e. with the same number of cancer cell spheroids and fibroblasts, but with different distribution. It is based on a tunable stochastic algorithm, which mimics the observed experimental distributions. Along with the cancer cells and fibroblasts, we also included a representation for collagen fibers. Some examples of the versatility of this framework are shown in Figure S4.5.

This framework was tested *in silico* by creating two identical capsules, one with and one without collagen fibers (Figure 4.5A, scenarios i and ii respectively). The diffusivity coefficient for the collagen fiber was set as zero (total barrier), as it has been reported that this ECM component hinders antibody diffusion [7–9], while the remaining TME elements maintained the previously described diffusivity parameters (Figure 4.5B). Antibody concentration distributions were compared for both capsules for the second and last time frames (Figure 4.5C-D). For the capsule without fibers, the antibody diffuses radially and homogeneously to the interior of the capsule (Figure 4.5C-D, scenario i). When fibers are added, antibody distribution throughout the capsule is highly heterogeneous as fibers perpendicularly aligned to the diffusion direction retain the antibody (Figure 4.5C-D, scenario ii). This difference is also clear in the antibody concentration profiles for the three selected clusters in each scenario (Figure 4.5E). Cluster 1 is near the periphery and the antibody diffusion profile is very similar for both settings. Cluster 2 is in the internal portion of the capsule and is surrounded by fibers that impede diffusion, which

in turn virtually nullifies the antibody concentration. Finally, cluster 3 displays an intermediate situation, the antibody concentration profile in the presence of fibers follows a similar trend than in the absence of fibers but with lower total.

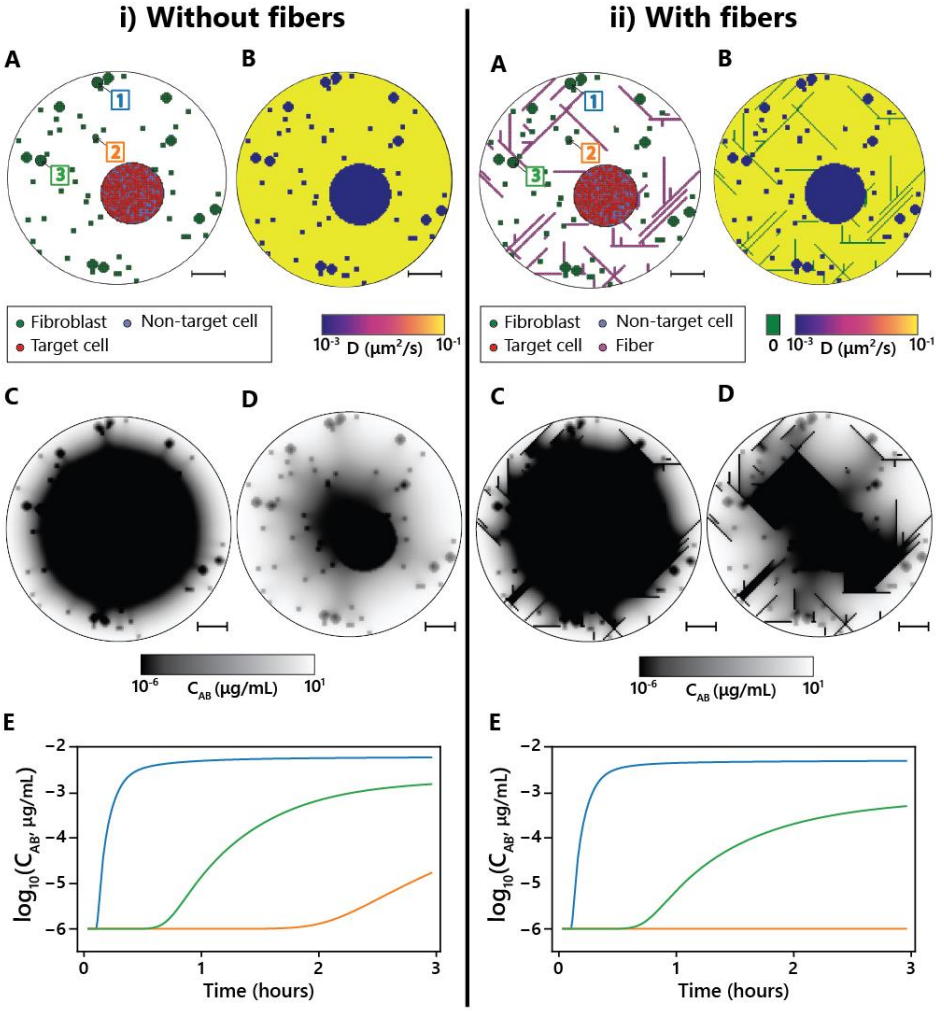

See caption in the next page.

Figure 4.5: Example of a tuned stochastic computational capsule with and without fibers. Simulation with D_{medium}=0.15 µm²/s, D_{cell}=0.0015 µm²/s, a=1, n=1, and p=1, for two scenarious: (i) without fibers and (ii) with fibers. **A)** Graphical representation of one random tuned capsule, with the indication of the selected clusters; **B)** Initial diffusivity coefficients throughtout the capsule; **C-D)** Antibody concentration for two different time points (30 and 180 minutes, respectively); **E)** Antibody concentration profile for the three cell clusters identified in A (blue – cluster 1, orange – cluster 2, green – cluster 3); scale bar: 100 µm.

3. Discussion

In the present work, we developed a computational model that reproduces *in silico* antibody transport within a 3D *in vitro* cancer model. The *in silico* model was trained with live tracking data of a fluorescent antibody, generated by LSFM. This microscopic technique allowed us to assess which cells within the alginate capsules, were binding to the antibody and to what extent. LSFM overcomes the limitations of classical fluorescent microscopy techniques, as it provides a good optical sectioning for volumetric rendering, being less aggressive to fluorophores and sample, reducing photo-bleaching and phototoxicity [24].

Experimental results show that the time delay until a detectable fluorescence intensity was attained for each cell cluster has a weak linear correlation with cell cluster distance to the capsule periphery. This hints at the capsule interior being an anisotropic medium with some degree of heterogeneity. Molecules secreted by the cells, such as collagens and glycosaminoglycans, cannot be detected under the microscope and cause antibody retention [7–9], being likely responsible by some of the observed gaps between the computational and experimental models. Additionally, it may be associated with heterogeneous antibody presentation, in particular because there are 2 cell types being analyzed together.

We assumed a purely diffusive mechanism of antibody transport, i.e. antibody transport is controlled exclusively by concentration gradients. Convection was considered negligible since no significant flow of culture medium was imposed on the experimental setup. The lack of significant flow implies a near zero Péclet number [29] and, therefore, corresponds to a diffusion-driven transport. However, convection could be incorporated in the model for different experimental conditions.

Kinetic equations for antibody binding described in the literature [30,31] require *a priori* knowledge of kinetic parameters, such as binding and dissociation constants. Because these values are not always available, we opted for a simpler approach, where a generic exponential equation was used to describe the saturation of binding sites as the antibody concentration increases and less antigens become available. Our simulated antibody distribution profiles showed that binding site saturation can be correctly represented using this approach. The saturation parameters *a*, *n* and *p* control the shape of the sigmoidal curve (Figure S4.6). Parameters *n* and *p* change the sigmoidal curve by controlling its slope. So, *n* and *p* can be biologically correlated with ease of antibody binding to the cell cluster. As *n* increases, a longer time is needed to observe any reduction in the diffusivity coefficient. As such, *n* can be correlated with the initial contact of the antibody to the cell cluster, when the antibody concentration is very small. Conversely, *p* controls the stages closer to saturation, when a much higher antibody concentration is present on the cell clusters. Parameter *a* controls mainly the time required to reach the plateau. Thus, *a* can be correlated with the amount of available binding sites on the cell cluster or with binding velocity. *Ergo*, cell clusters with

smaller *a* value require a higher antibody concentration to bind to all the available binding sites.

Computational model parameters were optimized to fit each selected cell cluster. This means that, for each fitted model, all clusters were given the same *a*, *n* and *p* parameters as the selected cluster. Following this procedure, we observed that different parameters fit different clusters. It was not possible to find a combination of *a*, *n* and *p* that provided a good fit (RMSE<5%) for all the cell clusters simultaneously. A modest but systematic deviation was observed in the simulated fluorescence profiles for all cell clusters, which suggests mechanisms that are not being considered are interfering with the antibody transport.

This framework can be used as a basis for future work, where further improvement can be attained by going from a 2D to a 3D *in silico* representation of the capsule. This will allow for a more relevant and realistic study of the antibody transport throughout the capsule.

4. Conclusions

We describe a computational model that reproduces antibody transport within an *in vitro* tumor microenvironment model, containing different cellular components. Moreover, we showed that the combination of 3D *in vitro* cell models and light sheet fluorescence microscopy enables the experimental assessment of therapeutic antibody distribution within the tumor microenvironment. Drug molecules with different properties (different sizes and charges), ranging from small molecules such as chemotherapeutic drugs, to larger molecules such as antibodies, can be studied using the same approach.

Ultimately, the combined experimental and computational framework can be employed not only to decipher how different elements within the TME can influence drug transport, but also, once that influence is understood, to work as a predictive tool. This would help reducing experimental burden and costs by performing a computational screening of specific conditions prior to experimental testing.

5. Methods

5.1. Experimental setup, data collection and processing

5.1.1. Cell lines and 2D cell culture

NCI-H157 (#CRL-5802; from now on referred as H157) Non-Small Cell Lung Carcinoma (NSCLC) cell line was obtained from American Type Culture Collection (ATCC). Human Dermal Fibroblasts (hDFs) isolated from human skin were obtained from Innoprot. Cells were cultured under 2D static conditions, maintained at 37 ºC in an incubator with humidified atmosphere containing 5% CO_2 and 21% of O_2.

Tumor cells were sub-cultured twice a week with a seeding density of 1×10^4 cell/cm^2 and maintained in Tumor Cell Culture Medium, composed of Dulbecco's Modified Eagle Medium (DMEM) supplemented with 1 mM sodium pyruvate (Life Technologies), 12 mM HEPES (Life Technologies) and 0.1 mM non-essential amino acids (Life Technologies). hDFs were split once a week, at a seeding density of 0.5×10^4 cell/cm^2 and cultured in Iscove's Modified Dulbecco's Medium (IMDM, Life Technologies) supplemented with 10% (v/v) fetal bovine serum (Gibco) and 100 U/mL penicillin-streptomycin (Gibco).

5.1.2. Cell microencapsulation and stirred suspension culture

H157 cell spheroids were generated in all-baffled spinner-flasks with a straight blade paddle impeller (Corning Life Sciences), according to the aggregation protocol previously established in-house [32]. Spheroids were collected 3 days after spinner inoculation for the establishment of co-cultures, as described previously [22]. Briefly, 2×10^4 spheroids were mixed with a single cell suspension of hDFs and the mixture was dispersed in 1.1% (w/v) of Ultrapure Ca^{2+} MVG alginate (UP MVG NovaMatrix, Pronova Biomedical), dissolved in 0.9% (w/v) NaCl solution [22,23]. Microencapsulation was performed using an electrostatic bead generator (Nisco Encapsulator) with an air flow rate of 10 mL/h, at 5.3 V with air pressure of 1 bar, to generate capsules of approximately 700 μm; alginate droplets were cross-linked in a 20 mM $BaCl_2$ bath. Encapsulated co-cultures were cultured for 2 weeks under agitation (shake flasks, 80 rpm), with medium exchange twice a week (half of the volume replaced by fresh Tumor Cell Culture Medium).

5.1.3. Light sheet fluorescence microscopy setup

All the images were acquired with a custom-made LSFM system, an improved version of the SPIM-fluid system [33]. The illumination path consists in three CW lasers with excitation wavelengths of 488, 561 and 637 nm (Cobolt; MLD 50 mW, DPL 100 mW and MLD 150 mW, respectively). Laser beams are expanded using a telescope system, composed of two achromatic doublets (Thorlabs, AC254-050-A-ML (f = 50 mm) and AC254-200-A-ML (f = 200 mm)), creating a flat top Gaussian beam profile. The light sheet is created by a pair of galvanometric mirrors (Thorlabs,

GVSM002), which pivoting planes are properly conjugated with the back focal aperture of the objective lens (Nikon, 4x PlanFluor NA 0.13). Double side illumination is achieved by duplicating these elements and adding a 50/50 beamsplitter cube (Thorlabs, CCM1-BS013). A relay lens set, with two achromatic lenses (Thorlabs, AC254-075-A-ML (f = 75 mm)) is used as a bridge, so optical planes are properly conjugated in the right arm. In the detection path, a water dipping objective (Nikon 10x 0.3) is used to collect the generated fluorescence from the top of the incubation chamber, as in an up-right microscope configuration. An achromatic doublet with focal distance of 200 mm (AC254-200-A-ML) is used to form the image onto the sCMOS camera chip (Hamamatsu Orca Flash4.0). Different emissions are selected using a motorized filter wheel (Thorlabs, FW102C), equipped with three filters (Chroma and Semrock: 520/15 (GFP), 590/50, 638LP (Cell tracker deep red)). The scanning of the sample is performed by translation of the whole physiological chamber with a motor (PI M-501.1DG) through a fixed horizontal light sheet plane (Figure S4.7). The Flexi-SPIM microscope features a custom developed software based on LabVIEW (National Instruments). This software allows the user to access settings of the various devices on a single graphical user interface. An Arduino UNO board, connected via USB to the workstation, is integrated in the LabVIEW software providing control of the shutters, bright-field illumination and sample rotation. The custom-made LSFM allows for different possibilities for the sample mounting. In order to provide flexible, fast and easy-to-use sample loading capabilities, an imaging chamber was designed and 3D printed using fluorinated ethylene propylene (FEP). FEP presents a refractive index similar to water (1.33) and is

CO_2 permeable. So, it allows for live imaging on specimens using water-dipping objectives. Prior to imaging acquisition, samples were loaded into FEP tubes and transported towards the detection objective field of view using a programmable syringe pump (Tecan, Cavro Centris). Once here, the two motors can rotate the sample, in order to choose the view of interest. This mounting system offers the possibility to easily insert, aspirate and discard the specimens without the need of agarose, enabling the possibility for high-throughput studies with relatively big samples (up to 1 mm diameter).

5.1.4. Antibody challenge, image acquisition and processing

The fluorescent antibody (anti-CD44 Monoclonal Antibody (IM7), PE, eBioscience) was diluted in Tumor Cell Culture Medium, to a final concentration of 13 µg/mL, close to the range of therapeutic antibody concentration found in patient serum [34,35].

Individual capsules were harvested from culture and loaded into the microscope tube in order to obtain a control image of the intrinsic autofluorescence and to assess general capsule features (in the bright-field). The capsule was then removed from the FEP tube, immersed in the antibody solution and reloaded in the microscope. Fluorescence was acquired in the 561 nm laser line. A 3D stack of the capsule containing 235 planes separated by 3 µm, covering 705 µm, was acquired every 2 minutes. Acquisition was performed over a total of 3 h.

The fluorescence intensity profiles for selected cell clusters (Figure 1-2) were obtained from the central plane of the capsule. Each cluster was marked using a ROI defined by a circular domain.

The fluorescence intensity over time was integrated and converted to a profile. All image processing was performed using Image J (Rasband, W.S., ImageJ, U. S. National Institutes of Health, Bethesda, Maryland, USA, https://imagej.nih.gov/ij/, 1997-2018). Further details on image processing are described in the Supplementary Materials and Methods.

To smooth the experimental data noise, the five cluster profiles were fitted to growth curve models [25] and the model type showing the best fit (highest R^2) was selected. For comparison between the profiles of the selected clusters, the delay time and the slope of log phase of the curve were calculated. The first of these parameters can be seen as a measurement of the time required for the antibody to reach that cell cluster in sufficient concentration to be detected. It was calculated as the time interval from the beginning of the experiment until the mean fluorescence value became larger than 5% of the total achieved fluorescence for that selected cluster. The slope of the log phase was obtained by calculating the slope of a linear fit, adjusted for this phase alone. For consistency, we assumed log phase of the curve to correspond to the portion of the model that takes place when the measured value (i.e. fluorescence and antibody concentration) corresponds to 15% to 85% of its maximum observed value.

5.2. Antibody diffusion model within the alginate capsule

Antibody transport within the alginate capsule was assumed to be purely diffusional. In fact, assuming the capsule is immersed in a static fluid, no relevant convective transport is expected to occur [36]. This diffusive behavior is modelled by Fick's second law, which in bidimensional space is defined by

$$\frac{\partial C}{\partial t} = D\left(\frac{\partial^2 C}{\partial x^2} + \frac{\partial^2 C}{\partial y^2}\right) \quad (3)$$

in which D is the diffusion coefficient (D_{medium} for the medium and D_{cell} for the cells), C is the concentration of the antibody, t is the time, and x and y are the Cartesian coordinates.

Cells detain a limited number of antigens where antibodies can bind. So, as the antibody binds, the number of available binding sites on the cell surface is reduced until reaching saturation, in which all or the vast majority of the binding sites are bound to an antibody molecule. This biological effect can be translated in terms of variation of diffusivity of the antibody in the cells and was assumed to follow an exponential saturation curve described by

$$D_{cell}^{t+\Delta t} = D_{cell}^{t} \times \exp\left(-a \times \frac{{C_{norm}}^{n}}{(1-C_{norm})^{p}}\right) \quad (4)$$

in which a, n and p are adjustable parameters, D_{cell} is the diffusivity coefficient in the cells and C_{norm} is a normalized concentration. The latter takes into account the fact that the concentration at which the cells get saturated is much smaller than the antibody concentration in the medium and is given by

$$C_{norm} = \frac{C_{i,j}^{t}}{C_{inj} \times 0.01} \quad (5)$$

in which C_{inj} is the antibody concentration of injection and $C^{t}_{i,j}$ is the concentration of antibody in a cell localized in the position i,j.

The model proposed here works under the following assumptions: (i) no significant antibody degradation occurs; (ii) the initial antibody concentration inside the capsule is zero; (iii) cell growth and death are not relevant; (iv) cell movement is neglected; (v) ECM formation, degradation or re-structure is negligible within the time interval of the experiment; (vi) initial D_{cell} was set as being

100 smaller than initial D_{medium} for all cells (single cells, cancer cell spheroids and fibroblasts) and (vi) D_{medium} is constant over time and through the extracellular space inside the capsule.

Additionally, we also consider that antibody diffusivity within the spheroid varied with the spheroid radius according with

$$D_{cell}^{d}=D_{cell}^{max}\times\left(\frac{d}{r_{sph}}\right) \quad (6)$$

in which D_{cell}^{d} is the diffusivity coefficient of a cell in the spheroid whose distance to the cancer spheroid center is d, D_{cell}^{max} is the diffusivity coefficient of the cells located in the outer layer of the spheroid and r_{sph} is the spheroid radius.

5.3. Computational model fitting and simulation

5.3.1. Definition of the initial setup: capsule domain

The computational model and all simulations were implemented and run in Python (version 3.7). To numerically solve Fick's second law in Eq. (3), the finite differences method was applied. This method to solve differential equations requires a discretized domain. So, a two-dimensional square grid (mesh) with 200×200 equally spaced nodes and a 1000 μm side was created. Method convergence was evaluated as described in Supplementary Materials and Methods section and Figure S4.8. Each element (node) was assigned a range of intrinsic attributes (coordinates: x and y; type: cancer cell, fibroblast or ECM; diffusivity; and concentration). This grid is further split between two major domains: a central circular domain, representing the alginate capsule (centered in the mesh and with a radius of 350 μm) and its surrounding medium, representing the culture medium outside the alginate capsule. For the definition of nodes within the alginate

capsule two alternative approaches were performed: one based on capsule digitization and another one based on tuned random distribution of TME elements (Figure 4.6A and B, respectively).

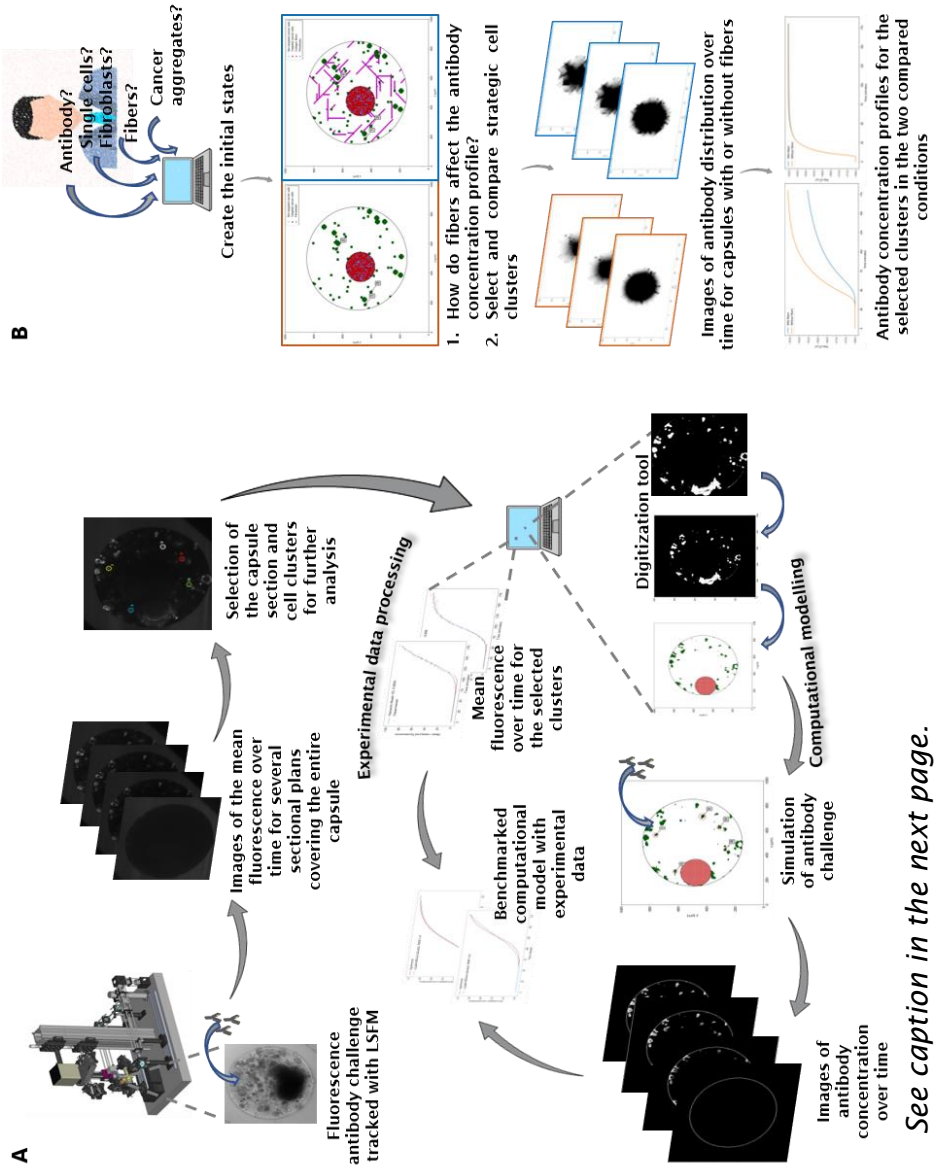

See caption in the next page.

Figure 4.6: Experimental and computational workflow. **A)** Methodology applied in the digitized capsule approach (LSFM: light sheet fluorescence microscopy). **B)** Methodology applied in the tunable stochastic approach on an example.

5.3.2. Capsule digitization from experimental capsule images

Digitization of the capsule allowed to reproduce the experimental capsule *in silico*, with cancer cell spheroids and fibroblasts localized in the same positions. Based on the last frame of the experimental antibody diffusion video for a specific capsule slice (Additional file 2), Python Imaging Library (PIL) was used to convert the figure into a binary input (Figure 4.6A). The cancer cell spheroid was added manually, according with the contrast phase images acquired experimentally.

5.3.3. Tunable random distribution of TME elements

A stochastic framework, in which the TME elements are randomly distributed inside the capsule was also implemented. This process is tunable by the user who can set the total number of each TME element to include in the capsule (Figure 4.6A). From images of several capsules, two circular regions of cell distribution can be identified inside the capsule. So, first, the capsule domain was divided in two rings, with the inner ring corresponding to 80% of total radius. Cancer cell spheroids were defined as circular entities with a selected radius, whose localization can be set by the user or randomly. Since antibody cell targets might not be present in all cells, targeted and non-targeted cells can be considered in the model. The pre-defined number of cancer cells and fibroblasts (as single cells or small clusters) were randomly distributed with a preference towards the outer ring, as the experimental results

showed they were more prevalent in this area. Fibroblast average radius was assumed to be 11.5 μm as single cells [37] or 17.5 μm in the cluster form (measured from the experimental images). Collagen fibers can also be included and randomly distributed within the capsule domain. These fibers were assumed to have 30 μm length [38], to have 4 possible orientations (0, 45, 90, 135º) and zero diffusivity. The overall process of model development is schematized in the workflow in Figure S4.9 and Figure 4.6.

5.3.4. Benchmark of the computational model with experimental data

Experimental fluorescence profiles and computational antibody concentration profiles were normalized so as to vary between 0 and 1 and thus allow their comparison (Figure 4.6A). The benchmarking of the computational model by the experimental data was performed by implementing the Broyden-Fletcher-Goldfarb-Shanno (BFGS) optimization algorithm to find the saturation parameters *a, n* and *p* of Eq. (4) which minimize the root mean square error (RMSE) for a set of selected cell clusters. The RMSE between the experimental and computational normalized profiles is given by

$$\text{RMSE}=\sqrt{\sum_{i=1}^{n}\frac{\left(\hat{y}_i-y_i\right)^2}{n}} \qquad (7)$$

in which n is the number of points in which computational and experimental values are compared, $\hat{y}_i$ is the predicted value from the computational model and y_i is the observed values in the experiments.

All cells were assumed to be target cells of the antibody, since CD44 is detected in both hDFs [39] and H157 cells [40].

5.3.5. Boundary conditions

The capsule external domain was defined as having a fixed antibody concentration of 13 μg/mL, as in the experimental setup. We assume that, for the modelled timeframe, the depletion of the medium is not significant since the volume of antibody solution is two orders of magnitude higher than the capsule volume.

6. List of abbreviations

BFGS: Broyden-Fletcher-Goldfarb-Shanno; ECM: extracellular matrix; FEP: fluorinated ethylene propylene; GAG: glycosaminoglycan; hDFs: Human Dermal Fibroblasts; LSFM: light sheet fluorescence microscopy; NSCLC: Non-Small Cell Lung Carcinoma; PIL: Python Imaging Library; RMSE: root mean square error; TME: tumor microenvironment

7. Declarations

Ethics approval and consent to participate

Not applicable.

Consent for publication

Not applicable.

Availability of data and materials

The dataset supporting the conclusions of this article is included within the article and its additional files.

Competing interests

The authors declare that they have no competing interests.

8. Funding

We acknowledge funding sources: Fundação para a Ciência e Tecnologia (FCT) for the PhD fellowship PD/BD/114047/2015; iNOVA4Health (UIDB/04462/2020), a program financially supported by FCT/Portuguese Ministry for Science, Technology and Higher Education, through national funds and co-funded by FEDER under the PT2020 Partnership Agreement; the Spanish Ministry of Economy and Competitiveness through the "Severo Ochoa" program for Centres of Excellence in R&D (SEV-2015-0522) and Ramon y Cajal program (RYC-2015-1793); Fundació Privada Cellex; Fundació Mir-Puig; Generalitat de Catalunya through the CERCA program; European Commission Horizon 2020 LASER LAB Europe (grant agreement 654148).

9. Authors' contributions

ALC, CB and II conceptualized the study. ALC, CB and EJG designed the experimental work. ALC performed the cell culture procedures. ALC, EJC and MM conducted the imaging experiments. ALC, JA and II designed and developed the computational work. ALC, CB and II wrote the manuscript. All authors revised the manuscript. All authors read and approved the final manuscript.

10. Acknowledgements

The author acknowledges Dr Adolfo V. T. Cartaxo for both mathematics and biophysics discussions during all the steps of the development of the computational model. The author would like to

acknowledge also Dr Manuel N. Melo for the help on the implementation of the BFGS tool.

11. References

1. Corraliza-Gorjón, I., Somovilla-Crespo, B., Santamaria, S., Garcia-Sanz, J. A. & Kremer, L. New strategies using antibody combinations to increase cancer treatment effectiveness. *Front. Immunol.* **8**, (2017).
2. Dalziel, M., Beers, S. A., Cragg, M. S. & Crispin, M. Through the barricades: Overcoming the barriers to effective antibody-based cancer therapeutics. *Glycobiology* **28**, 697–712 (2018).
3. Nizzero, S., Ziemys, A. & Ferrari, M. Transport barriers and oncophysics in cancer treatment. *Trends in Cancer* **4**, 277–280 (2018).
4. Rosenblum, D., Joshi, N., Tao, W., Karp, J. M. & Peer, D. Progress and challenges towards targeted delivery of cancer therapeutics. *Nat. Commun.* **9**, (2018).
5. Jain, R. K. Physiological barriers to delivery of monoclonal antibodies and other macromolecules in tumors. *Cancer Res.* **50**, (1990).
6. Fuso Nerini, I. *et al.* Intratumor heterogeneity and its impact on drug distribution and sensitivity. *Clin. Pharmacol. Ther.* **96**, 224–238 (2014).
7. Kihara, T., Ito, J. & Miyake, J. Measurement of biomolecular diffusion in extracellular matrix condensed by fibroblasts using fluorescence correlation spectroscopy. *PLoS One* **8**, e82382 (2013).
8. Netti, P. A., Berk, D. A., Swartz, M. A., Grodzinsky, A. J. & Jain, R. K. Role of extracellular matrix assembly in interstitial transport in solid tumors. *Cancer Res.* **60**, 2497–2503 (2000).
9. Davies, C. de L., Berk, D., Pluen, A. & Jain, R. Comparison of IgG diffusion and extracellular matrix composition in rhabdomyosarcomas grown in mice versus in vitro as spheroids reveals the role of host stromal cells. *Br. J. Cancer* **86**, 1639–1644 (2002).
10. Xie, H. *et al.* Modeling three-dimensional invasive solid tumor growth in heterogeneous microenvironment under chemotherapy. *PLoS One* **13**, 1–26 (2018).
11. Denisona, T. A. & Bae, Y. H. Tumor heterogeneity and its implication to drug delivery. *J Control Release* **164**, 187–191 (2012).
12. Karolak, A. & Rejniak, K. A. Micropharmacology: An In silico approach for assessing drug efficacy within a tumor tissue. *Bull. Math. Biol.* **81**, 3623–3641 (2018).
13. Karolak, A. *et al.* Targeting ligand specificity linked to tumor tissue topological heterogeneity via single-cell micro-pharmacological modeling. *Sci. Rep.* **8**, 1–14 (2018).
14. Van De Ven, A. L. *et al.* Integrated intravital microscopy and mathematical modeling to optimize nanotherapeutics delivery to tumors. *AIP Adv.* **2**, 1–13 (2012).
15. Rejniak, K. A. *et al.* The role of tumor tissue architecture in treatment penetration and efficacy: an integrative study. *Front. Oncol.* **3**, 1–13 (2013).
16. Groh, C. M. *et al.* Mathematical and computational models of drug transport in tumours. *J. R. Soc. Interface* **11**, (2014).
17. Minchinton, A. I. & Tannock, I. F. Drug penetration in solid tumours. *Nat.*

Rev. Cancer **6**, 583–592 (2006).
18. Erlanson, M., Daniel-Szolgay, E. & Carlsson, J. Relations between the penetration, binding and average concentration of cytostatic drugs in human tumour spheroids. *Cancer Chemother. Pharmacol.* **29**, 343–353 (1992).
19. Sutherland, R., Buchegger, F., Schreyer, M., Vacca, A. & Mach, J. P. Penetration and binding of radiolabeled anti-carcinoembryonic antigen monoclonal antibodies andtheir antigen binding fragments in human colon multicellular tumor spheroids. *Cancer Res.* **47**, 1627–1633 (1987).
20. Lee, C. M. & Tannock, I. F. The distribution of the therapeutic monoclonal antibodies cetuximab and trastuzumab within solid tumors. *BMC Cancer* **10**, (2010).
21. Fischer, R. S., Wu, Y., Kanchanawong, P., Shroff, H. & Waterman, C. M. Microscopy in 3D: A biologist's toolbox. *Trends Cell Biol.* **21**, 682–691 (2011).
22. Rebelo, S. P. *et al.* 3D-3-culture: A tool to unveil macrophage plasticity in the tumour microenvironment. *Biomaterials* **163**, 185–197 (2018).
23. Estrada, M. F. *et al.* Modelling the tumour microenvironment in long-term microencapsulated 3D co-cultures recapitulates phenotypic features of disease progression. *Biomaterials* **78**, 50–61 (2016).
24. Olarte, O. E., Andilla, J., Gualda, E. J. & Loza-Alvarez, P. Light-sheet microscopy: a tutorial. *Adv. Opt. Photonics* **10**, 111–179 (2018).
25. Tabatabai, M., Williams, D. K. & Bursac, Z. Hyperbolastic growth models: Theory and application. *Theor. Biol. Med. Model.* **2**, 1–13 (2005).
26. Gerlowski, L. E. & Jain, R. K. Microvascular permeability of normal and neoplastic tissues. *Microvasc. Res.* **31**, 288–305 (1986).
27. Clauss, M. A. & Jain, R. K. Interstitial transport of rabbit andsheep antibodies in normal and neoplastic tissues. *Cancer Res.* **50**, 3487–3492 (1990).
28. Brown, E. B., Boucher, Y., Nasser, S. & Jain, R. K. Measurement of macromolecular diffusion coefficients in human tumors. *Microvasc. Res.* **67**, 231–236 (2004).
29. Jenkins, W. J. Tracers of Ocean Mixing. *Treatise on Geochemistry* **6.08**, 223–246 (2003).
30. Guo, H. *et al.* Kinetic analysis of a high-affinity antibody/antigen interaction performed by planar waveguide fluorescence immunosensor. *RSC Adv.* **6**, 13837–13845 (2016).
31. Rhoden, J. J., Dyas, G. L. & Wroblewski, V. J. A modeling and experimental investigation of the effects of antigen density, binding affinity, and antigen expression ratio on bispecific antibody binding to cell surface targets. *J. Biol. Chem.* **291**, 11337–11347 (2016).
32. Santo, V. E. *et al.* Adaptable stirred-tank culture strategies for large scale production of multicellular spheroid-based tumor cell models. *J. Biotechnol.* **221**, 118–129 (2016).
33. Gualda, E. J. *et al.* SPIM-fluid: open source light-sheet based platform for high-throughput imaging. *Biomed. Opt. Express* **6**, 4447 (2015).
34. Quartino, A. L. *et al.* Population pharmacokinetic and exposure-response analysis for trastuzumab administered using a subcutaneous 'manual syringe' injection or intravenously in women with HER2-positive early breast cancer. *Cancer Chemother. Pharmacol.* **77**, 77–88 (2016).
35. Luo, Y. *et al.* Pharmacokinetics of pertuzumab administered concurrently with trastuzumab in Chinese patients with HER2-positive early breast cancer. *Anticancer. Drugs* **30**, 866–872 (2019).

36. Dewhirst, M. W., Secomb, T. W. & Carolina, N. Transport of drugs from blood vessels to tumour tissue. *Nat. Rev. Cancer* **17**, 738–750 (2019).
37. Zenuni, A., Zhang, C., Haeni, L., Rothen-Rutishauser, B. & Scheffold, F. Structure and Sedimentation Kinetics of Dense Suspensions of Fibroblast Cells. *Chim. Int. J. Chem.* **73**, 43–46 (2019).
38. Han, W. *et al.* Oriented collagen fibers direct tumor cell intravasation. *Proc. Natl. Acad. Sci. U. S. A.* **113**, 11208–11213 (2016).
39. Croce, M. A., Boraldi, F., Quaglino, D., Tiozzo, R. & Pasquali-Ronchetti, I. Hyaluronan uptake by adult human skin fibroblasts in vitro. *Eur. J. Histochem.* **47**, 63–73 (2003).
40. Penno, M. B. *et al.* Expression of CD44 in Human Lung Tumors. *Cancer Res.* **54**, 1381–1387 (1994).

12. Supplementary information

Table S4.1: Fitted D_{cell} and D_{medium} by application of the BFGS algorithm, assuming a purely diffusive mechanism without cell saturation.

Cell cluster	D_{medium} (μm²/s)	D_{cell} (μm²/s)	RMSE
I	0.164	0.126	0.06
II	0.659	0.110	0.09
III	0.712	0.156	0.11
IV	0.151	0.103	0.04
V	0.210	0.166	0.06

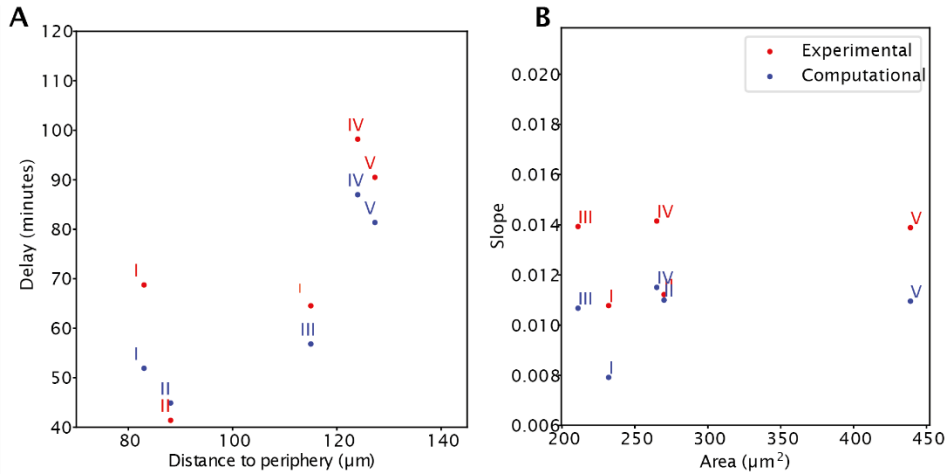

Figure S4.1: Comparison of profile features (delay time and slope) with cell cluster features (distance to capsule periphery and section area) obtained experimentally and for the computational model. **A)** Experimental delay vs distance to periphery. **B)** Slope of log phase of the curve vs area of the cell cluster.

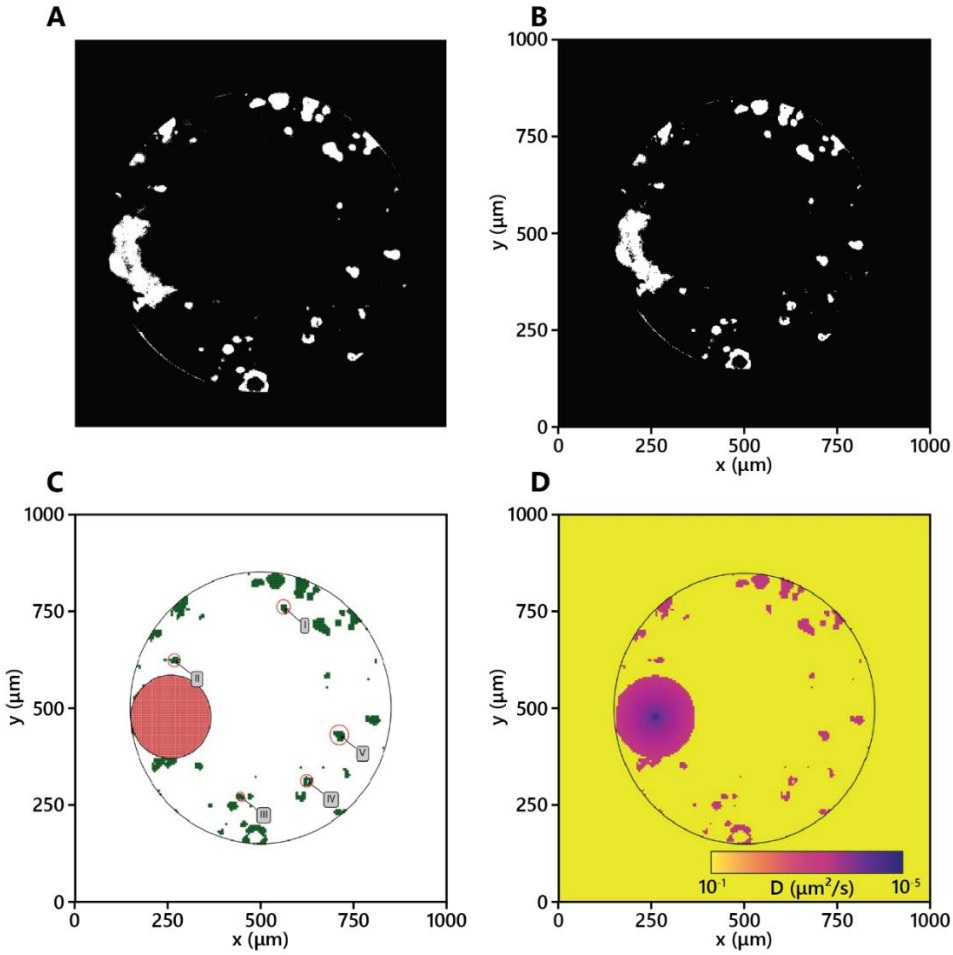

Figure S4.2: Definition of the initial setup by application of Python Imaging Library (PIL) tool. **A)** Read-out from Fiji of the last frame for the selected capsule section; **B)** digitized capsule obtained by application of PIL tool to A); **C)** component distribution and aggregate placement in accordance with B) and identification of the selected cell clusters equivalent to the experimental capsule section (Figure 2A); **D)** Diffusivity coefficient distribution within the capsule in the computational model for the digitized capsule.

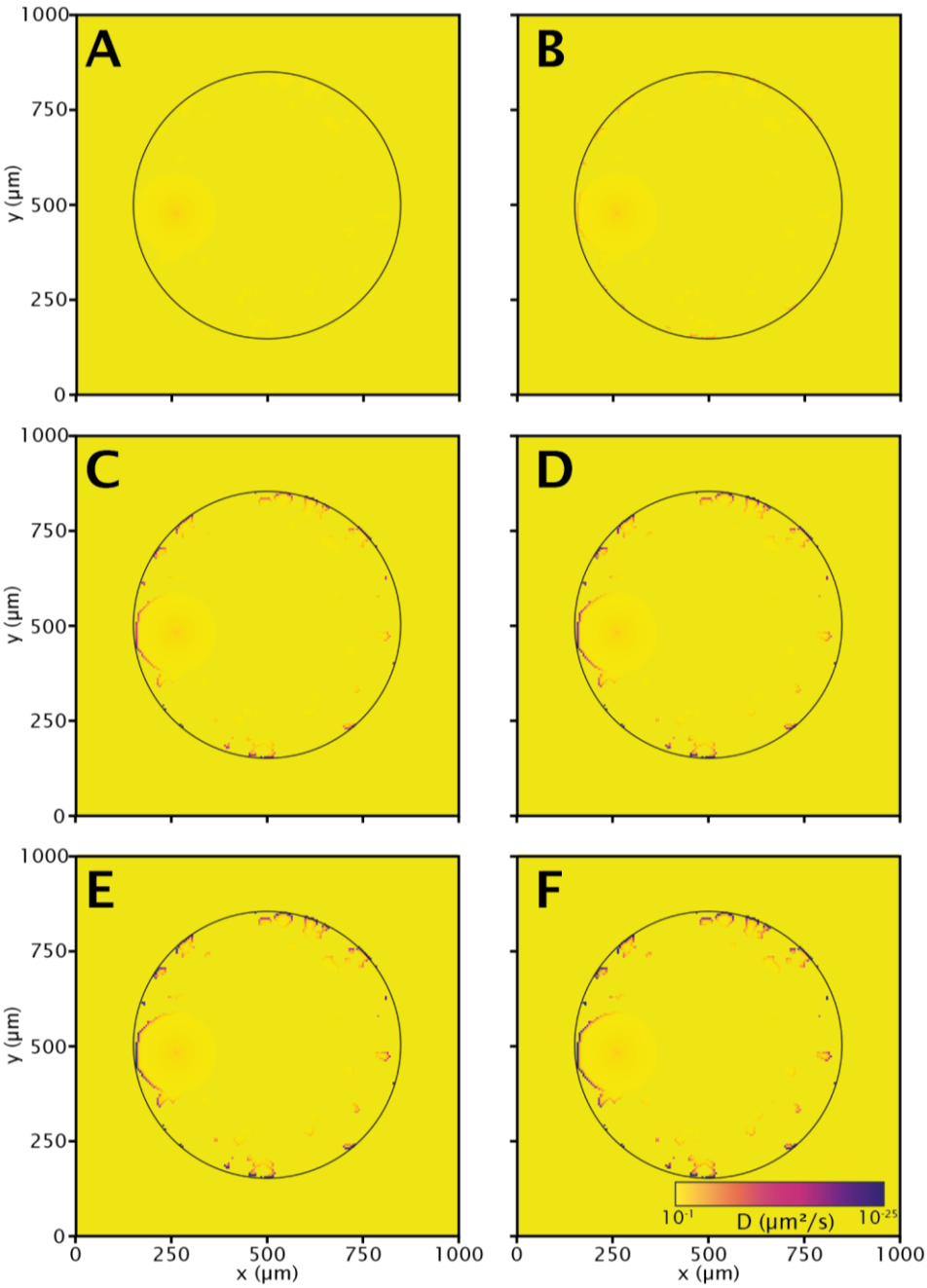

Figure S4.3: Diffusivity coefficient on the computational model over time, for the digitized capsule. Computational model was run for a=1, n=1, p=1: **A)** 0 min; **B)** 30 min; **C)** 90 min; **D)** 120 min; **E)** 150 min; **F)** 180 min.

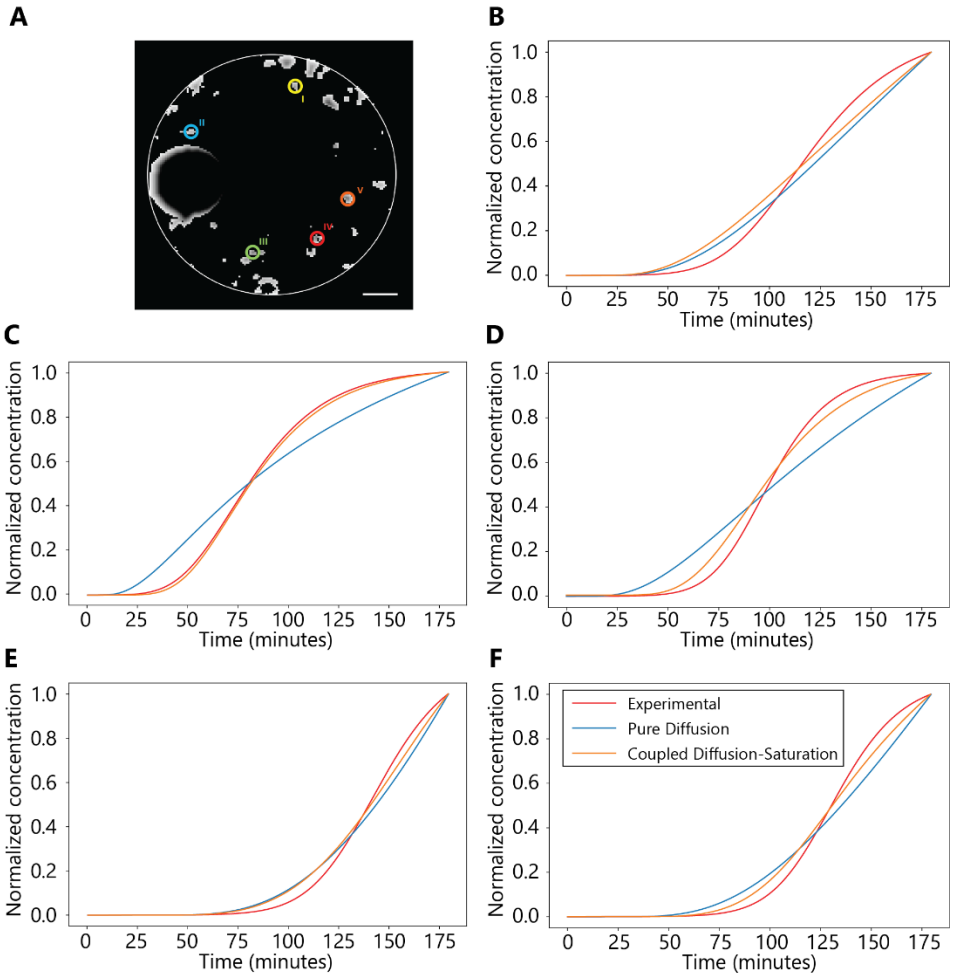

Figure S4.4: Comparison of best fittings obtained considering only Fick's law (blue curve) or Fick's law combined with exponential saturation (orange curve) to the experimental data (red curve).

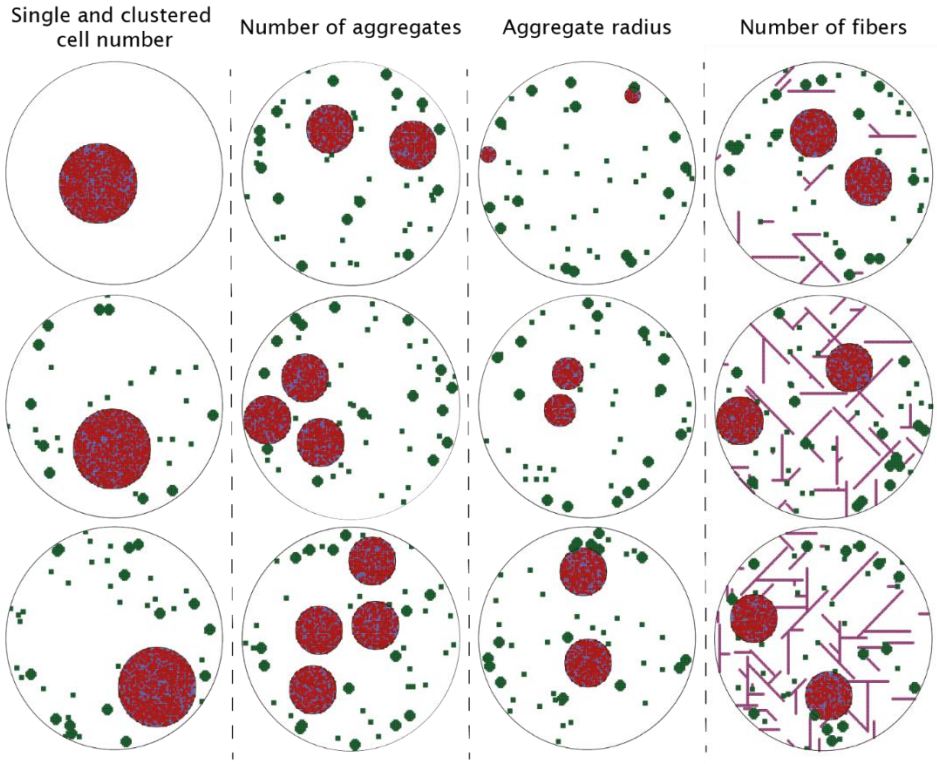

Figure S4.5: Tunable stochastic computational model examples. A modular tuned stochastic computational framework was developed and its versatility allows the user to set a defined amount of cancer cells aggregates and fibroblasts as single cells or clusters and also collagen fibers. First column shows models with varying amount of single and small clustered cells. Second column shows capsules with different number of aggregates. The third column shows variation in cancer aggregate radius. The fourth column shows the inclusion of several quantities of collagen fibers.

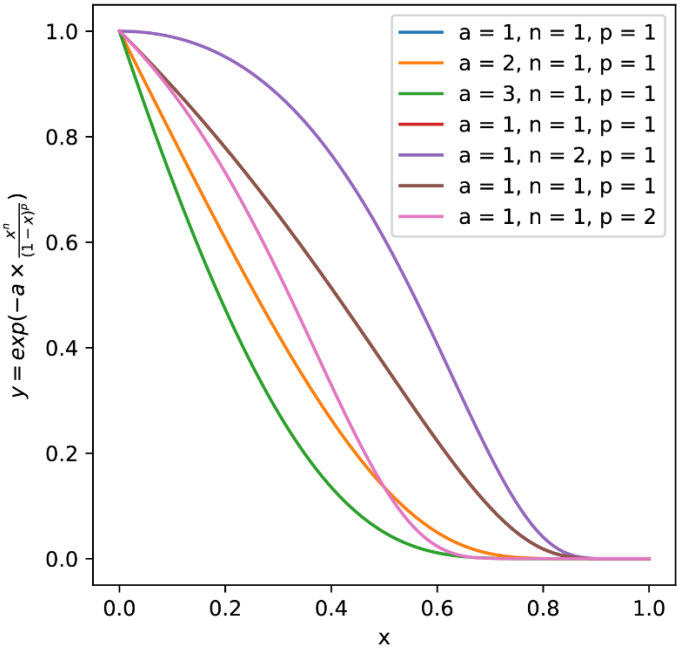

Figure S4.6: Exponential saturation equation for several different inputs.

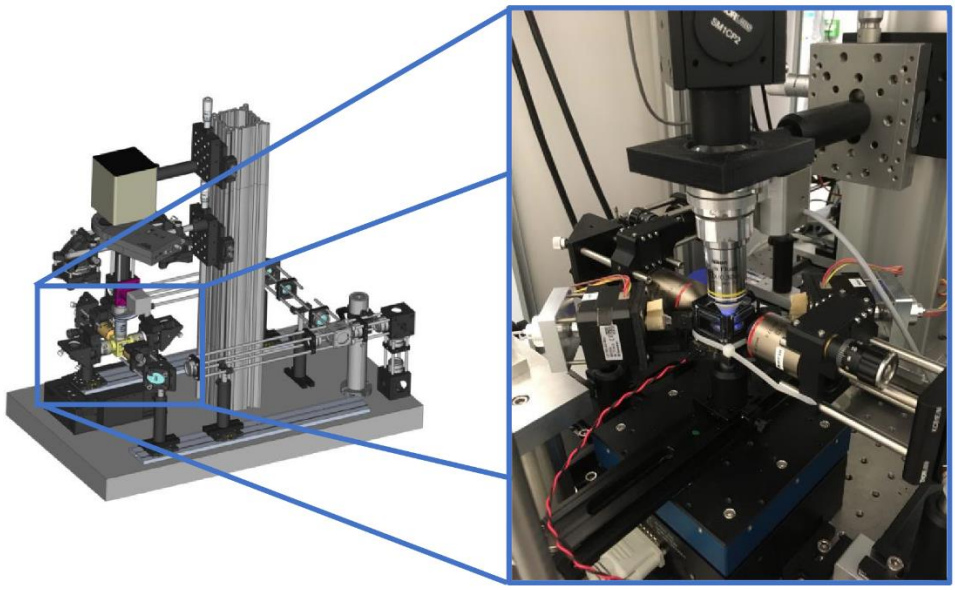

Figure S4.7: Schematic representation of the LSFM acquisition portion with a photography showing a zoom on the FEP chamber. Lasers illuminate the sample (loaded on a TEP tube) from two directions. The acquisition camera is located 90° in relation with the lasers plan.

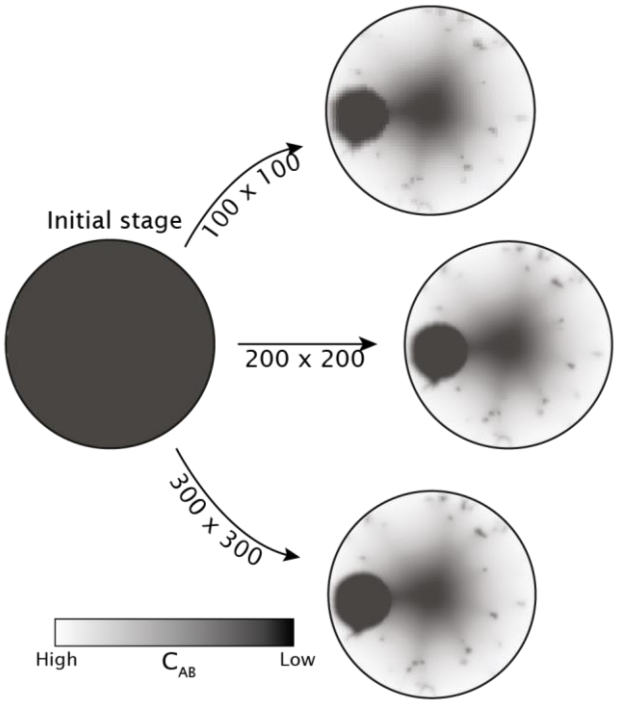

Figure S4.8: Mesh convergence study: 100x100, 200x200 and 300x300. Initial and final time-points for the model run with the specific mesh size.

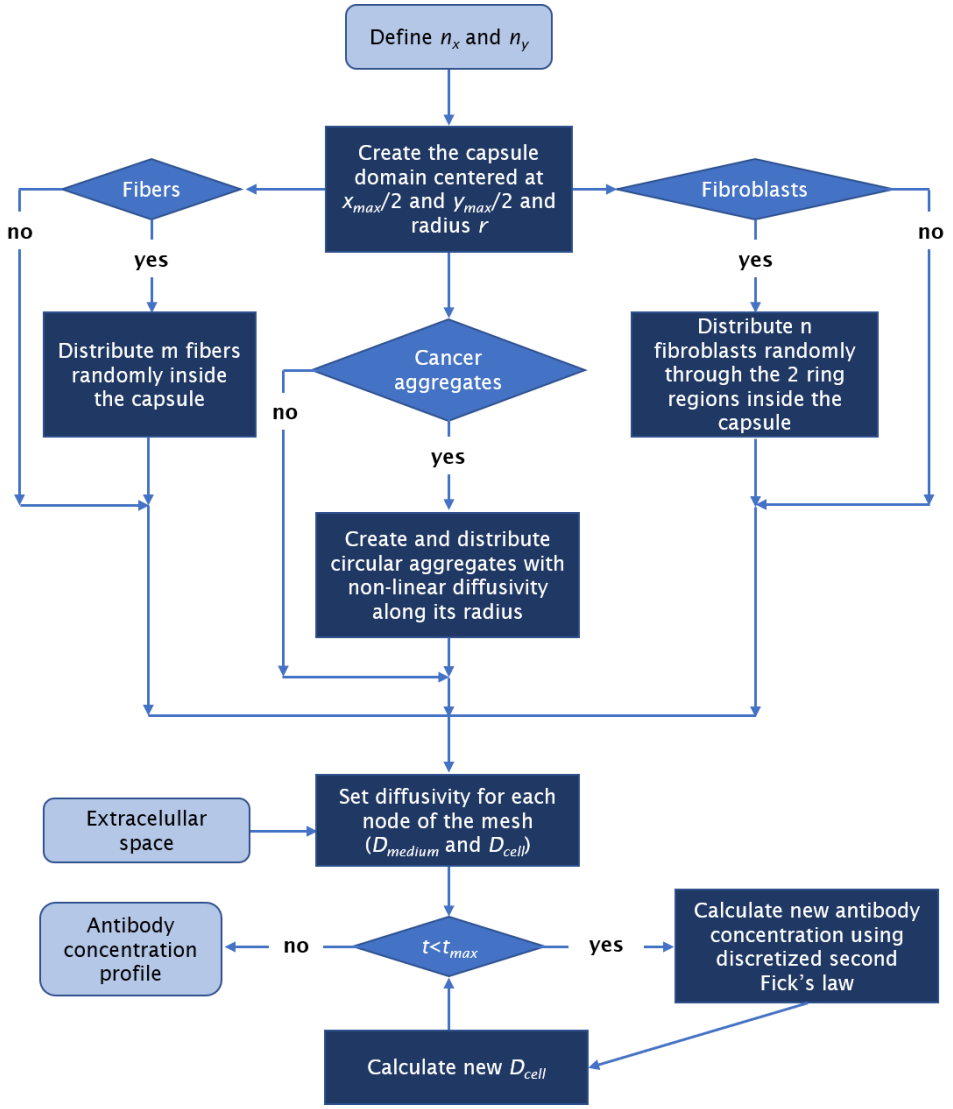

Figure S4.9: A flow diagram of the tunable stochastic computational framework. The model starts by defining the mesh and creation of the domain. Then, verifies if fibroblasts, cancer aggregates and fibers are to be included in the model. Then, the remaining free space in the mesh is defined as the extracellular space and the diffusivity for all the parts of the system is set. Then, it calculates the concentration of the antibody in each node of the mesh by using the discretised second Fick's law. With these new values, it calculates the new cell diffusivity coefficients. This process runs iteratively until reaching the maximum time, in which it closes the cycle and creates the antibody concentration profiles.

Supplementary Materials and Methods

S1. Image processing procedure

All image processing was performed using Fiji, ImageJ software (Rasband, W.S., ImageJ, U. S. National Institutes of Health, Bethesda, Maryland, USA, https://imagej.nih.gov/ij/, 1997-2018). Data collected from LSFM experiments were sets of sequential images of the fluorescence of several sections of each alginate capsule over time. For further analysis, only one capsule section corresponding to middle plan was selected. First, we selected regions of interest (ROI) corresponding to the areas where cluster of cells were identified. The image was converted to *8-bit*, a threshold mask was applied and the image was transformed into binary. The diffusion profiles (mean grey values over time) were obtained using the Z-axis profiler plugin. Five representative cell clusters of one capsule were selected for this analysis.

S2. Method convergence with varying mesh size

A method convergence study was performed choose the mesh size. Different mesh sizes were tested to assess if the obtained antibody concentration profiles were not significantly affected by increasing the mesh step. The step process was the following: 1) create a mesh using the fewest, reasonable number of elements and analyze the antibody concentration profile inside the capsule; 2) recreate the mesh with a denser element distribution, and compare the new obtained antibody concentration profiles to those obtained with the previous mesh. If the final antibody distribution throughout the capsule is equivalent in the tested conditions, then the mesh size selected for the study was thin enough to give accurate results. In this study, we

compared meshes with size (number of nodes in x and y) of 100x100, 200x200 and 300x300, maintaining the 1000 μm side (Figure S8).

13. Additional files

All additional files can be found in:

https://osf.io/yd5vu/?view_only=93e411b15dba44249811d82d74d9162a

Additional file 1: Video of the LSFM maximum intensity projection for all acquired frames, corresponding to 3h (AVI, 6044 kb)

Additional file 2: Video of the LSFM selected capsule central plane, corresponding to 3h (AVI, 4865 kb)

Additional file 3: Video of the simulated antibody concentration over the 3 h time interval (MP4, 483 kb)

Additional file 4: Video of the evolution of simulated diffusion coefficients over time throughout the capsule (MP4, 486 kb)

CHAPTER V

Discussion and perspectives

Table of contents

1. Discussion

Cancer is the second leading cause of mortality worldwide, despite the extraordinary advances in the last two decades due to the development of targeted therapies. These therapies target specific molecules required for cell growth and tumorigenesis; nonetheless, resistance often leads to patient relapse and disease progression. This resistance can be partially explained by the crosstalk and modulation by the several tumor microenvironment (TME) cellular and non-cellular elements. To study this intricate network, cancer models incorporating TME features have been proposed.

This thesis aimed to establish and characterize *ex vivo*, *in vitro* and *in silico* TME models, as tools to study cancer targeted therapies (Figure 5.1).

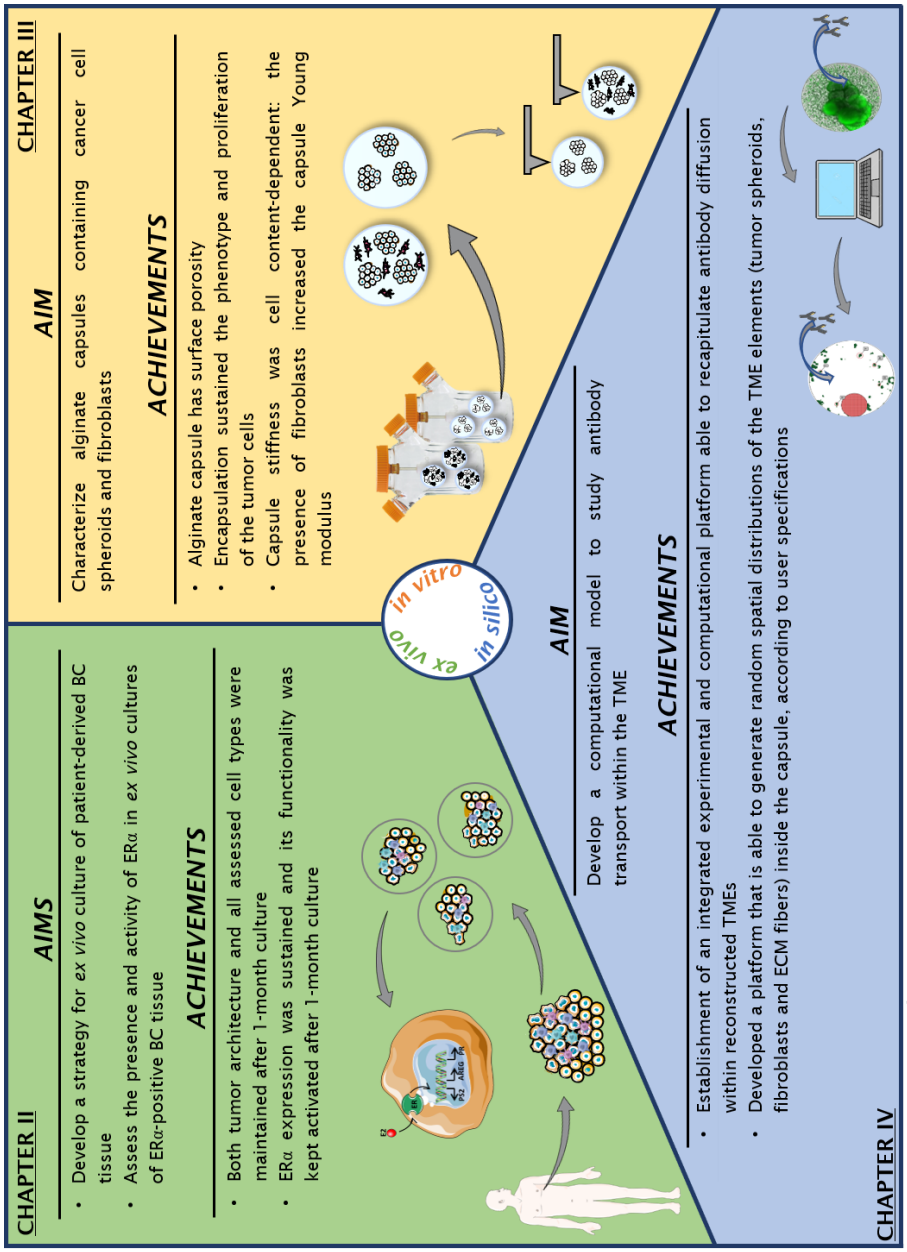

See caption in the next page.

Figure 5.1: Aim and achievements of each research chapter of the thesis. BC: breast cancer; ECM: extracellular matrix; ERα: estrogen receptor α; TME: tumor microenvironment.

1.1. Development of long-term ERα-positive breast cancer ex vivo model

Estrogen receptor α (ERα) represents one of the most relevant receptors in breast cancer (BC), since it a main driver of tumorigenesis in ERα-positive BC and, for that reason, is the focus of endocrine therapies. Despite the application of several of these therapies in the clinics for the treatment of ERα-positive BC, tumoral therapeutic resistance is an issue. To study the mechanisms that underly the resistance BC models in which ER signaling is sustained are needed.

We hypothesize that by combining alginate encapsulation and agitation-based culture, it would be possible to maintain BC tissue architecture for longer periods of time, with retention of the cellular components and, therefore functionality of ERα. When applied to partially digested ERα-positive BC tissue (tissue microstructures, **Chapter II**), we verified that this strategy allowed for the culture of microstructures with high cell viability, that maintained the original tissue architecture for at least one month. ERα expression and functionality were also assessed by protein and mRNA detection and by inhibition with a standard-of-care compound and stimulation with estrogen (an ERα ligand) and evaluation of ERα-targeted genes. We reported that gene expression of the individual ERα-targeted genes varied in BC microstructures from different patients, when the same stimuli was applied. This might be explained by the inherent heterogeneity both within and between patient-derived tissues. In agreement,

Centenera *et al.* observed a very heterogenous *PgR* mRNA level on patient-derived explants upon estrogen stimulation [1]. Gohno *et al.* reported the same results for *ESR1* and *PGR* for luminal A BC samples [2].

In the present thesis, the components responsible for the maintenance of the ERα signaling in the *ex vivo* model were not assessed. Though, we hypothesize that the maintenance of the TME, and specifically the stromal cells, greatly contribute to the preservation of ERα signaling. As a matter of fact, stromal cells are known to produce the enzyme aromatase, which increases intra-tumoral estrogen levels and, consequently, contribute to the activation of the receptor [3,4]. Additionally, in an *in vivo* mouse model of intraductal engraftment of ERα-positive cells, it was shown that the TME plays an important role in maintaining ERα-positive cells. While the mammary fat pad environment induces a basal phenotype on the implanted cells, an intraductal transplantation results in the maintenance of ERα-positive cells [5].

The relevance of our model is evident when comparing with both BC gold-standard 2D monolayer cell culture and mice models. In the first, both cell viability and ERα expression/functionality are kept, however, cells lack not only heterogeneity but also the three-dimensional (3D) architecture found in tumor tissue [6]. Most mice models are based on genetically engineered animals that develop ERα-negative tumors. In the case of xenograft mice models, hormonal supplementation is usually required, leading to unphysiological estrogen levels in mouse serum [5,7]. One exception can be found in Sflomos *et al.*, which reported an intra-ductal mouse model that does not require estrogen supplementation for the maintenance of transplanted ERα-positive cells [5].

Our results showed that alginate encapsulated microstructures have higher and more homogenous cell viability than their non-encapsulated counterparts. This may suggest that the alginate capsule has both a protective role against shear stress and a structural role in maintaining the TME inside the capsule. Additionally, the cultured microstructures revealed dense and organized/fibrillar collagen which hints that the developed culture method also allowed the maintenance of the extracellular matrix (ECM) elements. Both cell viability and ECM deposition were sustained for at least one month in culture. Some previously published explant models employed bioactive collagen as biomaterial [8,9]. One of these described culture under perfusion, attaining high cell viability sustained up to two weeks [8]. In this same report, tissue slices were treated with an anti-ERα drug and cell viability was assessed but, however, ERα signaling was not evaluated [8]. In other scaffold-free models, cell viability was maintained for only up to four [10] or seven days [11]. This reduced time hinders the use of these models to test of the long-term effects of ERα-targeted therapies.

The developed BC *ex vivo* model represents the longest reported culture time of BC tissue with maintenance of the ERα signaling and can be used to study the mechanism of resistance development against several hormonal therapies (e.g. reduction of ERα levels or upregulation of HER2 [12]). We challenged this model with fulvestrant, but other hormonal therapies could also be tested, namely selective ER modulators such as the clinically used tamoxifen. In addition, it can be used to study ERα-related signal transduction pathways, such as MAPK/Ras and PI3K/AKT signaling pathways [13]. Furthermore, it can be applied as a personalized

medicine tool since an individual patient's tumor can be challenged with several therapies prior to treatment, allowing for the selection of the best course of therapy. These models can aid in the discovery of novel therapeutic targets. In the future, the developed model can be better characterized in terms of the other BC relevant cellular receptors, such as progesterone receptor (PR) and human epidermal growth factor receptor 2 (HER2). Such a study may include the challenging of encapsulated microtissues with standard-of-care therapies that target these receptors, namely the pertuzumab therapeutic antibody.

Finally, some already available platforms to culture 3D *in vitro* cell models can be applied to patient-derived microtissues. Microfluidic techniques are suitable to be used with these, as the techniques are designed to work with small amounts of biological material. The tumor-on-a-chip strategy could be implemented with tumor tissue, rather than cell-based reconstruction of the TME. The flow of culture medium would promote both nutrient and gas diffusion and drug challenges can be easily implemented through the inlet channel. Additionally, the application of microfluidic techniques would allow for a reduction of reagent consumption. Further improvement can be attained by creating the more complex body-on-a-chip, in which tissue from several organs can be combined in a single chip. This could be used in the study of metastasis by including one tumor tissue and several healthy tissues in the chip. Bioprinting can also be used in combination with patient-derived tissues, since that technique allows to print ECM components in specific regions. This combination could be used to study how specific ECM elements can influence several cellular processes.

The work developed in **Chapter II** shows that the combination of alginate encapsulation with a dynamic culture system is a good strategy for long term maintenance of ERα-positive BC explants, *ex vivo*, and for the interrogation of the drug treatment effects on a culture setting more similar with the *in vivo* situation.

1.2. Experimental and computational cancer model as tools to study antibody targeted therapy

TME has been reported to play a role in anti-cancer therapy efficacy. For instance, ECM components such as collagen fibers and GAGs have been previously described as key influencers on the transport of therapeutic molecules [14–16]. The study of the role of several TME components on drug distribution can be achieved with the use of both computational and experimental models.

Several *in silico* models have been reported that describe and simulate tumors at different levels, ranging from molecule to tissue scale [17]. Previous contributions to the topic discuss drug distribution to and within the TME [18–20]. However, a computational model that can detail on the influence exerted by the amount or distribution of different individual TME components on antibody transport is still inexistent. As such, in **Chapter IV**, we developed a computational framework to tackle this problem.

Our group has been developing *in vitro* models of TME that include several non-cancer cell types, such as fibroblasts and immune cells, and ECM accumulation [21,22]. These models consist of alginate capsules containing the several cell types: tumor cells from distinct tumor types (such as breast, and lung cancer) and stroma. We focused on the biological characterization of these models,

including cell maturation and polarization; secretion and accumulation of cytokines and ECM, among others [21,22]. However, the mechanical characterization of these models is also relevant, as mechanotransduction can heavily influence cancer features [23–25]. Consequently, in **Chapter III**, we characterized our *in vitro* TME cell models. The mechanical properties of the alginate capsules were assessed in terms of their stiffness. Cell-filled capsules were softer than empty capsules, regardless of their cellular composition. This may be explained by the fact that the occupation of the capsule by cells interferes with alginate crosslinking, which reduces the number of binding sites between alginate and the counter-ion, finally leading to the formation of a softer hydrogel [23,24]. Different stiffnesses were also observed between mono- and co-culture. Nonetheless, the stiffness of capsules containing mono and co-cultures was within the range reported for BC tissue [26].

We further evaluated capsule surface's porosity by scanning electron microscopy. Results showed the commonly used alginate capsules are hydrogels with surface porosity, as it was already suggested in the literature [27,28]. In turn, this porosity allows for both gas and nutrient exchange [28]. We concluded that the average pore size in alginate capsules was c.a. 100 nm, 1 order of magnitude larger than antibodies (14.5 nm x 8.5 nm x 4.0 nm). As these are the largest therapeutic molecules [29], this would suggest that the capsule is not a physical barrier and that the *in vitro* model may be used to address antibody-based therapies. In fact, in **Chapter IV**, we developed a framework to study antibody transport consisting of an *in silico* model, benchmarked with experimental data acquired using Light Sheet Fluorescence Microscopy (LSFM) applied to the *in vitro* model characterized in **Chapter III**. To the best of

our knowledge: (1) this work represents the first usage of LSFM to live track antibody distribution within the TME; (2) no study exists detailing the influence of the amount or distribution of different individual TME components on antibody transport. As a matter of fact, routine assessment and tracking of antibody distribution within the spheroids or xeno-transplanted tumors is performed by either: a) incubation of antibodies or fragments followed by detection using avidin-biotin method and peroxidase [30], or b) by the use of fluorescence labelled antibodies and detection by immunohistochemistry using microscopy techniques [31,32]. We started by comparing confocal microscopy and LSFM. The selection of LSFM technique agrees with the conclusions of Lazzari *et al.*, in which they show that it is preferable to confocal microscopy on the assessment of drug distribution in tumor co-culture aggregates. As the latter only allows scanning up to a depth of 100 μm, information on deeper layers is lost, a problem that is circumvented by using LSFM [33]. When analyzing the fluorescence profiles for several cell clusters within the alginate capsule, we observed a weak correlation between cell cluster distance to capsule periphery and the time needed to detect a fluorescence signal. This might be explained by either different amounts of antigen on the surface of different cells or that the capsule interior has some degree of heterogeneity caused by localized ECM accumulations.

In **Chapter IV**, the transition from experimental to computational models derive from two key assumptions regarding antibody distribution. Firstly, we assumed that antibody transport is purely diffusive under Fick's law; and secondly, that antigen saturation during antibody binding follows a generic exponential growth curve. To test this hypothesis, we digitized the central

section of a co-culture alginate capsule, obtained using LSFM. To this digitized section, we applied what can described as a "hybrid" model, similar to the majority of recently developed models [34] of antibody transport. We used a combination of an on-lattice model (i.e. cell distribution) with continuous model techniques (i.e. solving the diffusion equation with a finite difference approach). Using the developed model, we created predictive computational profiles that closely mirror the observed experimental ones. As we used the experimental data to benchmark our computational model, any discrepancies between the two models hint at the absence of important components of the system in the computational model. The lack of discrepancies allows us to conclude that, as we previously assumed, antibody diffusion is the main transport mechanism within the alginate capsules. The benchmarked code was further used to generate virtual capsules. For this, we applied a stochastic tuned approach, which allows the user to set specific features and assess antibody diffusion patterns under different initial conditions. With this approach, we tested the influence of collagen fibers on antibody distribution profiles for the two identical capsules. As collagen fibers act as perfect barriers, our results show that their presence severely hinders the ability of the antibody to reach the target cells, as was experimentally demonstrated by Davies *et al.* and Kihara *et al.* [14,16].

In **Chapter III** we also evaluated ECM accumulation. This could clarify the differences observed between the stiffness of mono- and co-culture capsules (observed in **Chapter III**). Furthermore, it would help in the confirmation of the existence of a heterogeneous medium (an inherent physical barrier to antibody transport) present on the co-culture capsule (assessed in **Chapter**

IV). In fact, fibroblasts are the major producers of collagen in the TME [35]. Collagen has been linked to an increased stiffness [36] and to biomolecule hindered diffusion [14,16]. Collagen and GAGs deposition, which were assessed by immunohistochemistry were low in mono- and co-culture capsules. Conversely, we had observed higher levels using other detection techniques in other [21,22]. It should be possible however to increase ECM accumulation by implementing modifications in the alginate itself. Alginate alone does not promote cell adhesion, due to lacking of binding sites [28] which might be limiting ECM production. However, when alginate is combined with other polymers (e.g. chitosan) or ECM components (e.g. fibronectin peptide arginine-glycine-aspartic acid), cell adhesion is enhanced [28]. This helps promoting a tissue-like environment, where cells are adhered rather than in suspension.

The *in vitro* model characterization presented on **Chapter III** furthered the knowledge on both surface porosity and mechanical features of alginate capsules, which are extensively employed in several applications [21,22,37,38]. The model can be further improved by adding extra cell types (endothelial cells or immune cells) and assess how these variations can influence the mechanical properties of alginate capsules. Further testing would be required to verify the influence of cell types and/or ECM deposition on the surface pore size distribution. Additionally, as electrostatic charges can also play a role in drug-TME interactions, the alginate capsule's electrical charge should be also evaluated.

In **Chapter IV**, we showed that a combination of LSFM applied to 3D *in vitro* cell models and computational modelling is a stepping-stone to study therapeutic antibody distribution within a tumor. The developed *in silico* model can be used as a "testing

tool", in which potential experimental conditions can be tested before being pursued experimentally. This model can also work as a predictive tool, hinting at which specific TME conditions produce a given drug diffusion output. In the future, the computational framework could be further developed (and benchmarked) to account for the complexity of the *ex vivo* model developed in **Chapter II**. This in turn would imply a further knowledge on the diffusion barriers that exist in real tissue, as opposed to a reconstructed one. In the *ex vivo* model, a plethora of cell types and diffusion barriers (e.g. significant fibrillar collagen deposition as shown in **Chapter II**) are inherently present. By contrast, in *in vitro* models only some cell types are available, and ECM is not in its native form.

The *in silico* model could be enhanced by coupling it with a detailed measurement of the diffusivity coefficient by fluorescence recovery after photobleaching (FRAP) or fluorescence correlation spectroscopy (FCS). These can be performed in different regions of the capsule over time and would allow a better description of the experimental data, helping to decipher intra-capsule heterogeneity. In the developed computational model, we assumed a constant antibody diffusivity in the TME but this might not be the case. Having clear data on the spatio-temporal evolution of this coefficient would result, thus, on higher predictive power for the computation framework. We developed the *in silico* model in 2D conditions, due to computational power constraints. While 3D modelling would be more conclusive, using purely 2D models we were able to hint at a non-radial antibody diffusion. Labeling of cells with a fluorescence tracer prior to antibody challenging would allow to discern between cells with bound and unbound antibody.

This can help identify both possible regions where preferential diffusion of antibody occurs and regions where the antibody cannot reach.

2. Final Remarks

With this thesis we proposed three different types of TME models that can be used as mutually complementing tools for the assessment of targeted drug response. Overall, this work expanded the knowledge in the fields of experimental and computational cancer models and targeted cancer therapies.

Both experimental models described in the thesis were maintained in a dynamic system in which culture progression can be evaluated using non-destructive sampling [39]. Likewise, agitation helped sustaining high cell viability by ensuring a homogeneous distribution of both oxygen and nutrients as well as a reduced thermochemical gradients [40]. The *ex vivo* model maintained all the TME components architecturally organized as in the human tumors. Due to its human origin, the amount of tissue that can be obtained is a major problem. This in turn can be a major disadvantage in drug screening assays. Conversely, the *in vitro* model is based on virtually unlimited cell sources, which makes it suitable for assays requiring large numbers of cells. In these models, interpreting results is facilitated due to the easier separation and consequent analysis of the several components of the model. However, since the tumor is “reconstructed” in the lab, native tissue architecture is difficult to replicate. Finally, *in silico* models are cost-efficient when compared with cell and tissue culture. They allow for a pre-evaluation of several different

conditions before pursuing them experimentally. Nonetheless, they cannot simultaneously mimic all the biological and chemical processes that naturally occur in cancer.

To conclude, *ex vivo, in vitro* and *in silico* models should not be seen as separate tools but pieces of a larger puzzle. While strong as individual approaches to the study of cancer, they are at their finest when integrated in a larger framework.

3. References

1. Centenera, M. M. *et al.* A patient-derived explant (PDE) model of hormone-dependent cancer. *Mol. Oncol.* **12**, 1608–1622 (2018).
2. Gohno, T. *et al.* Individual transcriptional activity of estrogen receptors in primary breast cancer and its clinical significance. *Cancer Med.* **1**, 328–337 (2012).
3. Yamaguchi, Y. Microenvironmental Regulation of Estrogen Signals in Breast Cancer. *Breast cancer* **14**, 175–181 (2007).
4. Santen, R. J. *et al.* Estrogen production via the aromatase enzyme in breast carcinoma: Which cell type is responsible? *J. Steroid Biochem. Mol. Biol.* **61**, 267–271 (1997).
5. Sflomos, G. *et al.* A Preclinical Model for ERa-Positive Breast Cancer Points to the Epithelial Microenvironment as Determinant of Luminal Phenotype and Hormone Response. *Cancer Cell* **29**, 407–422 (2016).
6. Riedl, A. *et al.* Comparison of cancer cells in 2D vs 3D culture reveals differences in AKT-mTOR-S6K signaling and drug responses. *J. Cell Sci.* **130**, 203–218 (2017).
7. Articles, A. C. Ö., Sflomos, G. & Brisken, C. The challenges of modelling hormone-receptor positive breast cancer in mice. *Endocr Relat Cancer* **25**, 1–37 (2018).
8. Muraro, M. G. *et al.* Ex-vivo assessment of drug response on breast cancer primary tissue with preserved microenvironments. *Oncoimmunology* **6**, 1–12 (2017).
9. Dolcimascolo, A., Calabrese, G., Conoci, S. & Parenti, R. *Innovative Biomaterials for Tissue Engineering*. *Biomaterial-supported Tissue Reconstruction or Regeneration* (2019).
10. van der Kuip, H. *et al.* Short term culture of breast cancer tissues to study the activity of the anticancer drug taxol in an intact tumor environment. *BMC Cancer* **6**, 1–11 (2006).
11. Naipal, K. A. T. *et al.* Tumor slice culture system to assess drug response of primary breast cancer. *BMC Cancer* **16**, 1–13 (2016).
12. Osborne, C. K. & Schiff, R. Mechanism of endocrine resitance in breast cancer. *Annu Rev Med.* **62**, 233–247 (2011).
13. Fuentes, N. & Silveyra, P. Estrogen receptor signaling mechanisms. *Adv Protein Chem Struct Bioll* **116**, 135–170 (2019).
14. Kihara, T., Ito, J. & Miyake, J. Measurement of biomolecular diffusion in extracellular matrix condensed by fibroblasts using fluorescence correlation spectroscopy. *PLoS One* **8**, e82382 (2013).
15. Netti, P. A., Berk, D. A., Swartz, M. A., Grodzinsky, A. J. & Jain, R. K. Role of extracellular matrix assembly in interstitial transport in solid tumors. *Cancer Res.* **60**, 2497–2503 (2000).
16. Davies, C. de L., Berk, D., Pluen, A. & Jain, R. Comparison of IgG diffusion and extracellular matrix composition in rhabdomyosarcomas grown in mice versus in vitro as spheroids reveals the role of host stromal cells. *Br. J. Cancer* **86**, 1639–1644 (2002).
17. Materi, W. & Wishart, D. S. Computational Systems Biology in Cancer: Modeling Methods and Applications. *Gene Regul. Syst. Bio.* **1**, 91–110 (2007).
18. Groh, C. M. *et al.* Mathematical and computational models of drug transport in tumours. *J. R. Soc. Interface* **11**, (2014).
19. Chen, J., Weihs, D. & Vermolen, F. J. Computational modeling of therapy

on pancreatic cancer in its early stages. *Biomech. Model. Mechanobiol.* **19**, 427–444 (2019).
20. Rejniak, K. A. *et al.* The role of tumor tissue architecture in treatment penetration and efficacy: an integrative study. *Front. Oncol.* **3**, 1–13 (2013).
21. Estrada, M. F. *et al.* Modelling the tumour microenvironment in long-term microencapsulated 3D co-cultures recapitulates phenotypic features of disease progression. *Biomaterials* **78**, 50–61 (2016).
22. Rebelo, S. P. *et al.* 3D-3-culture: A tool to unveil macrophage plasticity in the tumour microenvironment. *Biomaterials* **163**, 185–197 (2018).
23. Dolan, E. B. *et al.* Advanced Material Catheter (AMCath), a minimally invasive endocardial catheter for the delivery of fast-gelling covalently cross-linked hyaluronic acid hydrogels. *J. Biomater. Appl.* **33**, 681–692 (2018).
24. Tian, X. & Chen, X. Effects of cell density on mechanical properties of alginate hydrogel tissue scaffolds. *J. Biomimetics, Biomater. Tissue Eng.* **19**, 77–85 (2014).
25. Taubenberger, A. V *et al.* 3D Microenvironment Stiffness Regulates Tumor Spheroid Growth and Mechanics via p21 and ROCK. *Adv. Biosyst.* **1900128**, 1–16 (2019).
26. Samani, A., Zubovits, J. & Plewes, D. Elastic moduli of normal and pathological human breast tissues: An inversion-technique-based investigation of 169 samples. *Phys. Med. Biol.* **52**, 1565–1576 (2007).
27. Arica, B. *et al.* In vitro and in vivo studies of ibuprofen-loaded biodegradable alginate beads. *J. Microencapsul.* **22**, 153–165 (2005).
28. Kang, S.-M., Lee, J.-H., Huh, Y. S. & Takayama, S. Alginate Microencapsulation for Three-Dimensional In Vitro Cell Culture. *ACS Biomater. Sci. Eng.* (2020)
29. Tan, Y. H. *et al.* A Nanoengineering Approach for Investigation and Regulation of Protein Immobilization. *ACS Nano* **2**, 2374–2384 (2008).
30. Sutherland, R., Buchegger, F., Schreyer, M., Vacca, A. & Mach, J. P. Penetration and binding of radiolabeled anti-carcinoembryonic antigen monoclonal antibodies andtheir antigen binding fragments in human colon multicellular tumor spheroids. *Cancer Res.* **47**, 1627–1633 (1987).
31. Minchinton, A. I. & Tannock, I. F. Drug penetration in solid tumours. *Nat. Rev. Cancer* **6**, 583–592 (2006).
32. Lee, C. M. & Tannock, I. F. The distribution of the therapeutic monoclonal antibodies cetuximab and trastuzumab within solid tumors. *BMC Cancer* **10**, (2010).
33. Lazzari, G. *et al.* Light sheet fluorescence microscopy versus confocal microscopy: in quest of a suitable tool to assess drug and nanomedicine penetration into multicellular tumor spheroids. *Eur. J. Pharm. Biopharm.* **142**, 195–203 (2019).
34. Chamseddine, I. M. & Rejniak, K. A. Hybrid modeling frameworks of tumor development and treatment. *Wiley Interdiscip. Rev. Syst. Biol. Med.* **12**, 1–16 (2019).
35. Yamaba, H. *et al.* Morphological change of skin fibroblasts induced by UV Irradiation is involved in photoaging. *Exp. Dermatol.* **25**, 45–51 (2016).
36. Cox, T. R. & Erler, J. T. Molecular pathways: Connecting fibrosis and solid tumor metastasis. *Clin. Cancer Res.* **20**, 3637–3643 (2014).
37. Bochenek, M. A. *et al.* Alginate encapsulation as long-term immune protection of allogeneic pancreatic islet cells transplanted into the omental bursa of macaques. *Nat Biomed Eng.* **2**, 810–821 (2018).

38. Torres, A. L. *et al.* Guiding morphogenesis in cell-instructive microgels for therapeutic angiogenesis. *Biomaterials* **154**, 34–47 (2018).
39. Kinney, M. A., Hookway, T. A., Wang, Y. & McDevitt, T. C. Engineering three-dimensional stem cell morphogenesis for the development of tissue models and scalable regenerative therapeutics. *Ann. Biomed. Eng.* **42**, 352–367 (2014).
40. Santo, V. E. *et al.* Adaptable stirred-tank culture strategies for large scale production of multicellular spheroid-based tumor cell models. *J. Biotechnol.* **221**, 118–129 (2016).

ITQB-UNL | Av. da República, 2780-157 Oeiras, Portugal
Tel (+351) 214 469 100 | Fax (+351) 214 411 277

www.itqb.unl.pt